Ducted Propeller Underwater Radiated Noise Mitigation through Leading-Edge Tubercle Modifications

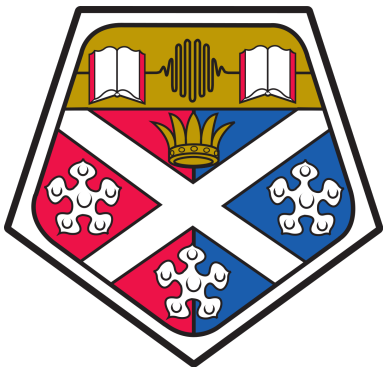

Callum Stark

Department of Naval Architecture, Ocean and Marine Engineering

University of Strathclyde

In fulfillment of the requirements for the degree of

Doctor of Philosophy

2023

This thesis is the result of the author's original research. It has been composed by the author and has not been previously submitted for examination which has led to the award of a degree.

Signed:

Date: 10/01/2023

Acknowledgements

My PhD journey has not been an easy one and nor did I expect it to be. There were many obstacles to overcome, particularly the unforeseen coronavirus pandemic which was a challenge for everyone all over the world and resulted in a lockdown only 6 months into my PhD journey. But, undertaking a PhD will always present obstacles and with perseverance and a positive mindset, they can be overcome.

Although a PhD is largely individual research, I could not have completed it to such a standard without a number of role models, friends and family who challenged and supported me throughout my journey.

Firstly, I would like to express my appreciation and thanks to my primary supervisor, Dr. Weichao Shi without whom this research would not have been possible. For pushing me to deliver the best quality research I could and fulfill my potential. I would like to also thank my secondary supervisor, Prof. Mehmet Atlar for sharing his knowledge and for always being positive and encouraging me.

Secondly, I would like to thank my colleagues and friends at Applied Biomimetics Marine Hydrodynamics Research Group; Moritz, Yunxin, Hongbo, Yang and Abel for their support. Also, I would like to thank my friend Savas for sharing his hydroacoustic knowledge and encouragement. I would like to wish all of them the best in the future. I would also like to thank and acknowledge BAE Systems Plc. for providing me a studentship to conduct the research.

Lastly, I would like to thank my mum, dad and sister, for giving me a great childhood and instilling in me the drive and hunger to be the best I can be both as a person and in my professional life.

This thesis is dedicated to my mum, Emma and dad, Frank

Abstract

Anthropogenic underwater radiated noise (URN) has a negative impact on marine life, disrupting key biological functions such as communicating, navigating and catching prey. One of the largest contributors to URN is the various types of marine vessels that occupy the world's oceans today and of this, the most significant proportion of the noise is emitted from the propulsor. Due to increasing public awareness on this topic, international bodies such as the International Maritime Organization (IMO) published non-mandatory guidelines in 2014 to accelerate the reduction in shipping URN.

Over the last few decades, there has been growing interest and research around leading-edge (LE) tubercles which are located on humpback whale pectoral fins. They are believed to enhance the manoeuvrability of the marine mammal through prolonged flow attachment and have shown to improve the hydrodynamic and noise performance of marine applications through the introduction of counter-rotating streamwise vortex pairs which alter the local flow-field. But, this concept has yet to be applied to ducted propellers and based on the available literature, they could have the capability to address the needs of the shipping industry by reducing the URN signature of marine vessels.

Therefore, this research study focuses on the noise mitigation capability of LE tubercles on ducted propellers. Two key areas of noise

mitigation were identified through a review of the state-of-the-art literature; LE tubercles applied to the duct to alter the vortex development in the ducted propeller slipstream and therefore, mitigate turbulence and vorticity-induced noise and LE tubercles applied to the blades to influence the sheet cavitation development over the blades and thus, mitigate cavitation-induced noise. This study aims to establish a proof of concept for both identified noise mitigation techniques and understand the core fundamental fluid dynamic mechanisms behind the performance changes using a numerical methodology known as Computational Fluid Dynamics (CFD).

In summary, it was found that through an initial design and optimisation study, LE tubercle modifications on the duct could improve the duct thrust performance, although this was dependant on the amplitude and wavelength of the tubercle geometry, the change in amplitude was more significant than the change in wavelength. Through further detailed analysis of the optimised LE tubercle modified duct it was found the duct thrust could be improved by over 7% due to the compartmentalisation of the flow separation on the outside of the duct with minimal impact on the overall hydrodynamic performance of the propulsor. Also, it could reduce the far-field URN by over 3dB overall sound pressure level (OASPL) through disruption of the coherent wake structure in the propeller slipstream.

It was found that LE tubercle modified ducted propeller blades could improve propulsive efficiency by up to 6.5% when comparing at the same thrust loading condition. Additionally it was found that the LE tubercle modified ducted propeller blades could produce a noise reduction in the far-field at most test conditions considered to a maximum

of 6dB OASPL and reduce the blade load fluctuation. Through analysis of the flow-field, it was found that this was predominantly due to the introduction of the counter-rotating vortex pairs and subsequent alteration of the local pressure field over the blade suction side, which ultimately reduced the sheet cavitation severity by a maximum of up to 50% over the blade surface by funnelling the cavitation behind the tubercle trough region.

To compliment the previous studies in the model scale, an investigation into the scaling effect of LE tubercle modified duct and propeller performance was conducted by performing an analysis of the optimised geometries at a larger scale. It was found that the duct thrust performance could be improved by a maximum of 3.6% with minimal impact on the overall hydrodynamic performance of the propulsor. The increase in scale and subsequent increase in Reynold's number resulted in the inception of LE flow separation to occur at a much later advance ratio on the outer duct section than in the model scale study and therefore no flow separation compartmentalisation was observed by the LE tubercles within the propulsor operational envelope. A reduction in far-field noise of 4dB OASPL was predicted and this was predominantly due to the disruption on the coherent wake structure in the propeller slipstream.

For the LE tubercle modified ducted propeller blades in the full scale study, it was found that a cavitation reduction of over 60% was observed due to the cavitation funnel effect and comparing at the same thrust loading condition, the propulsive efficiency could be enhanced by 7.5%. In the far-field, a maximum reduction of 13dB OASPL was observed while the blade load fluctuation was reduced which was pre-

dominantly due to the reduction in cavitation severity over the blades due to the LE tubercle cavitation funnel effect. Therefore, although a difference in magnitude was predicted in LE tubercle performance change between model and full scale, the general conclusions regarding hydrodynamic and hydroacoustic performance enhancement agreed well with the previous model scale studies.

Contents

List of Figures

List of Tables

LIST OF TABLES

Chapter 1

Introduction

The main aim of this chapter is to introduce the PhD project, which aims to mitigate the noise signature of marine ducted propulsors. The motivation behind the study is described in Section 1.1, followed by the main aim and objectives outlined in Section 1.2. The overview of the chapters within the thesis is defined in Section 1.3 with a summary of Chapter 1 presented in Section 1.4.

1.1 Motivation

Anthropogenic, or human-made, underwater radiated noise (URN) has a detrimental impact on the marine acoustic environment which is relied upon by a variety of marine organisms to understand the world around them. The shipping industry is one of the most ubiquitous sources of URN and because of increasing awareness of this, international bodies such as the International Maritime Organization (IMO) published non-mandatory guidelines, MEPC.1/Circ.833 [1], in 2014 to to give general advice related to the mitigation of underwater radiated noise to designers, ship operators, and owners. The guidelines focus on the primary sources of URN which are from the propeller, hull form and on-board

machinery while giving maintenance recommendations such as the cleaning of the hull. But, it was noted that there are still significant challenges to overcome before setting future URN reduction targets as noise is a complex issue and that further research in the measurement and reporting of shipping URN was necessary. Careful consideration should also be given to avoid implications with other environmental regulations such as the energy efficiency design index (EEDI) with the aim to reduce greenhouse gas (GHG) emissions from ships, as URN reduction should not come at a cost of increased ship fuel consumption and GHG emissions.

Additionally, this issue was put on the political agenda of the Marine Strategy Framework Directive (MSFD), D11 2017/848 [2], for a relevant qualitative descriptor for a good environmental status in the marine environment by the European Commission. It set out how to assess the extent to which good environmental status is being achieved for impulsive and continuous noise with the Member States to establish threshold values for these levels through cooperation at Union level with consideration to the regional and subregional specificities. More recently in early 2022, the IMO met with the aim to to provide updated recommendations based on the latest developments in ship design and technology and to address the barriers to their uptake in an effort towards a significant and measurable reduction of underwater radiated noise from ships and this will be submitted to the Marine Environment Protection Committee (MEPC) in 2023. Therefore, the reduction of the URN signature, which was typically only a consideration for naval vessels with special operational requirements, is now believed to be a key early design factor for vessels of the future.

Through the acknowledgement of this issue by the European Comission and the IMO, governments are becoming more aware of the need for URN reduction in the shipping industry. This has also led to a number of European Union (EU) funded projects related to reducing shipping URN, such as PIAQUO, a

continuation of EU-funded project AQUO. The three year project aims to implement the methodologies and tools developed during the previous project, AQUO. PIAQUO also involves port authorities and will look to create incentives to encourage the reduction of shipping URN at a shipowner level. Class societies like Bureua Veritas (BV), Det Norske Veritas (DNV) and Lloyds Register are now also involved in advising clients and developing their own URN class notations to increase awareness amongst the shipping community of the importance of reducing URN and provide URN calculations at the design stage so ships can achieve compliance and limit their environmental impact. Currently, the shipping industry is not ready to address the shipping URN challenge without the development of accurate standardised noise measurement methodologies and noise mitigation technologies that do not compromise ship fuel efficiency. Through technological developments, setting targets for shipping URN reduction will become much more feasible through mandatory policies and shipowner incentives like port fee discounts while class societies will be key in providing the shipowners a service to predict URN at an early stage and mitigate impact on the marine acoustic environment. Thus, it is clear that there are opportunities in many areas of the shipping industry from technology developers to policy makers to address the challenge of reducing shipping URN.

Generally, the most dominant source of shipping URN is from the propeller and therefore, it is of significant interest when considering the reduction of ship-related URN. The development of propulsor noise mitigation concepts focus heavily on open propellers and because of this, the development of noise mitigation concepts for ducted propellers is left behind. Ducted propellers are commonly used for the propulsion of tugboats and fishing vessels and so, noise mitigation concepts developed for ducted propellers could positively impact the propulsor noise reduction of such vessels which would otherwise be forgotten about if sole

focus was given to open propellers. One potential source of inspiration to develop such concepts is from the natural world.

Millions of years of evolution has shaped the world around us and because of this, the natural world is one of the best places to look for inspiration for human technology and design. This is known as biomimetics and has provided our world with many incredible designs such as the gecko's ability to climb on smooth surfaces inspiring the development of adhesives and the flying ability of birds inspiring the development of aircraft. Nature will always have potential solutions to our problems and so, it could provide a solution to the challenge of reducing shipping URN of ducted propulsors. Ironically, a marine mammal negatively impacted by URN emitted from marine vessels could be the answer to our problems. The humpback whale (*megaptera novaeangliae*) possesses small bumps located on the pectoral fins which aid in their ability to perform acrobatic maneuvers to catch prey. The small bumps are known as leading-edge (LE) tubercles and have shown the capability to improve the aero/hydrodynamic and noise performance on applications such as aerofoils [3; 4; 5]. The marine propulsor and duct are very similar to the aerofoil as their hydrodynamic performance is highly related to the lift and drag force vectors. In addition to this, when marine propulsors operate in off-design conditions they can experience phenomena such as flow separation and cavitation. In the presence of such phenomena in the marine environment, LE tubercles have shown to modify the flow separation behaviour [6] and have the potential to improve the hydrodynamic and noise performance of rotating machinery such as tidal turbines in cavitating conditions [7; 8]. Thus, LE tubercles may provide benefits which could address the present challenges and needs of the maritime industry related to the hydrodynamic and noise performance of marine ducted propulsors.

1.2 Aim and Objectives

1.2.1 Aim

The aim of the research study was defined based upon the author's motivation and the literature review presented in Chapter 2. The aim of the research study was as follows:

- To explore the bio-inspired leading-edge tubercles capability to reduce the underwater radiated noise (URN) of a reference marine ducted propulsor and minimise any compromise to its hydrodynamic performance.

1.2.2 Objectives

In order to achieve the above aim, the following objectives were specified:

1. Review the literature on state-of-the-art URN reduction techniques for marine propulsors and the application of LE tubercles and their influence on hydrodynamic and noise performance; conduct a comprehensive review to have a broader understanding of the research topic and identify the knowledge gaps which need to be addressed within the research area by the proposed research study and finally, propose a suitable research methodology to meet the aim and objectives of the research,

2. Select a reference marine ducted propulsor design and develop a tubercle modelling procedure to explore the effect of a LE tubercle modified ducted propulsor relative to the performance of the reference marine ducted propulsor,

3. Conduct an initial design and optimisation of the marine ducted propulsor with LE tubercles to achieve an optimised geometry of the LE tubercle profile in an economical manner,

4. Further analyse the optimised LE tubercle geometry and compare the hydrodynamic and noise performance of marine ducted propulsor with LE tubercles applied to the duct to the reference ducted propulsor (without tubercles) in the model scale, achieve an understanding into the influence of LE tubercles applied to the duct on the fundamental fluid dynamics in a ducted propulsor context,

5. Compare the hydrodynamic and noise performance of marine ducted propulsor with LE tubercles applied to the propeller blades to the reference ducted propulsor (without tubercles) in the model scale, achieve an understanding into the influence of LE tubercles applied to the blade on the fundamental fluid dynamics in a ducted propulsor context,

6. Investigate the scaling of the performance of LE tubercle modified ducted propellers.

1.3 Overview of the Thesis

The above aim and objectives of the research were achieved by the work conducted in this study presented in the nine chapters of the thesis, described as follows:

Chapter 1 introduced the research work presented in the thesis including the motivation of the author, aim and objectives of the research as well as the layout of the thesis as a condensed introduction to the research carried out.

Chapter 2 presents a comprehensive literature review on the URN reduction techniques for marine propulsors and the influence of LE tubercle modifications on the aero/hydrodynamic and noise performance of various applications, which targets "*Objective 1*". This was conducted to gain a broader understanding of the research topic and hence refine the aim and objectives of the thesis by identifying the knowledge gaps which needed to be addressed in this research.

Chapter 3 focuses on "*Objective 2*" whereby a reference ducted propeller was selected and the geometry is outlined. In addition, the tubercle modelling procedure is introduced.

Chapter 4 focuses on describing the numerical methodology used to achieve the aim and objectives of the thesis. The numerical methodology verification and validation studies are also presented within this chapter.

Chapter 5 discusses the design and optimisation of the LE tubercle geometry for a benchmark duct. The geometrical parameters of the LE tubercle geometry as applied to the duct were varied and the impact on the duct thrust was analysed. As such, an "optimum" design of tubercle was proposed for further analysis, addressing "*Objective 3*".

Chapter 6 discusses the influence of the optimised LE tubercle geometry applied to the duct on the hydrodynamic and noise performance of the reference ducted propulsor. The influence of the LE tubercles on the fundamental fluid dynamics in a marine ducted propulsor context is also examined, thus addressing "*Objective 4*".

Chapter 7 discusses the influence of LE tubercle modified ducted propeller blades on the hydrodynamic and noise performance of the ducted propulsor. The influence of the LE tubercles on the fundamental fluid dynamics in a marine ducted propulsor context is also examined, thus addressing "*Objective 5*".

Chapter 8 enhances the understanding of LE tubercle modifications on marine ducted propulsors by discussing the full scale study conducted to investigate the scaling effect on the hydrodynamic and noise performance enhancements by LE tubercle modifications found in the previous model scale studies in Chapter 6 and 7, addressing "*Objective 6*".

Chapter 9 presents an overall review of the research study conducted by scrutinising the aim and objectives as well as the main conclusions drawn from the

research work. The chapter also recommends further work for future studies.

1.4 Summary

Chapter 1 introduced the research study presented in this thesis. The motivation, aim and objectives of the research were described as well as the layout of the thesis to give a general introduction to the research study conducted.

Chapter 2

Literature Review

This chapter contains the review of literature conducted to establish the initial aim and objectives of the research study. This was achieved by identifying the current knowledge gaps in the state-of-the-art literature. Firstly, underwater radiated noise sources with a focus on propeller noise and the current mitigation technologies that are under development or implemented within the maritime industry today were reviewed (Section 2.1). This was conducted to understand the various propeller noise sources and how they can be reduced through current noise mitigation concepts that are commercially available or under development. Then, the fundamental flow behaviour and previous application of the bio-inspired concept, leading-edge tubercles, were reviewed to investigate the feasibility of the concept to achieve the main aim of the thesis (Section 2.2). Finally, the prediction and measurement techniques used to quantify underwater radiated noise were reviewed to establish the methodologies available to deliver the aim and objectives of the research study (Section 2.3). A summary of the findings and identified gaps within the state-of-the-art are given in Section 2.4.

2.1 Underwater Radiated Noise

Anthropogenic Underwater Radiated Noise (URN) has become an increasing concern amongst the scientific community due to the negative impact it can have on marine life, where it can disrupt key biological functions such as communication, navigation and catching prey [9]. Marine vessel URN contributes heavily to anthropogenic URN and is rising exponentially because of the continual increase in the world's oceans traffic [10]. A specialist committee on hydrodynamic noise for the 27^{th} International Towing Tank Conference (ITTC) stated that marine vessel URN could be split into three main categories; machinery noise comprising of of the propulsion and auxiliary components, hydrodynamic noise caused by the flow of water along the ship hull and behind the vessel and finally, propeller noise caused by flow phenomena during vessel operation and interaction with the hull. Of the three categories, propeller noise is generally the most dominant [11].

2.1.1 Propeller Noise Sources

Propeller noise sources can be categorised into two types, non-cavitating and cavitating noise [12]. If cavitation is present, such as sheet and tip vortex cavitation, this typically dominates the noise spectrum when compared to non-cavitating noise. Cavitation is the formation and implosion of water vapour cavities caused by the decrease (below the liquid vapour pressure) and increase in pressure as water moves across a propeller blade and this can cause efficiency loss, hull/shaft vibrations, blade erosion and increased URN levels [12]. But, in conditions like the larger water depths submarines and torpedoes operate at, cavitation is usually not present so the non-cavitating noise can be significant [13]. Figure 2.1 shows the various types of marine propeller sources in both cavitating and non-cavitating conditions.

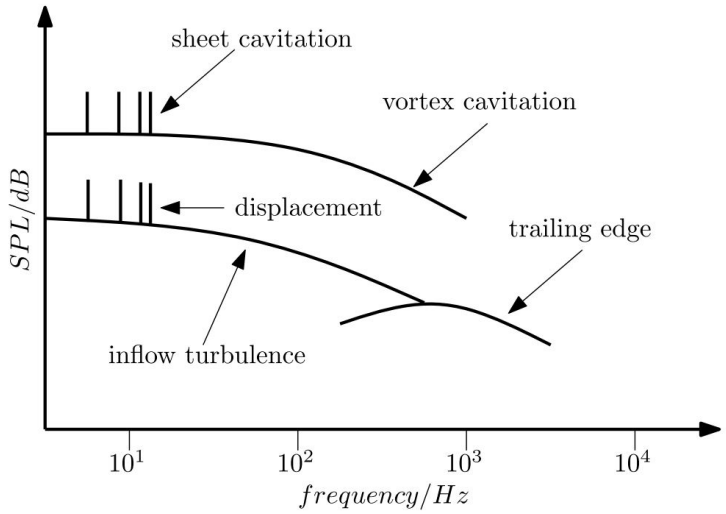

Figure 2.1: Marine propeller noise sources (reproduced from [14])

In the non-cavitating conditions, propeller noise is generated by many mechanisms which can generally be categorised into two types, discrete frequency also known as tonal noise and continuous spectrum also known as broadband noise. Firstly, the periodic blade rotation through the fluid will cause tonal noise, which is known as the blade-passage frequency (BPF) and is a product of the rotation rate and the blade number. In addition, the phenomenon known as propeller singing can cause tonal noise. This occurs due to the resonance between the local natural frequency of the propeller blade tip and the vortex shedding frequency at the trailing edge of the blade. This can occur in non-cavitating conditions and can be avoided through careful analysis of the propeller design [15]. Structural resonance is also a key consideration within propeller design as it could cause the propeller to fail, so quantifying the natural resonance of the marine propeller is paramount and reduces the risk of propeller failure. Broadband noise can be generated by the various turbulence and vorticity sources that a propeller can encounter or induce as a consequence of its rotational motion in the medium [11].

Such sources can include inflow turbulence and the various types of vortex

shedding that can occur, such as blade tip, flow separation and trailing edge vortices [14]. Figure 2.2 depicts the various types of turbulence and vortex mechanisms and a representative noise frequency spectra for such sources. In the context of marine propellers, Figure 2.3 illustrates the various types of vortex mechanisms that can occur in ducted and open propeller slipstreams, although the strength and structure of the vortex mechanisms will vary with parameters such as blade design and loading conditions [16].

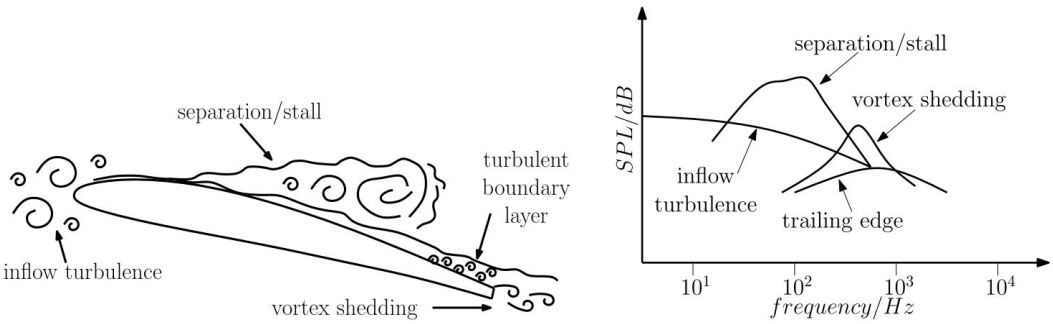

Figure 2.2: Turbomachinery broadband noise sources (left) and a representative noise frequency spectra (right) (reproduced from [14])

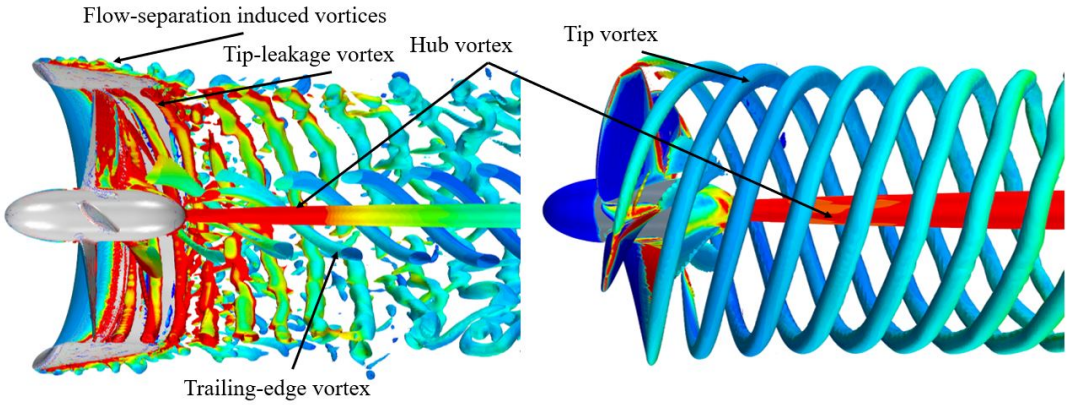

Figure 2.3: Typical vortex mechanisms present in ducted and open propeller slipstreams

In conditions where cavitation is present, there can be many different types

of cavitation (see Figure 2.4) that can arise on a marine propeller and contribute to the URN signature such as tip vortex, bubble, sheet and cloud cavitation. The bubbles created due to the low pressure regions induced by the rotating propeller collapse and this creates shockwaves in the flow which can be audible. Cavitation causes broadband noise and discrete peaks at harmonics of the blade passage frequency in the underwater noise spectrum. The broadband noise is caused by growth and collapse of a vast amount of individual cavitation bubbles in water while the discrete noise peaks are caused by the volume fluctuations of the sheet and tip vortex cavities [1]. The presence of the hull induces a non-uniform inflow due to the hull wake and this can influence the cavitation extent, type and thus the URN levels from the propulsor when compared to uniform flow conditions. Through experimental test campaigns, it was shown that when in the presence of non-uniform flow, the noise of marine propellers can increase between 10-15dB when compared to uniform flow due to cloud cavitation being present at scale, which is unsteady at large scales and can have violent bursts. Whereas in uniform flow, only tip vortex cavitation along with leading-edge suction side sheet cavitation was observed. However, a significant increase between 20-30dB in noise was observed when comparing the propeller operating at the range of cavitating conditions when compared to the non-cavitating conditions [17].

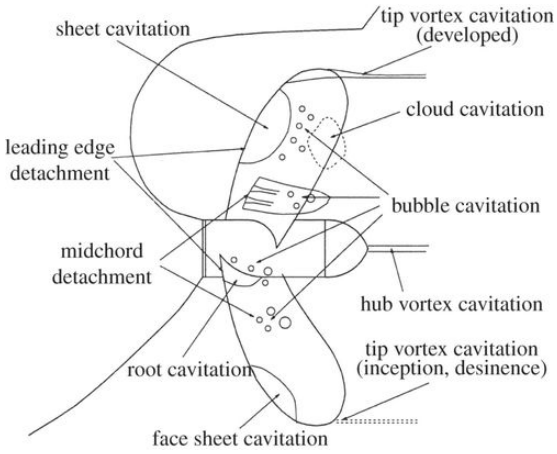

Figure 2.4: Different types of cavitation that can occur on a marine propeller (reproduced from [18])

2.1.2 Propeller Noise Mitigation Techniques

Noise mitigation methods concerning the marine propeller is a growing research area within the early design of marine vessels due to the increase in computational power making early technological developments in the research area more feasible and the creation of guidelines aimed to limit the impact of the shipping industry on the marine acoustic environment. The reduction of noise can be split into three categories; non-cavitating noise reduction, cavitating noise reduction and radiated noise reduction. Traditionally, this can be achieved through three types of modifications, propeller geometry modifications, inflow wake modifications and propeller isolation [19].

The noise mitigation techniques are mainly focussed on the propeller blades or the boss cap. Geometrical modifications of the blade such as; increase in skew angle, number of blades, blade area; distribution of blade pitch, trailing edge modifications and blade finishing can reduce the pressure oscillations of the propeller effectively [20]. Modifications such as the increased swept angle and higher blade number are utilised by submarines, where noise reduction is a

critical design factor due to its special operational requirements [21], an example of a model submarine propeller can be seen in Figure 2.5.

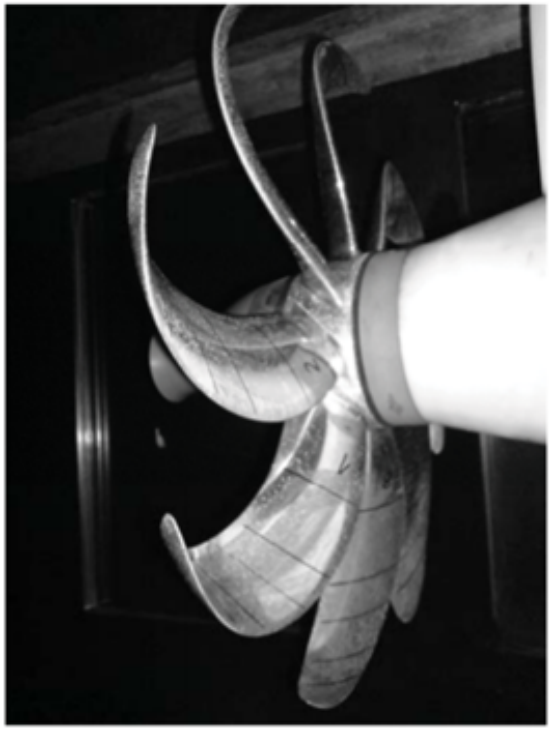

Figure 2.5: 8-bladed Kappel Propeller (reproduced from [21])

Modification like the Kappel and contracted and loaded tip (CLT) propeller are effective in reducing the URN of the propeller by modifying the blade tip. Kappel propellers, shown in Figure 2.6 are characterised by the trailing edge being curved towards the suction side of the propeller which can result in an increase in hydrodynamic efficiency while simultaneously reducing cavitation and the subsequent URN produced by such phenomena [22]. The Kappel propeller was first designed using the classical lifting line method proposed by Lerbs [23], however experiments by the Danish Maritime Institute (DMI) between 1980 to 1982 showed that the traditional methods were not appropriate for the calculation of propellers with curved blade tips. Because of this, Andersen and Andersen [24]

in 1987 developed a new method for computing the optimum load distribution for arbitrary curved mid-chord lines, which was then extended upon in 1992 by Andersen and Schwanecke [25] to trace the blade surface based on the vortex lattice method. The development of the numerical methods were then applied to the blade design and further model tests were conducted on Kappel propellers between 1991 and 2002 by facilities such as Schiffbau-Versuchsanstalt Potsdam (SVA) and Hamburgische Schiffbau-Versuchsanstalt (HSVA) showing efficiency gains of between 2 and 6%, summarised in Andersen et al [26]. Cavitation tests were conducted of the Kappel propeller in the HSVA's cavitation tunnel, HYKAT and it was found that a reduction in pressure fluctuation of up to 15% was observed, which showed that URN could be reduced in cavitating conditions by the Kappel propeller when compared to the reference design. During full scale trials, it was reported that on-board environmental conditions were improved due to a reduction in noise and vibration levels and the pressure fluctuation at the blade rate was reduced by 50% after installation of the Kappel propeller, while an increase in propulsive efficiency of 4% was confirmed [27].

The CLT propeller, first developed in the 1980s [28] after the first trials with the Tip Vortex Free (TVF) propeller in the 1970s, is shown in Figure 2.6. It is characterised by the end plates that are unloaded and face in the opposite direction to the thrust of the ship, restricting the recirculation of water. They differ from the Kappel propeller as the end plate is unloaded and faces in the opposite direction to the curved tip of the Kappel blade. The merits of CLT propellers are higher efficiency (5-8%), lower noise and vibration levels and better manoeuvrability characteristics and have been demonstrated in about 280 full scale applications on very different ship types [29]. Klaren and Sparenberg [30] investigated the impact of propeller end plates on the the optimimum circulation distribution of the propeller using linearised potential theory. It was found that

because of the end plates, the propeller could be more tip-loaded, in turn, this means that the optimum propeller diameter is smaller, and there is the possibility of reducing cavitation. They also stipulated that a reduction in noise could be possible because of the potential influence of the end plates on the tip vortex formation, although this was not investigated. Sparenberg and de Vries [31] used the linearised potential theory to design the CLT propeller and conducted model scale experimental tests in behind the wake of a ship, concluding that the propulsive efficiency could be enhanced up to 1.5% by the inclusion of end plates. In 1994, de Jong and Sparenberg [32] conducted model tests of the CLT propeller and found that an enhancement in propulsive efficiency could be achieved by the end plates when compared to the conventional propeller. More recently in 2012, Gaggero et al [33] and Bertetta et al [34] conducted a comparison between numerical and experimental cavitation patterns of a CLT propeller showing good agreement between both methods, however no comparison to a conventional propeller was made. It is unclear through the open literature if an URN noise reduction has been predicted using numerical and/or experimental methods for the CLT propeller when compared to a baseline design. However, it is claimed by Adalid and Gennaro [35] that a reduction in noise and vibration levels due to tip vortex cavitation mitigation have been reported during model and full scale tests.

Figure 2.6: Kappel (left) and CLT (right) propeller (reproduced from [20])

Another modification of the blade that has proved promising is the strategic placement of holes near the propeller tips, more recently described as pressure pore technology. This is done to unload the propeller tip, mitigate tip vortex cavitation (see Figure 2.7) and as a result, reduce the associated URN [17; 36; 37]. In 1990, Sharma et al. [17] conducted experimental tests on hole modifications on propeller blade tips to investigate their impact on cavitation. They proved to be very effective in delaying the cavitation inception of the tip vortex, particularly in heavy-loaded conditions. A reduction in URN of 17dB below 2kHz was observed and a reduction in hull vibrations due to cavitation was stipulated. No obvious penalty in hydrodynamic performance was observed. This technology was further investigated in 2020 using a model scale test campaign by Aktas et al. [37], where a reduction in URN of 17dB was also observed, similar to findings from Sharma et al. [17]. However on the contrary to Sharma et al. [17], a 2% reduction in propulsive efficiency was observed. Atlar et al. [36] conducted a comparative full scale trial of the pressure pore technology and found that a reduction of 10dB in URN was observed and that tip vortex cavitation could be mitigated (see Figure 2.7), agreeing with findings by Sharma et al. [17] and Aktas et al. [37].

However no results of the ship power consumption were presented so the influence of pressure pores on the hydrodynamic performance of the ship at full scale is not known. Further optimisation of the hole placement and full scale trials with different propeller designs is required to accelerate the commercial viability of this technology.

A more recent development is the addition of roughness to the propeller tip which reduces the loading at the blade tip and mitigates tip vortex cavitation [38; 39; 40]. Asnaghi et al. [40] conducted a numerical and experimental investigation into the influence of roughness applied to the blade tip on the propeller hydrodynamic performance and cavitation behaviour. Using the numerical methodology, it was found that the tip vortex cavitation could be mitigated by 37% and 22% in the model and full scale conditions, respectively. However, a hydrodynamic efficiency degradation of 1.8% and 1.4% was observed in model and full scale conditions, respectively. This shows that the scale of the study can influence the performance change incurred by the roughness application which is an important consideration when designing a noise mitigation concept. A clear reduction in tip vortex cavitation was observed in the model scale experimental tests (see Figure 2.7). Although no URN measurements were presented, it is reasonable to stipulate that a reduction in tip vortex cavitation could result in a reduction in URN by the application of the roughness on the blade tip through URN findings from a reduction in tip vortex cavitation using pressure pore technology [17; 36; 37]. Sezen et al. [41] conducted a CFD investigation into the effect of roughness on the URN of a marine propeller, showing that a 10dB reduction between 1-2kHz was achievable due to the tip vortex mitigation, however this came with up to a 30% loss in efficiency. Further research is necessary to optimise the roughness distribution and to conduct a full scale demonstration with quantification of the URN reduction. However, because both of these tech-

nologies result in a hydrodynamic performance penalty and thus, increased fuel consumption, this would mean that shipowners are less inclined to adopt this technology.

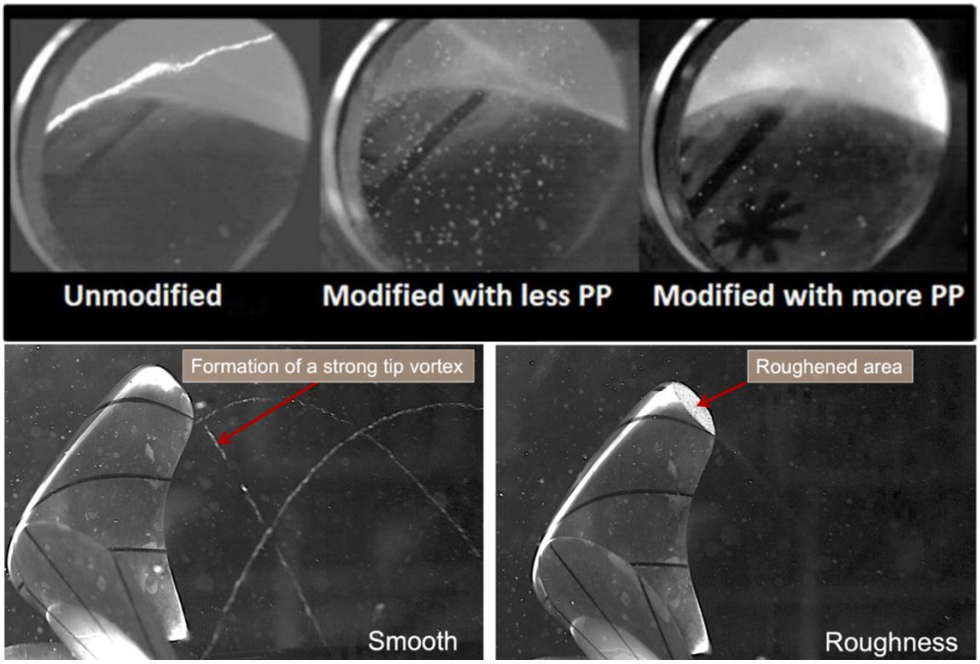

Figure 2.7: Pressure pore (PP) technology (top) and roughness application (bottom) tip vortex mitigation capability (reproduced from [36; 40])

Modifying the boss cap can also provide noise reduction benefits, the implementation of Propeller Boss Cap Fins (PBCF) have shown to reduce the URN and increase the efficiency of the propulsion system by mitigating hub vortex cavitation. The PBCFs were developed by TOKYO-Mitsui O.S.K. Lines, Ltd, West Japan Fluid Engineering Laboratory Co., Ltd., and Mikado Propeller Co., Ltd. (now Nakashima Propeller Co., Ltd.) and first introduced in 1987. Efficiency gains of up to 7% have been reported, however an independent study by Mewis and Hollenbach [42] suggested a more modest 3%. In 1991, Mitsui OSK Techno-Trade Ltd reported that the PCBF caused a reduction in sound pressure level of 3–6 dB for frequencies exceeding 1000 Hz during cavitation tunnel tests

[43]. The effect on the hub vortex cavitation with the inclusion of PBCFs during the cavitation tunnel tests are shown in Figure 2.8, where the hub vortex cavitation is clearly present in the reference design but indistinguishable with the inclusion of the PBCFs. In 2015 and 2016, MAERSK LINE, the world's largest container shipping company, modified eleven G-class container vessels to enhance the energy efficiency of their fleet. The retrofit included replacing the bulbous bow, derating the main engines for slow steaming and installing more efficient propellers with propeller boss cap fins to reduce cavitation, while the main aim was to improve energy efficiency, the reduction of underwater radiated noise was identified as another potential benefit [44]. It was found that the retrofit resulted in a reduction of 6dB between 8-100Hz and 8dB between 100-1000Hz when compared to the vessels before the retrofit. It was noted that the reduction in the low frequency was due to less cavitation because of the PBCFs and the propeller operating at a larger depth and therefore, higher ambient pressure. Because the retrofit included other changes than just the PBCFs, the overall URN reduction is not likely to be soley due to the inclusion of PBCFs but more of a combination of all modifications. More recently in 2020, Sun et al. [45] used scale-resolved Large Eddy Simulations (LES) with the Ffowcs-Williams Hawkings (FW-H) acoustic analogy to quantify the noise reduction capability of PBCFs. It was found that the SPL could be reduced by 1.51 dB and the hydrodynamic performance was improved by 1.47%. The PBCF is easy to install and provides a reduction in ship fuel consumption, so presents an attractive option for shipowners. However, further independent studies are necessary to provide a more reliable quantification in any URN reduction capability of the device.

Another modification to reduce the hub vortex cavitation is the Propeller Cap Turbine (PCT), where a series of hydrofoils are cast into the propeller hub. This can reduce the energy consumption of the propulsion system [22]. It is claimed

that they can provide a URN reduction similar to the PBCFs by mitigation of tip vortex cavitation, but no openly available studies are available that quantify the noise reduction so it would be recommended that further independent studies are conducted for this device to quantify the URN reduction from the PCTs.

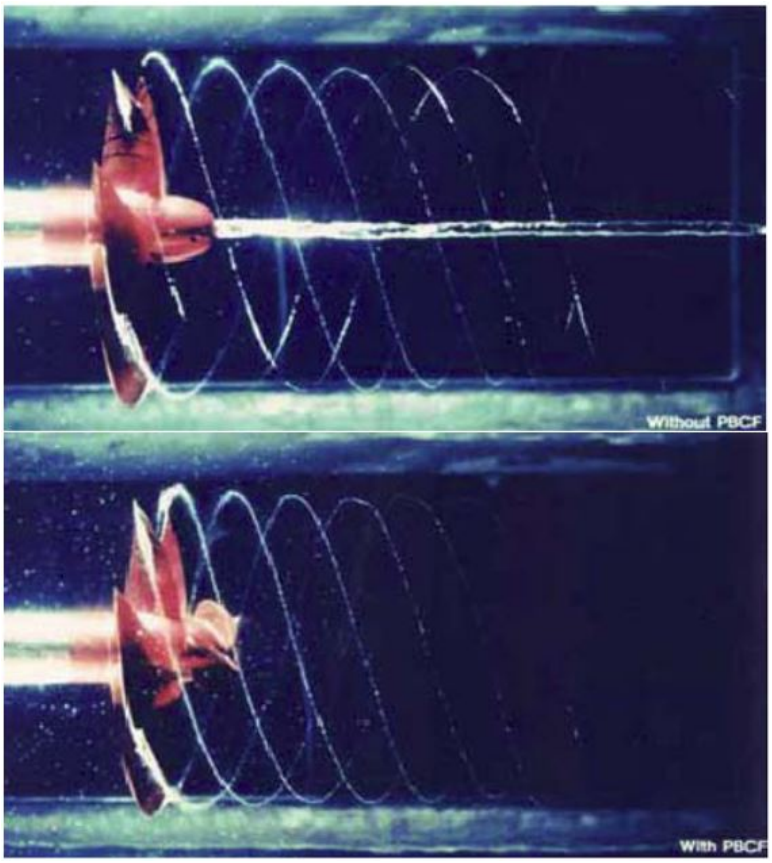

Figure 2.8: PBCF modification effect on hub vortex cavitation, no PBCF (top) vs with PBCF (bottom) from cavitation tunnel tests conducted on behalf of Mitsui O.S.K.Techno-Trade (reproduced from [22])

Although geometry modifications on the propeller blade and hub have shown a reduction in URN, wake inflow techniques can also be implemented to reduce the URN. In the presence of the hull, a non-uniform wake is induced. A more uniform wake is more desirable to improve efficiency, reduce cavitation and its associated URN. Therefore, noise mitigation methods through the modification of

the wake inflow using wake equalising devices (WEDs) can provide benefits to the propeller performance. A few products that are commercially available include the Schneekluth and Mewis duct. The WED, van Beek et al. [46] and Schneekluth [47], was proposed by Schneekluth and first introduced in 1984. It is depicted in Figure 2.9 and improves the uniformity of the wake over the propeller disk and therefore, increases the hydrodynamic efficiency. In addition, it can generate an additional thrust like accelerating ducts, reduce the propeller-excited noise and vibration due to the more uniform wake and improve the steering qualities because of the more straightened flow coming to the rudder [48]. However, there is a lack of openly available independent URN studies to verify this claim and provide a quantity of URN reduction that can be achieved.

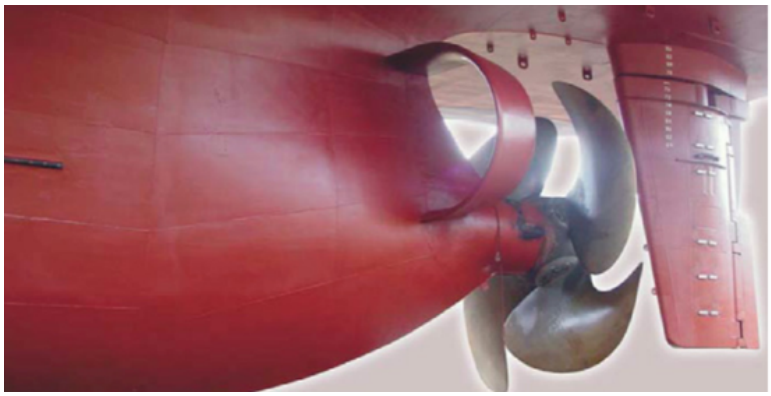

Figure 2.9: The Schneekluth duct (reproduced from [48])

The Mewis duct works similarly to improve the wake, it was originally developed for smaller container ships and bulk carriers which have speeds less than around 20kts and thrust coefficients greater than unity. However the concept has extended to faster ships. It increases the propeller efficiency and reduces cavitation-induced noise and vibration and can be shown depicted in Figure 2.10 [49]. Mewis [49] summarised the model tests and full scale demonstrations conducted for the Mewis duct, where a power saving of between 3 and 9% was pre-

dicted. Chang et al. [50] used CFD to investigate the impact of the Mewis duct on propulsive performance, it was found that the axial wake harmonic degress on the propeller disk had been significantly improved with the installation of the Mewis duct which means that the propeller noise and excited forces were effectively controlled. Similarly to the Schneekluth duct, a lack of openly available URN studies are available to quantify the URN reduction capability of the device and so it is recommended that independent studies are conducted to verify claims.

Figure 2.10: Mewis duct in model scale (reproduced from [49])

Another method of noise mitigation is through propeller isolation, where the inclusion of a duct surrounding the propeller can not only improve hydrodynamic performance, but also reduce cavitation and URN depending on the type of duct used. A series of common types of ducts can be shown in Figure 2.11, the most common being the accelerating and decelerating ducts. Figure 2.11a shows the benchmark Wageningen accelerating 19A duct, typically used on fishing and tugboats due to its high thrust capability in the heavy-loaded conditions and works by accelerating the flow through the duct and reducing the local pressure inside.

This duct is well suited for ships that don't operate in the reverse direction. If both forward and reverse direction performance is an operational requirement, a duct like that shown in Figure 2.11b would be more suited, trading a higher thrust capability in the forward direction with improved reverse direction performance when compared to the benchmark 19A duct. If the reduction of URN is important, a decelerating duct is most commonly used and shown in Figure 2.11d. The decelerating duct operates by decelerating the flow through the flow and increasing the local pressure in the duct which reduces the probability of cavitation to occur and its associated noise [51]. However, the inclusion of such a duct results in hydrodynamic performance degradation due to the induced drag from the duct [52; 53]. This type of duct is reserved for torpedoes, submarines and naval marine vessels that have special operational requirements and need to remain stealthy [12]. Due to the application of the decelerating duct, there is a lack of openly available studies that can verify that a reduction in URN is achievable when surrounding a propeller with a decelerating duct, so further studies on this are recommended.

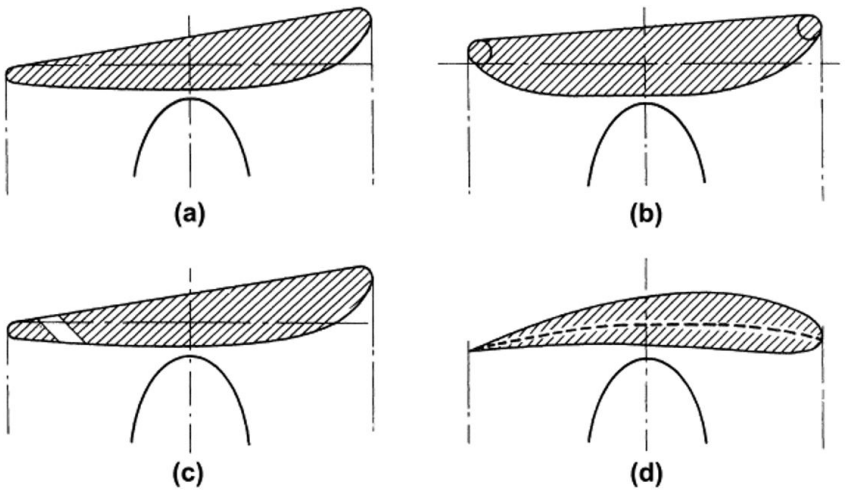

Figure 2.11: Typical duct cross sections (reproduced from [12])

More recently, another category of noise mitigation technique has emerged, called duct geometry modifications, where subtle changes could result in reduced URN. Inspired by the aviation's Chevron nozzle, trailing edge serrations have been added to pumpjet propulsor ducts, to understand the noise mitigation capability of such technology through numerical studies [54; 55]. Qin et al. [54] concluded that the inclusion of the serrated trailing edge reduced the noise levels of the pumpjet propulsor at all studied work conditions over almost the entire frequency range of 10-5000 Hz with only a slight increase in noise levels at 700-1000 Hz associated with the sawtooth duct induced vortex shedding frequency. At the low frequency range (below 1000 Hz) the trailing edge serrations resulted in a decrease in noise levels of roughly 5dB and when the pumpjet propulsor was operating at its design condition (J=1.9), the reduction was in the range of 2.5 dB to a maximum of 4.88 dB. However, this resulted in a 2% loss in hydrodynamic efficiency. The reduction in the URN was due to the acceleration in the vortex breakdown due to additional induced sawtooth trailing edge vortices which resulted in a more dissipated wake and lower turbulent kinetic energy (TKE) downstream (see Figure 2.12). Sun et al. [55] concluded the inclusion of serrated trailing edges could result in a reduction of 10-25dB in the axial direction in the low frequency range, with a 1dB increase in the high frequency range due to the vortex shedding induced by the trailing edge serrations. A 3-10dB reduction was observed in the radial direction. However, this came at a 0.37% loss in hydrodynamic efficiency.

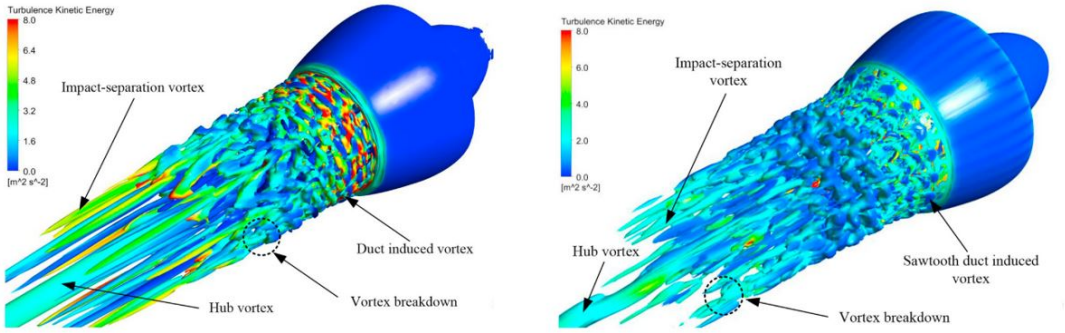

Figure 2.12: The spatial structures of the instantaneous vortices (using the Q-criterion and colored by TKE) for baseline (left) and sawtooth duct (right) (reproduced from [54])

Table 2.1 summarises the noise mitigation concepts discussed within the review and the evidence of URN reduction openly available. For a lot of commercially available technologies, it appears that evidence of URN reduction is not openly available with no quantified dB reduction, this may be due to commercial sensitivity or that evaluating URN is an afterthought when compared to the aim to reduce GHG emissions because of regulations like the Energy Efficiency Design Index (EEDI) that are mandatory to encourage the design of energy efficient ships. The URN reduction capability of the devices does change when comparing between model tests and full scale demonstrations, therefore it is likely that devices will have a *Re* dependency which is important to consider in any development of future innovative solutions. It is clear that further URN quantification of the devices is necessary through model testing, CFD and full scale demonstrations to provide more information in what URN reduction is achievable through the fitting of the devices.

Concept	Category	Source of URN reduction	Evidence of URN reduction	Efficiency Impact	Technological Maturity Level
Mewis Duct	Propeller Flow Conditioning Devices	Tip vortex cavitation, unsteady propeller URN	No openly available evidence of dB reduction quantified	Energy savings up to 9% [49]	Fully commercialised applied on numerous vessels
Schneekluth Duct				Energy savings up to 12% [22]	
CLT Propeller	Propeller Modifications	Tip vortex cavitation URN		Energy savings 5-8% [29]	
Kappel Propeller				Energy savings around 4% [22]	
Roughness Application			10dB reduction using CFD [41]	Loss of 1.8% [40] and 30% [41] in efficiency	Model scale tests conducted
Pressure Pores			17dB using model scale tests [17; 37] and 10dB using full scale demonstration [36]	Loss of 2% [37]	Full scale demonstration conducted
PBCFs	Hub Modifications	Hub vortex cavitation URN	3-6dB model testing [22] and 1.51dB using CFD [45]	Efficiency gain of between 1.47-7% [22; 42; 45]	Fully commercialised applied on numerous vessels
PCTs			No openly available evidence of dB reduction quantified	No openly available quantified evidence	
Decelerating Duct	Duct Inclusion	Tip vortex cavitation URN		Loss of efficiency [53]	
Trailing-edge Duct Modifications	Duct Modifications	Turbulence and Vorticity-induced URN	5-25dB reduction [54; 55]	0.37-2% loss of efficiency [54; 55]	Model scale CFD studies

Table 2.1: Summary of noise mitigation concepts and their URN reduction capability

2.1.2.1 Noise Mitigation through the Breakdown of Helical Vortex Structures

The quadrupole (non-linear) noise source predominately associated with turbulence and vorticity can be significant in the far-field acoustic signature [56]. This type of noise is largely generated from the propeller wake flow. Therefore within the wake flow, it is important to understand the various vortical structures present and their breakdown mechanisms. Within the propeller wake flow, a number of vortex structures exist (see Figure 2.3) and their presence, strength and breakdown depend on variables such as blade design, operating condition and the addition of a surrounding duct. The tip vortex from open propellers is believed to be the most dominant source of turbulence and vorticity-induced noise from the propeller, therefore it is assumed that the tip-leakage vortex induced noise will be significant within the non-linear noise contribution of a ducted propeller in non-cavitating conditions when compared to the other vortex structures [57]. The tip-leakage vortex is created by the rotation of the propeller in close vicinity to the duct wall. Understanding the breakdown mechanisms of the helical tip-leakage vortex into large scale flow structures and turbulence could present new opportunities to develop noise mitigation concepts that take advantage of vortex breakdown mechanisms. Widnall [58] discusses the stability and breakdown of a helical vortex filament. It was demonstrated that the helical vortex filament of finite core size is unstable to small sinusoidal displacements of the filament. The results of the stability calculations presented show that the helical vortex filament has three modes of instability: a very short-wave instability which likely exists on all curved filaments, a long-wave mode which is also found to be unstable by the local-induction model and a mutual-inductance mode which appears as the pitch of the helix decreases and the neighbouring turns of the filament begin to interact strongly. Figure 2.13 shows the instability mode shapes at varying

number of waves per cycle of the helix, y/k'.

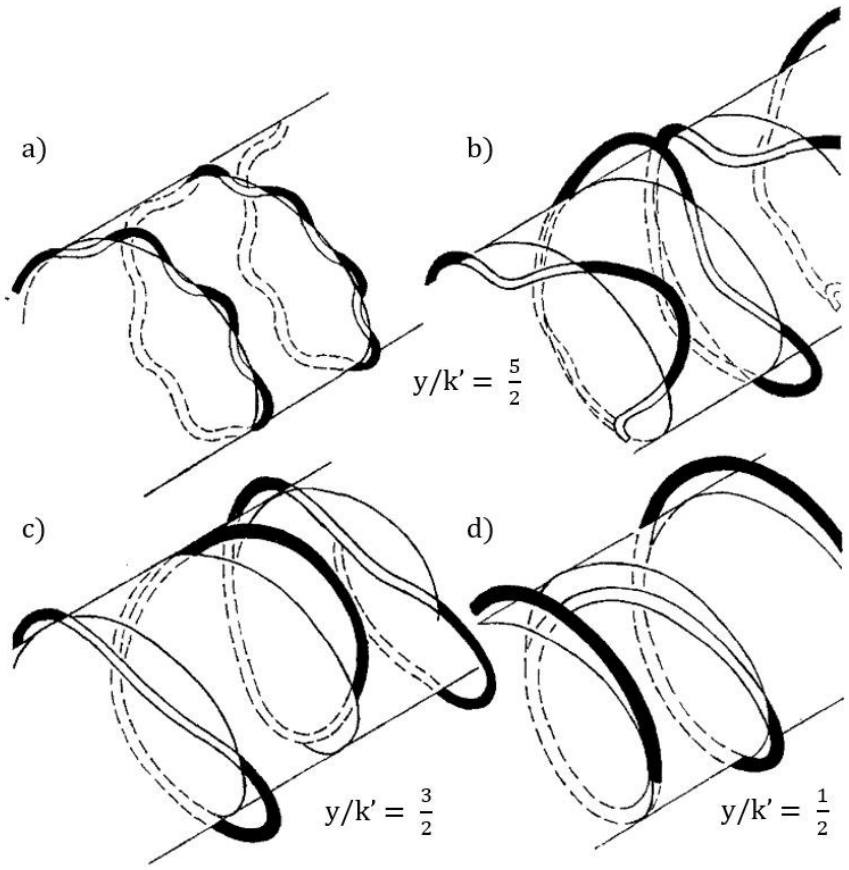

Figure 2.13: Instability mode shapes; a) the short-wave instability, b) the mutual-inductance modes with $y/k' = 5/2$ and c) the mutual-inductance modes with y/k' = 3/2 and d) the long-wave instability with $y/k' = 1/2$. The dark portions are outside the cylinder on the near side; the light portions are inside (reproduced from [58])

Zhang and Jaiman [16] applied the fundamental vortex breakdown of a helical structure by Widnall [58], to the ducted propulsor using a numerical investigation. Figure 2.14 shows the fundamental vortex dynamics of a ducted propulsor tip-leakage helical structure at a variety of different operating conditions, clearly labelling the leapfrogging, short-wave instability and secondary vortex system. The leapfrogging phenomenon is annotated in Figure 2.15a. The secondary vortex

system consists of small vortical structures that wrap around the main helical tip-leakage vortex structure (see Figure 2.15b). The short-wave instability can be described as small oscillations within the main helical filament and can be shown within Figure 2.15c. It was concluded that the primary breakdown mechanisms of the tip-leakage vortex were the short-wave instability and the secondary vortex system that interacts with the main helical structure. Therefore, one of the fundamental concepts of reducing the noise signature of the propulsor within this thesis is raised, where introducing additional instability into the initial helical tip vortex structure could encourage the breakdown of the vortex structure and result in reduced URN.

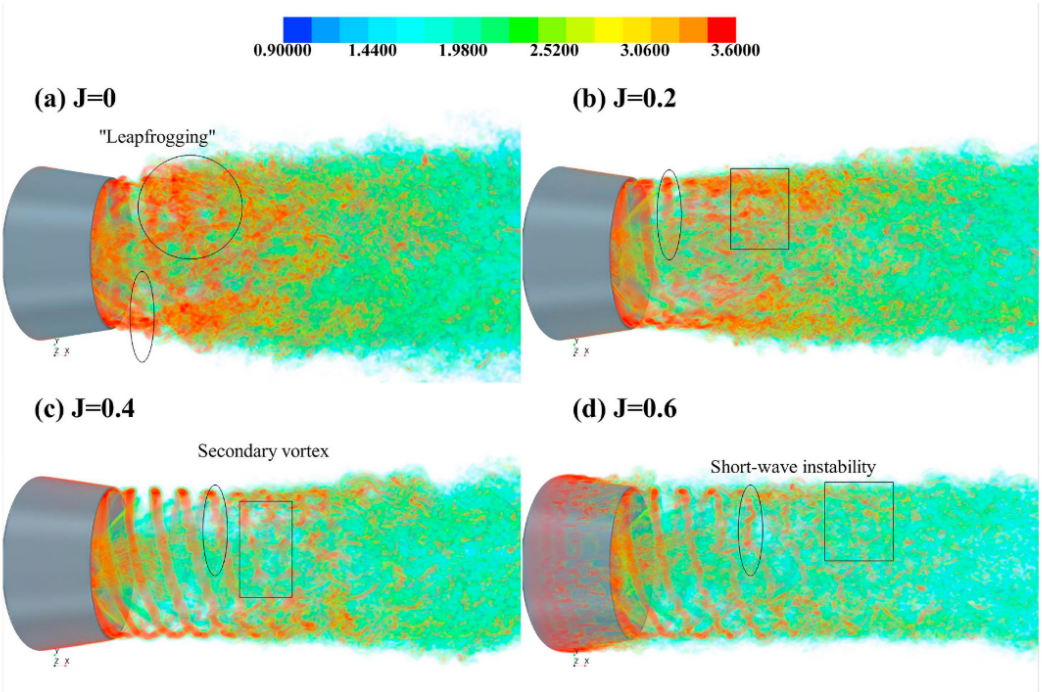

Figure 2.14: Volume rendering of the normalized vorticity magnitudes in the wake of ducted propeller at four different advance coefficients. The phenomena of leapfrogging (circles), short-wave instability (ovals) and secondary vortex (squares) are illustrated (reproduced from [16])

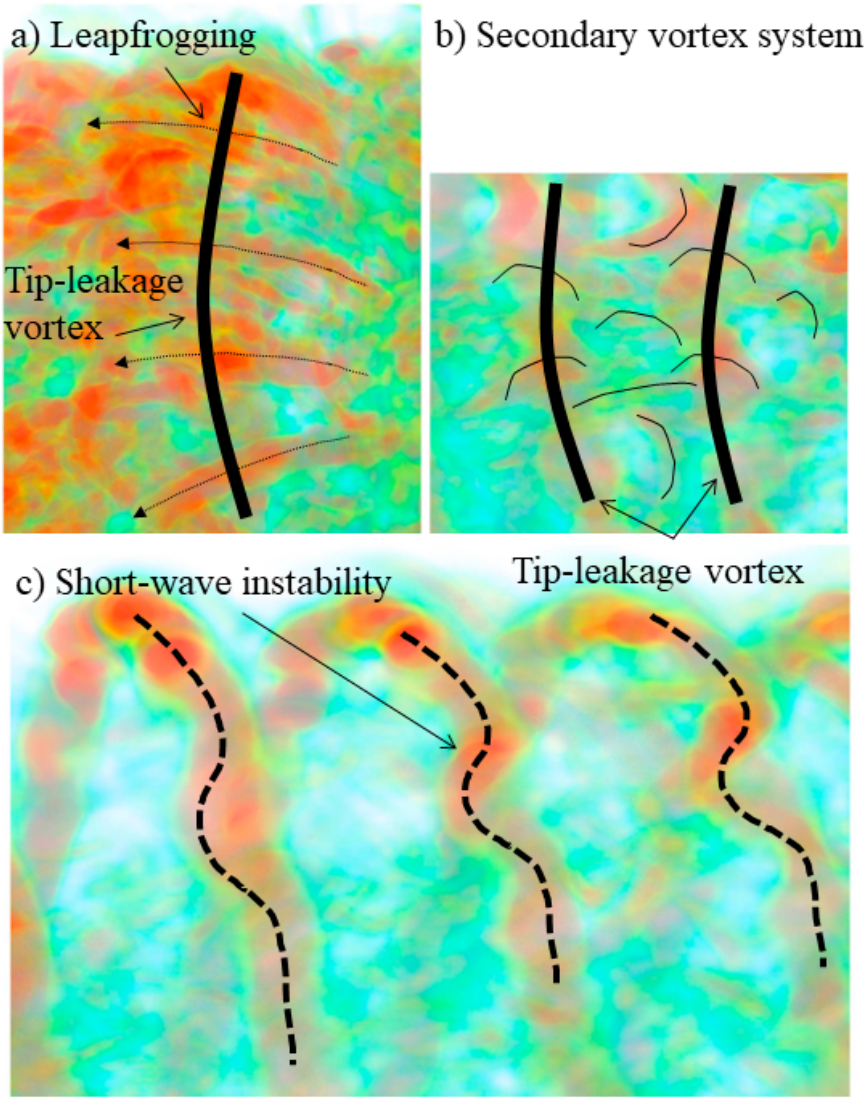

Figure 2.15: Close-up a) leapfrogging, b) secondary vortex system and c) short-wave instability (adapted from [16])

2.1.3 Summary

URN from marine vessels has a negative impact on the marine acoustic environment, where it can disrupt marine mammals' basic biological functions such as navigating and communicating, in some severe cases, even resulting in death.

The URN is and will become a crucial early design factor within the design of not just submarines, but commercial vessels as well. The largest proportion of URN from a ship is generated from the propeller and therefore, reducing noise from the propeller is key to reducing the overall URN from marine vessels. However, some mitigation methods can compromise the propulsive efficiency of the vessel and this is undesirable as this would result in increased fuel consumption and carbon emissions. Therefore, finding noise mitigation methods that have minimal or no compromise to the propeller hydrodynamic performance are critical in meeting targets set out by international bodies to improve the marine acoustic environment.

Propeller URN mitigation concepts have been developed over the years and are commercially available and new concepts are being developed continually and are at various stages of technological maturity. It was found that propeller flow conditioning devices such as the Mewis and Sckneedkluth duct could improve the uniformity of the propeller inflow which could lead to a reduction in tip vortex cavitation and unsteady propeller loading, and it is reasonable to assume that this would result in a reduction in URN. Propeller types such as the Kappel and CLT propeller are well-established concepts that can mitigate tip vortex cavitation and this is believed to result in a reduction in URN through on-board reports, however similar to the propeller flow conditioning devices, there are no openly available studies that quantify the URN reduction that is achievable.

Newer concepts such as the hole modifications and roughness application on the propeller have shown promising URN reduction capabilities of up to 17 and 10dB, respectively. However this does come with a hydrodynamic performance penalty of up to 2 and 30%, respectively. It was also shown that the URN reduction quantified for the hold modifications differed when comparing model tests and full scale demonstrations, so scaling effects are important to consider for fu-

ture URN mitigation concept development. Further optimisation is necessary for both of these new concepts to minimise the hydrodynamic performance penalty and provide a more attractive solution to the shipping industry that can contribute to the reduction in URN whilst not conflicting with other initiatives such as the reduction in GHG emissions.

Hub modifications such as the PBCFs and PCTs have shown to be successful in mitigation hub vortex cavitation and its associated URN signature by up to 6dB while also providing a fuel saving of up to 7%. The inclusion of the decelerating duct can reduce the local static pressure near the blade tip which can aid in mitigating tip vortex cavitation and it is believed that this would result in a URN reduction, however there are few openly available to verify this stipulation. Trailing-edge serration modifications to pumpjet propulsor ducts have shown to mitigate URN by up to 25dB through disruption of the coherence turbulent wake structure in the slipstream, however this does come at a slight cost of hydrodynamic performance of up to 2%.

It is clear that further URN quantification of the devices discussed is necessary through model testing, CFD and full scale demonstrations to provide more information in what URN reduction is achievable through the fitting of the devices. This could influence future targets set through policies and any potential incentives set for shipowners.

It was found that the primary breakdown mechanisms of the tip-leakage vortex were the short-wave instability and the secondary vortex system that interacts with the main helical structure. Therefore, one of the fundamental concepts of reducing the noise signature of the propulsor within this thesis was raised, where introducing additional instability into the initial helical tip vortex structure could encourage the breakdown of the vortex structure and result in reduced URN. Secondly, it is clear through the literature that controlling cavitation can result

in a reduced URN signature and so this is another noise source that could be mitigated through the development of a noise mitigation concept within the PhD project.

2.2 Leading-Edge Tubercles; Inspiration, Influence, Applications and Benefits

The inspiration from the natural world to advance and improve technology has been a constant throughout humankinds' existence. From early years, the fabrication of silk, the ability to fly, velcro and even a common household item like the umbrella were inspired by the natural wonders of the world. To more recent advances, where the Japanese bullet train was redesigned to the shape of the kingfisher's beak and head to mitigate the booming sound caused when the train travels under tunnels. Nature has always and will always inspired us to redesign and create a better world.

The humpback whale (*Megaptera Novaeangliae*) is an exceptional marine mammal, undertaking acrobatic manoeuvres despite its stocky build to catch prey as depicted in Figure 2.16. Such manoeuvres are assisted by leading edge (LE) tubercles, which are small bumps or perturbations located on the pectoral fin highlighted in Figure 2.16. LE tubercles have been at the focus of many studies over the last few decades to understand their fundamental flow behaviour and how they can benefit a variety of applications.

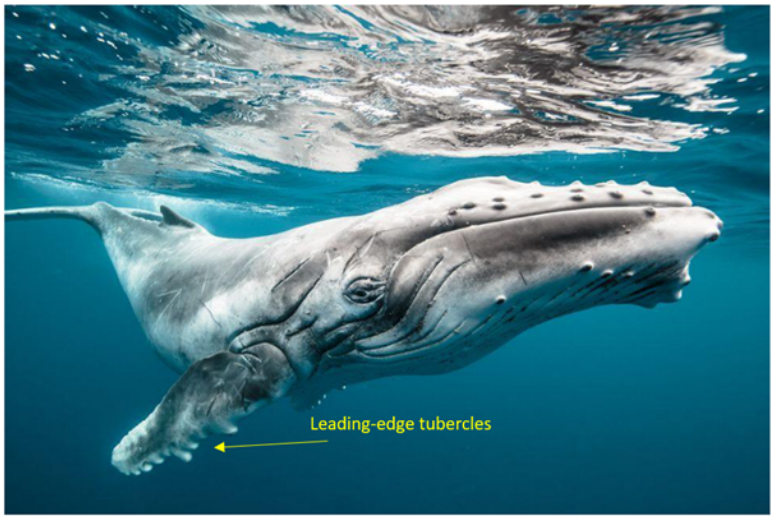

Figure 2.16: The Humpback Whale (*Megaptera Novaeangliae*) ©Karim Iliya, 2015. Reproduced with kind permission of the photographer.

Since initial findings in the early 21st century [4; 59], LE tubercles have been researched on a variety of devices applicable in an array of industries such as; marine, where they have been investigated on propellers [60; 61] and hydrofoils [3; 62; 63]; aviation, where the wing [5; 64] and propeller [65] components have been of particular interest; and energy, where fans [66], wind [67] and tidal turbines [7; 8; 68; 69] have also been benefactors of LE tubercle research where they have shown to provide enhanced aero/hydrodynamic and noise performance in certain operating conditions. This section aims to introduce the fundamental early findings of LE tubercles and the advantages they provide for practical engineering applications.

2.2.1 Fundamental Findings on Foil Sections

Watts and Fish [59] demonstrated the first proof of concept on the application of LE tubercles on a reference aerofoil geometry using a numerical panel method. An increase in lift of 4.8%, a reduction in induced drag of 10.9% and ultimately

an improvement in lift to drag ratio, L/D, of 17.6% was observed at a 10° angle of attack (AOA) when compared to the reference foil. It was stipulated that tubercles could increase the operating envelope of a foil by delaying the onset and severity of stall. Then, Miklosovic et al. [4] conducted an experimental investigation into the influence of LE tubercles on a model-scale humpback whale flipper. Through the wind tunnel measurements, the inclusion of the LE tubercles resulted in increased lift coefficient, C_L, reduced drag coefficient, C_D and improved L/D ratio, while also delaying stall as shown in Figure 2.17. This confirmed previous stipulations by Watts and Fish [59] and an analogy between LE tubercles and vortex generators was drawn. These pioneering research studies sparked interest in the LE tubercles ability to enhance performance and to this day, it is still a focus of interest in the biomimetics and engineering community.

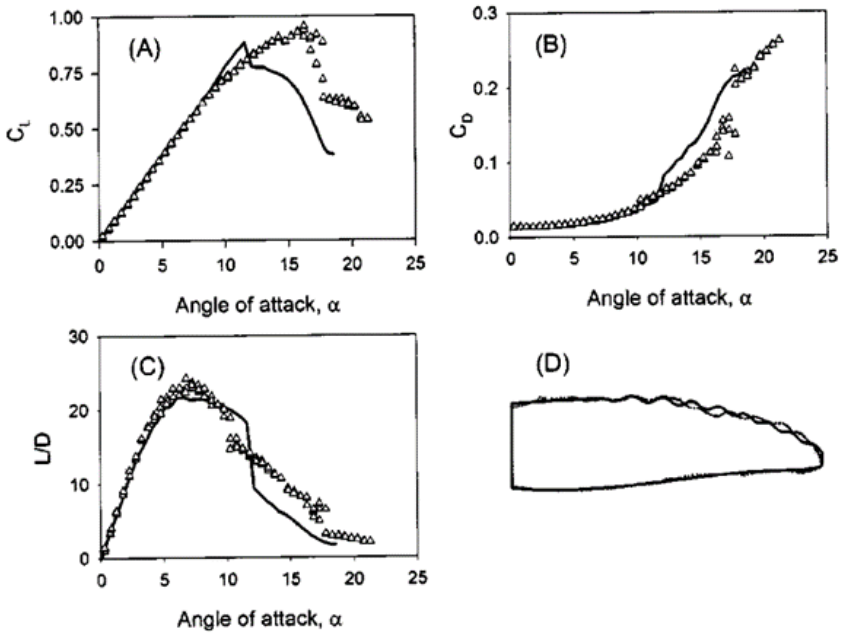

Figure 2.17: LE tubercle (triangles) vs baseline (solid line) scale model humpback whale flipper, showing delay in stall, increase in lift and reduction in drag (reproduced from [4])

Pedro and Kobayashi [70] conducted a numerical investigation into the influence of LE tubercles on the same scale model humpback whale flipper using Detached Eddy Simulations (DES), confirming the experimental findings by Miklosovic et al. [4]. The improvement in performance was deemed to be due to the counter-rotating streamwise vortices that carry momentum to the boundary layer delaying the trailing-edge separation and secondly confine the leading-edge separation to the tip region. This comparative numerical and experimental study between Pedro and Kobayashi [70] and Miklosovic et al. [4] was crucial in comparing LE tubercle numerical and experimental quantitative force measurements and providing flow visualisations of the fundamental flow changes incurred by LE tubercle modifications.

Stanway [62] conducted an experimental investigation in a water tunnel into the effects of LE tubercles on the hydrodynamic performance of control surfaces and flapping foils. Although the concept was not recommended for use on flapping foils, the inclusion of LE tubercles on control surfaces operating in stall conditions produced superior performance when compared to its reference counterpart. In addition to this, the first Particle Image Velocimetry (PIV) measurements for LE tubercles were captured, clearing showing the counter-rotating streamwise vortices produced by the tubercles where the strength of the vortices increased with increasing AOA. An illustration of the counter-rotating vortex pair induced by the LE tubercles can be shown in Figure 2.18. Experimental flow visualisation using PIV to observe the counter-rotating streamwise vortex pairs provided further support to discussions on the fundamental flow mechanisms of LE tubercles by Pedro and Kobayashi [70] and Miklosovic et al. [4]. It also inspired future fundamental fluid dynamics research with the aim to further understand the evolution of the streamwise vortex pairs by Rostamzadeh et al. [71] and Hansen et al. [72].

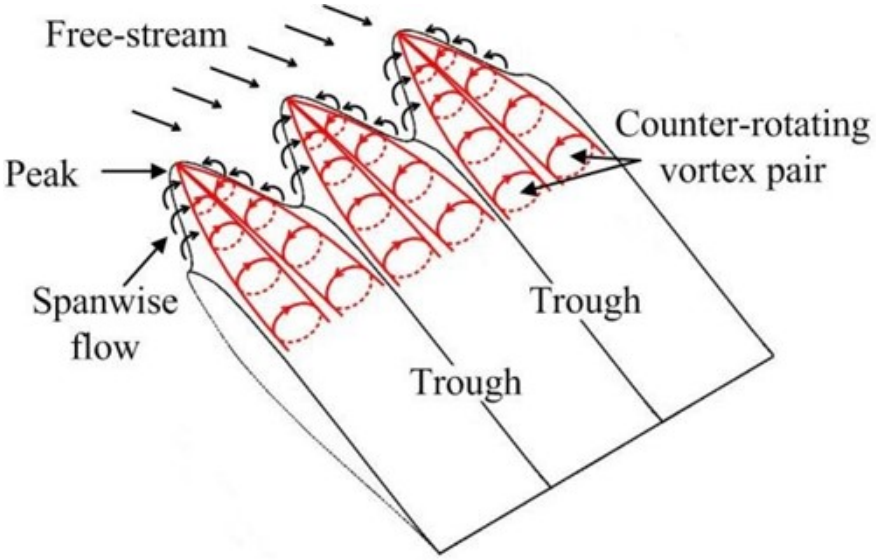

Figure 2.18: Illustration of the counter-rotating vortex pair induced by the LE tubercle geometry (reproduced from [6])

Similarly, Johari et al. [3] conducted experimental research in a water tunnel on LE tubercles at a high Reynolds number, Re, as applied to a two-dimensional (2D) hydrofoil while varying the amplitude and wavelength of the idealised sinusoidal waveform. It was noted that post-stall lift increased up to 50% with only ever a slight compromise in induced drag while pre-stall conditions were degraded with an increase in drag and a reduction in lift. In terms of the sinusoidal geometrical parameters, it was shown that amplitude had a much more significant effect on the performance of the hydrofoil compared to the wavelength, which had very little. This study also initiated the interest in tubercle geometry configuration optimisation in terms of wavelength and amplitude. Compared to research on the three-dimensional (3D) work on a flipper model by Miklosovic et al. [4] the results differed in that the flipper with protuberances had reduced drag in the post-stall regime and the stall angle was extended beyond the baseline flipper. Therefore, it was argued that the presence of protuberances affected the induced drag and the spanwise progression of stall on the 3D flipper model and this was

further stated by Miklosovic et al. [73]. Therefore the evidence suggests that LE tubercles are more beneficial for 3D foils which would be suitable for propulsor blades.

Hansen et al. [64] conducted similar experimental research in a wind tunnel at a lower Re to investigate the effect of wavelength and amplitude on the aerodynamic performance of 2D aerofoils. Similarly to Johari et al. [3], it was shown that amplitude had a significant impact on the aerofoil performance where reducing the amplitude resulted in a higher maximum lift coefficient and larger stall angle. However, in the post-stall region, the performance with larger amplitudes was more favourable. In addition to this, reducing the wavelength lead to improvements in all aspects of lift performance, including maximum lift coefficient, stall angle and post-stall characteristics. The advantages of tubercles also differ with foil section profile, where they had negligible influence on lift in the pre-stall regime and were beneficial in the post-stall regime for the NACA 65-021. On the other hand for the NACA 0021 profile, the improvement in lift in the post-stall regime came at the cost of degradation in lift performance in the pre-stall regime. However, this degradation in performance in the pre-stall regime was reduced by the optimisation of the tubercle amplitude, A and wavelength, λ. Tubercle optimisation is not solely restricted to geometrical parameters within the literature, spacing [74] and coverage [75] have also been investigated.

Not only can LE tubercles enhance key performance characteristics such as lift and drag, they have also shown promising noise mitigation capabilities. Hansen et al. [5] investigated the reduction of aerofoil tonal noise with the inclusion of LE tubercles in a wind tunnel at Re = 120,000. It was concluded that the implementation of the bio-inspired concept produced a reduction in tonal noise (see Figure 2.19), where the largest amplitude smallest wavelength configuration provided the greatest reduction in tonal and broadband noise. This was believed

to be due to the disruption of the coherent trailing edge wake structure by the counter-rotating vortices generated by the LE tubercles.

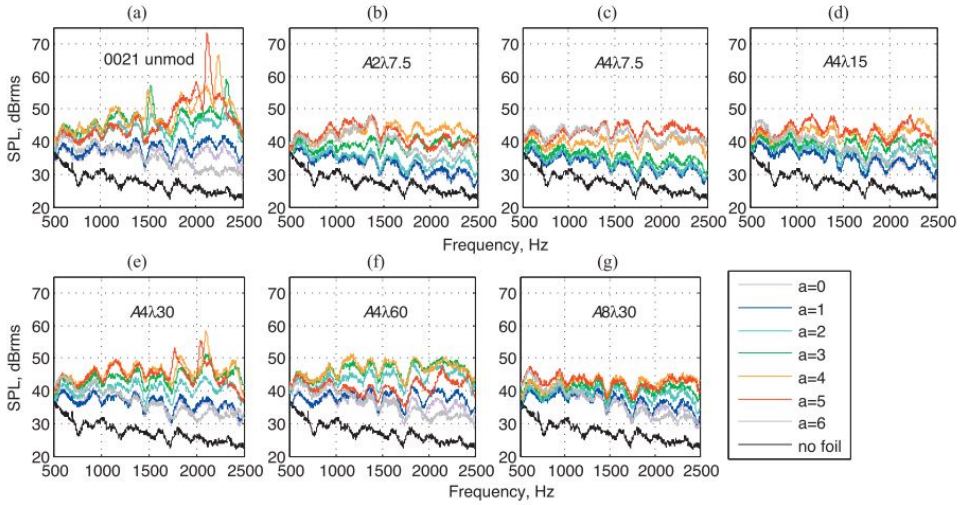

Figure 2.19: Sound Pressure Level (SPL) against frequency measured in anechoic wind tunnel (AWT) at a range of AOAs 0-6 for (a) unmodified aerofoil (b) $A2\lambda7.5$ (c) $A4\lambda7.5$ (d) $A4\lambda15$ (e) $A4\lambda30$ (f) $A4\lambda60$ (g) $A8\lambda30$, $Re = 120{,}000$ (reproduced from [5])

Lau et al. [76] conducted a numerical study on LE tubercles impact on aerofoil-gust interaction noise. From the results, it was shown that the LE tubercles successfully mitigate the aerofoil-gust interaction noise. Wang et al. [77] conducted Large Eddy Simulations (LES) on a popular NACA foil and it was shown that a reduction of 13.1dB-13.9dB was possibly with the inclusion of the LE tubercles.

Another important consideration within tubercle application on marine devices is the presence of cavitation. There have been a few key studies on LE tubercles influence on cavitation on hydrofoils. Weber et al. [63] used experimental methods to investigate the effect of LE tubercles on the lift, drag and cavitation onset operating at a low Re on a marine rudder. It was concluded that the inclusion of LE tubercles accelerated the onset of cavitation. However, the

distribution of cavitation was altered, compartmentalising the sheet/cloud cavitation into slots in the troughs (see Figure 2.20). Therefore, it was inferred that under heavy-loaded conditions in which sheet cavitation is occurring the rudder with LE tubercles would provide superior hydrodynamic performance due to this compartmentalisation phenomenon. In addition, the change in the number of tubercles included onto the rudder did have an influence on hydrodynamic performance. Generally, the LE tubercle modified rudder had negligible influence on the hydrodynamic performance in the pre-stall regime and that hydrodynamic stall occurred at a lower AOA. However, in the post-stall regime the loss of lift was not so sudden for the LE tubercle modified rudder when compared to the baseline. The peak L/D ratio was improved by LE tubercles at the lower Re between $Re = 200{,}00$ and 710,000 but was not improved in the higher Re studies at $Re = 800{,}000$ and 860,000. For the lower Re studies, the LE tubercle geometry provided an increase in drag and decrease in lift at between 15 and 22° AOA but for angles above 22°, the tubercles generated more lift. For the higher Re studies there was negligible difference in hydrodynamic performance between the designs, suggesting that there is a critical Re that when exceeded for a given tubercle geometry results in the tubercle providing no significant effect on hydrodynamic performance.

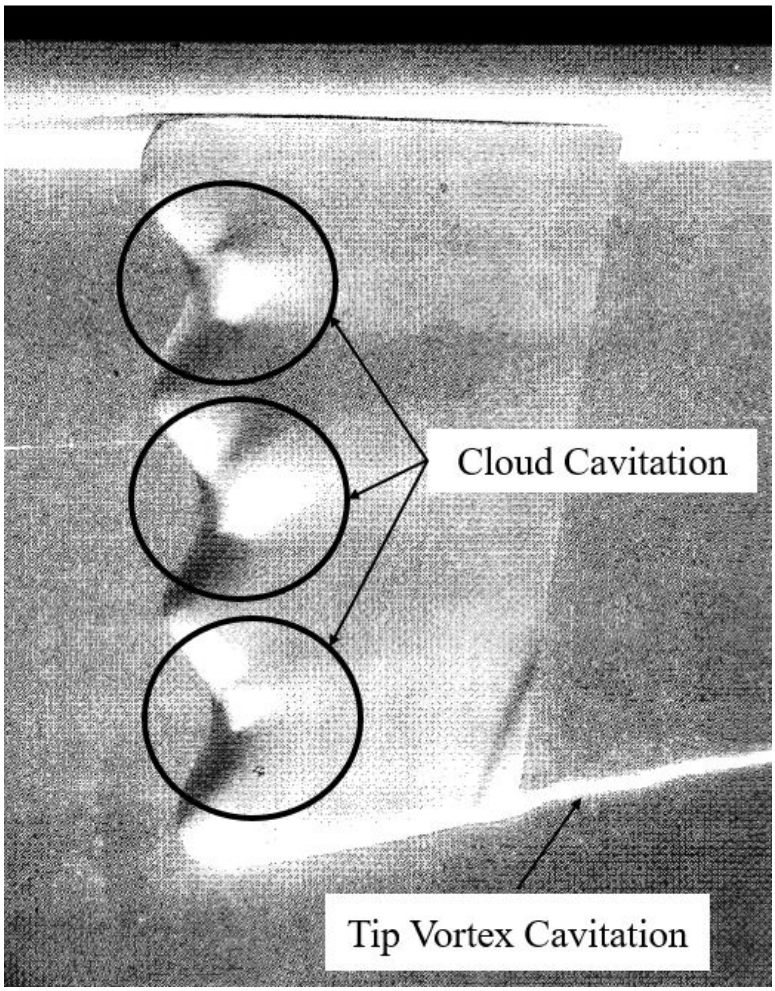

Figure 2.20: Experimental cavitation observation at Re = 786,000 of tubercle modified rudder (adapted from [63])

Custodio et al. [78] experimentally investigated the cavitation patterns and hydrodynamic performance of finite span rectangular and swept LE tubercle modified hydrofoils, in addition to exploring a variety of different tubercle designs at Re = 720,000 (see Figure 2.21). Three different amplitudes and two different wavelengths were explored on the rectangular hydrofoil. It was found that the two larger amplitude configurations largely contained the cavitation behind the low-pressure trough region, whereas the smaller amplitude and baseline foil produced cavitation along their entire leading-edge. It was also shown that the

cavitation extent for the larger amplitude tubercle was significantly smaller than when compared to the other designs. In terms of hydrodynamic performance in cavitating conditions, generally the L/D ratio for all tubercle designs was either less or equal to that of the baseline foil due to drag and lift of the smooth foil being superior to the modified foils but the small and medium amplitude LE tubercle modified hydrofoil at between 15 and 20° AOA showed an improvement in the L/D ratio because of the increase in lift and negligible impact on drag. This improvement in the L/D ratio was due to the cavitation compartmentalisation phenomenon. It was also stated that the drag in cavitating conditions was comparable between the baseline and modified models with the exception of the larger amplitude LE tubercle. This was a direct consequence of cavitation, where increased drag on the baseline hydrofoil due to sheet cavitation was balanced by the increased frictional drag caused by the extra surface area incurred by the LE tubercles on the modified models. Therefore, although sheet cavitation was confined, this came at a cost of hydrodynamic performance in the form of reduced peak L/D ratio.

The finding by Custodio et al. [78] that LE tubercles could contain cavitation behind the tubercle trough regions agrees with conclusions drawn by Weber et al. [63], but also there was a critical amplitude where this was achieved which was noted by the smaller tubercle amplitude not constraining the cavitation behind the trough region in heavy-cavitating conditions. Cavitation was incepted at earlier AOAs for the LE tubercle modified rectangular hydrofoil when compared to the baseline, agreeing well with findings by Weber et al. [63]. Weber et al. [63] also suggested wavelength was important for cavitation onset characteristics of the foil, but Custodio et al. [78] found that the cavitation pattern was unaffected by the wavelength of the LE tubercle. The difference in conclusions about the impact of wavelength on the cavitation drawn may be due to difference in the variation in

the range of wavelengths explored within both studies. On the contrary to Weber et al. [63] the peak L/D ratio was not improved by the LE tubercles, however Custodio et al. [78] found that the L/D ratio of the hydrofoil was improved by LE tubercles at a specific range of AOAs depending on the LE tubercle geometric configuration. This disparity in conclusions between both studies could be due to the difference in Re, because Weber et al. [63] found that the peak L/D ratio was not improved at all Re investigated. Additionally, the section profile and tubercle geometry were different in both studies and this can impact the LE tubercle influence on the lift and drag performance of the foil as found by Hansen et al. [64] and Johari et al. [3].

Li et al. [79] conducted a numerical investigation into the influence of LE tubercle modifications on hydrofoil cavitation using Large Eddy Simulations (LES). It was concluded that the LE tubercle modifications improved the hydrodynamic performance with an increase in lift and a small increase in drag while the cavitation severity was reduced by approximately 30% due to the cavitation compartmentalisation phenomenon. The profile section, Re, chord length and LE tubercle amplitude and wavelength configuration used for the hydrofoil was the same as the rectangular profile section considered within the study by Custodio et al. [78]. Compared to the experimental findings of the baseline foil of Custodio et al. [78], there was an 11% difference in C_L, C_D was heavily underpredicted by approximately 50% and the cavitation volume was underpredicted. Li et al. [79] only focussed on an AOA of between 12 and 24°. There is some disparity between the experimental and numerical findings, the numerical results predict an improvement in lift between 12 and 24° AOA while the experimental findings concluded that in the same range of AOA that an increase in lift is observed only between 12 and 20°. This could be due to the fact that stall is predicted by the experimental test at roughly after 21° for the baseline and after 22.5° for

the tubercle modified hydrofoil, whereas for the numerical findings, stall is not observed between 12 and 24° for either hydrofoil as lift progressively increases across this range. So, the disparity in results may be due to the numerical modelling not accurately capturing the stall behaviour. Additionally, there could be some laminar to turbulent flow transition in the experimental study which would not be accounted for in the numerical study that assumes fully turbulent flow although this is not explicitly stated. However, it is clear that more studies about LE tubercles and their impact on hydrofoil performance in cavitating conditions is needed for more reliable conclusions to be drawn.

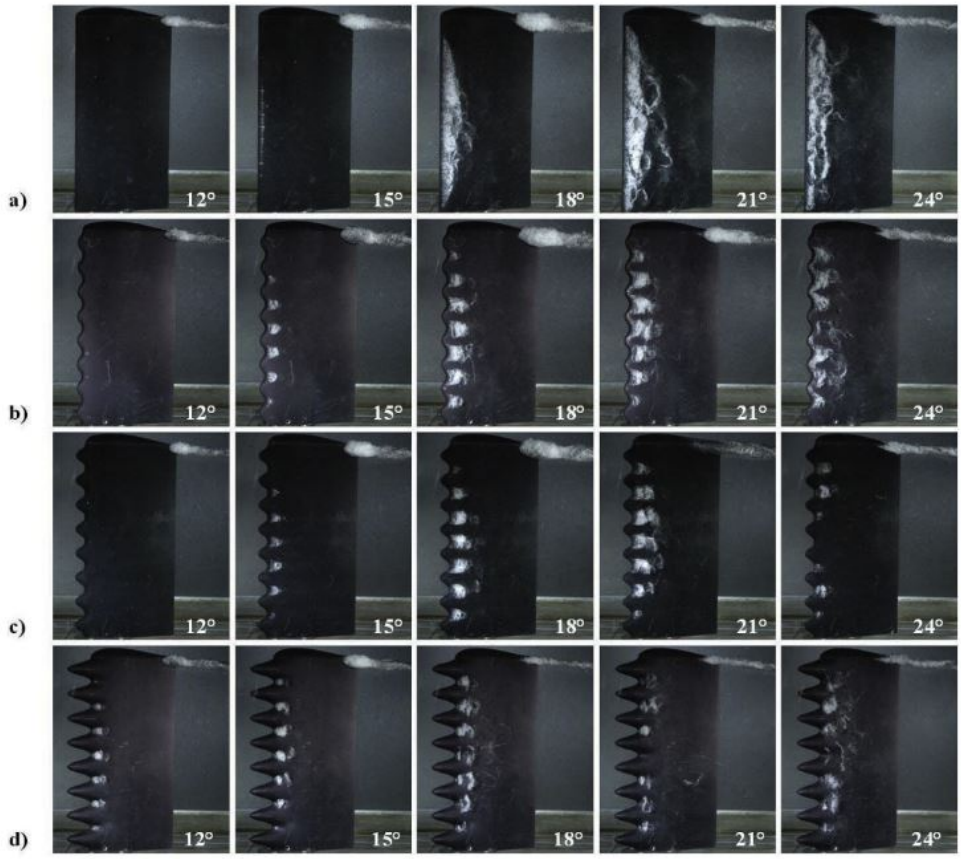

Figure 2.21: Cavitation on the rectangular hydrofoils at angles of attack 12°–24°: a) baseline foil, b, c and d) tubercle modified hydrofoils (reproduced from [78])

Based on the fundamental observations, the application of LE tubercles on both the duct and propeller blade of a ducted propulsor is attractive. It is attractive to apply to the duct as the LE tubercles have shown to influence flow separation behaviour which can occur on the outside of the duct. Applying LE tubercles in such conditions have resulted in an improvement in hydrodynamic performance on aero/hydrofoils and thus, applying LE tubercles to the duct could potentially improve duct thrust performance as the duct thrust is a resultant force from lift and drag. In addition, the LE tubercles have shown to interact with the downstream coherent wake of aerofoils which can result in a reduction in noise signature. This could be beneficial for ducted propulsors as they emit a coherent wake structure and LE tubercles could introduce streamwise vortex pairs which could disrupt this and reduce the URN levels which would positively impact the URN challenge for the commercial shipping sector.

It is also attractive to apply to the propeller blades as LE tubercles have shown to improve lift and reduced drag on 3D foils which could result in a more efficient propeller blade. They have also shown to reduce cavitation severity which is undesirable on propeller blades as it can reduce hydrodynamic performance and increase URN levels. But, the URN reduction capability in cavitating conditions of LE tubercle modified hydrofoils has not been clearly quantified. However, it is reasonable to assume that reducing the cavitation would result in a reduced URN signature but the influence of LE tubercles on cavitation and its associated URN requires further investigation. Improving propulsive efficiency with LE tubercle modifications in cavitating conditions is not clear from the current available literature on hydrofoils. Although, there is evidence to suggest that this is at least a possibility through evidenced improved lift performance and peak L/D ratio. This requires further investigation to provide clarity on the influence of LE tubercle modifications on the hydrodynamic performance of propulsors in cavitating

conditions. In addition to address the need to reduce the URN of marine vessels, this could have a further positive impact on reducing ship fuel consumption and thus, GHG emissions which is another key challenge to address for the shipping industry as mandatory policies are in place to limit GHG emissions such as the EEDI.

2.2.2 Further Applications and Commercialisation

From the key early findings from the foil research, this has led to the commercialisation of the concept through company WhalePower and further investigative studies into the applicability of the LE tubercle on rotating machinery such as fans, turbines and propellers. WhalePower first product was the industrial fan, where it is claimed that the fans use half the number of blades, move 25% more air and consume 25% less power than conventional fans turning at the same speed [80].

WhalePower are not the only group with interest in the application of the LE tubercle on rotating machinery, the concept has been researched on devices such as the wind and tidal turbine and more recently, the marine propeller. Howle [81] conducted an experimental investigation on the wind turbine blade with LE tubercles, showing that the inclusion of tubercles resulted in an increase in power output on the low wind speed range when compared to the smooth LE blade, this blade is illustrated in Figure 2.22.

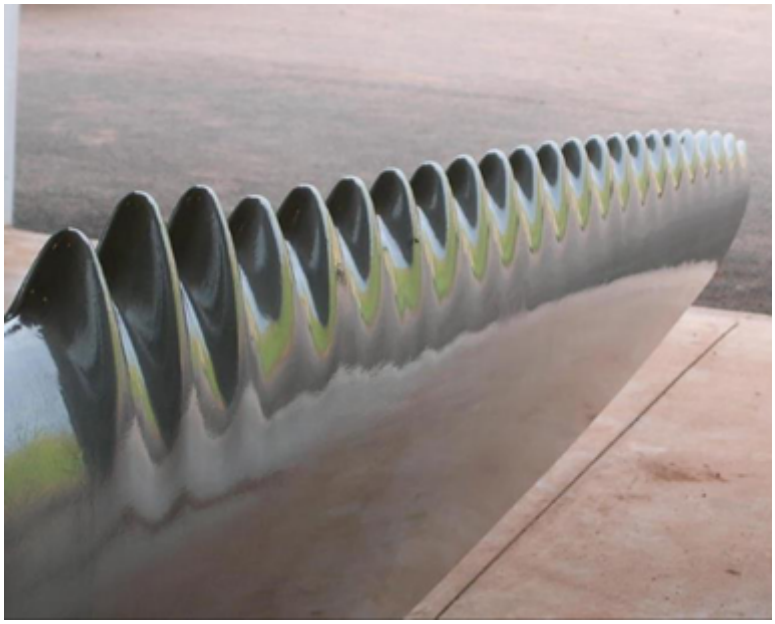

Figure 2.22: LE tubercles as applied onto a wind turbine blade (reproduced from [82])

The concept has also been researched on tidal turbines and more recently, marine propellers. Shi et al. [7; 8; 69] investigated tubercles on tidal turbines (see Figure 2.23). An in-depth numerical and experimental study was conducted into the feasibility of LE tubercles on such a device. The work showed an improvement in power coefficient at low tip speed ratios (TSR), containment of cavitation and reduction of URN (see Figure 2.24) in some operating conditions. Within this in-depth study, an optimisation investigation was conducted, where tidal turbines with tubercles along full and partial lengths of the leading-edge were trialled. It was found that the inclusion of LE tubercles resulted in cavitation inception occurring earlier at higher cavitation numbers similar to findings on rectangular hydrofoils by Custodio et al. [78]. In heavier cavitating conditions the cavitation was restricted to the troughs of the tubercles, similar findings to Weber et al. [63] and Custodio et al. [78].

During the experimental investigation of LE tubercles on a 3D tidal turbine-

based hydrofoil [83], a vortex fence due to the introduction of the counter-rotating streamwise vortex pairs was observed through experimental flow visualisation. This flow mechanism mitigated the spanwise cross-flow induced by the tip vortex and this was the reason for the difference between the impact of LE tubercles on the aero/hydrodynamic performance of two and 3D foils, previously discussed by Miklosovic et al. [73]. A full scale demonstration of a LE tubercle modified tidal turbine would provide further understanding of LE tubercle modified tidal turbines performance at a larger scale as the positive impact of LE tubercles on tidal turbines in model scale is clearly evidenced.

Figure 2.23: LE tubercles as applied to the tidal turbine (reproduced from [69])

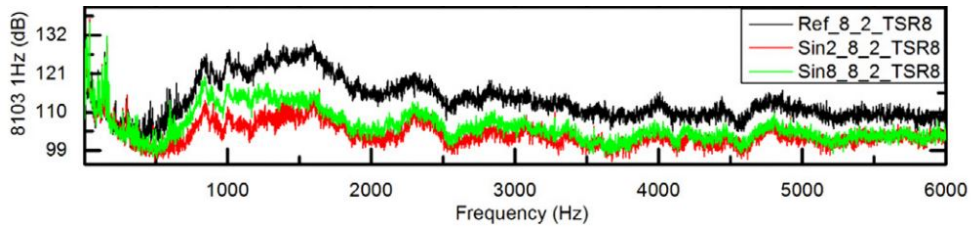

Figure 2.24: Noise reduction of LE tubercle modified tidal turbines at $TSR = 8$ (reproduced from [7])

Additionally, the influence of LE tubercles on marine propellers has been investigated, although the openly available research is very scarce and not in-depth [60; 61]. Ibrahim and New [61] conducted a numerical investigation using CFD to conclude that LE tubercles as applied to a marine propeller in non-cavitating

conditions can improve the total raw power output of the propulsive device, although an increase in torque resulted in a lower propulsive efficiency. This specific tubercle design created spanwise ridges across the blade which is undesirable because it creates an additional uncertainty when making a direct comparison between LE tubercles and a reference design. They also did not consider varying the tubercle geometrical parameters amplitude and wavelength. This study did not consider comparing the efficiency at the same thrust loading coefficient and instead compared at the same advance ratio, J. Comparing the efficiency at the same thrust loading coefficient is a key consideration amongst ship designers as this allows a direct comparison of the efficiency of the propulsor at the thrust required for a given vessel. Therefore it could be possible that LE tubercles shift the operational curve as oppose to degrading propulsive efficiency in non-cavitating conditions but this would require further investigation. Performance in cavitating conditions was not considered even though LE tubercles have previously shown inspiring impacts on the influence on cavitation behaviour and hydrodynamic performance on hydrofoils at the time this study was conducted in 2015. They also did not consider the impact of Re and scale on the impact of the performance change created by LE tubercle modifications which is important to consider.

Charalambous and Eames [61] used numerical methods to investigate the influence of LE tubercle modifications on marine propeller performance in cavitating conditions. It was shown that sheet cavitation is influenced by LE tubercles and in some conditions could improve propeller performance but only one cavitation number was explored which limits the conclusions that can be drawn. Moreover, no cavitation volume reduction was quantified and the fundamental flow mechanism behind the influence of LE tubercle modifications on propeller sheet cavitation was not explored. Crucially, no investigation into the impact on the URN signature was considered. Similarly to Ibrahim and New [61], this

study did not consider varying the tubercle geometrical parameters amplitude and wavelength, or the scaling effect on the influence of LE tubercle modifications on marine propulsors. Additionally, they made comparisons of hydrodynamic performance at J instead of comparable thrust loading coefficients.

In addition to rotating machinery, LE tubercles have been applied to other geometries and designs. Control surfaces like the rudder [63], dive planes, sailboat keels, kegs and the surfboard fin are believed to benefit from increased manoeuvrability due to the addition of LE tubercles [82]. Commercially, the company Fluid Earth markets a surfboard fin with tubercles on the leading-edge and is shown in Figure 2.25.

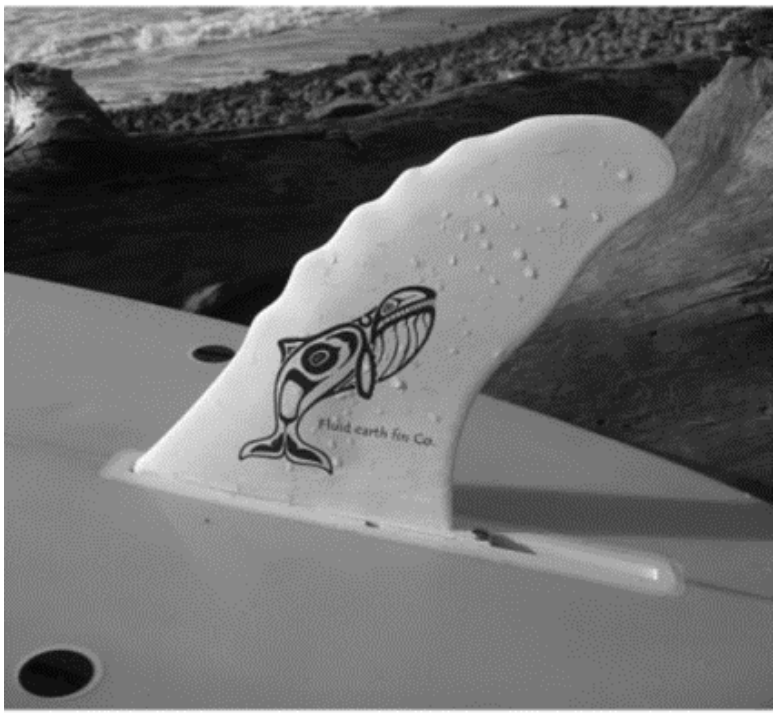

Figure 2.25: LE tubercles applied to the fin of surfboard courtesy of H.Swales and Fluid Earth [82]

Based on the findings from LE tubercle modified rotating devices, it is clear that there is a gap in the understanding of the impact of LE tubercle modifica-

tions on the cavitation behaviour, hydrodynamic and URN signature of propellers as well as the fundamental flow mechanisms behind the change in performance. In addition, LE tubercle modifications have not been applied to the duct, so there is a gap in the understanding of the influence of LE tubercle modifications on the hydrodynamic and URN signature of ducted propulsors as well as uncovering the fundamental flow mechanisms behind this performance change. Additionally, the scaling effect and influence of LE tubercle geometrical parameters on the performance change of LE tubercle modifications on the duct and propeller blade has not been considered. Within the previous literature, the geometrical parameters have shown to influence the impact of LE tubercle performance and in previously developed URN mitigation concepts scale has shown to influence the change in URN levels, so this is important to consider.

2.2.3 Summary

The origins, influence, application and benefits of LE tubercles have been discussed, showing through a review of literature that they have promising enhancements in aero/hydrodynamic, noise and cavitation performance on aerofoil sections to tidal turbines. Based on the above fundamental observations, it is believed that the duct and propeller could benefit from the inclusion of LE tubercles. The ducted propeller operates in a wide operational range and in some heavy-loaded conditions, flow separation and cavitation can occur which can result in performance degradation which is where the tubercle application can have a positive impact according to previous studies within the literature.

Specifically through evidence from previous studies, it is believed that LE tubercles applied to the duct could provide a noise reduction through the introduction of counter-rotating streamwise vortex pairs into the coherent wake structure in the ducted propulsor slipstream. An improvement in duct thrust performance

could be achieved in conditions where flow separation is present through LE tubercle modifications. Moreover, LE tubercles applied to the propeller blades could potentially improve hydrodynamic and noise performance through the influence on the sheet cavitation behaviour. This requires further investigation into their potential benefits and the fundamental mechanisms behind any performance change.

Furthermore, LE tubercles have shown to improve performance in the post-stall region but the geometrical parameters, amplitude, A and wavelength, λ are important in determining the trade-off between pre-stall and post-stall performance enhancement and therefore, the geometrical parameter of the LE tubercle must be explored in order to reach a balanced design.

2.3 The Evaluation of Underwater Radiated Noise

In order to reduce URN levels from propulsors, accurate and reliable numerical and experimental investigation methodologies must be developed and exploited in order to understand the different noise mechanisms and drive the mitigation of URN. Computational power is increasing and thus, numerical noise prediction using CFD is becoming more and more viable within the maritime industry which will be crucial in order to quantify and mitigate URN in the early design stages of ships. Therefore, numerical methods such as CFD will be critical in providing shipowners with the capability to meet URN targets and adhere to mandatory regulations that could be set in the future by international bodies such as the IMO.

This section aims to explore the different computational and experimental methodologies currently available to predict the hydrodynamic and noise performance of ducted propeller noise in order to select the most suitable methods in

the present study.

2.3.1 Numerical Methodologies

In addition to empirical, semi-empirical and statistical approaches for the prediction of ship propeller noise which can be found outlined in Ross [84], computational fluid dynamics (CFD) is a growing sector that provides engineers and researchers with the tools to predict marine propeller performance amongst a variety of other physical problems. This saves time and money, as CFD allows many geometries and designs to be considered, acting as an initial design and analysis phase to refine a final prototype before experimental testing. There are several commercial CFD codes available, namely STAR CCM+, ANSYS FLUENT and OpenFOAM that provide an environment to predict the performance of marine propellers. The most popular tool for hydroacoustics is the hybrid approach, where an incompressible solver like Reynolds-averaged Navier Stokes equations (RANS), Detached or Large Eddy Simulations (DES/LES) is used to solve the near field hydrodynamic flow field and an acoustic analogy known as the Ffowcs-Williams Hawkings (FW-H) approach is used to propagate the sound to the far-field. This approach is a popular approach within the literature and has been used to predict URN of marine propellers in both non-cavitating and cavitating flows [13; 54; 55; 56; 85]. In order to predict the noise of marine propellers accurately, the hydrodynamic flow field must be accurately captured. So therefore, the propeller and hydrodynamic modelling techniques will be outlined first. Then, the various methodologies to predict noise numerically will be explored, with focus on the utilisation of the the FW-H acoustic analogy for hydroacoustics.

2.3.1.1 Propeller CFD Modelling Techniques

The most popular methods to describe a marine propeller within CFD are as follows:

1. Actuator Disk (such as the Body Force Propeller (BFP) method)

   Using the actuator disk, the propeller is simplified to a disk using simplified actuator disk theory. The simplified disk is shown in Figure 2.26, where P is pressure and v is velocity while subscripts in is the freestream inflow characteristics at infinity upstream of the disk, f determines the downstream characteristics at a distance of infinity downstream of the disk and d describes the induced flow characteristics. The model allows the flow to pass through the permeable disk and at the same time it is subject to the influence of the disk surface forces. The 'classical' actuator disk model is based on the conservation of mass, momentum and energy, and makes up the main elements in the 1D momentum theory. It can be combined with a blade-element analysis to produce the blade element momentum (BEM) model. However, it can also be combined with the numerical solution of the Euler or Navier–Stokes equations which are typically solved by a second-order accurate finite difference/volume scheme, as in a usual CFD computation [86].

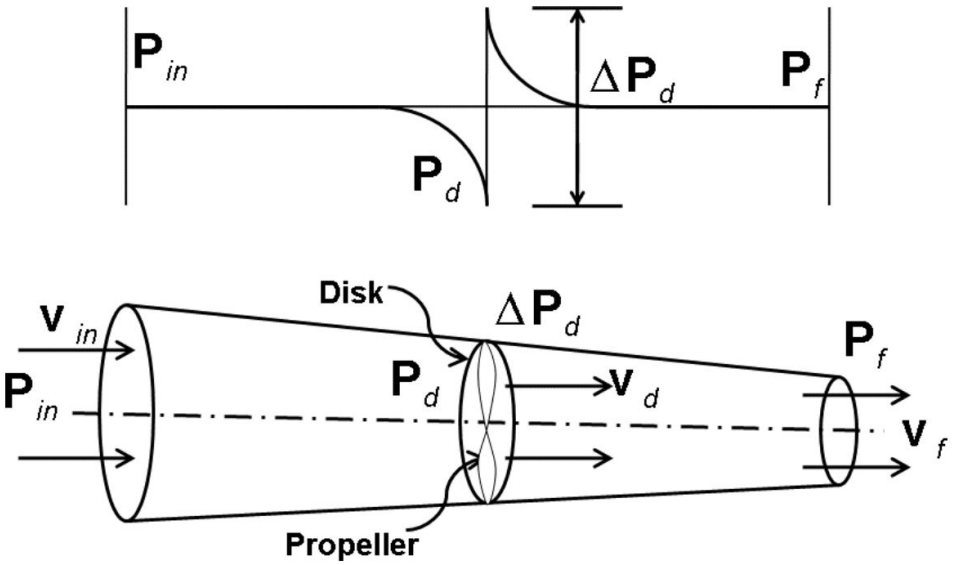

Figure 2.26: Actuator disk theory (reproduced from [87])

In a numerical actuator disk model, the Navier–Stokes (or Euler) equations are typically solved by a second-order accurate finite difference/volume scheme, as in a usual CFD computation. However, the geometry of the blades and the viscous flow around the blades are not resolved. Instead, the swept surface of the rotor is replaced by surface forces that act upon the incoming flow. This can either be implemented at a rate corresponding to the propeller rotation rate or by using local instantaneous values of tabulated airfoil data. The generalised actuator disk method resembles the BEM method in the sense that the aerodynamic forces have to be determined from measured airfoil characteristics, corrected for 3D effects, using a blade-element approach. For airfoils subjected to temporal variations of the angle of attack, the dynamic response of the aerodynamic forces changes the static aerofoil data and dynamic stall models have to be included.

The 'classical' actuator disk model adopts the following assumptions [88]:

- The fluid flow is ideal across the control volume, meaning that it is steady, homogenous, inviscid, incompressible and irrotational,
- There is an infinite number of blades, thus fits the actuator disk description,
- Both flow and thrust are uniform across the disk area and,
- Undisturbed ambient static pressure is assumed for the static pressure far upstream and downstream of the rotor disk.

The main limitation of the axisymmetric assumption is that the radial forces are distributed evenly along the actuator disk; hence, the influence of the blades is taken as an integrated quantity in the azimuthal direction. This differs from the radial thrust and torque distribution of a propeller blade which is not uniform. Therefore, the body force propeller method was developed by Stern et al. [89] in which the radial thrust and torque distribution could be varied. For propellers, the optimal circulation distribution is described by Goldstein [90] which is closely matched to the distribution introduced by Hough and Ordway [91] with no load at the blade tip or root.

This is a useful method within self-propulsion tests [92], where the mesh count and simulation time can be reduced by removing the physical propeller and using the disk with known experimental performance data. Or, for the use of ducted propeller optimisation, where the propeller thrust and torque can be fixed, and the duct's performance can be isolated [93]. However, the simplified actuator disk modelling has limitations such as the negation of the propeller blades which will disregard typical vortex mechanisms such as the tip vortex and blade trailing edge vortex from the numerical modelling, which may be crucial to certain areas of study like the prediction of propeller URN.

Blade resolved methods are also available to represent the propeller within the computational domain and they can be described as the following;

2. Moving Reference Frame (MRF) method

   The mesh motion is defined with respect to a reference frame, which can be stationary (global reference frame) or rotating and translating relative to the global reference frame. In steady simulations, or in transient simulations that do not require a time-accurate solution, moving reference frames provide a way of modeling rotations and translations as a steady-state problem, while leaving the mesh stationary. Consider a moving reference frame that is rotating and translating with constant velocity shown in Figure 2.27.

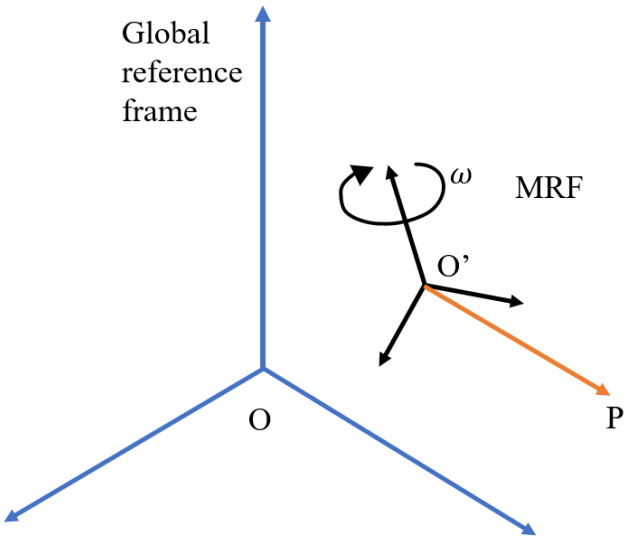

Figure 2.27: Moving Reference Frame (MRF) Method (adapted from [94])

The velocity of a material point P with respect to the moving reference frame (also called the relative velocity, v_r) can be written as shown in Equation 2.1:

$$v_r = v - v_{MRF,t} - \omega_{MRF} \times r_{P,MRF} \tag{2.1}$$

where v is the velocity in the global reference frame (also called the absolute velocity), $v_{MRF,t}$ is the moving reference frame translation velocity, that is, the velocity of its origin with respect to the global frame, ω_{MRF} is the angular velocity of the moving reference frame with respect to the global frame, and $r_{P,MRF}$ is the position vector of the material point with respect to the moving reference frame.

This is the most cost effective method to obtain hydrodynamic force coefficients of propellers and has been successfully validated with experimental data previously for open water performance of open and ducted marine propellers [95; 96].

3. Rigid Body Motion (RBM) method, also known as the 'sliding mesh' technique

The RBM method is where the propeller is rotated a fixed displacement over time and is widely regarded as the most accurate method to simulate marine propellers, although it is the most computationally expensive. It is also the most suitable method to solve the hydrodynamic flow field for noise prediction since it is considered to be the most accurate way to obtain the change of flow variables with time [85].

For a rotational rigid body motion the mesh velocity, $v_g = \omega_g r$, where ω_g is the prescribed angular velocity and r is the position vector of a mesh vertex. Whereas for the MRF method, $v_g = 0$ with respect to the moving frame as the mesh vertices remain static during the simulation.

The difference between MRF and RBM can be described through how the motion is incorporated into the discretised form of the convective flux term within

the governing conservation equations. The convective flux expresses the net rate of decrease of fluid property, ϕ, across the control volume boundaries due to convection [94]. Consider the grid flux, G, which modifies the discretised form of the convective flux term, $(\phi\rho v \cdot a)_f$, where ϕ is the fluid property at the face, ρ is the density of the fluid, v is the grid/face velocity, a is the face area vector and subscript f denotes the face. Where grid flux is the product of face area and velocity, the convective flux term for the purpose of this explanation can be simplified to $(\phi\rho G)_f$. The grid flux as a component of both MRF and mesh motion such as RBM is shown in Equation 2.2:

$$G = G_{MRF} + G_g \tag{2.2}$$

G_{MRF} is the contribution due to MRF, and G_g is the contribution due to mesh motion. G_{MRF} is calculated as shown in Equation 2.3:

$$G_{MRF} = (v_{MRF,t} + \omega_{MRF} \times r) \cdot a_f \tag{2.3}$$

where $v_{MRF,t}$ is the MRF translation velocity, ω_{MRF} , is the angular velocity of the MRF and r is the position vector of a material point. For a stationary reference frame, $G_{MRF} = 0$. For first-order time approximation, the contribution due to mesh motion, G_g, is calculated as shown in Equation 2.4:

$$G_g = \frac{\delta V_f^n}{\Delta t} \tag{2.4}$$

where V_f^n is the volume swept by the face f over time step t^n. When the mesh is stationary, $G_g = 0$.

If motion is accounted for only using MRF (e.g. $G = G_{MRF}$), then no discretisation in time is performed for the grid flux term, G, and the motion will not be time-accurate whereas for RBM a discretisation in time is performed and so it is

time-accurate. The difference between RBM and MRF methods using a propeller and rotating domain is shown in Figure 2.28.

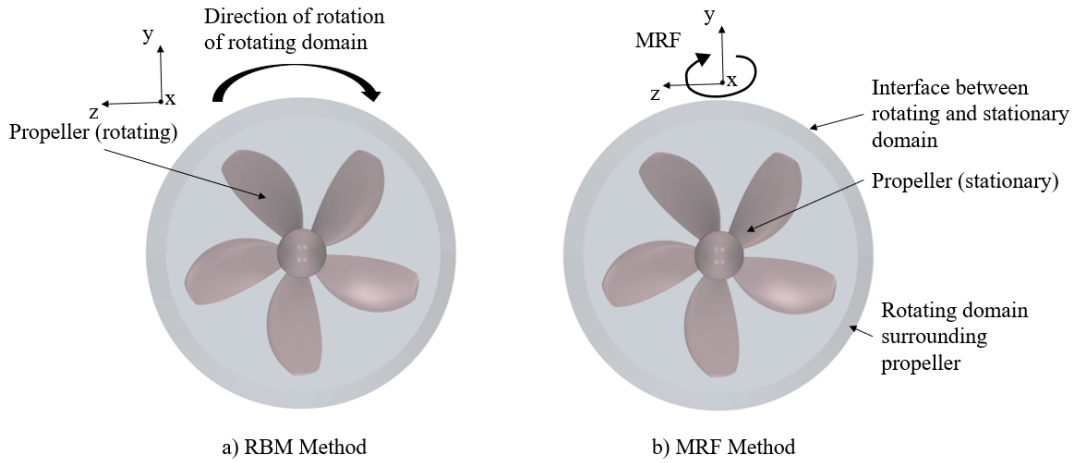

Figure 2.28: a) Rigid Body Motion (RBM) Method and b) Moving Reference Frame (MRF) Method

Table 2.2 summarises the advantages and disadvantages of the different methods to describe a propeller within a computational domain. Based on the above review, the actuator disk was selected for the initial hydrodynamic study to optimise the duct in an economical manner. However, the RBM method was selected for further detailed analysis and the hydroacoustic study because it represents the time-accurate behaviour of the flow field which is critical to capture the complex flow behaviour induced by the propeller rotation.

Method	Advantages	Disadvantages
Actuator Disk Body Force Propeller (BFP) Method [92; 94]	- Computational cost low compared to MRF and RBM - Useful for representation of propeller in self-propulsion simulations or isolating duct performance	- Blades not resolved so no unsteady blade loading due to period blade passage - No realisation of tip vortex, or trailing-edge vortex
Moving Reference Frame (MRF) [94; 95; 96]	- Computational cost lower than RBM method - Can be used with steady RANS to acquire open-water performance with good accuracy without the need for transient simulations	- Computational cost higher than BFP method due to extra mesh necessary to resolve blades - Only captures time-averaged flow behaviour
Rigid Body Motion (RBM) [94; 97]	- Capture time-accurate flow behaviour	- High level of computational cost compared to MRF and BFP methods as transient analysis necessary

Table 2.2: Advantages and disadvantages of the propeller modelling techniques available within CFD

2.3.1.2 Turbulence Modelling

In addition to the propeller modelling technique, selection of the turbulence model is also important. The incompressible Reynolds-averaged Navier Stokes (RANS) solver is the most conventional solver adopted, where the SST k-ω turbulence model developed by Menter [98] is a well-established turbulence model for the hydrodynamic performance prediction of ducted and open propellers with various researchers validating numerical results with experimental tests [85; 92; 96]. But, RANS fails to solve the instabilities within the wake flow of the propeller [99; 100]. Therefore, scale-resolved methods such as DES/LES are used to accurately predict the flow field where the physical situation makes it necessary, but this comes at increased computational cost when compared to RANS. Particularly, bodies operating in heavy-stall or flow separation conditions warrant the use of DES/LES as RANS fails to accurately predict such phenomena [101]. DES is seen as the trade-off between RANS and LES, allowing more accurate realisation

of the flow than RANS but computationally less expensive than LES. As can be seen, the trade-off between accuracy and cost is a constant consideration for the CFD user. But nevertheless, noise prediction is only as good as the hydrodynamic input and thus, if the flow field is solved more accurately, then the noise prediction should be more reliable.

Based on this, DES was selected for detailed hydrodynamic and hydroacoustic analysis within the PhD project as it can capture the vortex breakdown in the propeller slipstream which is not possible with RANS and it is less computationally expensive than LES. But, RANS was selected for the preliminary hydrodynamic optimisation study because it is less computationally expensive than DES.

2.3.1.3 Hydroacoustic Modelling

Hydroacoustics using CFD has really emerged over the last few decades thanks to inspiration and developments in aeroacoustics. There are various CFD approaches available within the aero/hydroacoustics field, direct numerical simulations (DNS), direct viscous-based methods (RANS/DES/LES) and the hybrid approach using either viscous or potential-based flow solvers. DNS has its advantages and challenges. While there are no modelling assumptions because the Navier-Stokes equations are directly solved without any turbulence model, it requires high mesh quality and a small time-step to obtain an accurate solution and is therefore computationally expensive compared to RANS/LES/DES and potential-based methods. Pressure fluctuations in the near field around the propeller can be solved directly from the CFD solution using a viscous or potential-based method. However, without adequate mesh resolution, the sound waves dissipate quickly into the far-field [97]. The mesh resolution required to directly calculate far field noise is practically unfeasible. In addition, using the incom-

pressibility assumption ignores the sound propagation from the near to the far field. Using the compressibility assumption for the propagation of sound is a computationally expensive approach so because of these reasons, generally the far field noise is predicted using a hybrid approach [102]. The hybrid approach is where the near field hydrodynamic flow field can be solved using viscous (RANS/DES/LES) or potential-based solvers and then the sound is propagated to the far field using an acoustic analogy.

The most common analogy employed within hydroacoustic research is the Ffowcs Williams-Hawkings (FW-H) acoustic analogy [103], The FW-H acoustic analogy is an extension of Lighthill's theory [104] which was formulated for the jet noise phenomena. Ffowcs-Williams and Hawkings made a fundamental step towards a full understanding of noise generated by bodies moving in a fluid. Multiple studies have been conducted with different formulations of the FW-H acoustic analogy on marine propeller noise prediction [13; 54; 55; 56; 85]. It considers all fundamental noise sources, monopole (thickness of blades and cavities), dipole (blade loading), and quadrupole (non-linear contributions associated with turbulent structures, products of cavity destruction and vortex-vortex interaction in propeller slipstream).

The monopoloe, dipole and quadrupole are idealised noise sources. The simplest idealised noise source is the monopole, which generates pressure waves radiating equally in all directions. Physically, this can be described as a sphere expanding and shrinking in an oscillatory manner, periodically pushing the fluid away from and attracting it towards the centre of the sphere. The dipole source consists of two monopole sources of equal strength but opposite phase and separated by a small distance compared with the wavelength of sound. While one source expands the other source contracts. The result is that the fluid near the two sources sloshes back and forth to produce the sound. If two opposite phase

monopoles make up a dipole, then two opposite dipoles make up a quadrupole source [105]. The pressure waves that the idealised acoustic sources produce can be shown in Figure 2.29.

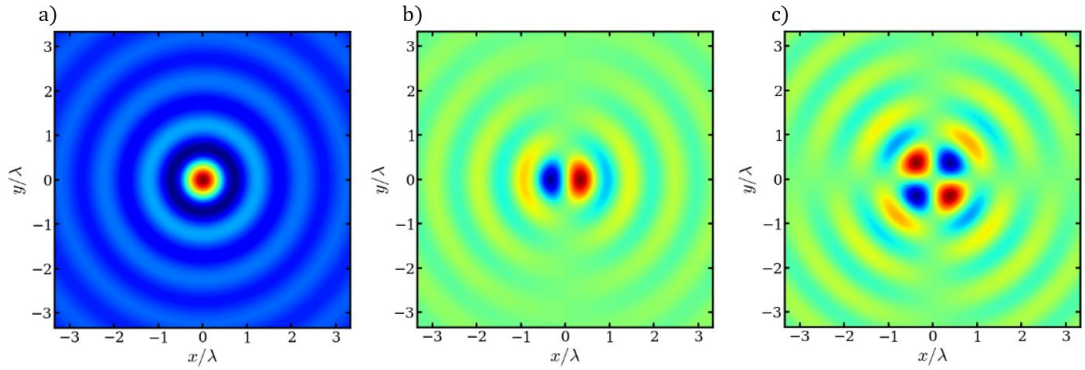

Figure 2.29: Examples of idealised acoustic noise sources, a) monopole, b) dipole and c) quadrupole, showing pressure iso-contours non-dimensionalised using maximum values over a 2D plane shown as a function of wavelength, λ (reproduced from [106])

While the contributions from monopole and dipole sources are evaluated by computing surface integrals on the respective noise sources using the FW-H acoustic analogy, the quadrupole term requires volume integration, which is very expensive. Therefore, instead the sound sources can be evaluated using a permeable control surface, a formulation derived by Francescantonio [107], which surrounds the propeller and a portion of the turbulent wake structure. An example of a permeable surface is shown in Figure 2.30, where the surface is shown to encompass the propeller and a portion of the downstream area where the wake structure will be produced, this captures the sound generated inside the permeable surface and propagates it into the far-field using the acoustic analogy. In such formulations, for example Farassat Formulation 1A [108], the terms responsible for monopole and dipole contributions lose their original strict meaning and become pseudo-monopole and pseudo-dipole terms, which include also the contribution from the

quadrupole (non-linear) term, provided that the permeable control surface encompasses a portion of the turbulent wake. The original FW-H acoustic model is used only to predict sound propagation in free space. It does not account for the effects of reflection, refraction or material property change in the domain of the receiver [109].

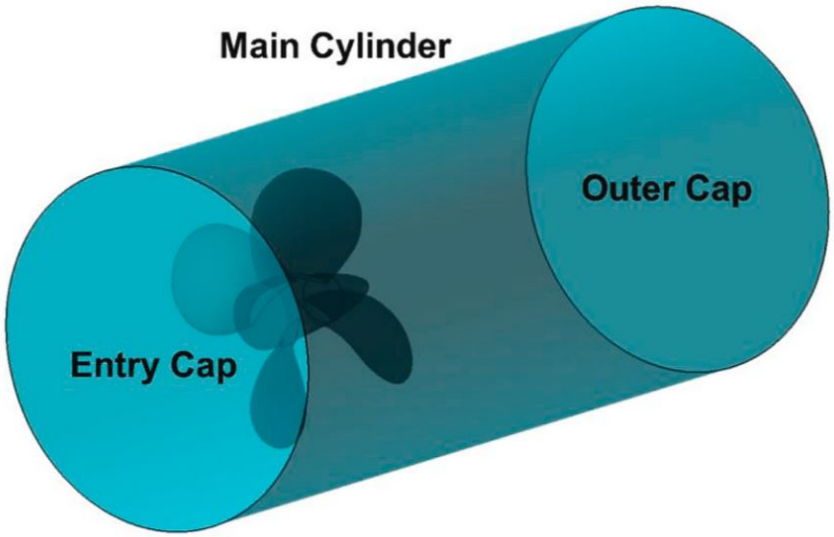

Figure 2.30: Permeable surface surrounding a marine propeller (reproduced from [57])

The FW-H analogy regarding its applicability within the hydroacoustic field is a relatively new research field with no clear standard. However, certain research has helped in the development of the FW-H analogy within the maritime field, particularly when used with viscous-based solvers such as RANS/LES/DES. Ianniello et al. [110] showed that while the quadrupole source is not significant for propellers at low rotational speeds in air and so can be neglected, it cannot be neglected within underwater radiated noise regardless of the blade rotational speed. It was also stated that the permeable/porous approach represents the most suitable way to performance a numerical prediction of noise in the far field and that the contribution of the linear noise terms reduce rapidly into the far

field. Further numerical investigations by Ianniello et al. [56] raised stipulations that RANS may be inadequate for hydroacoustic purposes due to the vorticity field being damped and the vortex breakdown in the slipstream being completely ignored. Lidtke et al. [111] explored different parameters such as time-step, permeable surface design and grid resolution on the URN predictions of a marine propeller using the permeable FW-H approach. The inclusion of an endcap resulted in an increase in spurious noise due to the crossing of the wake flow and it was concluded that special care in the grid structure is needed to avoid numerical diffusion through the changing grid sizes. Therefore, removing the endcap from the permeable surface and ensuring a uniform mesh size within the permeable surface were recommended to reduce the amount of noise distortion from numerical errors. Sezen et al. [57; 112] stated that more realistic predictions of propeller URN requires the use of more high fidelity modelling such as DES/LES, agreeing with stipulations made by Ianniello et al. [56]. Within this study, the end cap was removed based on the recommendation from Lidtke et al. [111].

In addition to viscous-based flow solvers using with the FW-H acoustic analogy, potential-based flow solvers have been combined with the FW-H acoustic analogy. This is because of their low computational cost, while it could be useful in the early design stage, they are not as capable as viscous-based methods. This is because they neglect turbulence and viscosity effects and so cannot capture the complex flow details which are important for the prediction of propeller URN [113].

The literature has shown that although there is no clear standard for the application of the FW-H acoustic analogy, there have been developments in the best practices that will accelerate the possibility of this in the future and that currently, the hybrid method of an incompressible flow solver and the FW-H acoustic analogy is the most accepted method within the maritime field to solve

for far-field hydroacoustic noise prediction. Table 2.3 summarises the application, advantages and disadvantages of the hydroacoustic methods using CFD; DNS, direct viscous-based method, and the potential and viscous-based hybrid approach. From reviewing the available methodologies, the hybrid approach using DES with a permeable FW-H acoustic analogy was deemed to be the most appropriate for far field noise prediction for the area of interest within the PhD project, while a direct hydrodynamic pressure obtained from the hydrodynamic flow solver was suitable for near field noise predictions. This is because DNS is too computationally expensive and two-way coupled flow-acoustic interaction was not of interest within the PhD project while the FW-H acoustic analogy is more suitable for far field noise prediction and it is less computationally expensive. In addition, potential-based flow solvers neglect turbulence and viscosity effects in the flow so cannot capture all the complex flow details when compared to viscous-based methods. In terms of viscous-based methods, DES presents the most attractive solution as it is less computationally expensive than LES and can capture instabilities within the propeller slipstream which are not captured by RANS. Comparing the permeable and impermeable FW-H approach, the permeable approach was selected as it can capture all the noise sources including the quadrupole noise source using a surface integral without the need for solving the quadrupole noise source as a volume integral which is more computationally expensive. The quadrupole noise source was considered critical to include in the analysis because it is typically dominated by the turbulence and vorticity-induced noise from the propeller slipstream.

Method	Application	Advantages	Disadvantages
DNS [57; 85; 94; 112]	- Measurement locations close to source - When hybrid methods cannot be used - Two-way coupled flow-acoustic interaction	- No modelling assumptions	- Computational cost is high - High requirements on numerical accuracy - High number of mesh cells required - Post-processing for acoustic analysis
Direct viscous based method (LES/DES/RANS) [94; 97]	- Measurement locations close to source	- Less time to set up without acoustic analogy	- Unsuitable for far field noise predictions using incompressibilty assumption - Compressibility assumption too expensive
Potential-based hybrid approach [57; 85; 94; 112; 113]	- Linear noise sources - Early design stage	- Low computational cost	- Neglects turbulence and viscosity effects so cannot capture complex flow details
Viscous-based hybrid approach with impermeable FW-H [94; 97; 109; 110; 111]	- Far-field noise prediction - Acoustically compact source regions - Rotating device noise in air - Lifting surface noise in air	- Post-processing for acoustic analysis - Can neglect quadrupole noise source which reduces computational cost	- Computational cost is high but not as high as DNS - Accuracy is required - No absorbent materials - No strong coupling with structures - Neglects reflection and refraction - If required, quadrupole noise source is computed using a volume integral which is computationally expensive
Viscous-based hybrid approach with permeable FW-H [56; 97; 109; 110; 111]	- Far-field noise prediction - Acoustically compact source regions - Jet/exhaust noise	- Can capture flow phenomena such as turbulence and vorticity - Post-processing for acoustic analysis - Reduces computational cost compared to impermeable FW-H when quadrupole noise source is included	- Computational cost is high but not as high as DNS - Accuracy is required - No absorbent materials - No strong coupling with structures - Neglects reflection and refraction - If of interest, high mesh quality necessary to resolve vortical structures in domain to be included within hydroacoustic analysis

Table 2.3: Summary of CFD hydroacoustic methodologies for URN prediction; application, advantages and disadvantages

2.3.2 Experimental Methodologies

The use of CFD has been revolutionary for many industries like the maritime industry with cost savings and quick, accurate results. But many researchers are still sceptical in solely relying on the predictions from the commercial CFD software and therefore, experimental tests are still paramount in the accurate prediction of marine propeller performance. Even more specifically, hydroacoustics using CFD is still relatively new and as shown in the previous chapter, there is no clear standard for predicting the noise of marine propellers within the industry. Noise is very complex in both cavitating and non-cavitating flows with many linear and non-linear sources as previously discussed. CFD cannot capture all the flow phenomena accurately as shown with available numerical and experimental comparisons showing large disparities in predictions when compared to experimental data, where most work focuses on the cavitation of open propellers [85; 111; 114; 115; 116; 117]. As part of EU-funded project SONIC, Lafeber and Bosschers [118] made computational and experimental URN predictions for a marine propeller in cavitating conditions. It was concluded that the model tests underpredicted the URN levels when compared to full scale trials, but after applying a new tip vortex scaling method at one condition, the results were similar. The computational methods could predict the URN levels with a reasonable degree of accuracy. The tip vortex scaling method for URN is detailed in Bosschers [119]. Bosschers [119] showed that the proposed methodology improved the noise predictions in situations where the tip vortex cavity observed in model scale was much smaller than that observed in full scale and is now used in the depressurised wave basin at MARIN.

In addition to disparity in results between numerical and experimental evaluation techniques for URN, there is also disparity between different testing facilities. Tani et al. [116] presented URN results from an organised round-robin test of

a marine propeller from research vessel 'The Princess Royal' in cavitating conditions at multiple different facilities. The cavitation extent was similar when comparing the observations in the test facilities, however several discrepancies were observed. Large discrepancies were found in the prediction of URN when comparing the URN results from the different facilities and it was concluded that further investigation was needed to explain such discrepancies. It is worth noting that the propeller was not manufactured by the same manufacturer and thus, the difference in surface finish could be a contribution to the disparity in results. Based on these conclusions, further aspects were recommended for investigation in the future, not only including the development of cavitation but also the generation, propagation, acquisition and processing of noise data. This included several main aspects such as the effects of; water quality on noise generation and propagation, the acoustic response of the facility, the oblique flow and the adoption of different scaling laws to compare results of the round-robin campaign. This shows that different experimental facilities do not always provide similar URN results which needs to be addressed because accurately quantifying URN is paramount if any targets for URN reduction are to be set in the future.

Many researchers in the field have more confidence in experimental results than CFD and this will be the case until a standardised methodology and more advanced numerical tools are created for noise prediction of marine propellers. However, there is still large disparities in URN results when comparing different experimental model testing facilities and between model and full scale results which needs to be further understood and explained. This also highlights the need for development of new methodologies to quantify and scale URN. More experimental validation of numerical noise data is necessary and in the case of ducted propellers in both non-cavitating and cavitating flows, there is very limited openly available benchmark data sets. Therefore, although CFD is a useful tool

that can provide new insights, it is recommended to compliment experimental work and vice-versa depending on the type of engineering problem and handled with care, with special consideration to boundary layer meshing, turbulence modelling and domain parameters. But, like CFD, experiments also come with their drawbacks.

2.3.2.1 Underwater Radiated Noise Measurements

Underwater radiated noise measurements of marine propellers using experimental methods can be split into two categories, model-tests and full scale trials. The model-tests are usually conducted in what is called a cavitation tunnel or a depressurised towing tank. The set-up and post-processing of model-scale noise requires the utmost attention to detail to ensure accurate measurements and reasonable conclusions can be drawn. Important considerations including the manufacturing of the propeller blades to ensure a smooth surface and avoid propeller singing, the wake inflow and scaling methods must all be met with care [120]. A full procedure was recommended by the ITTC, including the set-up, background noise measurements, data acquisition, scaling methods and uncertainty and validation [121]. This recommendation only included the recommended procedure for cavitation noise, where non-cavitating noise was not included although it is assumed that the procedure would be almost identical. The main challenge for noise prediction using model-scale tests is finding an appropriate method of scaling the near-field measurements to full scale and then predicting accurate far-field measurements from them [11]. The second method to experimentally measure URN is through full scale trials, also known as sea trials. This involves placing an array of hydrophones at a specified distance away from the ship and recording the ship as it passes. Special consideration must be given to the levels of ambient noise, other passing ships, water depth and the seabed type. Although this is feasible, it would

be far too expensive and difficult to use if regulations were put in place requiring each new ship built to assess its URN characteristics and also compared to model-tests, it is much more expensive and less accessible [106]. Although there has been a heavy focus on cavitating open propellers, there is almost no openly available experimental URN prediction conducted for ducted propellers in either non-cavitating and cavitating flows. This may be because ships that use ducted propellers like submarines have special operational requirements and there would be security issues with releasing such data.

2.3.3 Summary of Underwater Radiated Noise Evaluation Techniques

Computational and experimental methods are always developing, but URN is a challenge to accurately predict in different ways either using computational or experimental methods. Nevertheless, it is a challenge that must be overcome if the mitigation of URN is a primary goal for the maritime industry. It will not be possible without the accurate prediction of URN and of which, both computational and experimental methodologies will be crucial. Although many computational and experimental studies have been conducted for open propellers in both cavitating and non-cavitating flows, there is limited studies or benchmark data sets on the ducted propeller in either non-cavitating or cavitating conditions.

2.4 Summary

This chapter presented a literature review of firstly, the sources of propeller noise and the current URN mitigation methods available. This review shed light on the importance of noise mitigation, a fundamental understanding of the different mechanisms of propeller noise and the commercially available and developing

noise mitigation technologies.

Secondly, a review of the fundamental flow mechanisms induced by LE tubercles and the concepts application to more complex rotating devices like the tidal turbine and the marine propeller were considered, showing the concept has not yet been applied to ducted propellers although they show promising hydrodynamic and noise performance enhancements on other applications.

Lastly, the methodologies available to predict URN were reviewed in order to understand the available methods that could be used to address the main aim of the PhD project, showing that both numerical methods such as CFD and experimental techniques have their advantages and drawbacks.

Therefore, the major research gap that needs to be addressed is **the application of LE tubercles on marine ducted propulsors and their effect on the hydrodynamic and noise performance of the propulsor**.

This research gap can be divided into various sections that will be addressed within the following chapters:

1. How do the tubercles influence the hydrodynamic performance of a ducted propeller?

2. What is the sensitivity of the hydrodynamic performance to varying configurations of tubercle geometrical parameters?

3. Can tubercles improve noise performance of the ducted propeller?

4. If this is the case, what are the aspect(s) of hydrodynamic and noise performance benefit that are being affected by LE tubercles and if not, what is the main reason(s) for performance deterioration?

5. Is there a compromise in hydrodynamic and/or noise performance at certain operating conditions that need to be considered?

6. What are the detailed flow mechanisms that result in the performance variation due to the inclusion of LE tubercles on the ducted propeller?

Chapter 3

Ducted Propeller and Leading-Edge Tubercle Design

This chapter defines the benchmark ducted propeller geometry used within all future studies in Section 3.1, while the LE tubercle duct and propeller modelling technique is described in Section 3.2. A summary of the chapter is given in 3.3.

3.1 Benchmark Ducted Propeller Geometry

Figure 3.1 depicts the 4-bladed Kaplan series propeller, KA4-55 and the accelerating, 19A duct which were selected as the reference geometry for this study. The main particulars can be described in Table 3.1. This ducted propeller combinations is one of the most widely used within the maritime sector and detailed blade section and duct profile geometry can be found in [12].

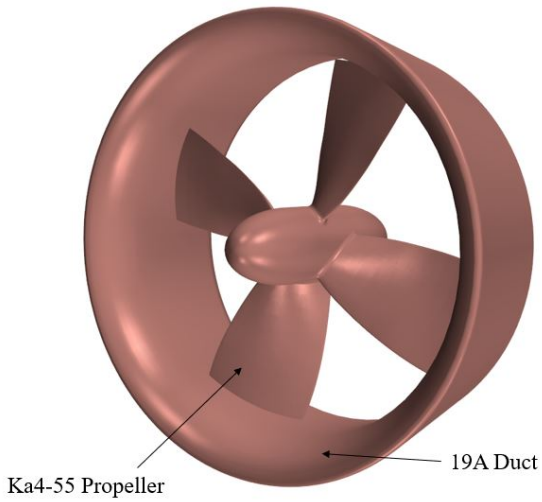

Figure 3.1: Benchmark KA4-55 and 19A ducted propeller geometry

Propeller		Duct	
Type	Kaplan	Type	19A
Blade Number, N	4	Chord Length, L_{Duct}	$0.5D$
Expanded Area Ratio, EAR	0.55		
Diameter, D	0.25m		
Pitch Diameter Ratio, P/D	1		
Tip clearance, t	$0.008D$		
Position	$0.5L_{Duct}$		

Table 3.1: Main reference ducted propeller geometry parameters

3.2 Leading-Edge Tubercle Design

A 2D aerofoil profile top view, with tubercle geometrical annotations can be shown in Figure 3.2 and cross-sectional profile of trough and peak of the 19A duct in Figure 3.3. Tubercle geometrical parameters height, H, amplitude, A and wavelength, λ, peak and trough are defined. Although the LE tubercles on the humpback whale pectoral fin are not an idealised sinusoidal waveform in

reality and differ in height and spacing along the fin span, the sinusoidal waveform was selected to improve the manufacturability of the modified duct and blade.

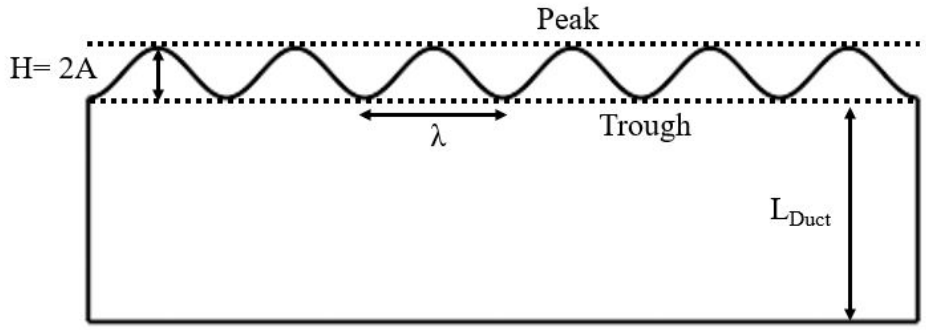

Figure 3.2: Tubercle geometric parameters

The LE tubercle modified ducts (SLE) were modelled using 3D modelling software. The peak section profile (see Figure 3.3) was varied dependant on the selected A. The section profiles were then defined at specific planes along a circular arc, dependant on the tubercle count selected.

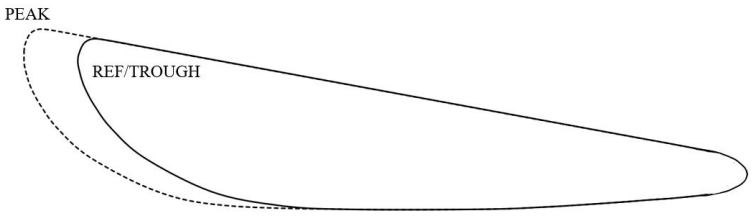

Figure 3.3: Cross-section tubercle peak and trough profiles

The sinusoidal curve used to define the LE tubercle profile is depicted as in Equation 3.1.

$$x_t = A \sin \beta t - A \tag{3.1}$$

The circular arc profile to which the sinusoidal curve is constrained to is

defined by Equations 3.2 and 3.3. The origin of the duct profile is defined at $(0, 150, 0)$ mm.

$$y_t = 150 \sin t \tag{3.2}$$

$$z_t = 150 \cos t \tag{3.3}$$

Equation 3.4 defines the start and end point to create the quarter circular arc profile. The quadrant geometry was then mirrored in both planes to create the complete duct.

$$t_1, t_2 = (0, \frac{\pi}{2}) \tag{3.4}$$

The tubercle blade (TUB) design was also completed using 3D modelling software. The pitch and chord length distributions were kept the same as the reference blade and the profile of leading-edge tubercles as applied to the blade followed Eqn. 3.5.

$$H = Asin\left[\frac{2\pi}{\lambda}(r - r_h) - \frac{\pi}{2}\right] + A \tag{3.5}$$

Where H, is the height of the tubercle, A, is the amplitude of the tubercle, λ, is the wavelength of the tubercle, r, is the blade radius and r_h, is the blade hub radius.

3.3 Summary

This chapter outlined the reference marine ducted thruster design and the 3D LE tubercle modelling technique for both duct and propeller applied to the reference design.

Chapter 4

Numerical Methodology

This chapter contains the numerical methodology used to achieve the aim and objectives of the thesis. The computational domain, mesh generation, verification and validation procedures for all studies are described within this chapter.

4.1 Governing Equations

The Navier-Stokes equations govern the motion of fluids and are the backbone of fluid dynamics. The fundamental laws that govern the mechanics of fluids and solids are the conservation of mass, linear momentum, angular momentum, and energy. These fundamental laws are presented here in differential form, for an infinitesimal control volume.

The first of the Navier-Stokes equations is known as the continuity equation and is described in Eqn. 4.1.

$$\frac{\partial \rho}{\partial t} + \nabla \cdot (\rho \mathbf{v}) = 0 \tag{4.1}$$

where ρ is density and $\mathbf{v}$ is the continuum velocity.

When incompressible flow is assumed, it simplifies to the following as density

is constant, as described in Eqn. 4.2

$$\nabla \cdot \mathbf{v} = 0 \tag{4.2}$$

The second of Navier-Stokes equations is the conservation of momentum and is another way to formulate Newton's second law ($F = ma$). The conservation of linear momentum equation in general form is described in Eqn. 4.3.

$$\frac{\partial(\rho \mathbf{v})}{\partial t} + \nabla \cdot [\rho \mathbf{v} \otimes \mathbf{v}] = -\nabla \cdot \boldsymbol{\sigma} + \boldsymbol{f_b} \tag{4.3}$$

where $\otimes$ denotes the outer product, $\boldsymbol{f_b}$ is the resultant of the body forces (such as gravity and centrifugal forces) per unit volume acting on the continuum. For a fluid, the stress tensor, $\boldsymbol{\sigma}$ is often written as sum of normal stresses and shear stresses, $\boldsymbol{\sigma} = -p\boldsymbol{I} + \boldsymbol{T}$, where p is the pressure and $\boldsymbol{T}$ is the viscous stress tensor as shown in Eqn. 4.4.

$$\frac{\partial(\rho \mathbf{v})}{\partial t} + \nabla \cdot [\rho \mathbf{v} \otimes \mathbf{v}] = -\nabla \cdot (p\boldsymbol{I}) + \nabla \cdot \boldsymbol{T} + \boldsymbol{f_b} \tag{4.4}$$

Conservation of angular momentum requires that the stress tensor is symmetric as described in Eqn. 4.5.

$$\boldsymbol{\sigma} = \boldsymbol{\sigma^T} \tag{4.5}$$

When the first law of thermodynamics is applied to the control volume, the conservation of energy can be written as in Eqn. 4.6.

$$\frac{\partial(\rho E)}{\partial t} + \nabla \cdot (\rho E \mathbf{v}) = \boldsymbol{f_b} \cdot \mathbf{v} + \nabla \cdot (\mathbf{v} \cdot \boldsymbol{\sigma}) - \nabla \cdot \boldsymbol{q} + S_E \tag{4.6}$$

where E is the total energy per unit mass, $\boldsymbol{q}$ is the heat flux, and S_E is an energy source per unit volume.

4.2 Finite-Volume Discretisation Schemes

Commercial package STAR CCM+ was used to conduct the CFD analysis, where the finite-volume method is used to discretise the governing equations in space and time.

All conservation equations can be written in terms of a generic transport equation. By integrating the generic transport equation over a control volume and applying Gauss's divergence theorem, the following integral form of the transport equation is obtained as described in Eqn. 4.7. The terms from left to right are as follows; transient term, convective flux, diffusive flux and finally, the source term.

$$\frac{d}{dt}\int_V \rho\phi dV + \int_A \rho\mathbf{v}\phi \cdot da = \int_A \Gamma\nabla\phi da + \int_V S_\phi dV \tag{4.7}$$

where ϕ represents the transport of a scalar property, A is the surface area of the control volume and da denotes the surface vector. Special forms of the partial differential equations for mass, momentum, energy and species conservation are obtained by selecting appropriate values for the diffusion coefficient, Γ, and source terms while setting ϕ equal to 1, u, v, w, E, or H (enthalpy), Y_i (local mass fraction of each species).

The following diagram in Figure 4.1 shows two polyhedral computational cells that illustrate the discretisation of the generic transport equation:

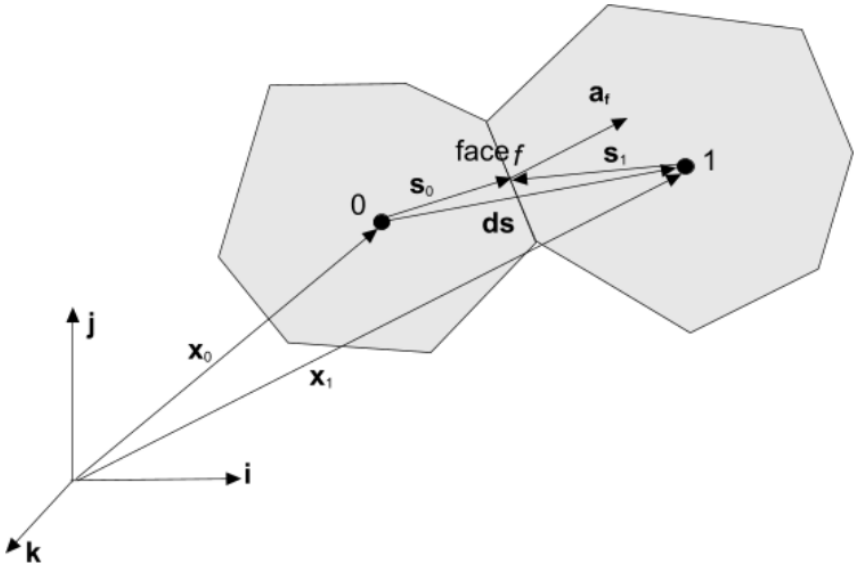

Figure 4.1: Illustration of the generic transport equation discretisation between two polyhedral computational cells (reproduced from [94])

4.2.1 Convective Flux

The discretied convective term at a face can be rearranged as shown in Eqn. 4.8.

$$(\phi\rho \cdot a)_f = (\dot{m}\phi)_f = \dot{m}_f\phi_f \tag{4.8}$$

where $\dot{m}_f$ is the mass flow rate at the face. The manner in which the fluid property face value ϕ_f is computed from the cell values will impact the stability and accuracy of the numerical scheme.

The two schemes employed to compute the convective flux within this study are described below, the second order upwind scheme was used with the RANS method, while the convective hybrid second-order upwind/bounded-central scheme was employed when using a formulation of the DES method, known as Improved Delayed Detached Eddy Simulations (IDDES).

For a second-order upwind (SUO) scheme, the convective flux is computed as

shown in Eqn. 4.9

$$(\dot{m}\phi)_f = \begin{cases} \dot{m}_f\phi_0, & \text{for } \dot{m}_f \geq 0. \\ \dot{m}_f\phi_1, & \text{for } \dot{m}_f < 0. \end{cases} \tag{4.9}$$

where the face values $\phi_{f,0}$ and $\phi_{f,1}$, are linearly interpolated from the cell center values on either side of the face as shown in Eqns 4.10 and 4.11.

$$\phi_{f,0} = \phi_0 + s_0 \cdot (\nabla\phi)_{r,0} \tag{4.10}$$

$$\phi_{f,1} = \phi_1 + s_1 \cdot (\nabla\phi)_{r,1} \tag{4.11}$$

where

$$s_0 = x_f - x_0 \tag{4.12}$$

$$s_1 = x_f - x_1 \tag{4.13}$$

The convective hybrid second-order upwind/bounded-central was employed when using a formulation of the DES method and is shown in Eqn. 4.14.

$$(\dot{m}\phi)_f = \dot{m}(\sigma_{HU}\sigma_{SOU} + (1 - \sigma_{HU})\phi_{BCD}) \tag{4.14}$$

where at face, f, the values of ϕ are ϕ_{SOU} for the second-order upwind scheme and ϕ_{BCD} for the bounded central-differencing scheme. σ_{HU} is a blending factor that is chosen as appropriate for the flow regime. For DES, Travin et al [132] proposed the blending coefficient and this can be found in detail within the STAR CCM+ user manual [94].

4.2.2 Diffusive Flux

The diffusive flux within the general transport equation shown in Eqn. 4.7, is discretised as defined in Eqn. 4.15.

$$D_f = (\Gamma \nabla \phi \cdot a)_f \tag{4.15}$$

where Γ is the face diffusivity, $\nabla\phi$ is the gradient of the fluid property, and a is the surface area vector.

To obtain an accurate second-order expression for an interior face gradient that implicitly involves the cell values ϕ_0 and ϕ_1, the following decomposition is used as defined in Eqn. 4.16.

$$\nabla\phi_f = (\phi_1 - \phi_0)\alpha + \overline{\nabla\phi} - (\overline{\nabla\phi} \cdot ds)\alpha \tag{4.16}$$

where $\alpha = \frac{a}{a \cdot ds}$, $ds = x_1 - x_0$ and $\overline{\nabla\phi} = \frac{\overline{\nabla\phi_0} + \overline{\nabla\phi_1}}{2}$.

4.2.3 Transient Term

For the transient simulations, a second-order temporal discretisation scheme was used throughout the study. It uses the solution at the current time level, $n+1$, as well as the solutions from the previous two time levels, n and $n-1$, in a backward differentiation formula first proposed by Curtiss and Hirschfelder [134], BDF2. BDF2 can be shown in Eqn 4.17.

$$\frac{d}{dt}(\rho\chi\phi V) = ((\frac{3}{2}(\rho\chi\phi V)_{n+1} - 2(\rho\chi\phi V)_n + \frac{1}{2}(\rho\chi\phi V)_{n-1})\frac{1}{\Delta t} \tag{4.17}$$

On the first time-step, a first-order discretisation is performed since only two time levels are available.

4.2.4 Gauss-Seidel Iteration Method

The result of the discretisation approach is a linear system as in Eqn. 4.18.

$$Ax = b \tag{4.18}$$

representing the algebraic equations for each computational cell. The matrix A represents the coefficients of the linear system, x represents the unknowns in each cell and the vector b represents the residuals from each cell. The resultant linear system of equations is solved using the Gauss-Seidel iteration method first proposed in [133] throughout the study.

The general principle behind the iterative method is that, given an approximate solution x^k, a better approximation x_{k+1} is sought, and then the process is repeated.

If the error at iteration k is defined as in Eqn. 4.19:

$$e^k = x - x^k \tag{4.19}$$

where x represents the exact solution and the residual as in Eqn. 4.20:

$$r^k = b - Ax^k \tag{4.20}$$

it follows that as in Eqn. 4.21:

$$Ae^k = r^k \tag{4.21}$$

Therefore, continuing the iteration until the residual is driven to a small value, drives the error to a smaller value. The procedure is generally continued until the changes made by an iteration are below some tolerance, such as a sufficiently small residual. The iterative method involves visiting each cell in sequence, and

updating the value of x_i in each cell i using the coefficients of its n neighbour cells as follows in Eqn 4.22:

$$x_i = \frac{1}{A_{i,i}}(b - \sum_n A_{i,n}x_n) \tag{4.22}$$

The Gauss-Seidel iteration method uses the available values that have been updated, resulting in better convergence when compared to the Jacobi method [94].

4.2.5 Pressure-Velocity Coupling

The segregated flow solver was used, whereby the non-linear governing equations are solved iteratively one after the other for the solution variables such as velocity components u,v,w and pressure, p. The SIMPLE (Semi-Implicit Method for Pressure-Linked Equations) algorithm was used for the pressure-velocity coupling and is essentially a guess and correct procedure for the calculation of pressure on the grid arrangement [94].

A summary of the algorithm is described below:

1. Set the boundary conditions
2. Compute the reconstruction gradients of velocity and pressure
3. Solve the discretised momentum equation, this creates the intermediate velocity field $\mathbf{v}^*$
4. Compute the uncorrected mass fluxes at faces $\dot{m}^*{}_f$
5. Solve the pressure correction equation. This produces cell values for the pressure correction p'.

6. Update the pressure field: $p^{n+1} = p^n + \omega p'$ where ω is the under-relaxation factor for pressure.

7. Update the boundary pressure corrections p'_b.

8. Correct the face mass fluxes: $\dot{m}_f^{n+1} = \dot{m}^*{}_f + \dot{m}'_f$

9. Correct the cell velocities: $\mathbf{v}_p^{n+1} = \mathbf{v}^*{}_p - \frac{V\nabla p'}{\boldsymbol{a}'^{\mathrm{v}}_p}$ where $\nabla p'$ is the gradient of the pressure corrections, $\boldsymbol{a}'^{\mathrm{v}}_p$ is the vector of central coefficients for the discretized velocity equation, and V is the cell volume.

10. Update density due to pressure changes.

11. Free all temporary storage.

4.3 Reynolds-Averaged Navier Stokes Equations (RANS)

Implicit unsteady incompressible Reynolds-Averaged Navier Stokes (URANS) was employed within the intial paramteric design and optimisation study within Chapter 5.

To obtain the RANS equations, each solution variable ϕ, in the instantaneous Navier-Stokes equations is decomposed into its mean, or averaged value $\overline{\phi}$ and its fluctuating component, ϕ':

$$\phi = \overline{\phi} + \phi' \tag{4.23}$$

where ϕ represents velocity components, pressure, energy, or species concentration.

The averaging process may be thought of as time-averaging for steady-state situations but for repeatable transient situations, it can be thought of as an ensemble averaging.

The mean mass, momentum and energy equations can be written as shown in Eqns. 4.24, 4.25 and 4.26, respectively.

$$\frac{\partial \rho}{\partial t} + \nabla \cdot (\rho \overline{\mathbf{v}}) = 0 \tag{4.24}$$

when incompressible flow is assumed, density is constant ($\frac{\partial \rho}{\partial t} = 0$).

$$\frac{\partial (\rho \overline{\mathbf{v}})}{\partial t} + \nabla \cdot [\rho \overline{\mathbf{v}} \otimes \overline{\mathbf{v}}] = -\nabla \cdot \overline{p} \boldsymbol{I} + \nabla \cdot (\overline{\boldsymbol{T}} + \boldsymbol{T}_{RANS}) + \boldsymbol{f_b} \tag{4.25}$$

$$\frac{\partial (\rho \overline{E})}{\partial t} + \nabla \cdot (\rho \overline{E} \overline{\mathbf{v}}) = -\nabla \cdot \overline{p} \overline{\mathbf{v}} + \nabla \cdot (\overline{\boldsymbol{T}} + \boldsymbol{T}_{RANS}) \overline{\mathbf{v}} - \nabla \cdot \overline{\boldsymbol{q}} + \boldsymbol{f_b} \overline{\mathbf{v}} \tag{4.26}$$

where ρ is density, $\overline{\mathbf{v}}$ is the mean velocity, $\overline{p}$ is mean pressure, $\boldsymbol{I}$ is the identity tensor, $\overline{\boldsymbol{T}}$ is the mean viscous stress tensor, $\boldsymbol{f_b}$ is the resultant of the body forces (such as gravity and centrifugal forces), $\overline{E}$ is the mean total energy per unit mass and $\overline{\boldsymbol{q}}$ is the mean heat flux.

The equations above are very similar to the original Navier-Stokes equations outlined in Eqns. 4.1, 4.4 and 4.6 but there is an additional terms in both the momentum and energy transport equations, this additional stress term, $\boldsymbol{T}_{RANS}$ is defined in Eqn. 4.27.

$$\boldsymbol{T}_{RANS} = -\rho \begin{pmatrix} \overline{u'u'} & \overline{u'v'} & \overline{u'w'} \\ \overline{u'v'} & \overline{v'v'} & \overline{v'w'} \\ \overline{u'w'} & \overline{v'w'} & \overline{w'w'} \end{pmatrix} + \frac{2}{3} \rho k \boldsymbol{I} \tag{4.27}$$

where k is turbulent kinetic energy.

The challenge within CFD is to model T_{RANS} in terms of the mean flow quantities and hence, provide closure to the governing equations. This was achieved using an eddy viscosity model known as the Shear Stress Transport (SST) k-ω turbulence model within the PhD study.

4.3.1 The Shear Stress Transport (SST) k-ω Turbulence Model

The Shear Stress Transport (SST) k-ω turbulence model developed by Menter [98] was used throughout the study, it has shown good agreement with experimental results in marine propeller simulations [97]. It employs the k-ω within the inner boundary layer while switching to a k-ϵ behaviour in the free-stream. The SST k-ω model is similar to the standard k-ω model, but the turbulent viscosity is modified where in SST k-ω rotating tensor and blending function are included [98]. The SST k-ω model has a blending function and the addition of a cross-diffusion term in the ω equation to ensure that the model equations behave appropriately in both far-field zones and the near-wall. The kinetic energy (k) and specific dissipation rate (ω) are obtained from the following transport equations in Eqns. 4.28 and 4.29, respectively:

$$\frac{\partial}{\partial t}(\rho k) + \nabla \cdot (\rho k \overline{\mathbf{v}}) = \nabla \cdot [(\mu + \sigma_k \mu_t)\nabla k] + P_k - \rho\beta^* f_{\beta^*}(\omega k - \omega_0 k_0) + S_k \quad (4.28)$$

$$\frac{\partial}{\partial t}(\rho \omega) + \nabla \cdot (\rho \omega \overline{\mathbf{v}}) = \nabla \cdot [(\mu + \sigma_\omega \mu_t)\nabla \omega] + P_\omega - \rho\beta f_{\beta(\omega^2} - \omega_0^2) + S_\omega \quad (4.29)$$

where, $\overline{\mathbf{v}}$ is the mean velocity, μ is the dynamic viscosity, σ_k, σ_ω, $C_{\varepsilon 1}$ and

$C_{\varepsilon 2}$ are model coefficients, P_k and P_ω are production terms, $f_{\beta*}$ is the free-shear modification factor, f_β is the vortex-stretching modification factor, S_K and S_ω are the user-specified source terms and k_0 and ω_0 are the ambient turbulence values that counteract turbulence decay [135].

4.4 Improved Delayed Detached Eddy Simulations (IDDES)

In order to improve the prediction of the propeller wake flow, implicit unsteady incompressible Detached Eddy Simulation (DES) was used to solve the hydrodynamic flow-field in Chapters 6, 7 and 8. The specific formulation of DES used was the Improved Delayed Detached Eddy Simulations (IDDES) formulated by Shur et al [138], this solves the near-wall regions using a RANS approach, with the large eddy simulation (LES) method used to solve the rest of the domain [136].

The momentum equations for the RANS averaged velocity $\overline{\mathbf{v}}$ and the LES filtered velocity, $\widetilde{\mathbf{v}}$ are defined in Eqns 4.30 and 4.31, respectively.

$$\frac{\partial(\rho\overline{\mathbf{v}})}{\partial t} + \nabla \cdot [\rho\overline{\mathbf{v}} \otimes \overline{\mathbf{v}}] = -\nabla \cdot \bar{p}\boldsymbol{I} + \nabla \cdot (\overline{\boldsymbol{T}} + \boldsymbol{T}_{RANS}) + \boldsymbol{f_b} \tag{4.30}$$

$$\frac{\partial(\rho\widetilde{\mathbf{v}})}{\partial t} + \nabla \cdot [\rho\widetilde{\mathbf{v}} \otimes \widetilde{\mathbf{v}}] = -\nabla \cdot \widetilde{p}\boldsymbol{I} + \nabla \cdot (\widetilde{\boldsymbol{T}} + \boldsymbol{T}_{SGS}) + \boldsymbol{f_b} \tag{4.31}$$

For a RANS model, the Reynolds-stress tensor $\boldsymbol{T}_{RANS}$ is a function of a time and length scale as defined in Eqn 4.32.

$$\boldsymbol{T}_{RANS} = f(\nabla \cdot \overline{\mathbf{v}}, k, \epsilon) \tag{4.32}$$

and for LES,

$$\boldsymbol{T}_{SGS} = f(\nabla \cdot \widetilde{\mathbf{v}}, \Delta) \tag{4.33}$$

where ϵ is the rate of dissipation of turbulent kinetic energy and Δ is the local measure of the grid size.

For the SST k-ω Detached Eddy model and the IDDES formulation of Shur et al [138] used within the PhD study, the specific dissipation rate, ω in the transport equation for turbulent kinetic energy as shown in Eqn. 4.28 is replaced by $\widetilde{\omega}$ which is defined in Eqn. 4.34.

$$\widetilde{\omega} = \frac{\sqrt{k}}{l_{hybrid} f_{\beta^*} \beta^*} \tag{4.34}$$

where f_{β^*} is the free-shear modification factor, k is the turbulent kinetic energy and β^* is the k-ω model coefficients that can be found in [94].

The length scale, l_{hybrid}, is calculated as shown in Eqn. 4.35.

$$l_{hybrid} = \widetilde{f_d}(1 + f_e) l_{RANS} + (1 - \widetilde{f_d}) C_{DES} \Delta_{IDDES} \tag{4.35}$$

where C_{DES} is a model coefficient that can be found in [94]. The length scale calculation adds a Wall-Modelled LES (WMLES) capability by adding two additional functions, a blending function, f_B and an 'elevating' function, f_e. They are calculated as defined in Eqns 4.36 - 4.44.

$$f_B = min[2exp(-9\alpha^2), 1] \tag{4.36}$$

$$\alpha = 0.25 - \frac{d}{\Delta} \tag{4.37}$$

$$f_E = max[(f_{e1} - 1), 0] \psi f_{e2} \tag{4.38}$$

$$f_{e1} = \begin{cases} 2exp(-11.09\alpha^2) & \text{if } \alpha \geq 0 \\ 2exp(-9\alpha^2) & \text{if } \alpha < 0 \end{cases} \tag{4.39}$$

$$f_{e2} = 1 - max(f_t, f_l) \tag{4.40}$$

$$f_t = tanh[(C_t^2 r_{dt})^3] \tag{4.41}$$

$$f_l = tanh[(C_l^2 r_{dl})^{10}] \tag{4.42}$$

$$r_{dt} = \frac{v_t}{\sqrt{\nabla \mathbf{v} : \nabla \mathbf{v}^T \kappa^2 d^2}} \tag{4.43}$$

$$r_{dl} = \frac{v}{\sqrt{\nabla \mathbf{v} : \nabla \mathbf{v}^T \kappa^2 d^2}} \tag{4.44}$$

where C_t and C_l are model coefficients that can be found in [94], v is kinematic viscosity, $v_t = \frac{\mu_t}{\rho}$ where μ_t is the turbulent eddy viscosity, κ is the von Karman constant which can be found in [94] and d is the distance to the wall.

The introduction of the low-Reynolds number correction function ψ in the formulation of f_e is unrelated to the low-Reynolds number correction role of this function in the LES mode of DDES and is purely empirical.

The WMLES and DDES branches of the model are combined using a modified version of the DDES f_d function as follows in Eqn 4.45:

$$\widetilde{f}_d = max((1 - f_{dt}), f_B) \tag{4.45}$$

where

$$f_{dt} = 1 - tanh[(C_{dt}^2 r_{dt})^3] \tag{4.46}$$

and C_{dt} is a model coefficient that can be found in [94].

The IDDES model also uses an altered version of the mesh length scale, Δ_{IDDES} which is computed as shown in Eqn 4.47.

$$\Delta_{IDDES} = min(max(0.15d, 0.15\Delta, \Delta_{min}), \Delta) \tag{4.47}$$

where Δ_{min} is the smallest distance between the cell center under consideration and the cell centers of the neighbouring cells.

An important consideration within DES simulations is the Courant–Friedrichs–Lewy (CFL) number. It expresses that the distance that any information travels during the time step length within the mesh must be lower than the distance between mesh elements, $C = \frac{u\Delta t}{\Delta x} \leq C_{max}$ where u is velocity magnitude, Δt is the time-step, Δx is the length interval and C is the Courant number, where C_{max} is 1. Therefore, it is recommended to keep the Courant number below 1 which was achieved for all DES simulations conducted within the PhD study [137].

4.5 Hydrodynamic Performance Coefficients

The hydrodynamic performance of the ducted propeller was predicted using the traditional open-water characteristics. Ducted propeller performance coefficients can be outlined in Eqns. 4.48 - 4.54.

$$J = \frac{V_A}{nD} \tag{4.48}$$

$$K_{TP} = \frac{T_P}{\rho n^2 D^4} \tag{4.49}$$

$$K_{TD} = \frac{T_D}{\rho n^2 D^4} \tag{4.50}$$

$$K_{TT} = K_{TP} + K_{TD} \tag{4.51}$$

$$K_Q = \frac{Q}{\rho n^2 D^5} \tag{4.52}$$

$$\eta_P = \frac{K_{TP} J}{2\pi K_Q} \tag{4.53}$$

$$\eta = \frac{K_{TT} J}{2\pi K_Q} \tag{4.54}$$

Where J, is advance ratio, K_{TP}, is propeller thrust coefficient, K_{TD}, is duct thrust coefficient, K_{TT}, is total thrust coefficient, K_Q, is the torque coefficient, η_P is efficiency (propeller only), η is overall propulsive efficiency, n $[rps]$, is rotation rate, V_A $[m/s]$ is incoming velocity, D $[m]$ is propeller diameter and ρ $[kg/m^3]$, is density.

Thrust coefficient, C_t, can be defined in Eqn. 4.55

$$C_t = \frac{T_P + T_D}{0.5\rho V_A^2 A} \tag{4.55}$$

Where area, A $[m^2]$, is calculated based on the propeller swept area.

4.6 Rotation Rate Specification and Reynolds Number

In the model scale, the propeller rotation rate, n, was fixed at 15rps and advance velocity, V_A varied as according to the experimental campaign by CTO in Poland.

The Reynolds number (Re) based on rotation rate was estimated as $1.05e10^6$ as defined in Equation 4.56. The Re was based on rotation rate, however it can also be based on the advance velocity experienced at 70% blade chord but the Re is similar and does not vary considerably over the advance velocities considered within the current study.

$$Re = \frac{nD^2}{v} \tag{4.56}$$

where v $[m^2/s]$, is kinematic viscosity.

In the full scale study, the duct and propeller geometries were scaled using a scale factor, $\lambda_s = 4$, resulting in a propeller diameter of 1m, within the range of a typical ducted propeller diameter, for the open-water full scale flow conditions. The geometry particulars followed Table 3.1 as a function of propeller diameter, D. The full scale rotation rate, n_s, was scaled to 7.5rps from the previously used model scale rotation rate, n_m, of 15rps using Froude's similarity law, which can be simplified in this case to Eqn. 4.57. This resulted in a Reynolds number of 8.4x10^6.

$$n_s = \frac{n_m}{\sqrt{\lambda_s}} \tag{4.57}$$

Froude's similarity law was used to scale the propeller rotational speed while the non-dimensional coefficient, J, was kept the same between model and full scale. The model scale rotation rate was 15rps to validate with the experimental results, but this results in a lower Re that is experienced in full scale. This is a typical issue within ship hydrodynamics and so can result in differences in performance changes for devices such as the Mewis duct for example as shown in [130]. Therefore, this study allows the difference in performance for LE tubercles between model and full scale Re flows to be assessed.

4.7 The Actuator Disk Body Force Propeller (BFP) Method

The Body Force Propeller (BFP) actuator disk method used for the model scale paramteric optimisation study in Chapter 5, was implemented through commercial CFD software, STAR CCM+. The approximated forces applied by a propeller to the flow are applied as source terms in the RANS equation of momentum conservation, and solved together with a mass continuity equation. The source terms are only applied at elements within the propeller region [131].

The BFP method employs a uniform volume force f_b, distribution over the cylindrical virtual disk. The experimental data for the KA4-55 propeller within the 19A duct can be shown in Figure 4.2. and was used as an input into the actuator disk. The key actuator disk parameters can be shown in Table 4.1. The operating point was specified based on rotation rate, 15rps and the velocity inflow boundary was selected as the computational domain velocity inlet, from which the advance ratio could be varied. The thrust and torque radial distribution is specified, and this was based on an author-modified Goldstein's Optimum Distribution. The default Goldstein's Optimum Distribution [90] can be defined as in Eqn. 4.58.

Hub radius, R_H	0.02m
Tip radius, R_P	0.125m
Thickness, Δ	0.01m
Position	$0.5L_{Duct}$
Handedness	Right-handed

Table 4.1: Actuator disk parameters

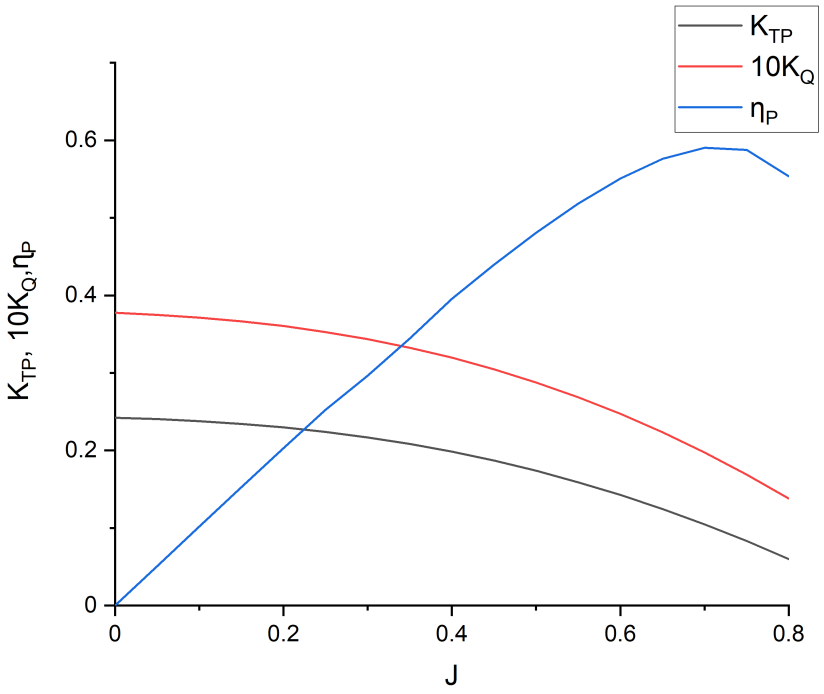

Figure 4.2: Experimental KA4-55 propeller data inside 19A duct

$$f_{bx} = A_x r^*(1-r^*)^{0.5} \tag{4.58}$$

$$f_{b\theta} = A_\theta r^* \frac{(1-r^*)^{0.5}}{r^*(1-r_h^{'}) + r_h^{'}} \tag{4.59}$$

$$r^* = \frac{r^{'} - r_h^{'}}{1 - r_h^{'}} \tag{4.60}$$

$$r_h^{'} = \frac{R_H}{R_P} \tag{4.61}$$

$$r^{'} = \frac{r}{R_P} \tag{4.62}$$

Where, f_{bx} $[N]$ is the body force in the axial direction, $f_{b\theta}$ $[N]$ is the body force in the tangential direction, r [m] is the radial coordinate, R_H $[m]$ is hub radius and R_P $[m]$ is the tip radius from the propeller centre. r^* is the normalised disk span (values from 0 through 1 where 0 corresponds to the inner hub radius and 1 corresponds to the outer tip radius of the virtual disk). The constants A_x and A_θ can be calculated as in Eqns. 4.63 and 4.64, respectively.

$$A_x = \frac{105}{8} \frac{T_P}{\pi \Delta (3R_H + 4R_P)(R_P - R_H)} \tag{4.63}$$

$$A_\theta = \frac{105}{8} \frac{Q}{\pi \Delta R_P (3R_H + 4R_P)(R_P - R_H)} \tag{4.64}$$

Where Δ $[m]$, is the virtual disk thickness. The two author-modified radial thrust and torque distributions based on the Goldstein's Optimum Distribution are defined in Eqn. 4.65 and 4.66 for heavy-loaded conditions ($0 \leq J \leq 0.4$). The distributions for lightly-loaded ($0.4 < J \leq 0.7$) conditions can be defined in Eqn. 4.67 and 4.68. The graphic illustration of the radial distributions can be shown in Figure 4.3. As can be shown, the location of the maximum axial force (thrust) has been shifted from 67% of the blade radius, to approximately 77% for lightly-loaded condition and 83% for heavy-loaded conditions. With the author-modified distributions, the thrust produced below the maximum thrust point has been reduced and redistributed to above the maximum point where the degradation of thrust force from the maximum point to the blade tip has been reduced. This is typical of a duct application as the 3D effect due to the suppression of a fully-developed tip vortex is reduced when compared to open rotating machinery and therefore, the tip of the blade can be designed to be more loaded. The Goldstein's Optimum Distribution was formulated for open rotating applications as oppose to ducted propeller applications, therefore this is

the justification for the modifications.

$$f_{bx} = A_x r^*(1-r^*)^{0.2} \tag{4.65}$$

$$f_{b\theta} = A_\theta r^* \frac{(1-r^*)^{0.2}}{r^*(1-r_h^{'}) + r_h^{'}} \tag{4.66}$$

$$f_{bx} = A_x r^*(1-r^*)^{0.3} \tag{4.67}$$

$$f_{b\theta} = A_\theta r^* \frac{(1-r^*)^{0.3}}{r^*(1-r_h^{'}) + r_h^{'}} \tag{4.68}$$

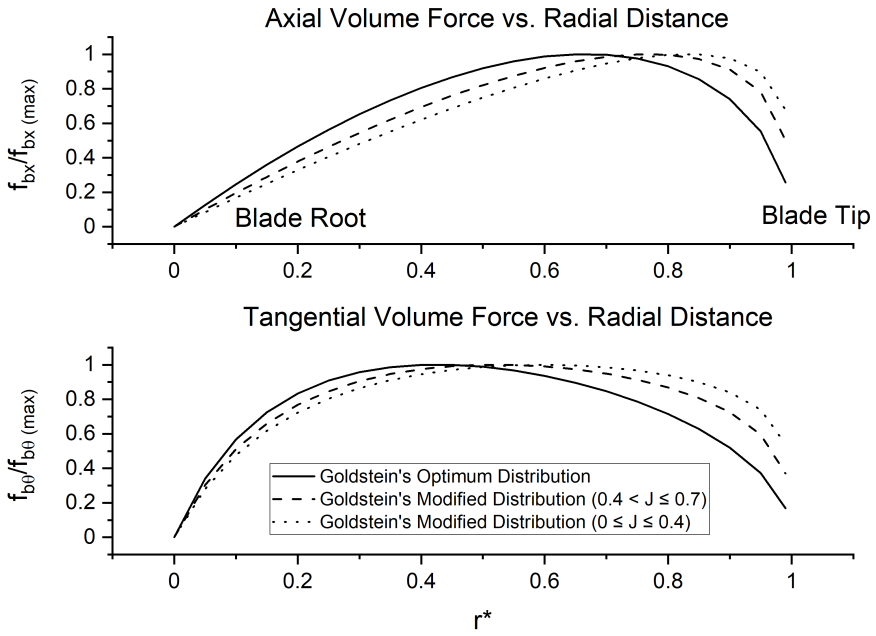

Figure 4.3: Goldstein Optimum and author-modified axial and tangential volume force distributions

4.8 Cavitation Modelling Approach and Test Conditions

In the tubercle blade study where cavitation was investigated, the multiphase flow was modelled using the volume of fluid (VOF) model and the cavitation behaviour was described using the Schnerr-Sauer model. The Schnerr-Sauer model is based on the reduced Rayleigh-Plesset equation, and neglects the influence of bubble growth acceleration, viscous effects, and surface tension. Nonetheless, this cavitation model has provided good agreement with experimental sheet cavitation observations [85]. The cavitation number, σ_N, can be described in Equation 4.69.

$$\sigma_N = \frac{P_0 - P_v}{0.5\rho(nD)^2} \tag{4.69}$$

where P_0 is the static pressure including the atmospheric pressure in Pascals, $[Pa]$; P_v is the vapour pressure of the water, $[Pa]$. n is the rotational speed, $[rps]$; ρ is the water density, $[kg/m^3]$, D is propeller diameter, $[m]$. Table 4.2 describes the range of cavitation test case conditions, C and advance ratios that were considered in the model scale analysis, where one light cavitating condition was considered, σ_N=1.9 and one heavy cavitating condition was considered, σ_N=1.3 over a range of advance ratios. This was replicated in the full scale tubercle blade study and the table of test conditions can be seen in Table 4.3.

C	V_A [m/s]	n [rps]	Re	J	σ_N
C1	0.375			0.1	
C2	1.125			0.3	1.3
C3	2.0625	15	1.05x10^6	0.55	
C4	0.375			0.1	
C5	1.125			0.3	1.9
C6	2.0625			0.55	

Table 4.2: Cavitation test case conditions in model scale study within Chapter 7

C	V_A [m/s]	n [rps]	Re	J	σ_N
C1	0.75			0.1	
C2	2.25			0.3	1.3
C3	4.125	7.5	8.4x10^6	0.55	
C4	0.75			0.1	
C5	2.25			0.3	1.9
C6	4.125			0.55	

Table 4.3: Cavitation test case conditions in full scale study within Chapter 8

4.9 Ffowcs-Williams Hawking's Acoustic Analogy

The Ffowcs-Williams Hawkings (FW-H) formulation, was used propagate the sound to the far-field [103]. The governing equation to describe the FW-H formulation can be shown in Equation 4.70.

$$\left(\frac{1}{c_o^2}\frac{d^2}{dt^2} - \nabla^2\right)\hat{p}(x,t) = \frac{d}{dt}\{[\rho_0 v_n + \rho(u_n - v_n]\delta(f)\} - \frac{d}{dx_i}\{[\Delta P_{ij} + \rho(u_i - v_n]\delta(f)\} + \frac{d^2}{dx_i dx_j}T_{ij}H(f) \tag{4.70}$$

where

$$T_{ij} = \rho u_i u_j + P_{ij} - c_0^2\tilde{\rho}\delta_{ij} \tag{4.71}$$

and

$$\tilde{\rho} = \rho - \rho_0 \tag{4.72}$$

Where c_0 denotes the sound velocity in the far field (within this PhD project, $c_0 = 1500$m/s was used) and $\hat{p}$ is sound pressure at the far field and v_i is fluid and surface velocity components, respectively. t and x are observer time and location, respectively. n indicates the projection along the outward normal to the surface. T_{ij}, Lighthill Stress tensor can be written as Equation 4.71. $\tilde{\rho}$ is the density perturbation of the fluid where ρ denotes the density of the fluid and ρ_0 is the free stream density as defined in Equation 4.72. ∇^2, is the Laplace operator, H, is the Heavside function, δ is the Kronecker operator. P_{ij}, is the compressive stress tensor ($\Delta P_{ij} = P_{ij} - \rho\delta_{ij}$).

The FW-H acoustic analogy considers all fundamental noise sources and are described on the right-hand side of Equation 4.70 – monopole, the first term, dipole, the second term and finally the quadrupole contribution. While the contributions from monopole and dipole sources are evaluated by surface integrals on the respective noise sources for example the propeller blade, the quadrupole term requires volume integration, which is very expensive. This is known as the impermeable approach, which generally focusses on the linear terms as calculating the volume integral quadrupole term is very costly. But, as has been shown in previous literature, non-linear terms associated with propeller noise cannot be neglected as it can dominate in the far-field [56; 110]. Therefore, the porous surface approach was developed, a formulation derived by Francescantonio [107]. The surface surrounds the propeller and a significant portion of the propeller slipstream to contain all major sources of non-linear noise. In such formulations like Farassat Formulation 1A [108], the terms responsible for monopole and dipole contributions lose their original meaning and become pseudo-monopole

and pseudo-dipole terms, which include the contribution from the quadrupole (non-linear) term if the porous surface encompasses a significant portion of the turbulent wake. This results in all noise sources being solved by a surface integral, which includes the quadrupole term while reducing the computational cost [109].

The equation for the FW-H porous surface approach and an incompressible flow assumption can be defined firstly by the two acoustic variables, modified velocity, U_i and modified stress tensor, L_i in Equation 4.73 and 4.74.

$$U_i = u_i \tag{4.73}$$

$$L_i = P_{ij}\hat{n}_j + \rho u_i(u_n - v_n) \tag{4.74}$$

Where u and v are the fluid and porous surface velocities. In the assumption of incompressible flow and a fixed, stationary data surface, $\rho = \rho_0$ and $v_n = 0$ and a Mach number, $Ma = |v|/|c_0| << 1$, the porous surface FW-H equation simplifies to the definition in Equation 4.75.

$$4\pi p(x,t) = \int_S \left[\frac{\rho_0 \dot{U}_n}{r}\right]_\tau dS + \int_S \left[\frac{\dot{L}_r}{c_0 r}\right]_\tau dS + \int_S \left[\frac{L_r}{r^2}\right]_\tau dS + p_Q(x,t) \tag{4.75}$$

Here r $[m]$ is the distance from the noise source to the receiver. Where the dot accent defines a source time derivative with respect to retarded time. Subscripts r and n defined the product of a quantity with a unit vector in either radiation or normal directions, respectively. The last term, $p_Q(x,t)$, represents the non-linear noise contribution outwith the permeable surface domain, however as in similar studies [56; 57; 106; 112; 112], this can be neglected if the permeable surface contains all meaningful non-linear source contributions.

Acoustic pressure is collected in the time domain at each time step. By using FFT (Fast Fourier Transform), it is transferred to the frequency domain and then sound pressure level (SPL) values are calculated in the frequency domain as follows in Equation 4.76;

$$SPL = 20log\left(\frac{p}{p_{ref}}\right) \tag{4.76}$$

Here, p is acoustic pressure in the frequency domain, Pascals $[Pa]$; p_{ref} is reference acoustic pressure (for water $p_{ref} = 1x10^{-6}\ Pa$). In addition, overall sound pressure level ($OASPL$) is calculated by Equation 4.77:

$$OASPL = 20log\left(\frac{p_{rss}}{p_{ref}}\right) \tag{4.77}$$

where p_{rss} is total acoustic pressure which is obtained within this study by summing the acoustic pressures in the 3^{rd} octave band frequency domain in accordance with root sum square (RSS) rule.

4.10 Computational Domain and Mesh Generation

4.10.1 Actuator Disk Method

Figure 4.4 depicts the definition of computational domain and its associated boundary conditions. The boundary conditions were selected as velocity inlet on the left face, pressure outlet on the right face, and a symmetry plane on the cylindrical revolving face. The velocity magnitude at the velocity inlet was altered to vary the advance ratio, J. The pressure outlet was defined as 0 Pascal with respect to the reference pressure. The duct was modelled as a non-slip wall

boundary. Computational domain dimensions are taken from the propeller plane and are as follows: $3D$ upstream to the velocity inlet, $7D$ downstream to the pressure outlet and a radius of $2.5D$.

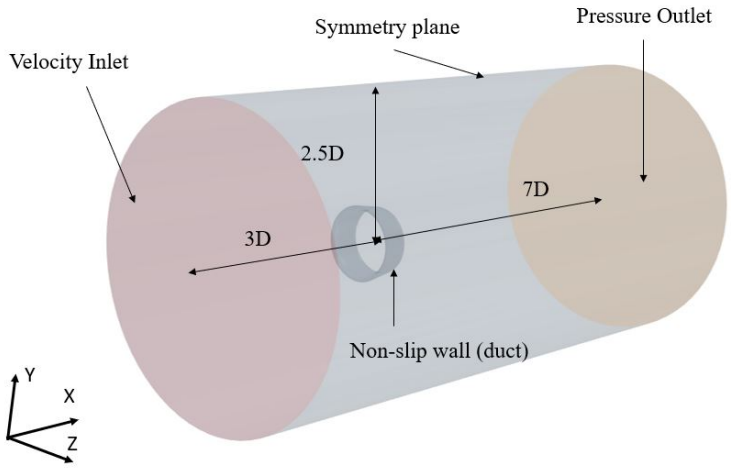

Figure 4.4: Computational domain used in actuator disk method

The boundary layer was resolved using a prism layer mesh, and the rest of the domain consisted of polyhedral mesh cells. Polyhedral cells were used as Two volumetric controls were created to ensure a high-quality mesh surrounding the duct, especially in the downstream direction to capture the turbulent wake structure accurately and can be shown in Figure 4.5, resulting in a final mesh count of approximately 8 million cells. Figure 4.6 shows the reference duct surface mesh using in the study.

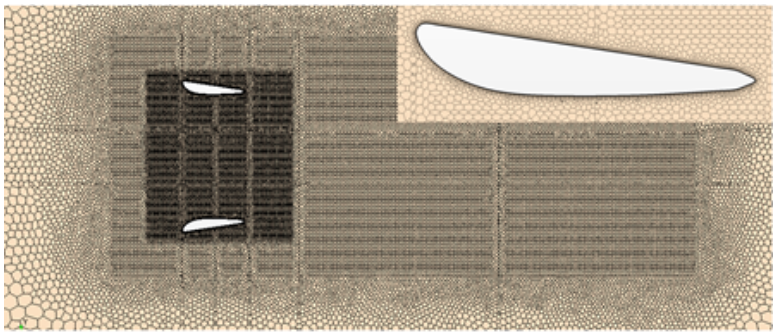

Figure 4.5: Volume mesh used in actuator disk method

Figure 4.6: Duct surface mesh used in actuator disk method

4.10.2 Model Scale Propeller Resolved Method

Using the propeller resolved method, the computational domain consisted of a cylindrical domain, where the propeller was located $3D$ from the inlet and $8D$ from the outlet and $2.5D$ from the outer circumferential wall. The inlet was defined as a velocity inlet, outlet as pressure outlet (0 Pascal) and symmetry plane on the circumferential face as shown in Figure 4.7. A rotating region was defined to rotate the propeller using the RBM method, while the surrounding region was defined as static. An interface between both regions was created to

ensure mesh alignment of the cells. The duct and propeller were defined as no-slip walls. The total mesh count was around 13 million cells. The boundary layer was resolved using a fine prism layer mesh with a y^+ <1, and the rest of the domain consisted of unstructured hexahedral mesh cells. A plane cut section of the volume mesh can be shown in Figure 4.8, and blade and duct surface mesh shown in Figure 4.9.

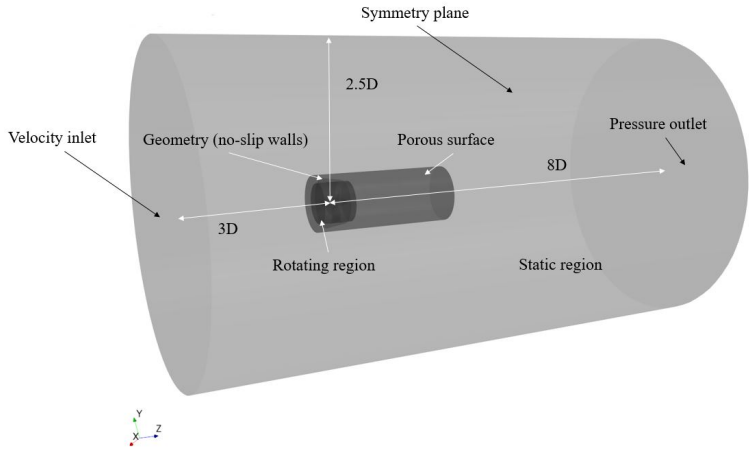

Figure 4.7: Computational domain used in model scale propeller resolved method

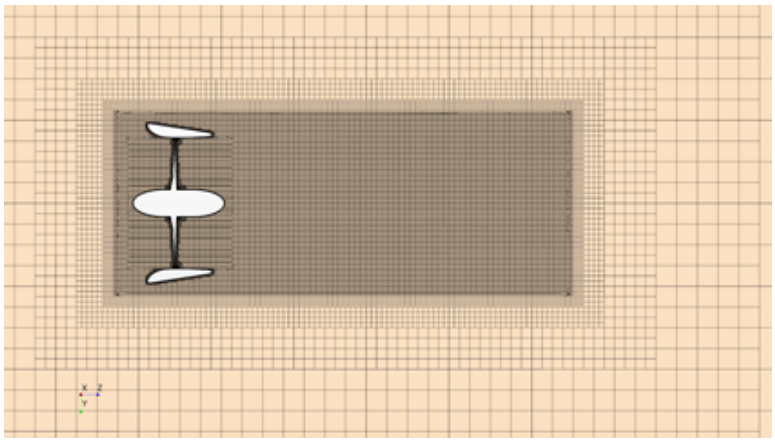

Figure 4.8: Volume mesh used in model scale propeller resolved method

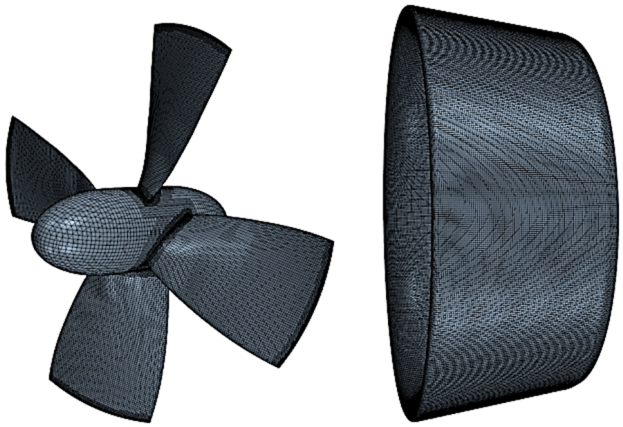

Figure 4.9: Propeller (left) and duct (right) surface mesh used in model propeller resolved method

4.10.3 Full Scale Propeller Resolved Method

The computational domain was scaled by the same factor as the ducted propeller, $\lambda_s = 4$, from the model scale computation domain described above as shown in Figure 4.7.

The mesh was generated using unstructured hexahedral mesh to the count of approximately 13.5 million cells. An all y^+ wall approach was employed, where an average $y^+ < 1$ for the duct and $30 < y^+ < 300$ for the propeller was achieved. The boundary layer was resolved using a fine prism layer mesh for the duct, while standard wall functions were used for the boundary layer of the propeller to save computational expense in terms of the near-wall mesh resolution.

The ducted propeller surface mesh is shown in Figure 4.10. A section of volume mesh shown in Figure 4.11 denotes the mesh refinement region inside the porous surface with a maintained uniform mesh inside the porous data surface.

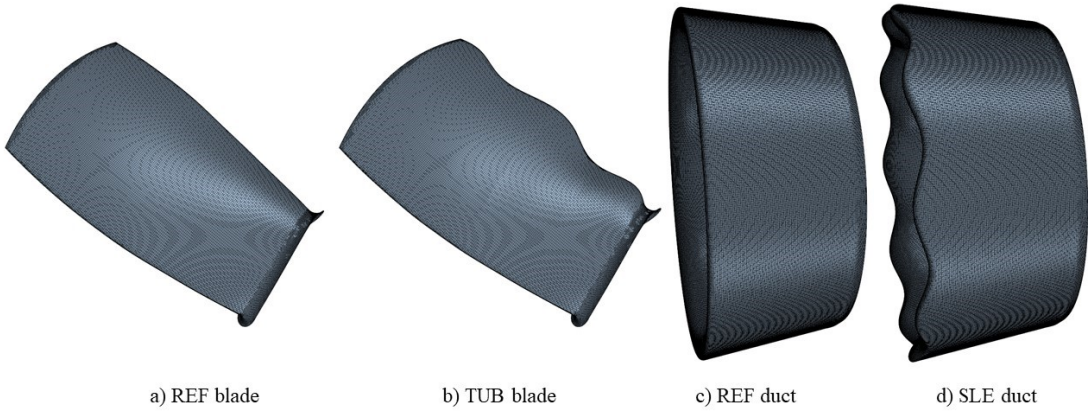

Figure 4.10: Surface mesh of a) reference blade, b) tubercle-modified (TUB) blade, c) reference duct and d) SLE duct

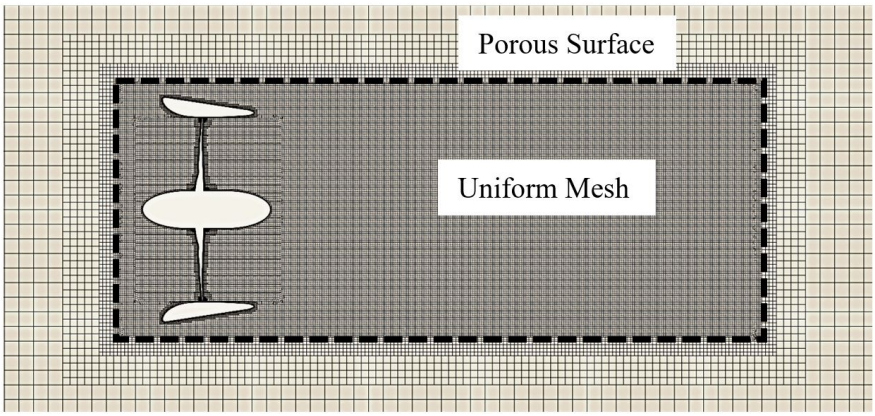

Figure 4.11: Cut-section volume mesh

4.11 Permeable Surface Design and Receiver Locations

Where hydroacoustic analysis was considered as in Chapters 6, 7 and 8, a porous surface was included within the domain. The porous surface was $0.7D$ from the propeller rotational axis and $3.5D$ in length to allow for a portion of the turbulent wake structure to be accounted for within the noise prediction, as it

has been suggested that the quadrupole term – mainly dominated by turbulence and vorticity-induced noise – cannot be neglected in the far-field noise analysis of marine propellers [56]. It is also recommended to remove the 'end-caps' from the porous surface to reduce the extent of the wake structure crossing over the porous region, which could result in noise pollution, and this was implemented within the analysis [111].

In terms of porous surface dimensions, the exact dimensions and location of the integral surface have not been defined clearly in the present literature and it is still being investigated [85]. The porous surface and the near-field receiver positions can be shown in Figure 4.12. The near-field receivers were used to validate the FW-H analogy against the direct hydrodynamic pressures. The near field locations can also be shown in Figure 4.12 and can be described in terms of x, y and z coordinates and normalised by the propeller diameter, D in Table 4.4. Far-field receivers were located at $100D$ from the propeller and at increments of 30^0 to cover the 360^0 range, this can be shown in the schematic in Figure 4.13.

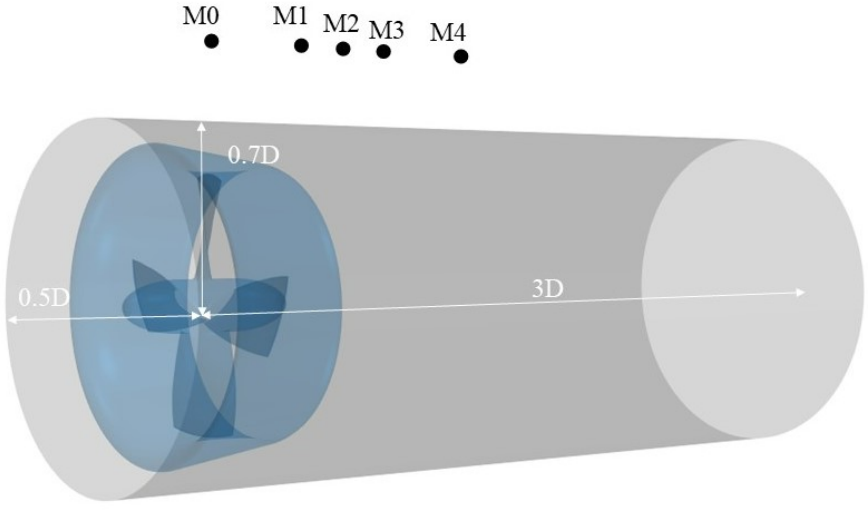

Figure 4.12: Porous surface and near-field receiver locations

Receiver	Location
M0	[0, $1D$, 0]
M1	[0, $1D$, $0.4D$]
M2	[0, $1D$, $0.6D$]
M3	[0, $1D$, $0.8D$]
M4	[0, $1D$, $1.2D$]

Table 4.4: Near-field receiver locations

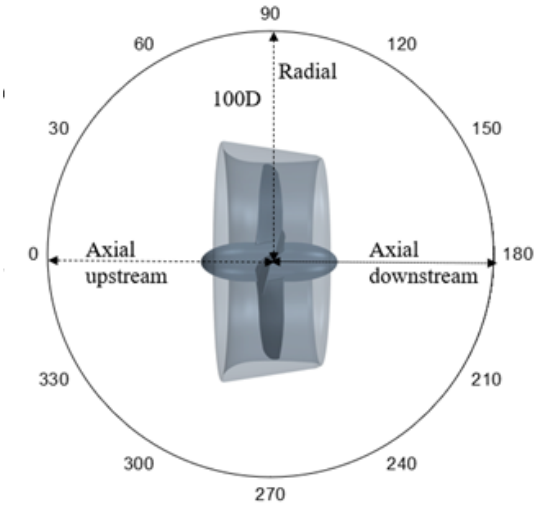

Figure 4.13: Far-field receiver locations in 360^0 range

4.12 Time-Step and Physical Time Selection

Using the actuator disk modelling, a time-step of 0.001 was selected. The simulation ran for 3s where the key hydrodynamic variables had converged. In the propeller resolved method a time-step of 1 (model scale) and 0.5 (full scale) degree of rotation per time step was used, approximately $1.85e^{-4}$s, a time-step of between 0.5 and 2 degrees is recommended by ITTC [121]. The ducted propeller ran for 10 revolutions, where hydrodynamic variables had converged, and the propeller wake flow had developed sufficiently downstream. This allowed for time-averaged

hydrodynamic coefficients to be obtained. The operating conditions where the acoustic data were collected were ran for an additional 10 propeller revolutions to allow a period to collect the pressure fluctuations.

4.13 Verification and Validation

4.13.1 Mesh Convergency Studies

A verification study was conducted to determine the uncertainty of the numerical simulations. This was completed using the grid convergence (GCI) method first proposed by Roache [124] and based on Richardson [125]. Additionally, this method is also recommended in the ITTC procedure [127]. The full methodology implemented in this study was defined by Celik et al [126]. As propeller torque and thrust coefficients were kept constant during this investigation for the BFP method, the duct thrust coefficient K_{TD} was selected as the variable to determine the convergence of the solution whereas K_{TT} and $10K_Q$ were selected for the propeller resolved method. Both studies were completed at J=0.55, the maximum operating efficiency point.

The difference between the solution scalars (ϵ) acquired using three grid structures, fine (1), medium (2) and coarse (3), should be determined by Eqn. 4.78.

$$\epsilon_{21} = \phi_2 - \phi_1, \epsilon_{32} = \phi_3 - \phi_2 \tag{4.78}$$

where, ϕ_1, ϕ_2 and ϕ_3 represent the results using fine, medium and coarse mesh grids, respectively. The ratio of solution scalars is used to calculate the convergence condition by Eqn. 4.79.

$$R = \frac{\epsilon_{21}}{\epsilon_{32}} \tag{4.79}$$

Solution type is determined with respect to the convergence condition, R: oscillatory convergence where -1< R <0; monotonic convergence where 0< R <1; oscillatory divergence where R <-1; and finally monotonic divergence where R >1. If R is found to be meet the criteria for monotonic convergence, the procedure can be directly employed. GCI index is calculated by the following in Eqn. 4.80:

$$GCI_{FINE}^{21} = \frac{1.25e_a^{21}}{r_{21}^p - 1} \tag{4.80}$$

Here, p is apparent order, e_a is an approximate relative error and r_{21}, is the grid refinement factor between fine (1) and medium (2) grid structures. For the BFP method, the fine mesh was 8 million cells, the medium mesh was 4 million cells and the coarse mesh was 1 million cells. For the propeller resolved method, the fine mesh was 13 million cells, the medium mesh was 7.5 million cells and the coarse mesh was 3 million cells. Detailed information about the verification procedure can be found in Celik et al [126].

Results obtained for the duct thrust coefficient and uncertainty level using the BFP method and total thrust and torque coefficient results and uncertainty levels using the propeller resolved method are given in Table 4.5. As can be shown, the convergence condition (R) was between 0 and 1 (monotonic convergence) for both the BFP and propeller resolved methods and each key independent variable. As a result of the uncertainty study at J=0.55, the fine mesh was selected for each method which contained 8 million cells for the BFP method and 13 million cells for the propeller resolved method. The same grid structure was then applied for all model scale case studies, although this grid structure differed for both BFP and propeller resolved methodologies.

Method	Variable	ϕ_1	ϕ_2	ϕ_3	R	$\%GCI^{21}_{FINE}$
BFP	K_{TD}	0.0262	0.0263	0.0267	0.189	0.54
Propeller Resolved	K_{TT}	0.178	0.177	0.172	0.13	0.23
	$10K_Q$	0.279	0.278	0.276	0.33	0.83

Table 4.5: Uncertainty result for J=0.55 using BFP and propeller resolved method

For the full scale propeller resolved study, a mesh convergency study was also conducted. The mesh numbers are the following; fine (1), 23 million, medium (2), 13.5 million and coarse (3), 5.4 million. Cavitation volume results and uncertainty levels are given in Table 4.6. As can be shown, the convergence condition (R) was between 0 and 1 (monotonic convergence) for both variables.

Variable	ϕ_1	ϕ_2	ϕ_3	R	$\%GCI^{21}_{FINE}$
Cavitation Volume	0.001358	0.001348	0.00097	0.0265	1

Table 4.6: Cavitation volume uncertainty result at J=0.3, σ_N of REF design

However it was noted the variation in results between fine and medium mesh was minimal as depicted in Figure 4.14 which shows the variation of cavitation volume over a number of mesh structures that were varied systematically in cell number. As a result of the uncertainty study of cavitation volume at J=0.3, σ_N = 1.3, the medium mesh was selected for each method which contained 13.5 million cells to save computational time. The same grid structure was then applied for all full scale case studies.

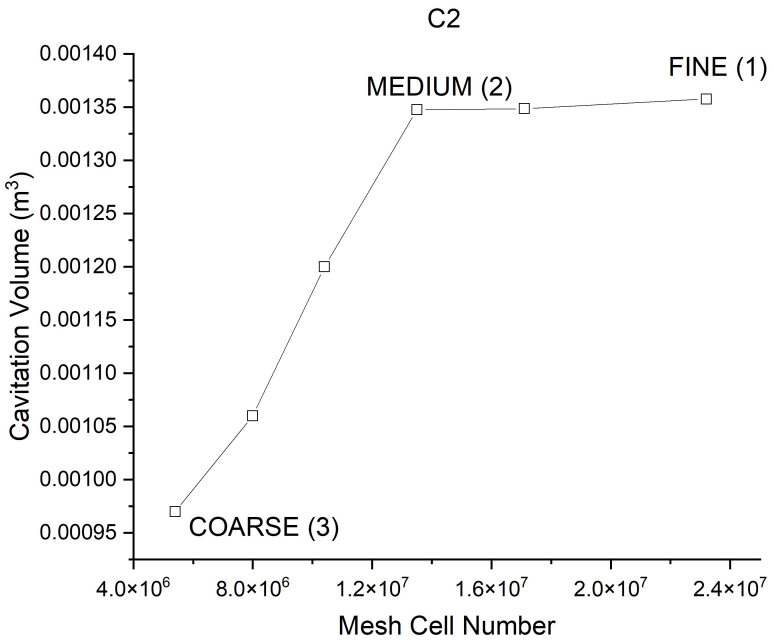

Figure 4.14: Cavitation volume vs. mesh number at condition C2

4.13.2 Hydrodynamic Validation with Experimental Test

The validation was done by comparing experimental data acquired by an internal test campaign at CTO, Poland. Figure 4.15 depicts the results acquired using the BFP (CFD 1) and propeller resolved (CFD 2) methods, where advance ratios ranging from 0.001 to 0.7 were considered and compared to the experimental data. During the simulation, the BFP method was used to isolate the comparison only to the performance of the duct while K_Q and K_{TP} are used as direct inputs from the experimental data so are therefore exactly the same as the experimental data. Therefore, only the duct thrust is varying due to the changing design of ducts. From this validation study, it can be observed that the developed method can accurately predict the duct thrust and the results matched well with the experimental data. In addition, the results acquired using the propeller resolved method can be shown and compared to the same experimental data. The

computational environment generated can be used to determine the open water characteristics of the ducted propeller selected in this study to within a good degree of accuracy, with relative errors of total thrust and torque coefficient; 5.1 and 1.4% respectively.

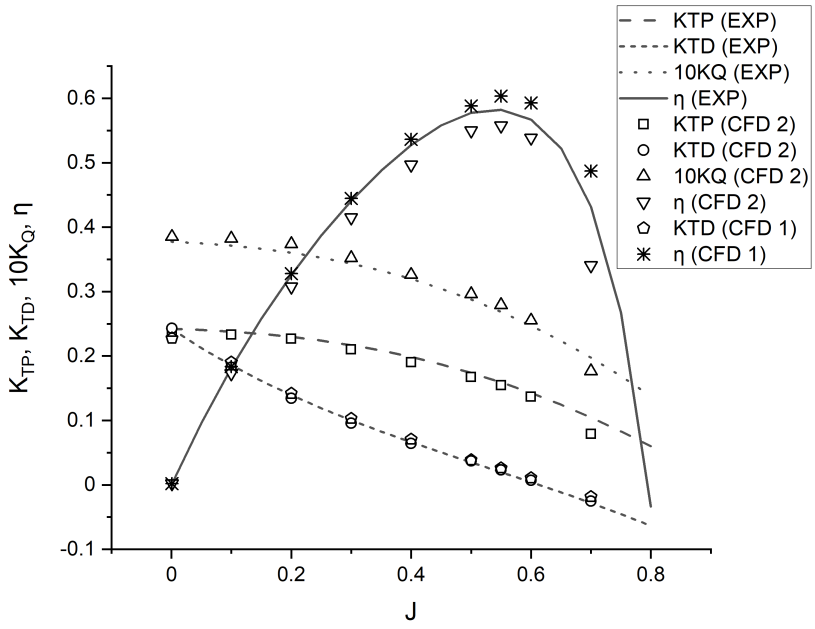

Figure 4.15: Hydrodynamic validation against experimental data for KA4-55 and 19A duct for BFP (CFD 1) and model scale propeller resolved (CFD 2) methodologies

The open-water hydrodynamic coefficients for the full scale (FS) reference ducted propeller were compared to model scale (MS) open-water experimental and numerical hydrodynamic coefficients and can be shown in 4.16.

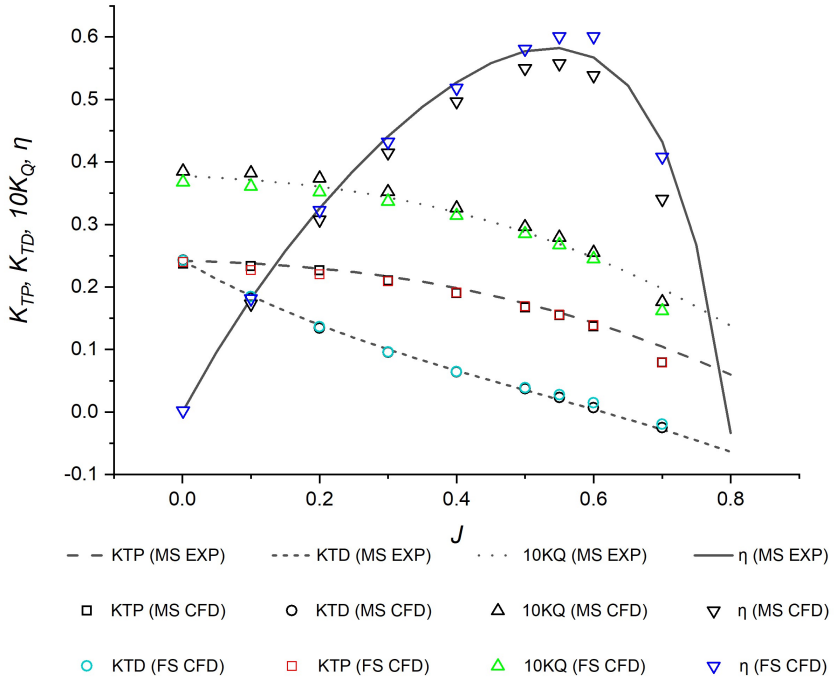

Figure 4.16: Full scale open-water hydrodynamic coefficients compared to model scale experimental and numerical open-water hydrodynamic coefficients

When comparing the numerical full scale to model scale open-water hydrodynamic coefficients, it can be shown that propeller torque coefficient reduces, there is minimal change in propeller thrust coefficient and duct thrust coefficient does not degrade as significantly in the higher advance ratios ($J > 0.55$). The reduction in torque coefficient is believed to be due to a reduction in the frictional component, while there is minimal change in the propeller thrust coefficient which is believed to be due to the change in the pressure and frictional component balancing each other out as evidenced in Bhattacharyya et al. [95]. The reduction in duct thrust degradation is due to flow separation over the pressure side of duct being delayed to a later advance ratio. In model scale, flow separation was first observed at $J = 0.5$, in full scale, flow separation was not observed until $J = 0.8$ outwith the design envelope of this ducted propeller combination as propeller

thrust is close to zero at advance ratio $J = 0.8$ (see Figure 8.4). The change in scale and thus, Re, results in higher efficiency at a shifted higher advance ratio in full scale at $J = 0.6$ and higher efficiency above the optimal efficiency advance ratio. The tendencies observed in the current research agree well with previous ducted propeller scale effect research [95; 129], therefore the current numerical methodology is deemed valid within the limitations of current open available research.

4.13.3 Sheet Cavitation Validation with Experimental Test

In order to ensure the cavitation model used was appropriate to describe the sheet cavitation on the Kaplan propeller, the numerical cavitation observations were compared with experimental results. However, to the author's knowledge there is no experimental cavitation observations openly available of the KA4-55 +19A, therefore, the KA4-70 + 19A was used for validation purposes. The experimental campaign was conducted in MARIN's Depressurized Wave Basin (DWB) where a variety of cavitation numbers and advance ratios were investigated to observe the cavitation behaviour. To the author's knowledge, the thrust and torque from the experimental campaign is not openly available. But, a selection of the cavitation observations can be found in Moulijn et al. [128]. The cavitation observation at $J = 0.2$ and $\sigma_N = 1.9$ in the test campaign was compared to the numerical results acquired at the same operating conditions and can be shown in Figure 4.17. The numerical cavitation visualisation was achieved by using an iso-surface of the vapour fraction ($\alpha = 0.1$). As can be seen, there is a good agreement between experimental and numerical cavitation observations and therefore, the numerical modelling technique to describe cavitation was validated.

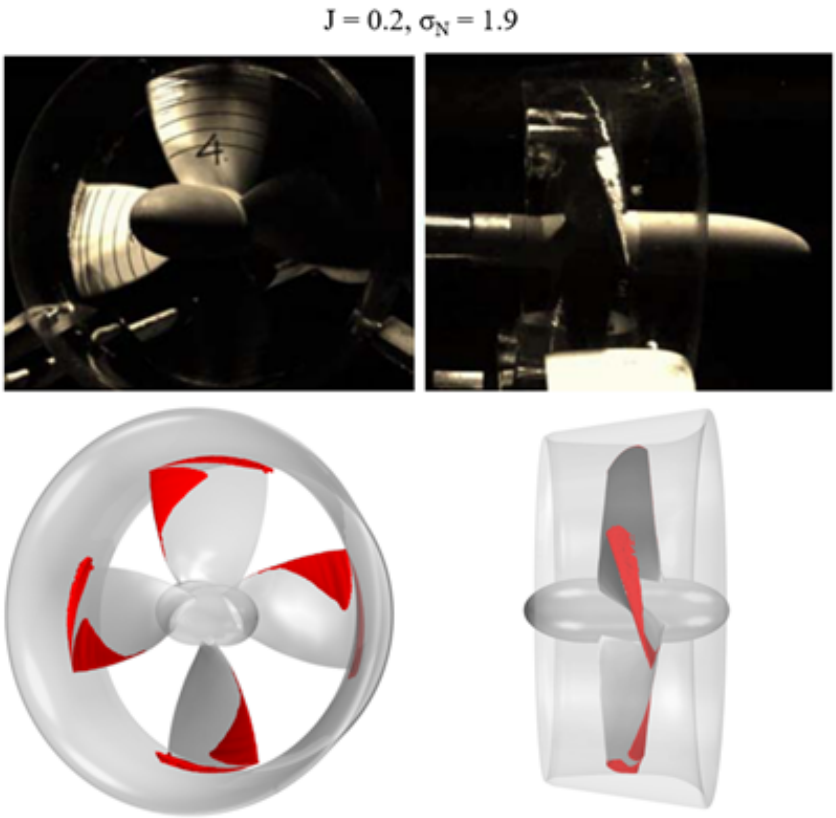

Figure 4.17: Numerical cavitation observations (present study) compared to experimental data for KA4-70 +19A acquired from Moulijn et al [128] at $J = 0.2$, σ_N= 1.9

4.13.4 Validation of the Ffowcs Williams-Hawkings (FW-H) acoustic analogy

To validate the FW-H acoustic analogy, the near-field direct hydrodynamic and hydroacoustic pressures were compared for the KA4-55 open propeller at the radial receiver, M0. This has been conducted in numerous studies within the literature for validation of the FW-H acoustic analogy [56; 97; 110]. As can be shown in Figure 4.18 there is good agreement between the direct hydrodynamic and hydroacoustic (FW-H) pressure.

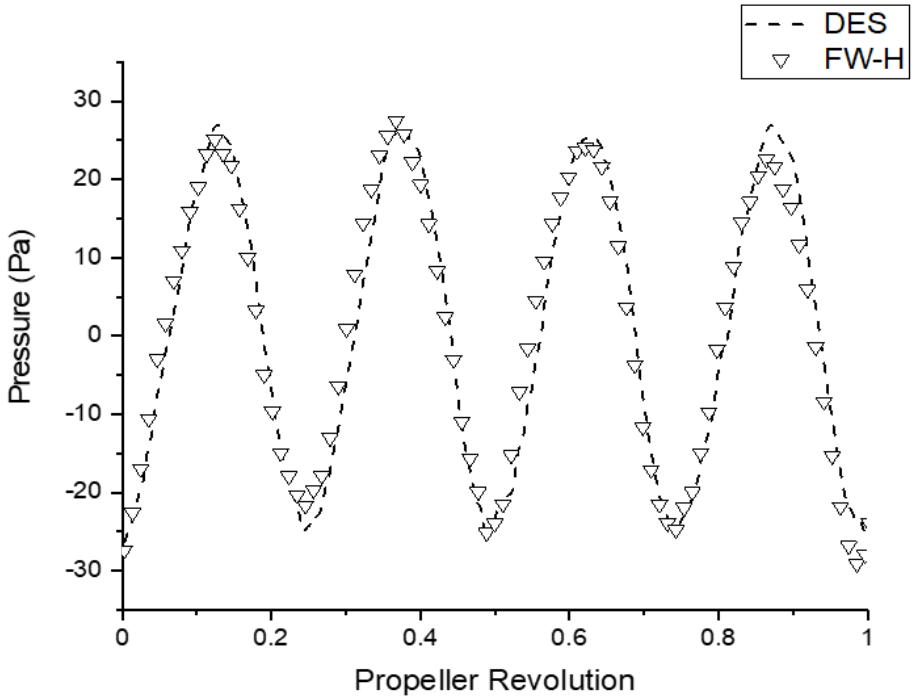

Figure 4.18: Near-field hydrodynamic and hydroacoustic pressure for open model scale KA4-55 propeller at $1D$ from propeller centre in radial position (M0) at $J = 0.55$ in non-cavitating conditions

For the full scale propeller resolved method, the same validation procedure was conducted and illustrated in Figure 4.19. As shown, there is good agreement between the direct hydrodynamic and hydroacoustic (FW-H) pressure.

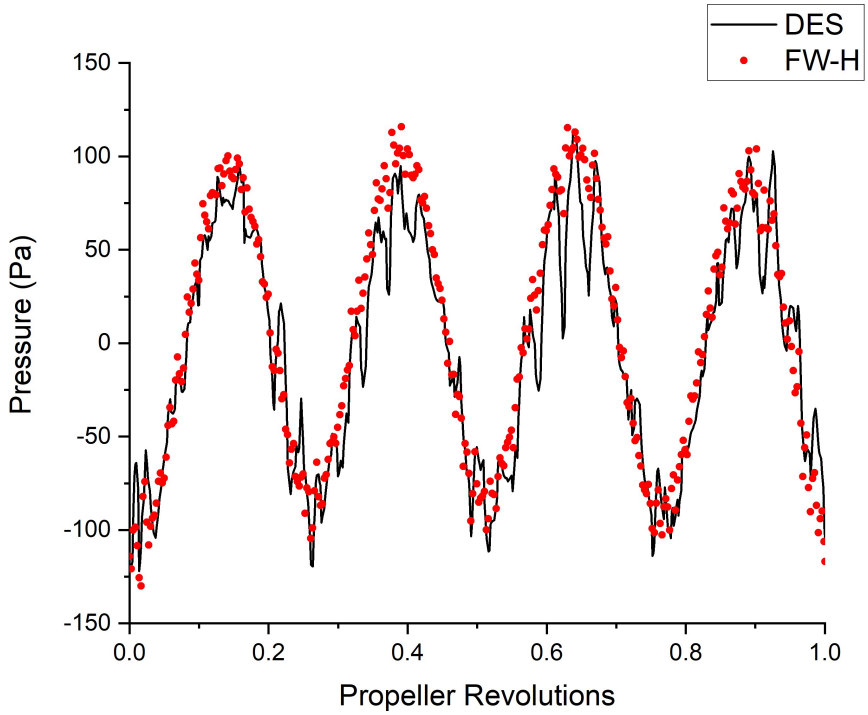

Figure 4.19: Near-field hydrodynamic and hydroacoustic pressure for open full scale KA4-55 propeller at $1D$ from propeller centre in radial position (M0) at J = 0.55 in non-cavitating conditions

4.14 Summary

In summary, the numerical methodology used to achieve the aim and objectives of the PhD study was described. The computational domain, mesh generation and other key CFD specifics such as rotation rate and time-step were outlined. In addition, the verification and validation studies for the CFD modelling were presented.

Chapter 5

Leading-Edge Tubercle Parametric Optimisation Study

This chapter focuses on the design and optimisation of the LE tubercle geometry as applied to a benchmark ducted propulsor. In this chapter, the influence of tubercle geometry parameters, amplitude, A and wavelength, λ on the duct thrust performance are investigated. The different configurations and optimisation methodology is discussed in Section 5.1. The results are presented and discussed in Section 5.2 and 5.3, with the overall summary in Section 5.4.

5.1 Optimisation Methodology

A response surface methodology was employed for the optimisation process using multi-order regression analysis. The propeller was replaced with an actuator disk (see Figure 5.1) to fix the propeller thrust T_P $[N]$, and torque, Q $[Nm]$ and thus, isolating the duct thrust, T_D $[N]$ as the dependant response surface variable. Replacing the resolved propeller with an actuator disk also made the optimisation more economical and cost-effective. Ten different ducts with varying, amplitude,

A $[mm]$ and wavelength, λ $[mm]$ configurations were modelled. The range of λ and A explored was roughly based on a previous optimisation study on a 2D tidal turbine-based hydrofoil [83]. The tubercle duct geometries investigated in the optimisation study are illustrated in Figure 5.2 and the main particulars can be found in Table 5.1.

The family of tubercle ducts were designed systematically using parametric modelling and based on a design of experiment approach, the relationship between the response output, duct thrust, T_D and variables A and λ, were explored independently at the operating conditions considered. Then, an optimal candidate was selected based on the response surfaces and further analysis was conducted.

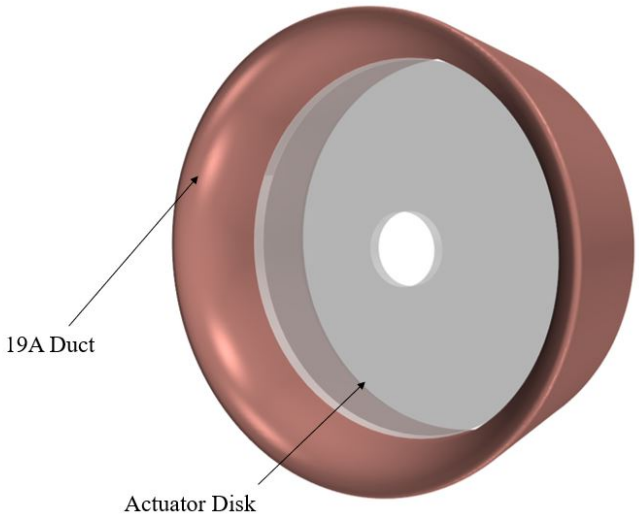

Figure 5.1: Actuator disk model used for optimisation study

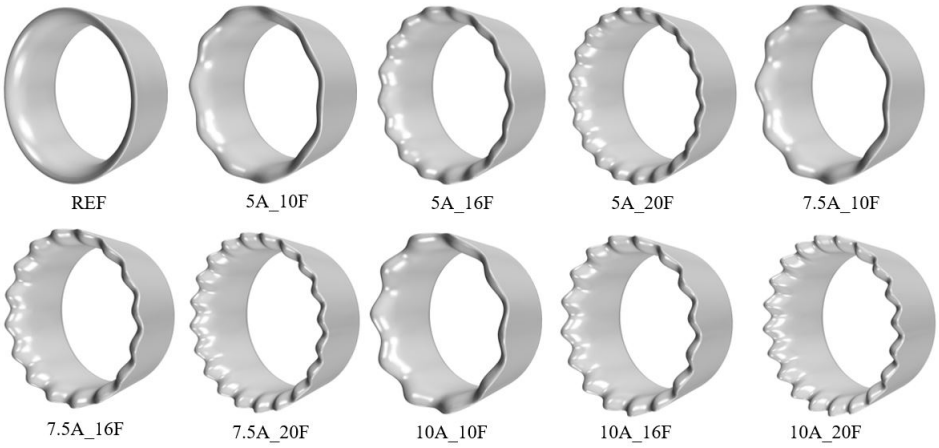

Figure 5.2: Parametric family of tubercle ducted propeller geometry for optimisation study

Model	Label	Tubercle Count	λ, mm	A, mm
1	REF	-	-	-
2	5A_10F	10	94 ($0.75L_{Duct}$)	5 ($0.04L_{Duct}$)
3	5A_16F	16	59 ($0.47L_{Duct}$)	5 ($0.04L_{Duct}$)
4	5A_20F	20	47 ($0.38L_{Duct}$)	5 ($0.04L_{Duct}$)
5	7.5A_10F	10	94 ($0.75L_{Duct}$)	7.5 ($0.06L_{Duct}$)
6	7.5A_16F	16	59 ($0.47L_{Duct}$)	7.5 ($0.06L_{Duct}$)
7	7.5A_20F	20	47 ($0.38L_{Duct}$)	7.5 ($0.06L_{Duct}$)
8	10A_10F	10	94 ($0.75L_{Duct}$)	10 ($0.08L_{Duct}$)
9	10A_16F	16	59 ($0.47L_{Duct}$)	10 ($0.08L_{Duct}$)
10	10A_20F	20	47 ($0.38L_{Duct}$)	10 ($0.08L_{Duct}$)

Table 5.1: Ducts investigated in optimisation study

5.2 Results and Discussions using BFP Method

5.2.1 Optimisation of Duct Hydrodynamic Performance

The bollard pull condition and the maximum efficiency operating condition, with advance ratios J=0.001 and J=0.55 were considered to investigate the effect of

geometrical parameter variations on the tubercle (SLE) duct. At $J = 0.001$, the duct experiences a high negative angle of attack, however at $J = 0.55$, the inflow angle is much more modest as can be seen from Figure 5.3. Through conducting the above demonstrated CFD simulations, the hydrodynamic results in terms of the propulsive indicators can be extracted and summarised as shown in Table 5.2.

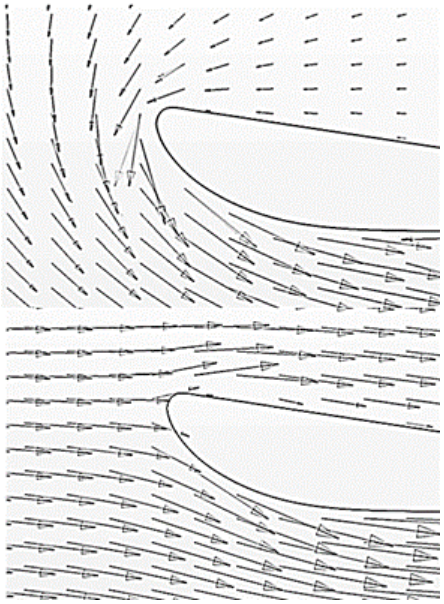

Figure 5.3: Induced inflow angle for J=0.001 (top) and 0.55 (bottom), showing variation in inflow angle

Label	J	K_{TD}	η	C_t
REF	$J = 0.001$ (Bollard Pull)	0.2278	1.996E-03	1.186E+06
5A_10F		0.2362	2.032E-03	1.207E+06
5A_16F		0.2298	2.004E-03	1.191E+06
5A_20F		0.2243	1.981E-03	1.177E+06
7.5A_10F		0.2205	1.965E-03	1.167E+06
7.5A_16F		0.2141	1.937E-03	1.191E+06
7.5A_20F		0.2102	1.9203E-03	1.151E+06
10A_10F		0.2085	1.913E-03	1.191E+06
10A_16F		0.2009	1.880E-03	1.141E+06
10A_20F		0.1942	1.852E-03	1.136E+06
REF	$J = 0.55$ (Optimum Efficiency)	0.0262	0.604	1.56
5A_10F		0.0246	0.598	1.55
5A_16F		0.0241	0.597	1.54
5A_20F		0.0248	0.599	1.55
7.5A_10F		0.0239	0.596	1.54
7.5A_16F		0.0241	0.597	1.54
7.5A_20F		0.0243	0.598	1.54
10A_10F		0.0239	0.596	1.54
10A_16F		0.0242	0.597	1.54
10A_20F		0.0246	0.598	1.55

Table 5.2: Tubercle geometrical parameter optimisation data

At $J = 0.001$, K_{TD} can be correlated to the varying wavelength and amplitude as a function of chord length, c, where c=L_{DUCT}. In the bollard pull condition, the following general trend can be observed. First, while maintaining constant λ, a reduction in A results in an increase in K_{TD}. Second, while maintaining A, increasing λ also results in an improvement of K_{TD} in all cases. Therefore, in the current range of optimisation for the bollard pull condition, the simulation results indicate smaller amplitude and larger wavelength to be favourable, which directs the optimisation to the reference design with A=0 and λ=$+\infty$. The trend is monotonic and ends in 5A_10F, which shows to be the optimum design. Further extending the optimisation range is feasible numerically but the tubercle feature became less noticeable. But, between the tubercle duct and the reference duct,

the design did show a noticeable improvement in K_{TD}.

On the other hand, at $J = 0.55$, K_{TD} is not very sensitive to the varying A and λ. It is noted that there is a limited change to K_{TD}, therefore the later optimisation is focused on the bollard pull condition. Following on general trend observation, a further regression analysis was conducted for both operating points to statistically interpret the impact of variables λ and A on the response, K_{TD} and to fit a model to predict the response at different configurations. The regression equation fitted to the optimisation data set for $J = 0.001$ was as shown in Eqn. 5.1 with Table 5.3 showing the regression analysis uncoded coefficients, coefficient (Coef), standard error of the coefficient (SE Coef), the ratio between the coefficient and the standard error (T-Value), the variable to determine the statistical significance of the term (P-Value) and finally, the variance inflation factor (VIF). Table 5.4 shows the model summary, where S represents how far the data values fall from the fitted values in addition to R^2 and adjusted R^2 values, respectively.

$$\begin{aligned} K_{TD} = 0.22754 - 1.026\left(\frac{A}{c}\right) - 0.1192\left(\frac{\lambda}{c}\right) \\ +1.83\left(\frac{A}{c}\right)^2 + 0.0852\left(\frac{\lambda}{c}\right)^2 - 0.155\left(\frac{A}{c}\right)\left(\frac{\lambda}{c}\right) \end{aligned} \tag{5.1}$$

Term	Coef	SE Coef	T-Value	P-Value	VIF
Constant	0.224789	0.000506	444.31	0.000	-
A/c	-0.03284	0.00209	-15.74	0.000	20.56
λ/c	0.02306	0.00216	10.67	0.000	21.45
$(A/c)^2$	0.00293	0.00208	1.41	0.232	11.20
$(\lambda/c)^2$	-0.01208	0.00224	-5.38	0.006	15.24
$(\lambda/c)(A/c)$	0.00234	0.00155	1.51	0.205	4.81

Table 5.3: Regression analysis uncoded coefficients at $J = 0.001$

S	R^2	R^2 (adj)
0.0008640	99.82%	99.59%

Table 5.4: Regression analysis model summary at $J = 0.001$

The regression equation fitted to the optimisation data set for $J = 0.55$ was as shown in Eqn. 5.2 with Table 5.5 and Table 5.6 showing the regression analysis uncoded coefficients and model summary, respectively.

$$\begin{aligned} K_{TD} = 0.02603 - 0.0186\left(\frac{A}{c}\right) - 0.00408\left(\frac{\lambda}{c}\right) \\ +0.354\left(\frac{A}{c}\right)^2 + 0.00572\left(\frac{\lambda}{c}\right)^2 - 0.0563\left(\frac{A}{c}\right)\left(\frac{\lambda}{c}\right) \end{aligned} \tag{5.2}$$

Term	Coef	SE Coef	T-Value	P-Value	VIF
Constant	0.024449	0.000124	197.55	0.000	-
A/c	-0.000461	0.000510	-0.90	0.418	20.56
λ/c	-0.000764	0.000528	-1.45	0.222	21.45
$(A/c)^2$	0.000567	0.000509	1.11	0.328	11.20
$(\lambda/c)^2$	0.000810	0.000549	1.48	0.214	15.24
$(\lambda/c)(A/c)$	-0.000848	0.000378	-2.24	0.088	4.81

Table 5.5: Regression analysis uncoded coefficients at $J = 0.55$

S	R^2	R^2 (adj)
0.0002113	95.72%	90.36%

Table 5.6: Regression analysis model summary at $J = 0.55$

A p-value lower than 0.05 indicates that the variable is statistically significant and therefore both predictor variables - wavelength and amplitude at J=0.001 are statistically significant on the response, K_{TD} as shown in Table 5.5. Additionally at J=0.001, the variation in A resulted in a larger impact on response variable, K_{TD}, than λ which agrees similarly with previous optimisation studies

on hydrofoils in the pre-stall regime [3], however, λ still had an impact on the resulting K_{TD}. At J=0.55, it was not determined if λ or A were statistically important as shown in Table 5.5.

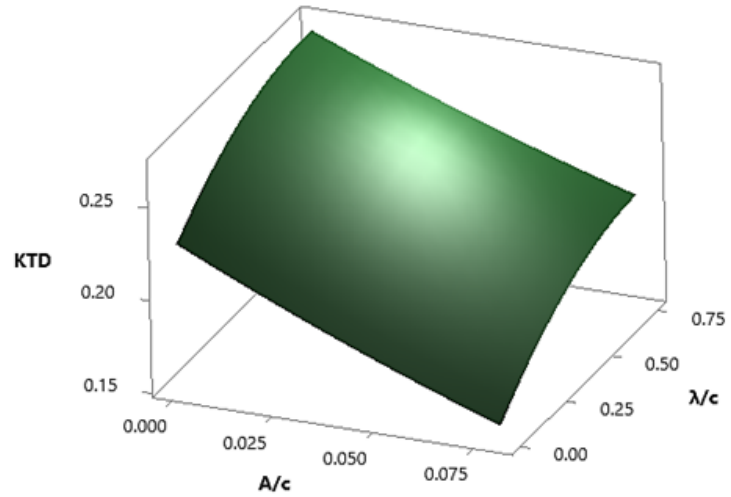

Figure 5.4: Surface optimisation plot at J=0.001

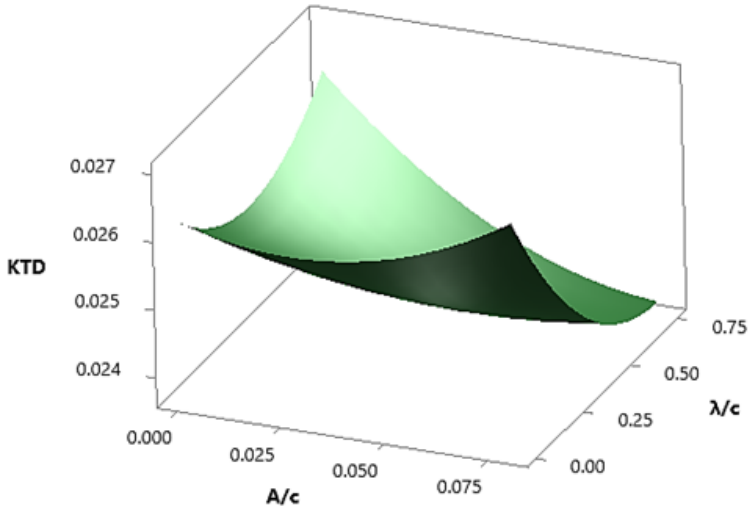

Figure 5.5: Surface optimisation plot at J=0.55

As can be shown in Figure 5.4, the surface plot predicts the optimal duct performance at low A, high λ configuration, 5A_10F, at J=0.001. Figure 5.5 shows

the surface plot at J=0.55, showing the low amplitude high wavelength configuration, 5A_10F, to be one of the top performers at this condition. Therefore, it is believed that 5A_10F is the optimal design candidate which consists of an $A = 0.08L_{DUCT}$ and $\lambda = 0.75L_{DUCT}$. This finding shows that leading-edge tubercle design favours large but mild candidates, which have the capacity to energise the vortex flow but do not consume too much energy in generating these secondary vortices.

5.2.2 Duct Surface Pressure Distributions

Figure 5.6 and Figure 5.7 illustrates the scalar plot of the static pressure distribution on the reference and SLE ducts, 5A_10F, 10A_10F, 10A_20F at operating conditions $J = 0.001$ and 0.55 respectively. At the heavy-loaded condition, the influence of the tubercles can be shown clearly with high to low pressure pattern observed on the inner side of the duct from peak to trough, respectively. In the heavy-loaded condition the tubercle peak experiences increased pressure behind the peaks with increasing A and reducing λ. However, this increase in A or reduction in λ resulted in a degradation in K_{TD} when comparing 5A_10F to the other SLE ducts. The degradation in K_{TD} can also be related to the increasing steepness of the tubercle (A/λ).

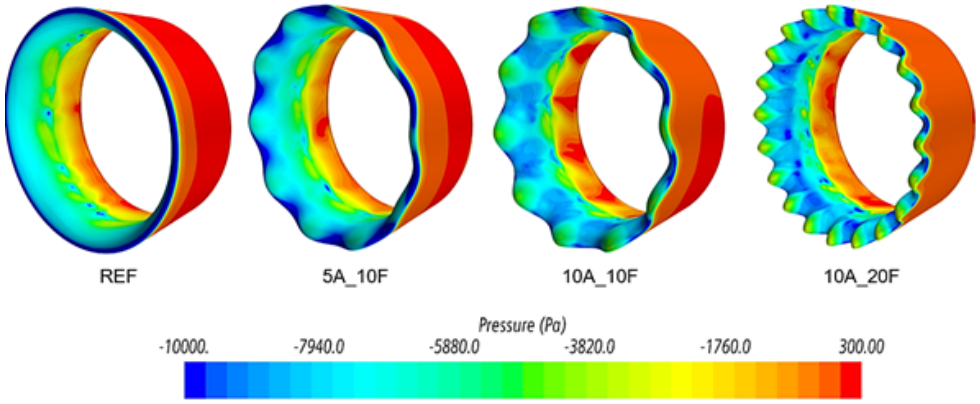

Figure 5.6: Surface static pressure distribution at J=0.001

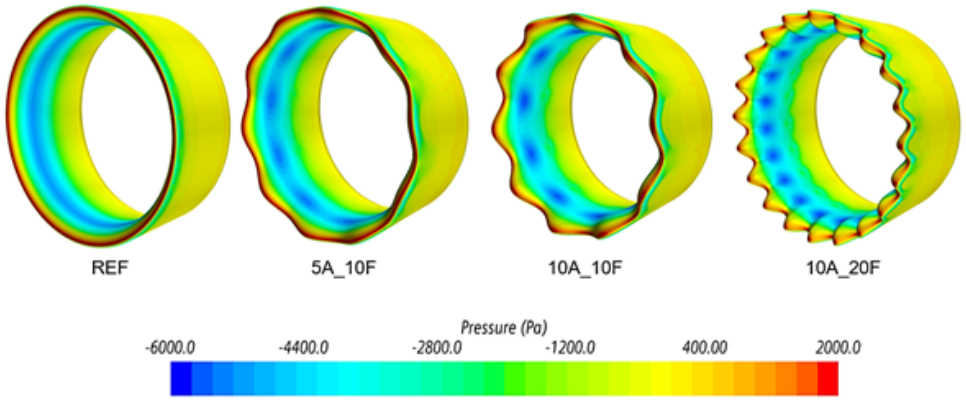

Figure 5.7: Surface static pressure distribution at J=0.55

The improvement in duct thrust at the heavy-loaded condition can be further confirmed by comparing 2D static pressure coefficient plots between REF and SLE, 5A_10F duct in Fig. 5.8a, where the inclusion of tubercles induces a larger low-pressure region behind the tubercle trough on the inner duct section when compared to the REF design and the addition of a peak which increases the surface area where a useful pressure gradient between outer and inner duct boundaries can be obtained, resulting in an improved lift. The improved K_{TD} for the optimal configuration is due to the increase in lift being larger than the likely

increase in skin friction drag due to an increase in duct wetted surface area from the addition of tubercles. However, as tubercle A is increased, the duct surface area will increase. Once the tubercle A is increased above the optimal configuration the likely increase in skin friction drag will be larger than any additional useful horizontal lift produced by the tubercles as evidenced by the thrust degradation at the higher A tubercle configurations. The static pressure coefficient, C_P, can be defined as in Eqn. 5.3, where P_0 $[Pa]$, is static pressure.

$$C_P = \frac{P_0}{0.5\rho V_A^2} \tag{5.3}$$

At the lightly-loaded condition $J = 0.55$, the variation in surface pressure distribution on the outer duct side of the duct is minimal. The 2D static pressure coefficient plots are shown in Fig. 5.8b.

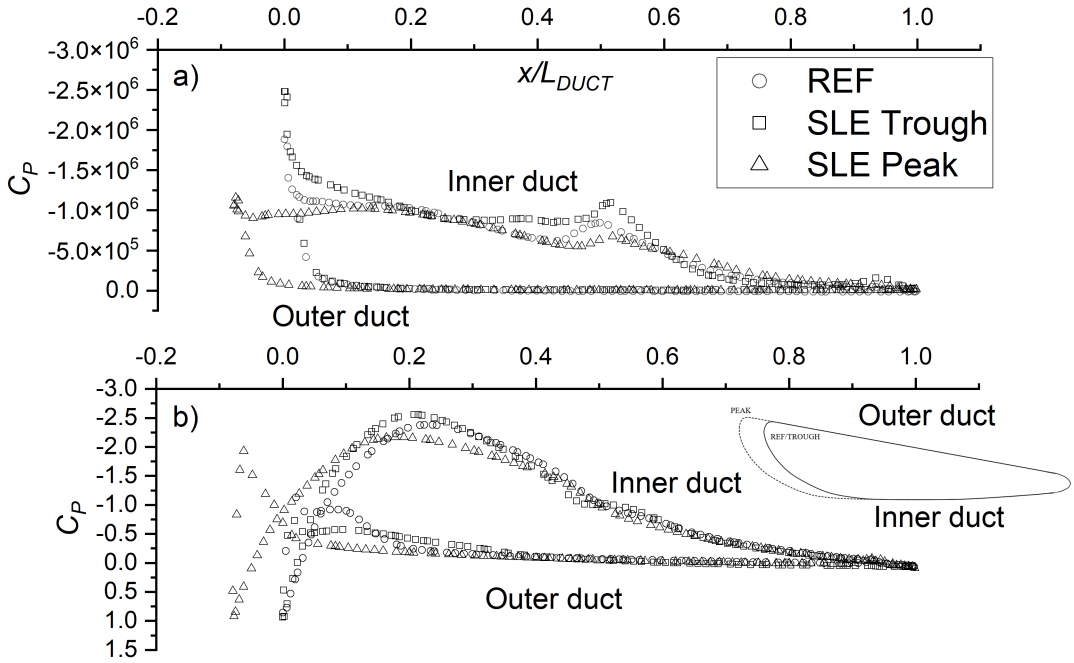

Figure 5.8: 2D pressure coefficient plots for REF and SLE (5A_10F) ducts at a) J=0.001 and b) J=0.55

5.2.3 Vorticity Distribution and Turbulent Wake Structure

Figure 5.9 and Figure 5.10 shows the SLE tubercle ducts 5A_10F, 10A_10F and 10A_20F streamwise vorticity on the duct surface at $J = 0.001$ and 0.55, respectively. As can be seen, the number of counter-rotating pairs is directly proportional to the tubercle count within the configuration. At $J = 0.001$ and 0.55, an increase in A and a reduction in λ results in an increase in counter-rotating vortex strength on the inner side of the duct cross-section. At $J = 0.55$, the vortex pairs can be visible on the pressure side of the duct, which increase in strength with an increase in A and a reduction in λ, although an increase in A has a larger impact

on vortex pair strength when compared to λ. As A is increased and λ is reduced, the steepness of the tubercle, A/λ ratio increases. Therefore, J, A, λ and A/λ ratio of the tubercle will influence the strength of the induced vortex pair. At J = 0.001, the strength of the vortex pairs become stronger with increasing A/λ ratio while at $J = 0.55$ over the pressure side of the duct, both vortex pairs can be seen to increase in strength with increasing A/λ ratio.

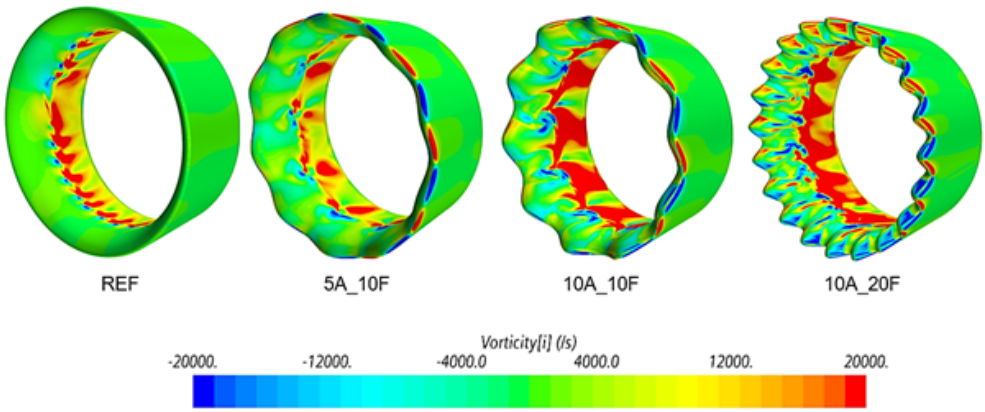

Figure 5.9: Surface streamwise vorticity at J=0.001

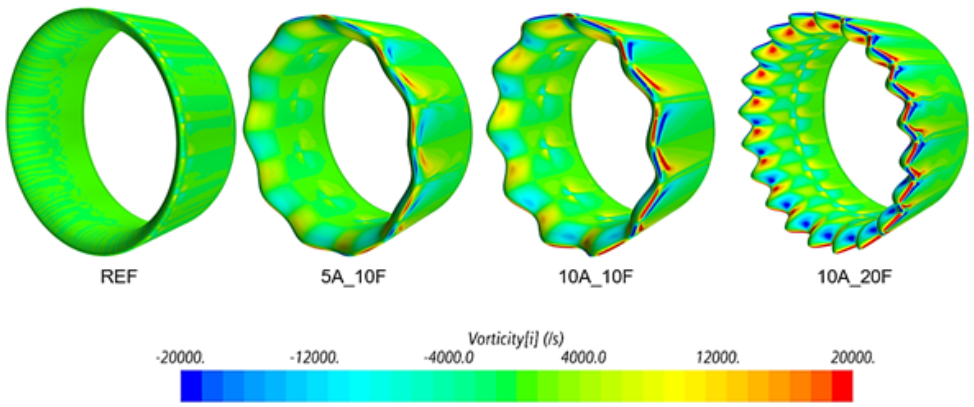

Figure 5.10: Surface streamwise vorticity distribution at J=0.55

From Figure 5.11, it is interesting to note that the petal-shaped vortex pattern can be observed clearly and there is a marginal reduction in maximum vorticity strength for all SLE ducts when compared to the reference duct, although the

vortex structure spans over a larger area. Figure 5.12 illustrates the vorticity magnitude in the stream-wise direction at X/D = 0.6, 1.2 and 1.5 from the duct entrance for the LE modified (5A_10F) and reference duct at the optimum operating efficiency point. As can be seen, the LE tubercle duct disrupts the typical ring vortex structure from the reference design.

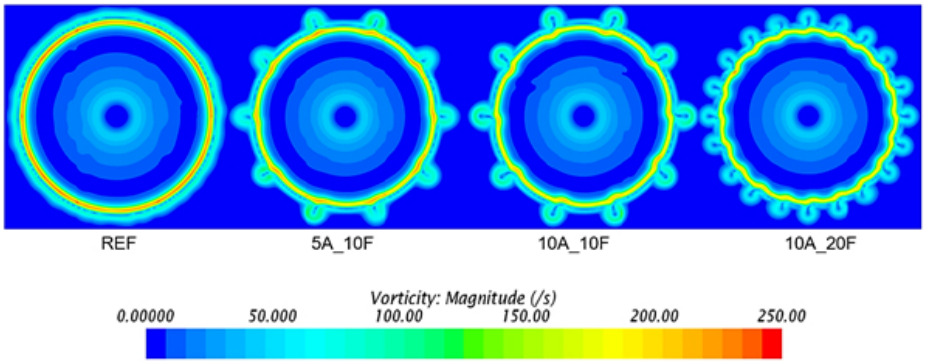

Figure 5.11: SLE tubercle ducts 5A_10F, 10A_10F and 10A_20F vorticity magnitude at X/D = 0.6 and J = 0.55

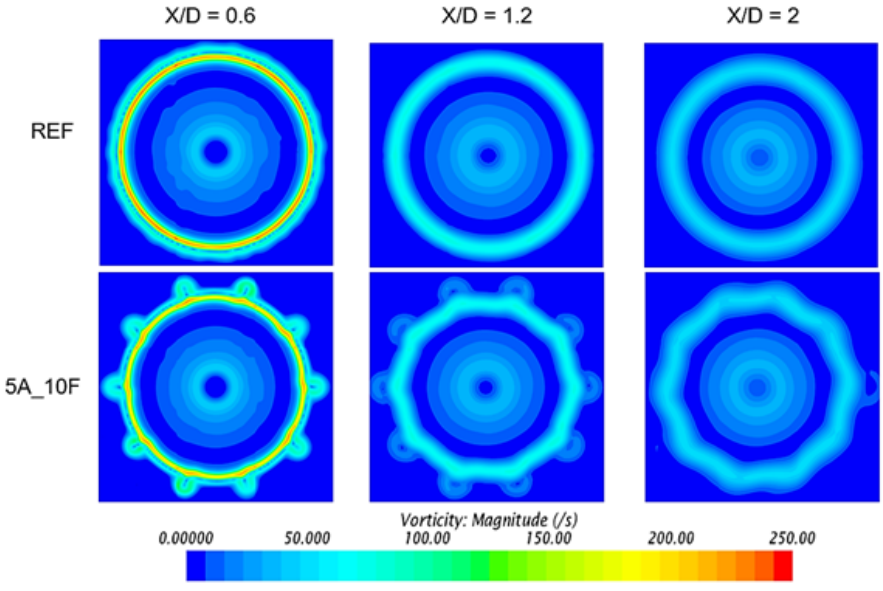

Figure 5.12: Reference and modified (5A_10F) ducts vorticity magnitude at X/D = 0.6, 1.2 and 2 for J = 0.55

Based on the above simulations, the SLE, 5A_10F duct was selected for further investigation due to the improvement in performance at the heaviest-loaded condition. This was conducted by replacing the actuator disk with a physical propeller model to understand the resulting influence of the LE tubercles on key propeller performance characteristics such as blade thrust and torque which will affect the final propulsive efficiency.

5.3 Results and Discussions using Propeller Resolved Method

5.3.1 Global Hydrodynamic Performance

Through the optimisation study, the SLE (5A_10F) duct can be seen to show favourable performance in both operating conditions considered when compared to the alternative designs. Therefore, further analysis was conducted on the SLE (5A_10F) duct using a propeller resolved method. Although the actuator disk modelling provided an inexpensive environment to perform the optimisation study efficiently, it is a simplified environment and does not take into account the effect tubercles will incur on the propeller, therefore using the propeller resolved method will shed light on such effects. The difference in performance variables due to the inclusion of LE tubercles can be shown for a variety of J in Figure 5.13. Generally, there is a good agreement between both methods in terms of K_{TD} as it is enhanced at the heaviest loaded conditions and then there is a performance degradation in the lightly loaded conditions, similar to the previous results using the BFP method. The difference in results at some operating conditions is due to the propeller resolved method including the physical propeller, which will predict the tip leakage vortex, the resulting difference in pressure distributions on the duct

which will arise from this and, the tubercle's influence on other key performance variables such as K_{TP} and K_Q, which will affect η.

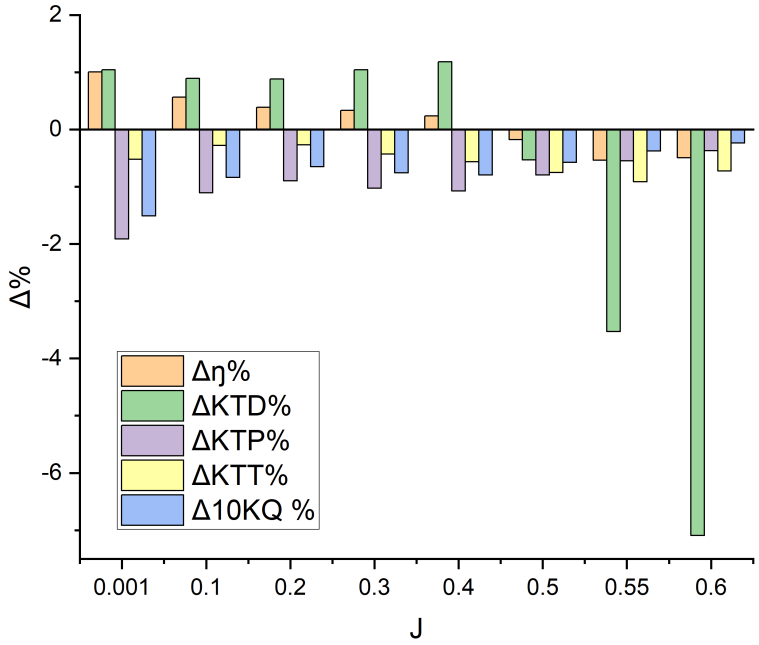

Figure 5.13: Change in performance when comparing SLE (5A_10F) to REF ducted propulsors

The propulsive efficiency, η, vs. total thrust coefficient, C_t, for both ducted propeller combinations can be compared in Figure 5.14. Although there is an improvement in K_{TD} at the heavier-loaded conditions, the resulting reduction in K_{TP} results in a lower K_{TT} at each J, but, as there is also a reduction in K_Q, the η is increased. Therefore, at the same η, the total thrust coefficient, C_t, is very similar.

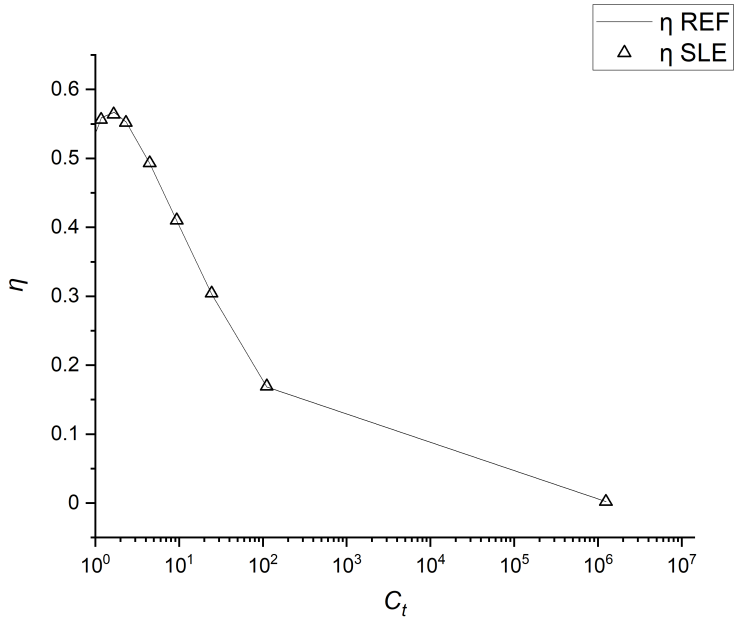

Figure 5.14: C_t vs η for REF and SLE (5A_10F) ducted propulsors

5.3.2 Propeller Inflow Characteristics

As was noted in the global hydrodynamic performance, the inclusion of the LE tubercles reduce the propeller performance characteristics K_{TP} and K_Q. Therefore, the inflow characteristics must be affected by the LE tubercles inside the duct. Figure 5.15 shows the inflow pressure, velocity and streamwise vorticity characteristics taken at $0.26L_{DUCT}$ at operating condition $J = 0.3$. As can be seen, although there is no appreciable difference in velocity or pressure distributions at this cross-section, the streamwise vortices produced by the tubercles can be observed.

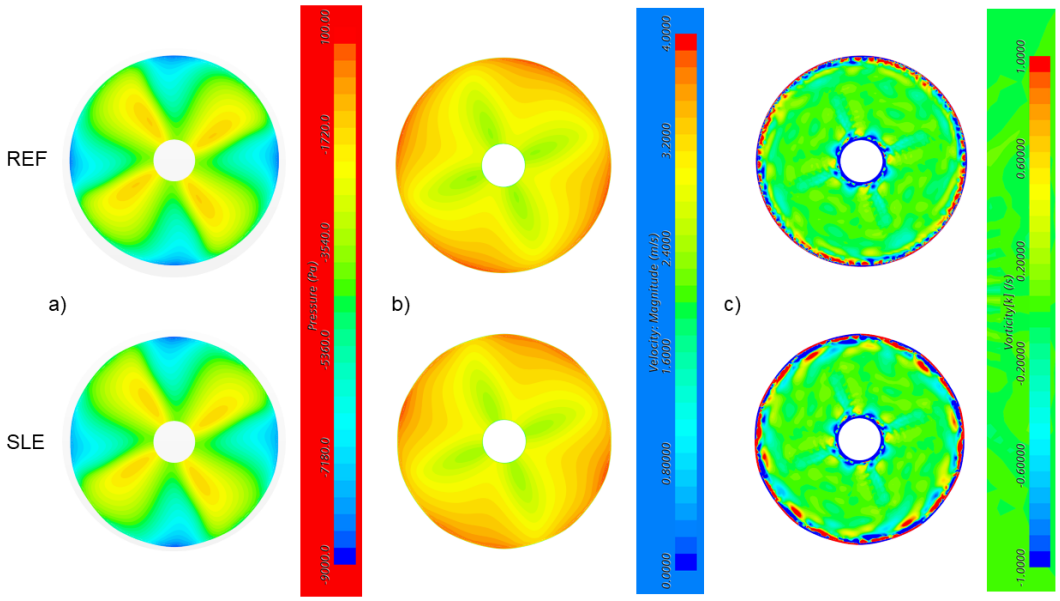

Figure 5.15: a) Inflow static pressure, b) velocity and c) streamwise vorticity distributions of REF and SLE ducted propeller combinations at $J = 0.3$

5.3.3 Pressure, Velocity and Vorticity Distributions

Figure 5.16 - Figure 5.7 show the surface pressure distributions of REF and SLE (5A_10F) duct for $J = 0.1$, 0.3 and 0.55 at both propeller suction and pressure sides, respectively. The inclusion of the physical propeller results in the tip leakage vortex to be predicted, which can be illustrated by the sharp pitching low pressure line around the mid-point of the duct and this effects the pressure distribution on the duct surface. This is the reason for the difference in performance results between the two methods as the BFP method simulates the propeller as a disk and thus, there are no blades within that computational environment.

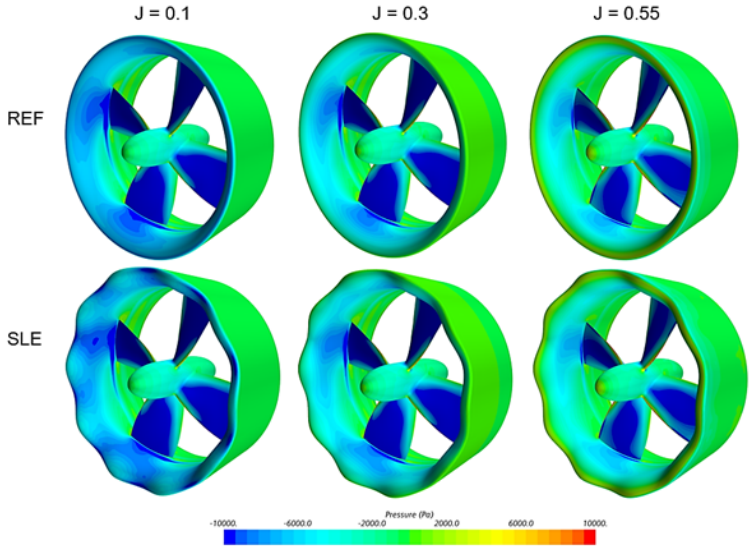

Figure 5.16: Surface static pressure distributions (propeller suction side) of REF and SLE ducted propellers at $J = 0.1$, 0.3 and 0.55

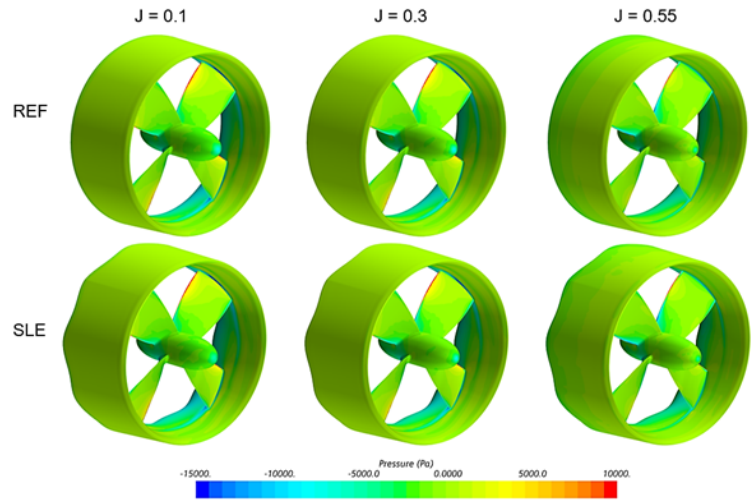

Figure 5.17: Surface static pressure distributions (propeller pressure side) of REF and SLE ducted propellers at $J = 0.1$, 0.3 and 0.55

Figure 5.18 shows the surface streamwise vorticity distributions of REF and SLE (5A_10F) duct for $J = 0.1$, 0.3 and 0.55. The results are in good agreement with the BFP method, where s similar streamwise vorticity can be shown for the

SLE (5A_10F) duct and a vortex pair can be shown on the outer side of $J = 0.55$. The tip leakage vortex can be observed for both configurations on the inner side of the duct at $0.5L_{DUCT}$.

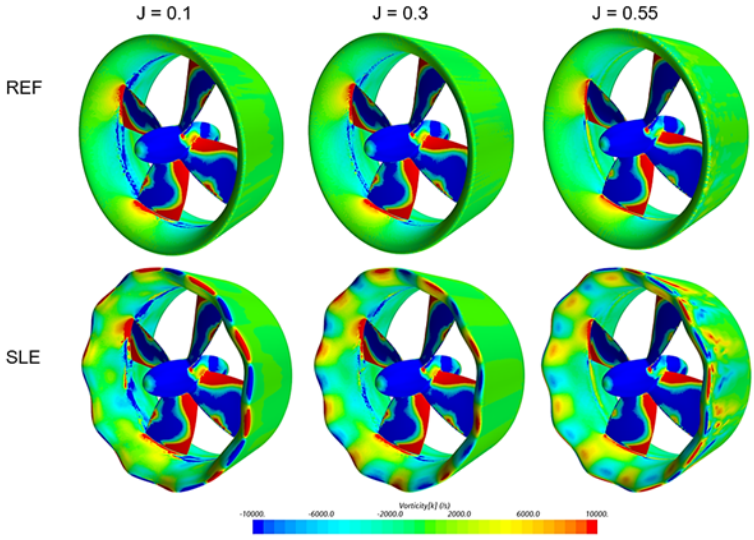

Figure 5.18: Surface streamwise vorticity distributions of REF and SLE (5A_10F) ducts at $J = 0.1$, 0.3 and 0.55

Figure 5.19 shows the velocity streamlines on the outer side of both REF and SLE duct. The white streamlines show streamwise velocity in the positive direction, from leading-edge to trailing-edge of the duct, and the black streamlines show streamwise velocity in the opposite direction. This shows that the flow-separation is more extensive behind the troughs of the SLE duct when compared to the REF duct which is the reason for the reduction in the thrust at the higher J's.

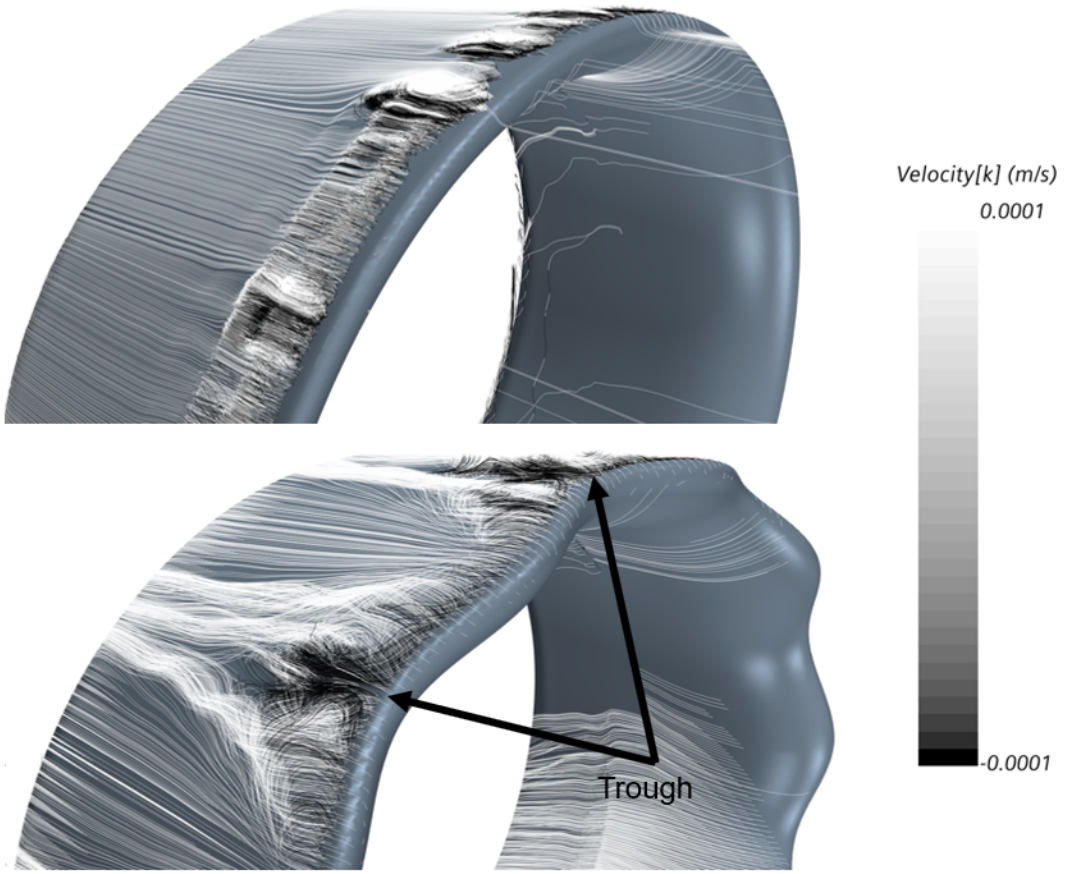

Figure 5.19: Velocity streamlines coloured by streamwise velocity on the outer duct surface at $J = 0.55$ for both REF (top) and SLE (bottom) ducts

5.4 Summary

This chapter presented the design and hydrodynamic performance optimisation study of LE tubercles applied to the duct of a ducted propeller using a RANS-based CFD approach. The two main tubercle parameters, which are the A and λ, were optimised for the hydrodynamic performance in terms of K_{TD}. Further analysis was conducted using propeller resolved modelling to understand the influence of the tubercles as applied to the duct on the holistic ducted propeller hydrodynamic performance. The results were discussed and the following con-

clusions were drawn:

Through completion of the optimisation process, it is evident that the optimum tubercle λ and A combination is application dependant as they affect the operating conditions studied differently. The LE tubercle configuration small A and larger λ configuration, $A = 0.04L_{DUCT}$ and $\lambda = 0.75L_{DUCT}$, provided the best compromise at the key operating conditions considered where K_{TD} was enhanced at the heavy-loaded conditions. It was noted that both A and λ had an impact on the K_{TD} at $J = 0.001$. As A was reduced and λ kept constant, an improvement in K_{TD} was predicted while increasing λ and maintaining A resulted in an improvement in K_{TD}. The change in A had a more significant impact on the K_{TD} than the change in λ. When comparing at the same thrust loading coefficient, C_t, there was minimal difference in η when comparing optimal tubercle ducted propeller configuration to the reference design using the blade-resolved method.

At $J = 0.55$, all tubercle models predicted a degradation in K_{TD} due to the influence on the flow-separation behaviour of the duct, but this needs to be further analysed using scale-resolved methods such as Detached Eddy Simulations (DES). This is because the suitability of RANS to accurately capture and predict the complex flow phenomena induced by tubercles and the resulting performance variables such as lift and drag, particularly in flow separation conditions (which occur above $J = 0.5$) have been questioned [122].

The observed streamwise counter-rotating vortices induced by the tubercle duct in the propeller inflow are believed to be a fundamental mechanism which could lead to the creation of additional instabilities within the tip-leakage vortex. This could lead to the acceleration of the vortex breakdwon in the propeller slipstream and thus, a reduction in URN. However, further analysis is necessary using more high-fidelity computational tools such as DES, as RANS cannot pre-

dict the instabilities within the propeller wake flow [100]. The further analysis mentioned above is presented in the following chapter, Chapter 6.

Chapter 6

Leading-Edge Tubercle Duct Hydrodynamic and Noise Performance Study

This chapter focuses on the influence of LE tubercle ducts on the non-cavitating URN signature of the ducted propulsor using a hybrid approach, whereby Detached Eddy Simulations (DES) are used to solve the hydrodynamic flow-field and the Ffowcs-Williams Hawkings (FW-H) acoustic analogy is used to propagate the noise into the far-field.

The first concept identified in which LE tubercles could mitigate URN within the literature review is investigated within this chapter; tubercles as applied to the duct to interact with the main tip-leakage vortex structure to encourage the vortex breakdown in the propeller slipstream and reduce the turbulent and vorticity-induced noise.

The test case geometry for the study are presented in Section 6.1. The results are presented and discussed in Section 6.2, with the overall summary in Section 6.3.

6.1 Test Case

The reference geometry 'REF' was selected the same as Chapter 5, the benchmark 19A ducted propeller and Kaplan series, KA4-55 propeller, detailed geometry can be found in Carlton [12]. The rendered geometry can be found in Figure 6.1a and the parameters in Table 3.1 in Chapter 3.

The tubercle duct was created as an idealised sinusoidal waveform with an amplitude of 5mm ($A/L_{DUCT} = 0.04$) and a tubercle count of 10 ($\lambda/L_{DUCT} = 0.75$), labelled as 'SLE' duct. The 3D design is shown in Figure 6.1b. The geometrical parameters of the tubercle were selected based on the optimisation study in Chapter 5 where several amplitude and wavelength configurations were investigated. It was noted that an increase in amplitude and reduction in wavelength degraded the hydrodynamic performance of the ducted propeller in the lower J range. However, the current design configuration produced an improvement in duct thrust capability at the heavy-loaded condition, while showing compartmentalisation of flow separation at the optimum operating point and was therefore selected for further analysis.

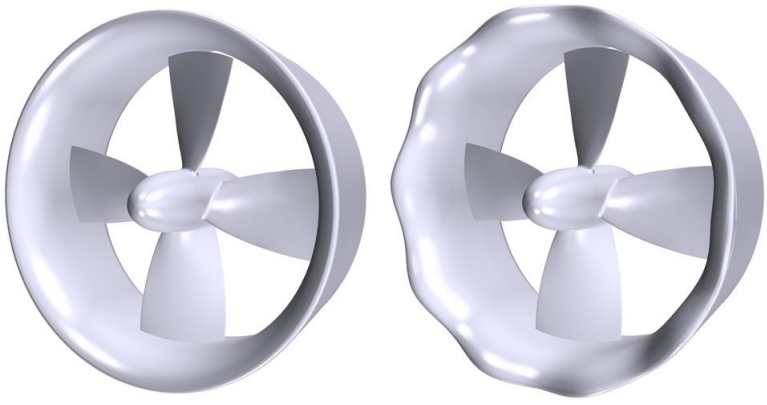

Figure 6.1: Geometry investigated within the LE tubercle duct-modified marine ducted thruster study, a) REF and b) SLE

6.2 Results

6.2.1 Time-Averaged Hydrodynamic Performance

Figure 6.2 shows the percentage difference ($\Delta\%$) of key time-averaged hydrodynamic global performance coefficients for the SLE ducted propeller combination when compared to REF at a range of operating conditions. As can be seen, the duct performance can be enhanced by a maximum of 7.15% at the maximum operating efficiency, increasing the optimum efficiency by roughly 0.55%. It appears that at $J = 0.5$ and 0.6, there is performance degradation due to the inclusion of tubercles. This is due to earlier-inception of flow separation occurring in the troughs on the duct outer side at $J = 0.5$, and the geometrical configuration of tubercles not being prominent enough to manipulate the flow at $J = 0.6$ which will be explained with further analysis. Nonetheless, in between these flow separation conditions, the tubercles can enhance the performance of the duct. Additionally, the LE tubercles result in a reduction of propeller thrust and torque. Therefore, the LE tubercles must influence the inflow characteristics of the propeller.

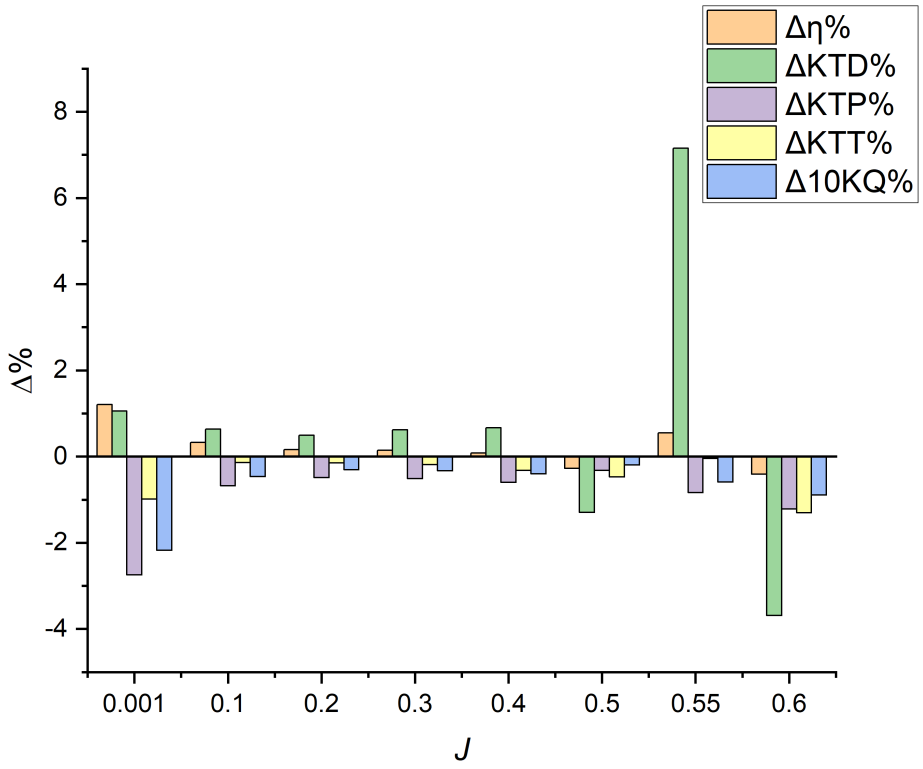

Figure 6.2: Open-water performance variable change when compared SLE to REF ducted propeller

The results using DES compares well to previous performance comparisons using a RANS-based solver (see Figure 5.13). However, in the flow-separation conditions, there is a slight discrepancy where DES predicts an improvement in duct performance in mild flow-separation conditions on the outer side of the duct at $J = 0.55$, whereas RANS predicts a performance degradation for all conditions where flow-separation occurs ($J \geq 0.5$). The ability of RANS to accurately predict key performance variables in flow-separation conditions is a well known challenge within the CFD community [101], and has been previously questioned in the accurate prediction of the performance of tubercle modified foils [122]. The findings above align with other researchers hesitations regarding RANS-based solvers for

accurate performance prediction in flow-separation conditions and highlights the necessity for experimental validation on this matter.

6.2.2 Transient Blade Thrust Analysis

Figure 6.3 and 6.4 shows the comparison of blade thrust for REF and SLE ducted propeller combinations at $J = 0.1$, 0.3 and 0.55 in time and frequency domains, respectively . Figure 6.3 shows that the peak-to-peak value of blade thrust variation for the SLE can be seen to be larger when compared to REF for all operating conditions. Figure 6.4 illustrates the distinct peaks observed at the 1^{st} BPF ($60s^{-1}$) and two sub-harmonics 15 and $30s^{-1}$ for both ducted propeller combinations. However, a distinct peak can also be observed at $150s^{-1}$ for the SLE duct, this is due to the stream-wise vortex pairs induced by the 10 evenly distributed tubercles along the duct LE and can be described as the tubercle passage frequency (TPF) which is the product of the number of tubercles, 10, and the propeller rotation rate, 15rps. This peak is more dominant than the 1^{st} BPF at $J = 0.1$. Therefore, the interaction between the blade and the induced stream-wise vortices will contribute to the predicted reduction in time-averaged propeller thrust at all operating conditions considered. This was previously stipulated in Chapter 5 from propeller inflow characteristics shown in Figure 5.15.

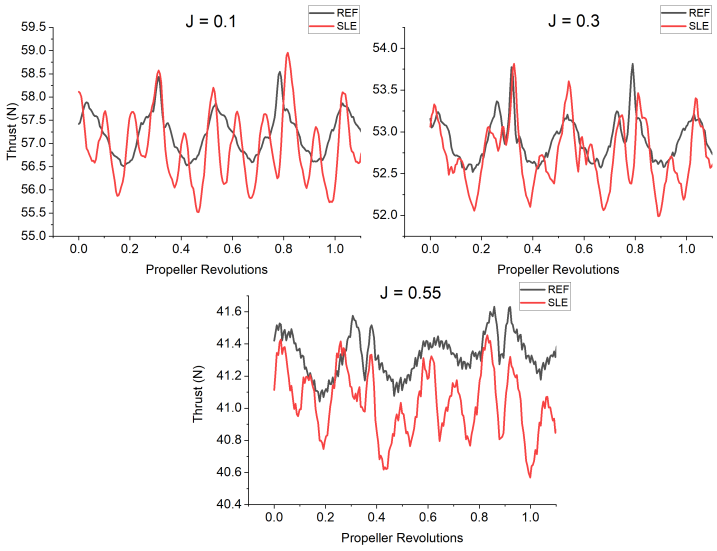

Figure 6.3: Comparison of single-blade thrust over one propeller revolution at J = 0.1, 0.3 and 0.55

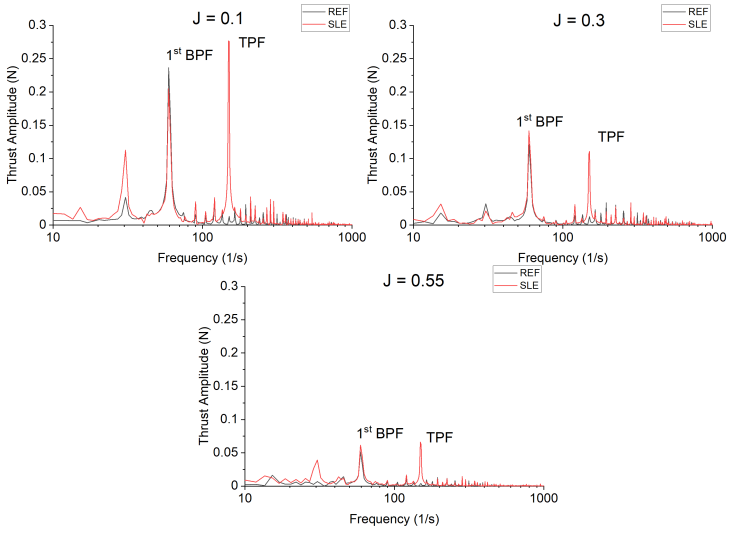

Figure 6.4: Comparison of single-blade thrust in the frequency domain at J = 0.1, 0.3 and 0.55

6.2.3 Pressure and Velocity Distributions

The distribution of pressure on the SLE and REF duct surface (inner side) at $J = 0.1$, 0.3 and 0.55 can be shown in Figure 6.5. On the suction side of the blade tip a low-pressure area can be observed which is caused by a vortex that is formed by the rotation of the blade close to the duct wall and is known as a tip-leakage vortex. This type of vortex has a pitch that is considerably lower than the pitch of the blade. The high-low pressure pattern created by the inclusion of the tubercles at the leading-edge can be seen more prominently at the heavier-loaded condition, $J = 0.1$. At this condition, the duct experiences a high negative angle of attack with respect to the incoming flow. Downstream of the blade, a pressure trail can be shown in all configurations which can be described as the development of the tip-leakage vortex into the propeller slipstream. The inclusion of the LE tubercles can be seen to disrupt this vortex, creating fluctuations in the pressure trail, particularly at the lower J ratio.

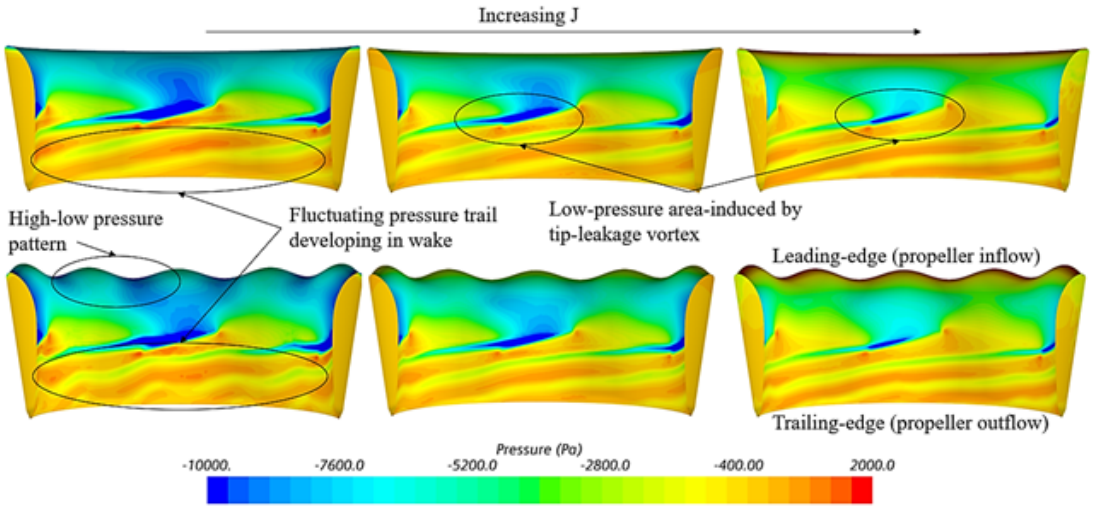

Figure 6.5: Surface static pressure distributions (inner side) of REF and SLE duct at $J = 0.1$ (left), 0.3 (middle) and 0.55 (right)

Figure 6.6 displays velocity streamlines on the outer duct sections of REF and

SLE ducts. At $J = 0.5$, the flow separation is initiated earlier behind the troughs of the tubercle than compared to REF duct. This results in an increase in drag which would correspond to the degradation in duct thrust performance at this condition. At $J = 0.55$, the isolation of flow separation can be shown behind the troughs, with flow attachment behind the peaks, compared to spanwise flow separation of the REF duct, this corresponds to a 7.15% improvement in duct thrust at this condition. At $J = 0.6$, the SLE duct does not appear to be able to manipulate the flow at this condition, showing flow separation behind the peaks and troughs, this is likely due to the geometrical configuration of the tubercle not being prominent enough to control. The flow separation occurs over a larger surface area for the SLE duct and this, in addition to the added frictional drag caused by the increase in surface area from the inclusion of the LE tubercle geometry, results in duct thrust degradation when compared to the REF duct at $J = 0.6$.

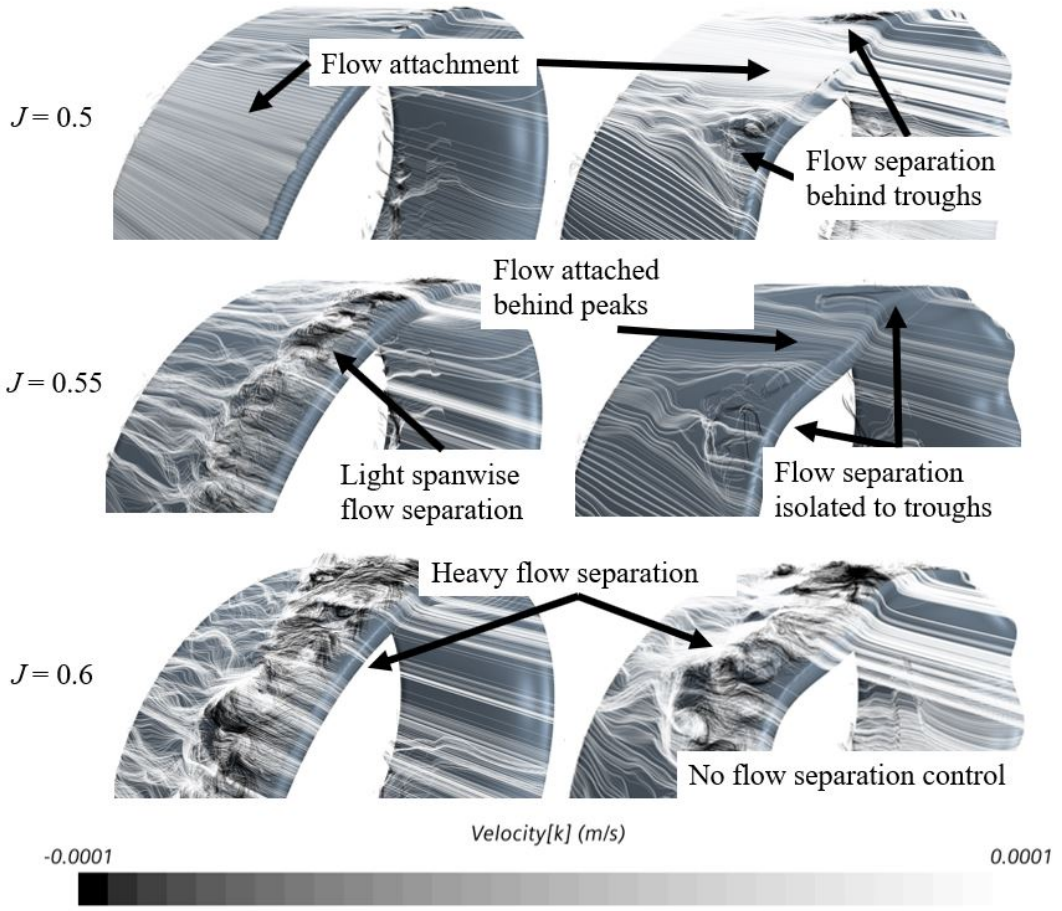

Figure 6.6: Velocity streamlines coloured by streamwise velocity on outer duct section at $J = 0.5$, 0.55 and 0.6 respectively, for both REF (left) and SLE (right) ducts

6.2.4 Vortex Wake Dynamics

Turbulent Kinetic Energy (TKE) surface integrals for 7 cross-sections downstream of the ducted propeller, normalized by L_{DUCT}, for both REF and SLE were computed. Comparing the SLE to the REF duct, there was a reduction in TKE at the further downstream sections for all operating conditions considered as shown in Figure 6.7. Figure 6.7 shows the percentage reduction of computed surface

integral TKE at several plane sections for the 3 operating conditions considered, where the positive y-axis denotes a reduction in TKE by the SLE design. The SLE duct initially increases the TKE in the propeller wake but dissipates quicker than the REF duct for all operating conditions further downstream. A maximum of 16% reduction in TKE is observed at $J = 0.1$. The initial increase in TKE is due to the introduction of additional vortex structures (the streamwise counter-rotating vortex structures) into the propeller inflow by the LE tubercle geometry, the increased dissipation downstream is largely due to the interaction of said additional vortex structures with the main helical tip-leakage vortex structure in the slipstream and marginal reduction in propeller loading by SLE design at the same operating condition, this understanding was achieved through further analysis below of the Q-criterion surfaces in the slipstream. Q-criterion defines vortices as areas where the vorticity magnitude is greater than the magnitude of the rate of strain, $\frac{1}{2}(||\Omega||^2 - ||S||^2)$ where Ω is the vorticity tensor and S is the strain rate tensor [123].

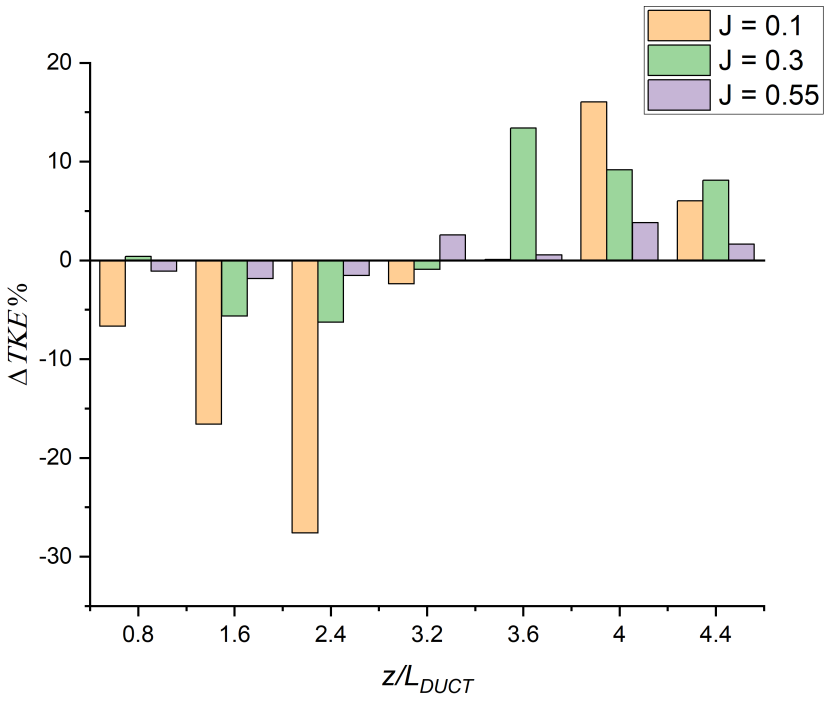

Figure 6.7: TKE reduction (denoted as positive y-axis) of SLE duct compared to REF at several plane sections in the propeller slipstream for $J = 0.1$, 0.3 and 0.55, respectively.

Figure 6.8 shows the instantaneous half-section Q-criterion plots of the propeller wake coloured by TKE at $J = 0.1$, 0.3 and 0.55 for the REF and SLE ducted propeller combinations. The helical vortex structure known as the tip-leakage vortex created by the rotation of the propeller and interaction with the duct wall, blade trailing edge vortex, hub vortex and "leapfrogging" vortex phenomenon can be observed and are highlighted - previously explained in Chapter 2 using Figure 2.14. The short-wave instability within the helical vortex structure and the secondary vortex system that wraps around the helix can also be shown and highlighted. At the operating condition where the blade loading is the highest, the tip-leakage vortex breaks down at a shorter distance from the duct exit downstream when compared to the lower blade loading ($J = 0.55$) where the

delayed breakdown in the tip-leakage vortex structure can be shown. In addition, at $J = 0.1$, the earlier breakdown of the vortex structure leads to a larger distribution of TKE further downstream. The primary mechanism for the breakdown of the tip-leakage vortex is the short-wave instability, followed by the secondary vortex system, similarly observed by Zhang and Jaiman [16].

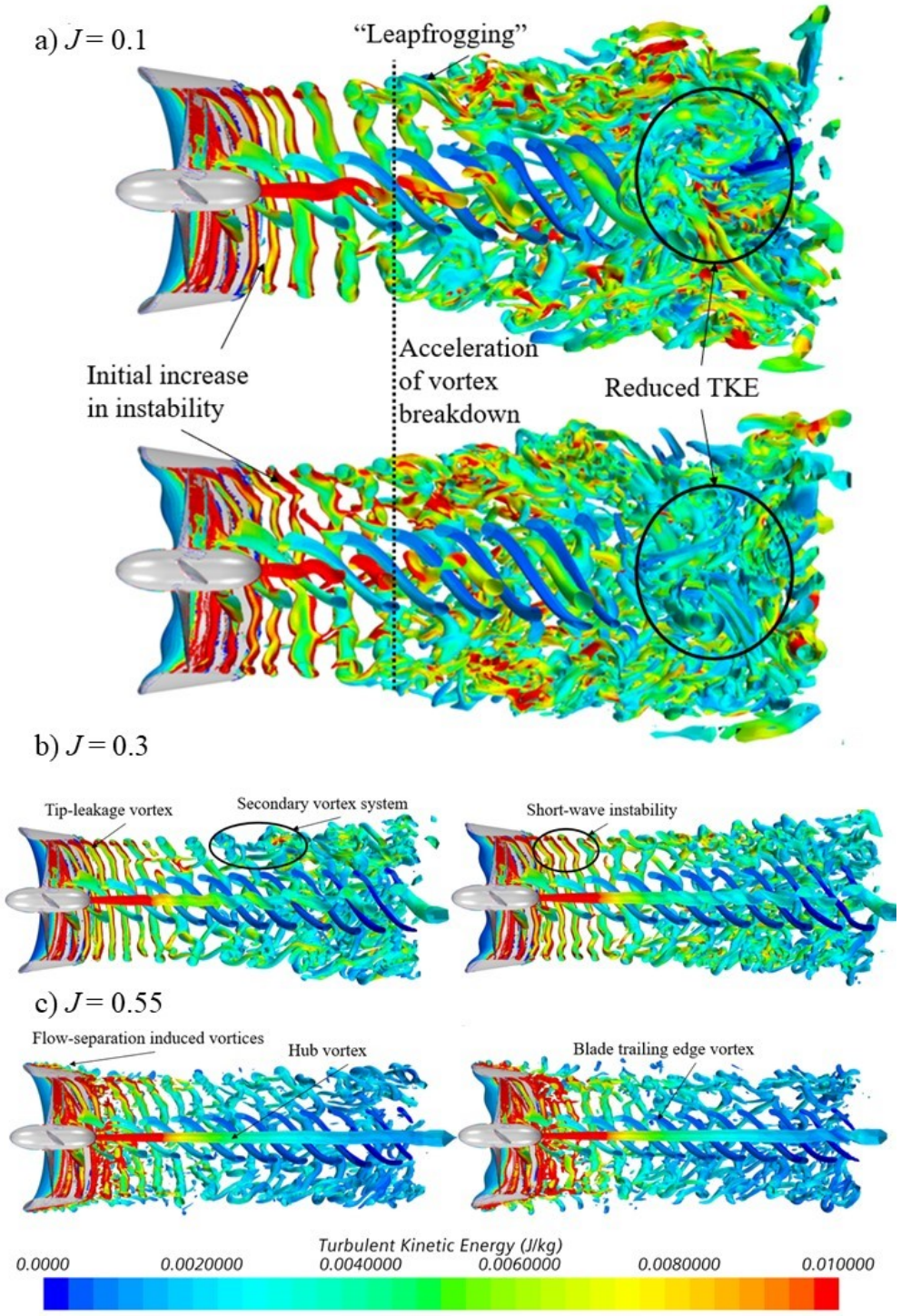

Figure 6.8: Q-criterion plots, $\alpha = 1000/s^2$ (coloured by TKE) of REF and SLE ducts at $J = 0.1$, 0.3 and 0.55

As can be seen, the SLE duct influences the wake dynamics of the ducted propeller when compared to the REF. Immediately at the exit of the ducted propeller, the inclusion of the LE tubercles appear to create additionally instability within the helical tip-leakage vortex structure, particularly at $J = 0.1$ (see Figure 6.8a). This leads to an acceleration in the vortex breakdown into large-scale flow structures and turbulence. At $J = 0.55$, the flow-separation induced vortex structure can be observed over the outer side of the duct.

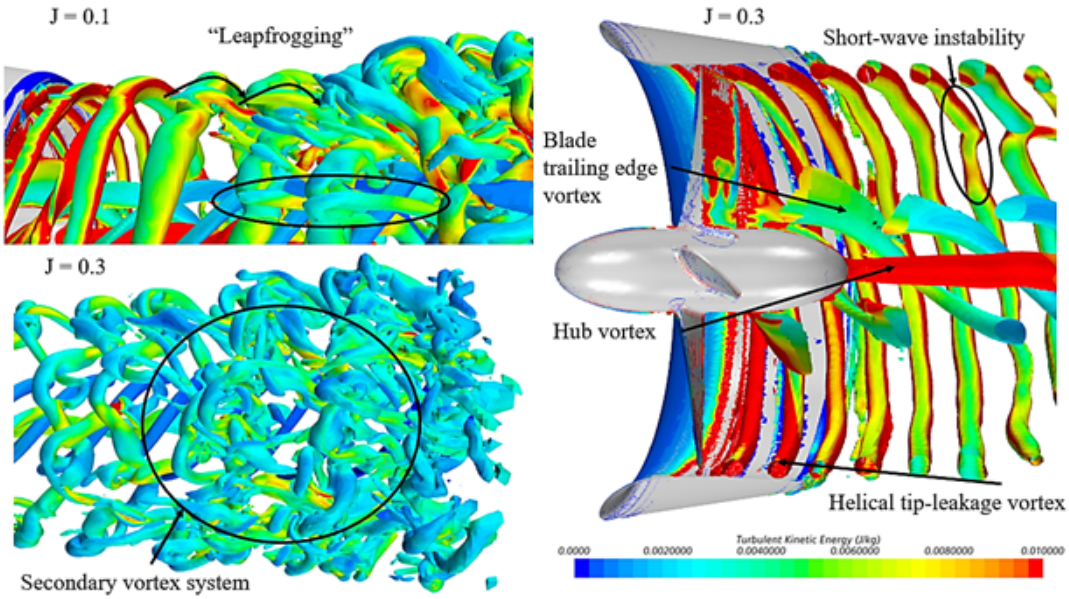

Figure 6.9: Close-up Q-criterion plots, $\alpha = 1000/s^2$ (coloured by TKE) of REF to illustrate fundamental wake vortex dynamics

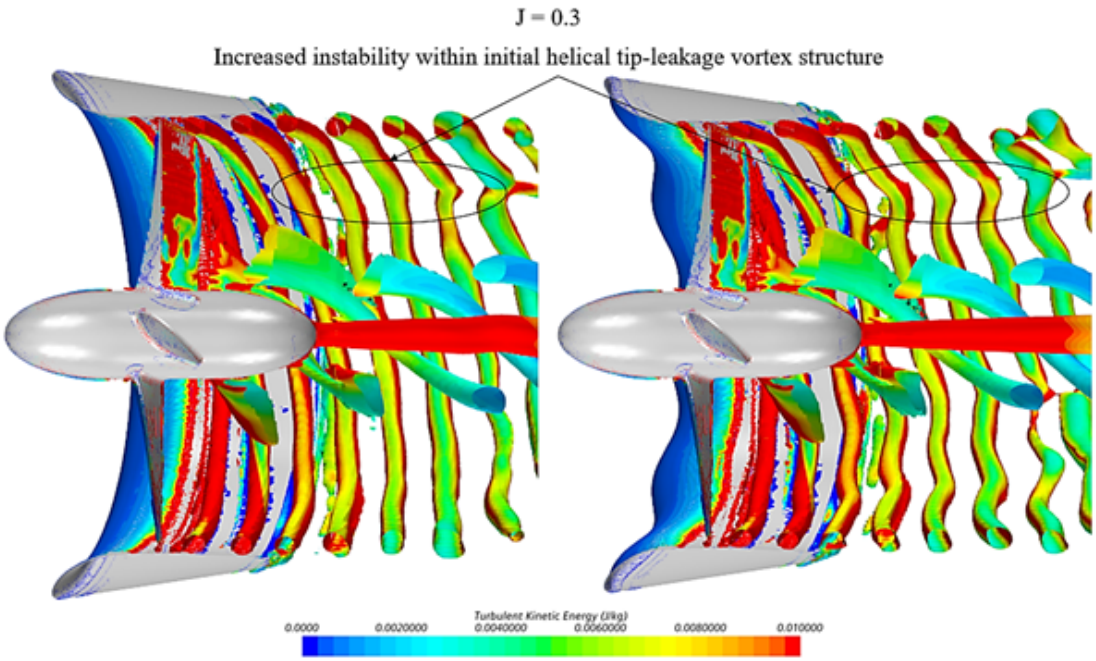

Figure 6.10: Close-up Q-criterion plots, $\alpha = 1000/s^2$ (coloured by TKE) of REF and SLE to illustrate influence of LE tubercles on the helical-tip leakage vortex structure

The fundamental mechanisms of the wake dynamics of the REF ducted propeller can be shown clearly in the zoomed in isometric views depicted in Figure 6.9. Figure 6.10 shows the close-up views of the influence of the LE tubercles on the short-wave instability within the initial tip-leakage vortex structure. Figure 6.11 shows the classic tubercle effect, where flow separation occurs on the outer side of the ducted propeller at $J = 0.55$, the flow separation can be compartmentalised by encouraging the flow separation to behind the trough region and maintaining a flow separation free zone behind the peak.

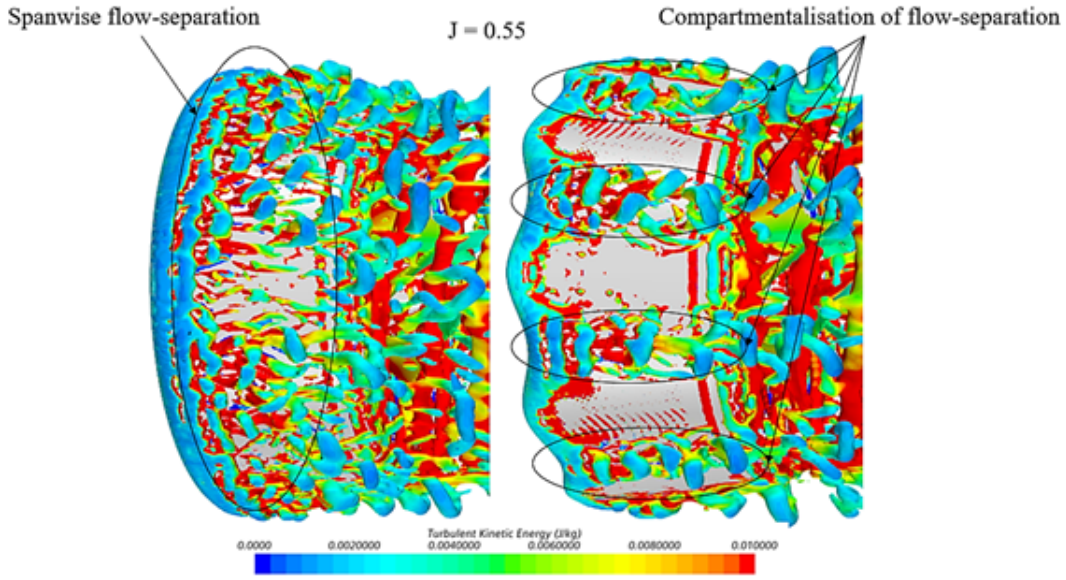

Figure 6.11: Close-up Q-criterion plots, $\alpha = 1000/s^2$ (coloured by TKE) of REF and SLE to illustrate influence of LE tubercles on the flow-separation induced vorticity

6.2.5 Noise Performance

6.2.5.1 Near-Field Noise

Figure 6.12 shows the narrowband SPL spectrum for the REF and SLE ducted propeller combinations at the near-field receiver located in the radial position with respect to the propeller plane (M0) and furthest downstream receiver (M4) at $J = 0.1$, 0.3 and 0.55. At all operating points at M0, the 1^{st} and 2^{nd} BPF's can be clearly observed by the distinct tonal peaks at 60 and $120s^{-1}$ (note: BPF = rotation rate (rps) x blade number). In the heavier-loaded conditions at receiver M4, the BPF's, although distinguishable, are not as prominent when comparing to the narrowband spectrum at M0. Although this is the case, the 1^{st} and 2^{nd} BPF can still be observed at all operating conditions, although they are not as distinct especially in the heavier-loaded conditions when compared to spectra at M0.

This is due to the role of turbulence and vorticity-induced noise, which is more significant at receivers located downstream of the propeller plane than from the radial position (M0) due to being in the vicinity of the propeller slipstream which is where the majority of the turbulent and vorticity-induced noise is generated from.

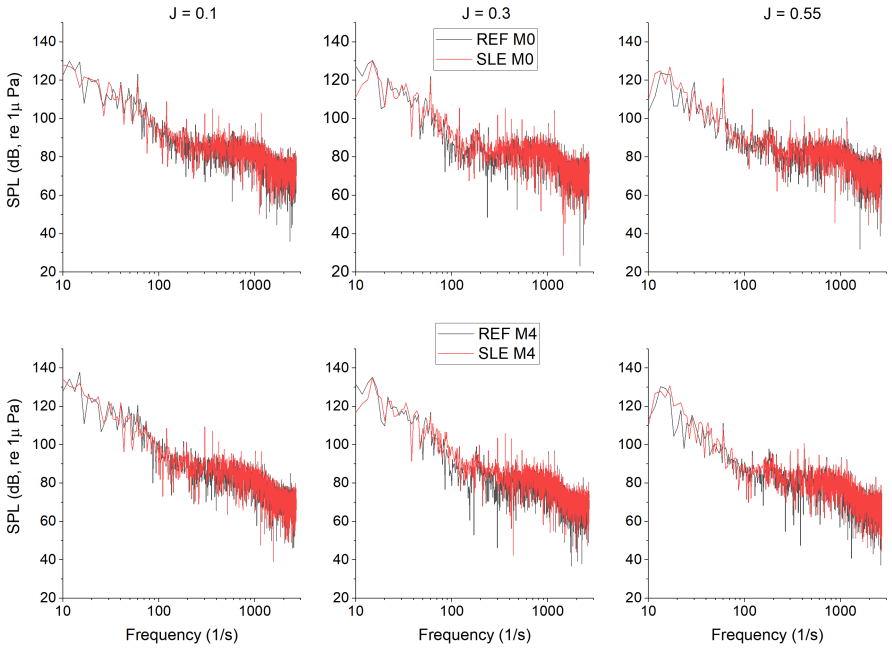

Figure 6.12: Narrowband plot at M0 (top) and M4 (bottom) for REF and SLE combinations at $J = 0.1$ (left). $J = 0.3$ (middle) and $J = 0.55$ (right)

Figure 6.13 shows the 3^{rd} octave band sound spectrum for the REF and SLE ducted propeller combinations at the near-field receiver located in the radial position with respect to the propeller plane (M0) and furthest downstream receiver (M4) at $J = 0.1$, 0.3 and 0.55. In the low frequency range at the M4 receiver at $J = 0.1$, a distinct reduction in noise, approximately 3dB can be shown which correlates well with the acceleration in the vortex breakdown observed at this

operating condition (see Figure 6.8) which will reduce the the turbulent and vorticity-induced noise contribution to the overall noise signature.

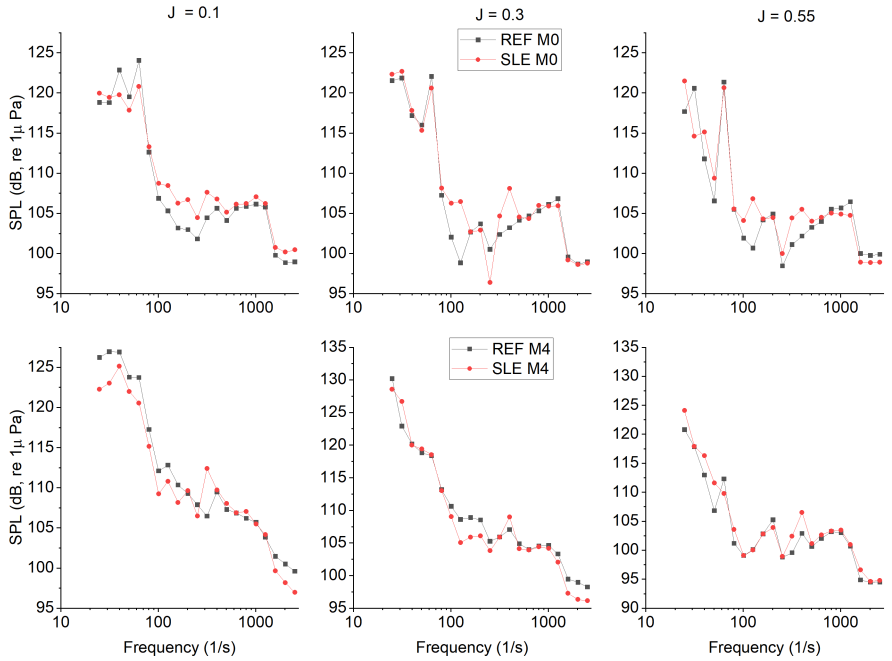

Figure 6.13: 3^{rd} octave band plots at M0 (top) and M4 (bottom) for REF and SLE combinations at $J = 0.1$ (left). $J = 0.3$ (middle) and $J = 0.55$ (right)

6.2.5.2 Far-Field Noise

Figure 6.14 shows the narrowband and 3^{rd} Octave Band plots for REF and SLE ducts at the radial plane ($100D$) at operating conditions, $J = 0.1$, 0.3 and 0.55, respectively. As can be shown, the SLE duct can reduce the noise at all operating conditions when compared to the REF ducted propeller combination. The change in SPL in the 3^{rd} octave band can be shown for the same receiver at the same operating conditions in Figure 6.15. The maximum level of reduction at certain frequency ranges is 3.5dB, 4dB and 11dB at $J = 0.1$, 0.3 and 0.55 respectively.

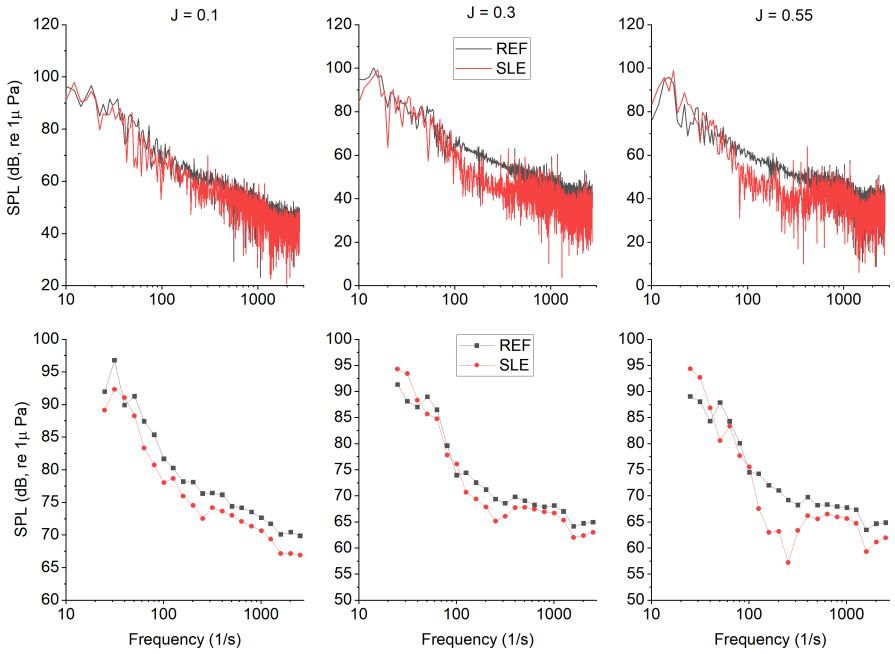

Figure 6.14: Narrowband plots and 3^{rd} octave band plots for REF and SLE ducts at radial plane (90^o, $100D$), $J = 0.1$ (left), $J = 0.3$ (middle) and $J = 0.55$ (right)

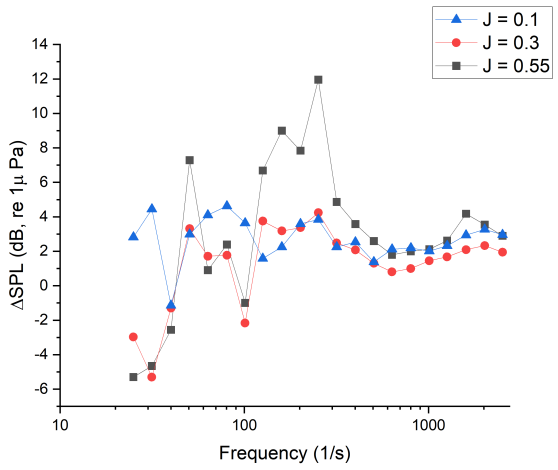

Figure 6.15: ΔSPL of 3^{rd} octave band plots for SLE compared to REF duct at radial plane (90^o, $100D$) where positive y-axis denotes noise reduction.

Figure 6.16 shows the OASPL directivity plots for REF and SLE ducted propeller combinations. As can be seen, the SLE duct can reduce the OASPL by a maximum of 3.4dB at $J = 0.1$, where there is negligible difference at $J = 0.3$ and an approximate 3dB increase at $J = 0.55$. The increase in OASPL at the higher J number is likely due to the increase in noise in the low-frequency range (0-100s^{-1}) which is where the highest levels of SPL occur in the spectrum and thus, has the largest weighting when calculating the OASPL and the difference between the two ducted propulsors.

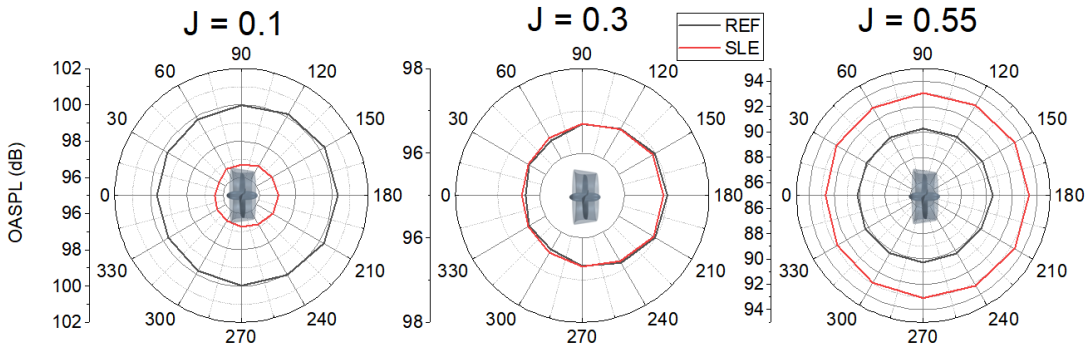

Figure 6.16: OASPL directivity plots (in degrees) for REF and SLE ducts at $J = 0.1$ (left), $J = 0.3$ (middle) and $J = 0.55$ (right)

6.3 Summary

This chapter has shown the influence of LE tubercles applied to the duct of a model scale ducted propeller on the hydrodynamic and hydroacoustic performance of the propulsor with detailed flow analysis of the vortex dynamics of the ducted propeller slipstream using the IDDES method to solve the hydrodynamic flow-field and the FW-H acoustic analogy to propagate the noise to the far-field. A summary of the findings can be found below:

The inclusion of LE tubercles on the duct improved the maximum duct thrust

capability at most operating conditions considered to a maximum of 7.15% at the maximum efficiency point, $J = 0.55$. At this condition, the improvement was believed to be due to the compartmentalisation of flow separation observed on the outer side of the duct. At all operating conditions, the inclusion of the SLE duct results in an increase in turbulent kinetic energy initially within the slipstream due to the introduction of additional vortex structures into the inflow, but then this reduces further downstream at all operating conditions analysed to a maximum reduction of 16% at $J = 0.1$.

At $J = 0.1$ the OASPL was reduced with the inclusion of the SLE duct, where a maximum reduction of 3.4dB was predicted at $J = 0.1$ and in some frequency ranges in other operating conditions, a maximum of 11dB reduction was observed. This is largely due to the disruption of the ducted propeller wake structure which will affect the turbulence and vorticity-induced noise in the far-field.

6. LEADING-EDGE TUBERCLE DUCT HYDRODYNAMIC AND NOISE PERFORMANCE STUDY

Chapter 7

Leading-Edge Tubercle Ducted Propeller Blade Application Hydrodynamic and Noise Performance Study

This chapter focuses on the influence of the LE tubercle modified ducted propulsor blades on the URN signature of the ducted propulsor using a hybrid approach, whereby Detached Eddy Simulations (DES) are used to solve the hydrodynamic flow-field, the cavitation is modelled using the Schnerr-Sauer cavitation model and the Ffowcs-Williams Hawkings (FW-H) acoustic analogy is used to propagate the noise into the far-field.

The second concept identified in which LE tubercles could mitigate URN within the literature review is investigated within this chapter; tubercles applied to blades to reduce cavitation and thus, mitigate cavitation-induced URN.

The test case geometry for the study is presented in Section 7.1, while the results are presented and discussed in Section 7.2, with the overall summary

provided in Section 7.3.

7.1 Test Case

The reference geometry 'REF' was selected as the benchmark 19A ducted propeller and Kaplan series KA4-55 propeller. Detailed reference geometry can be found in Carlton [12]. The rendered geometry can be found in Figure 7.1 and the parameters in Table 3.1 in Chapter 5.

Two tubercle (TUB) blade designs were considered. The pitch and chord length distributions were kept the same as the reference blade, where the height (H), peak to trough, of the leading-edge tubercles was fixed at $0.1c$ (c: local chord length) for both designs as the initial designs, while the wavelength, λ, was varied ($0.5c$ and $0.9c$). The tubercle parameters were roughly based on the previous optimisation study in Chapter 5 and on a 2D tidal turbine-based hydrofoil study [83] as an initial design. They can be shown in Figure 7.1.

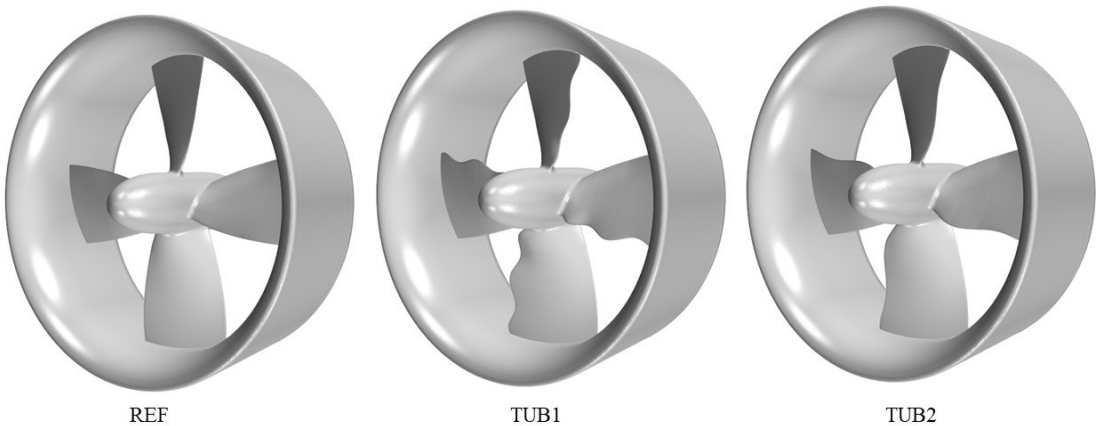

Figure 7.1: Geometry investigated within the LE tubercle blade modification study, REF, TUB1 and TUB2

7.2 Results

7.2.1 Non-Cavitating Hydrodynamic Analysis

7.2.1.1 Global Hydrodynamic Performance

The open-water curve characteristics over a range of advance ratios for all propeller designs were first determined to assess the influence of the varying tubercle geometrical configurations in non-cavitating conditions. The percentage change, $\Delta\%$, in time-averaged key variables, thrust, torque and efficiency for all tubercle models compared to the baseline design can be shown in Figure 7.2. A general trend can be observed, showing all tubercle designs increase the propeller thrust coefficients. Due to this increase in blade loading, an improvement in duct thrust is observed, which increases with increasing J to a maximum of roughly 6% by TUB1 and 4.5% by TUB2 at J = 0.55. Because of this, an increase in total thrust coefficient is observed at all advance ratios, to a maximum of roughly 2% by TUB1 and 1.64% by TUB2 at J = 0.55. At all advance ratios considered, the torque coefficient is increased also by the inclusion of LE tubercles, which ultimately results in a reduction in propulsive efficiency by a maximum of 0.63% and 0.51% by TUB1 and TUB2 at $J = 0.1$, respectively. The shorter wavelength tubercle propeller design (TUB1) has a more severe impact on the torque and thus, propulsive efficiency in the condition where the blade loading is the highest. Therefore, for this propeller design, the inclusion of LE tubercles results in an increase in total thrust and torque, but reduction in propulsive efficiency at all operating advanced ratios investigated in this present study when operating in non-cavitating conditions. The general findings agree well with previous research conducted on open propellers in non-cavitating conditions, where although thrust improved, the torque also increased which resulted in a net reduction in propulsive efficiency at the same J [60].

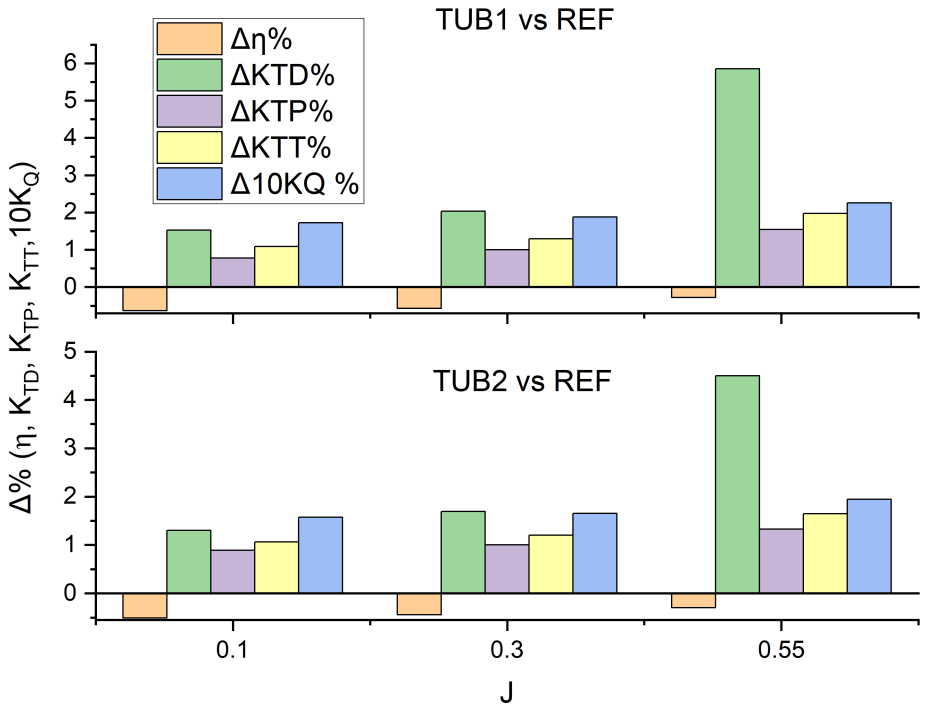

Figure 7.2: $\Delta\%$ in open-water key performance variables of tubercle propeller models when compared to the reference design

However, the question arises, whether the tubercles have compromised the efficiency of the thruster or the tubercles have just shifted the thrusters' operational point. In order to compare the efficiency of the different designs, the results have been further analysed by comparing at the same thrust loading coefficients C_t, which is the key parameter indicating the thruster operating condition: a given size thruster provides thrust for a vehicle at a specified velocity. The comparison is made using linear interpolation between neighbouring points to extract the results at the same C_t and the raw data and interpolation points (shown in the dashed lines) are presented in Figure 7.2a and 7.2b. The efficiency can be seen to be improved for both tubercle propeller designs in the heavy-loading conditions whereas there is a minimal compromise in the lightly-loaded conditions. The

maximum efficiency improvement of TUB1 and TUB2 propeller designs are 0.93 and 1.03% respectively (see Figure 7.2c). Therefore, the tubercle modifications have shifted the propulsor operational curve with respect to the J number instead of compromising the propulsor's efficiency (see Figure 7.2d).

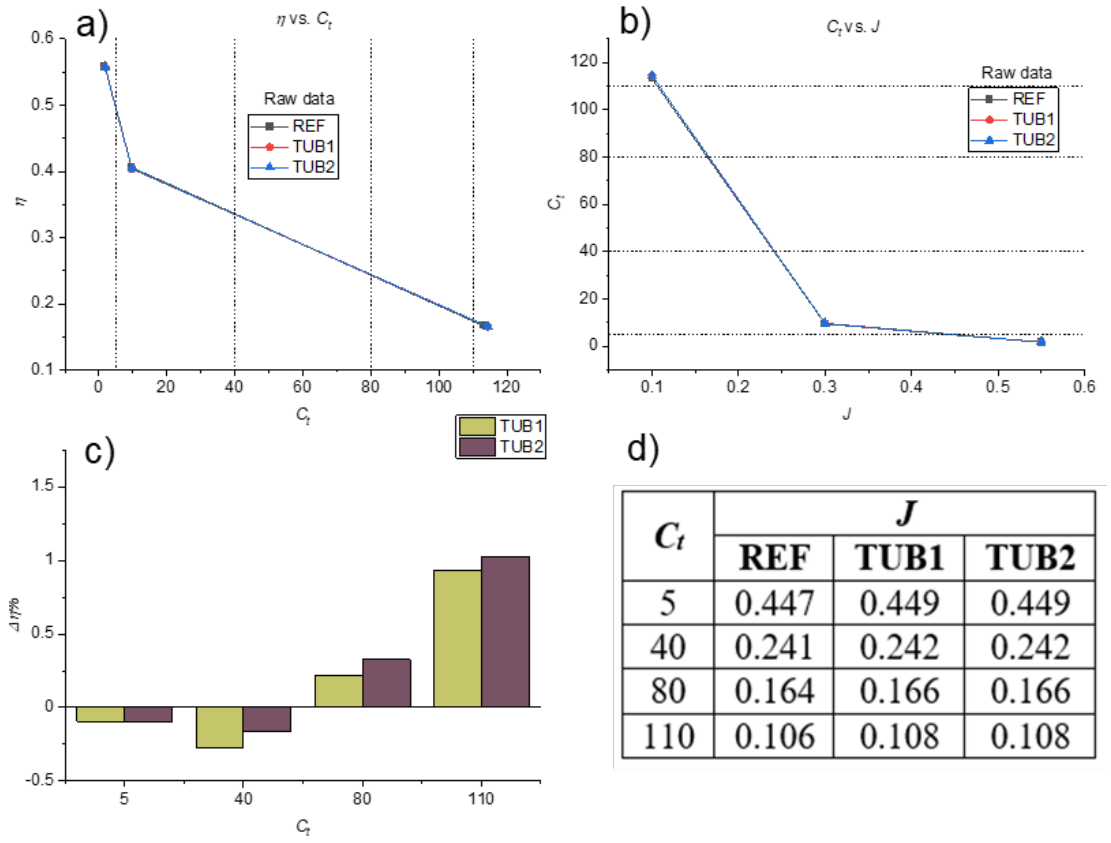

C_t	J		
	REF	TUB1	TUB2
5	0.447	0.449	0.449
40	0.241	0.242	0.242
80	0.164	0.166	0.166
110	0.106	0.108	0.108

Figure 7.3: a) raw data of η vs. C_t and interpolation points b) raw data C_t vs. J and interpolation points c) Percentage improvement in propulsive efficiency when comparing at the same C_t for tubercle propellers compared to REF, d) J number at each C_t considered within the interpolation in non-cavitating conditions

7.2.1.2 Blade Surface Pressure and Vorticity Distributions

Figure 7.4 shows the pressure distributions on the suction side of different blade designs at all advance ratios. Comparing the different propeller models, this low-

pressure strip can be seen to be redistributed in the presence of LE tubercles, concentrating the low pressure zone of the leading-edge into the trough region (shown in dark blue) and creating a higher pressure region at the leading-edge peak located at the blade tip, although less distinct for TUB2 due to the steepness of the tubercle, and is highlighted in Figure 7.4.

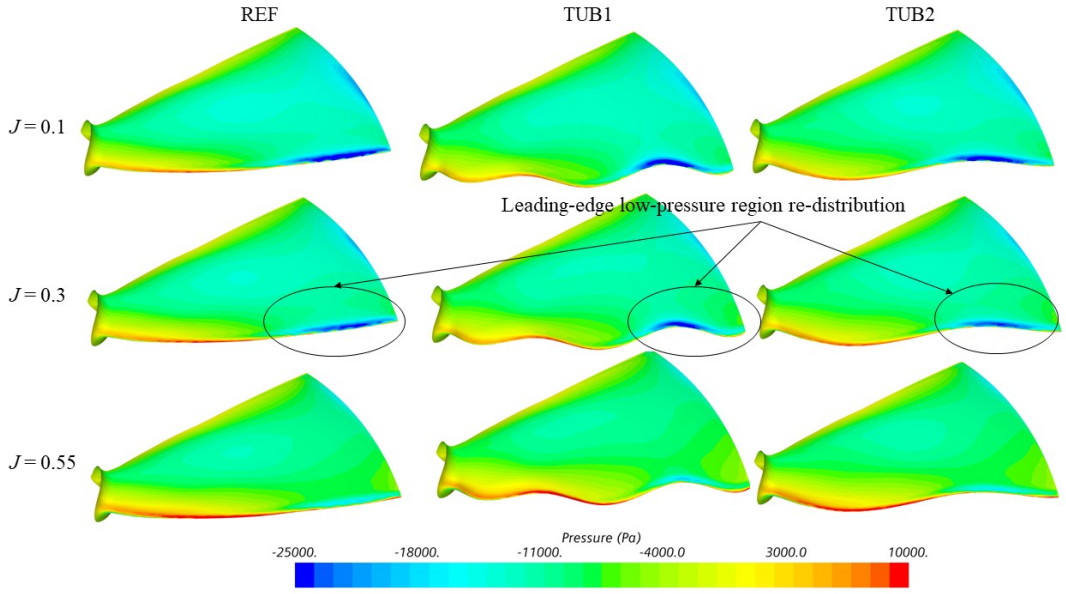

Figure 7.4: Surface static pressure distributions of a single blade, suction side, from REF, TUB1 and TUB2 at $J = 0.1$, 0.3 and 0.55

Figure 7.5 shows the streamwise vorticity along the blade surface for all designs at all advance ratios considered, respectively. The counter-rotating streamwise vortices can be seen, although they are very subtle. The counter-rotating vortex pair of TUB1 closest to the blade root is the most distinct, where TUB2's is not. Most likely this is due to the steepness of tubercle, blade cross-section and the trough's proximity to the blade tip.

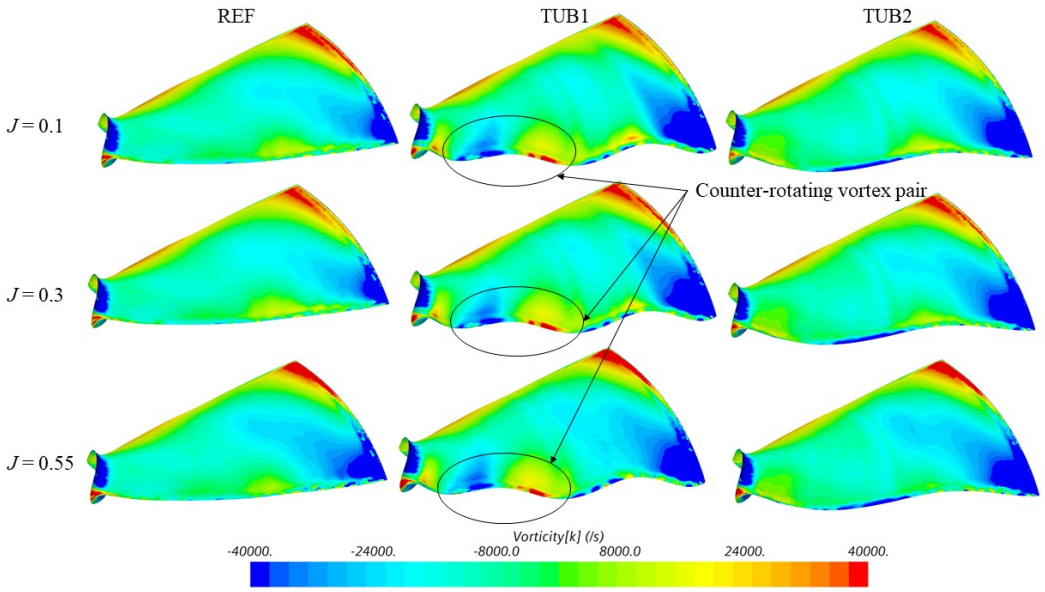

Figure 7.5: Surface streamwise vorticity distributions of a single blade, pressure side, from REF, TUB1 and TUB2 at at $J = 0.1$, 0.3 and 0.55

7.2.1.3 Vortex Development

Figure 7.6 shows a mid-section Q-criterion iso-surface ($\alpha = 1000/s^2$) coloured with turbulent kinetic energy (TKE) for all ducted propeller designs at $J = 0.1$, 0.3 and 0.55. The figure depicts the vortex development around the ducted propulsors with different design with various operating conditions. Between the conditions, differences can be observed at $J = 0.55$ when compared to the other operating conditions as the vortex shedding from the flow separation on the outer side of the duct has been introduced. Meanwhile, the breakdown in the vortex structure appears to be accelerated by the tubercle blade design due to the introduction of the streamwise counter-rotating vortices. A zoom-in figure, Figure 7.7 illustrates this phenomenon, whereby the helical tip-leakage vortex structure generated by the TUB designs tend to intertwine within themselves at a shorter distance from the duct exit causing quicker decay of the vortex system and energy.

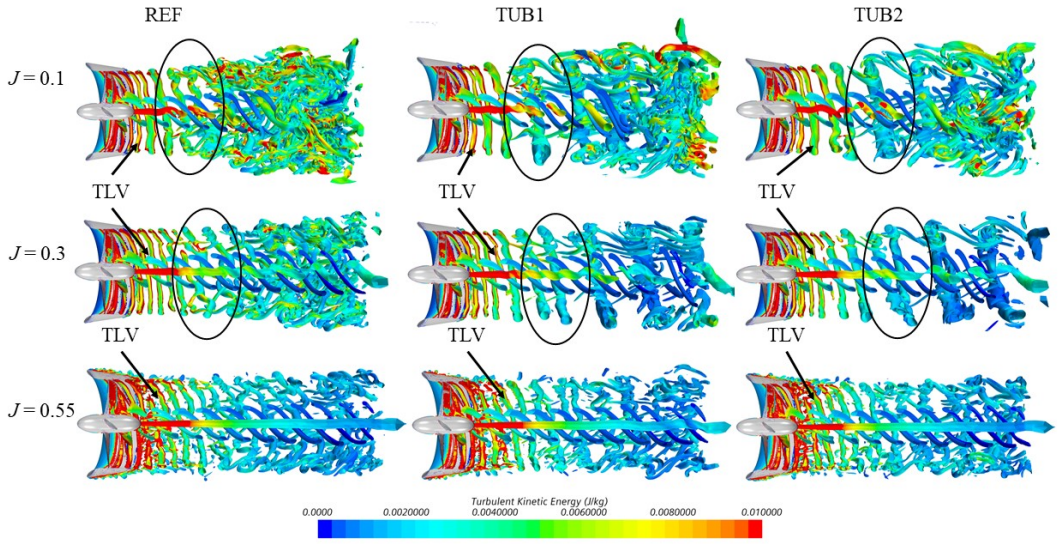

Figure 7.6: Half-section Q-criterion iso-surface ($\alpha = 1000/s^2$) coloured by TKE for all ducted propeller designs at $J = 0.1$, 0.3 and 0.55

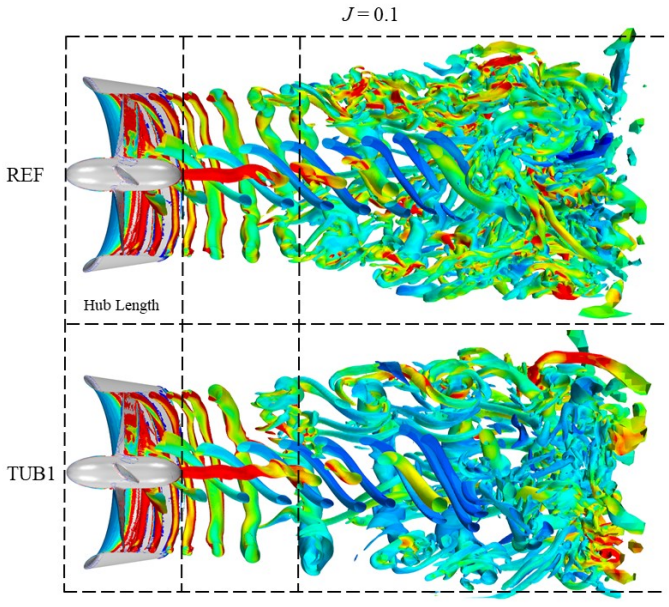

Figure 7.7: Mid-section Q-criterion iso-surface ($\alpha = 1000/s^2$) coloured by TKE at $J = 0.1$ to highlight difference in vortex structure

7.2.1.4 Near-Field Pressure Pulses

Monitoring the hydrodynamic pressure using a point probe, 1D away from the propeller centre in the radial direction, the pressure signal was recorded at $J = 0.1$, 0.3 and 0.55 for all designs. The pressure signals in the near-field can be seen illustrated in Figure 7.8. The periodic pressure fluctuations associated with the blade passage can be shown clearly for $J = 0.1$ and $J = 0.3$. But, this is less distinct at $J = 0.55$, which could be due to the low-blade loading. Figure 7.9 shows the standard deviation, σ, explaining the statistical behaviour of the pressure pulses in non-cavitating conditions. It can be shown that generally the tubercle propeller designs have a higher standard deviation than the REF design, however the difference is minimal. Figure 7.10 shows the FFT analysis of the pressure pulses in non-cavitating conditions for all ducted propeller designs. At all conditions, the frequency spectra are dominated by the 1^{st} BPF for all operating conditions considered and the difference between ducted propeller designs is negligible. However, at $J = 0.55$, the low frequency range is chaotic when compared to the other operating conditions, this could be due to the flow-separation induced vortex occurring on the outside of the duct together with the reduced blade loading.

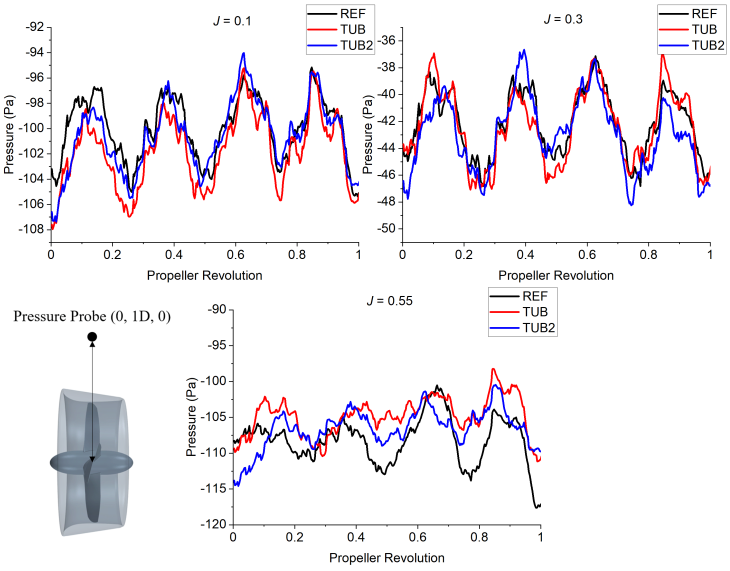

Figure 7.8: Near-field pressure signals for all propeller designs $1D$ radially from propeller centre (M0) at $J = 0.1$, 0.3 and 0.55.

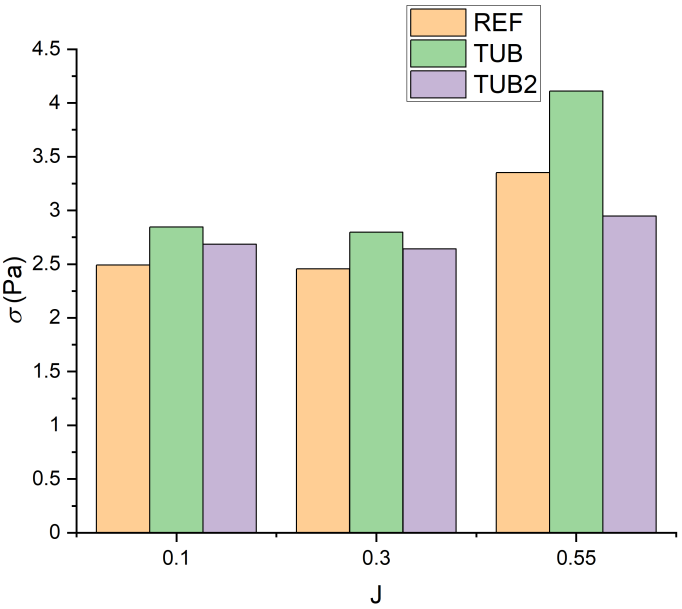

Figure 7.9: Standard deviation, σ, of pressure pulse (Pa) time history in non-cavitating conditions for all ducted propeller designs

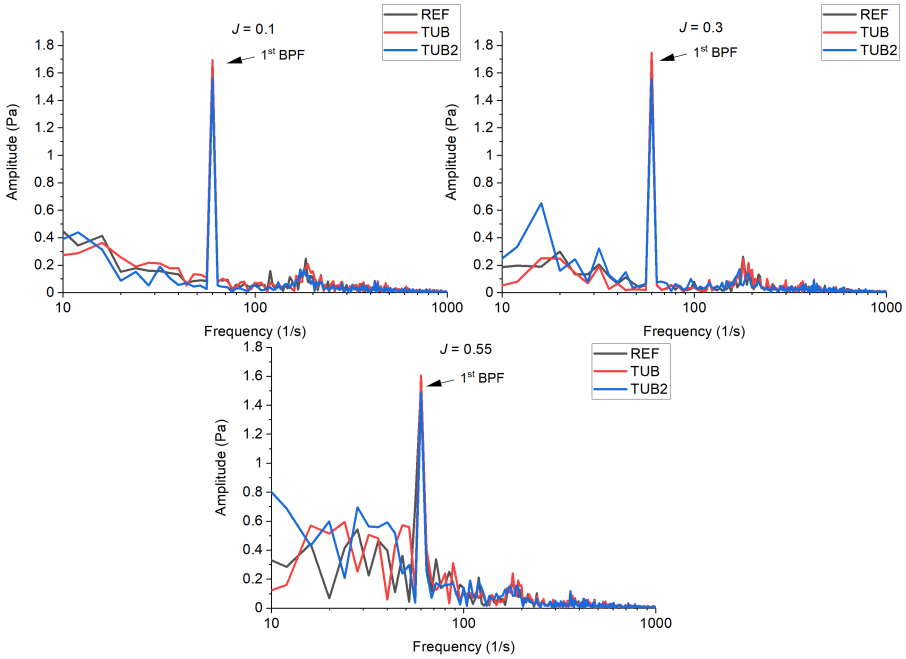

Figure 7.10: Frequency spectra of pressure pulse in non-cavitating conditions for all ducted propeller designs

7.2.2 Cavitating Hydrodynamic Analysis

In the above sections, performance in non-cavitating conditions was analysed and compared between the different designs. In the following section, the analysis of the propellers under cavitating conditions is presented.

7.2.2.1 Time-Averaged Hydrodynamic Performance

Figure 7.11 depicts the time-averaged propulsive efficiency data for non-cavitating, light-cavitating and heavy-cavitating conditions for all ducted propeller designs. As can be seen from all ducted propeller designs, the presence of cavitation creates a degradation in propulsive efficiency. The propulsive efficiency is further

decreased, as the cavitation number reduces. Although the difference in efficiency is minimal between non-cavitating and light-cavitating conditions at $J = 0.55$ due to only a very small sheet cavity volume present on the blade surface at the light-cavitating condition at this operating condition. It can be seen that tubercle design can generally improve the efficiency performance in cavitating conditions.

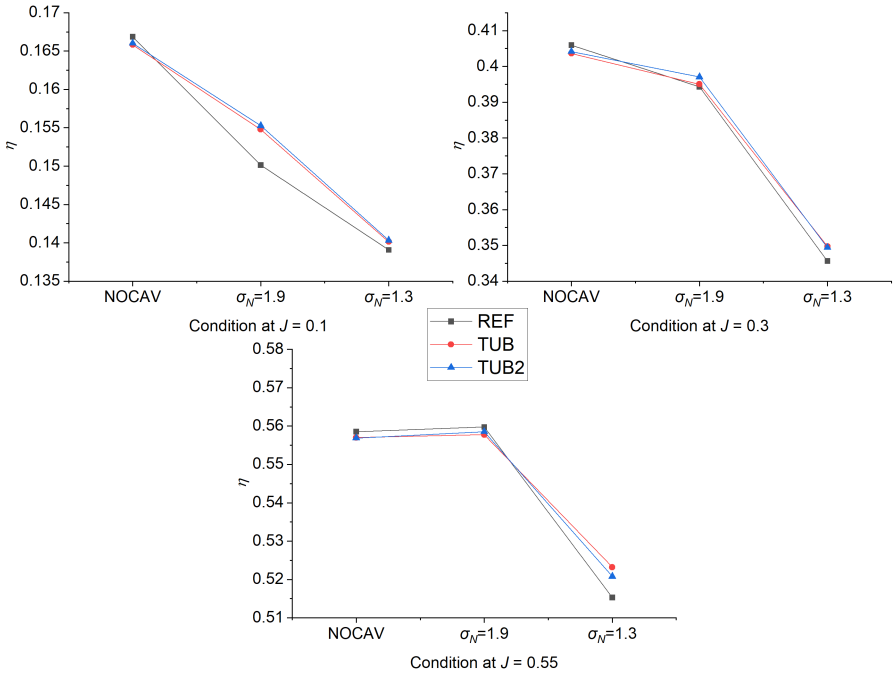

Figure 7.11: Comparison of time-averaged non-cavitating (NOCAV) and cavitating propulsive efficiency data for all ducted propeller designs

Figure 7.12 summarises the percentage change in the time-averaged key performance variables, thrust, torque and efficiency for all tubercle propeller designs against the reference design. The TUB1 and TUB2 designs improved the total thrust coefficient and propulsive efficiency to a maximum of 10% and 3.1%, respectively. The duct thrust improved in all conditions considered as well by a maximum of 71%, although at this condition it is worth mentioning the duct

thrust coefficient was to the order of 10^{-3}. Generally, the improvement ranged from 5-10%.

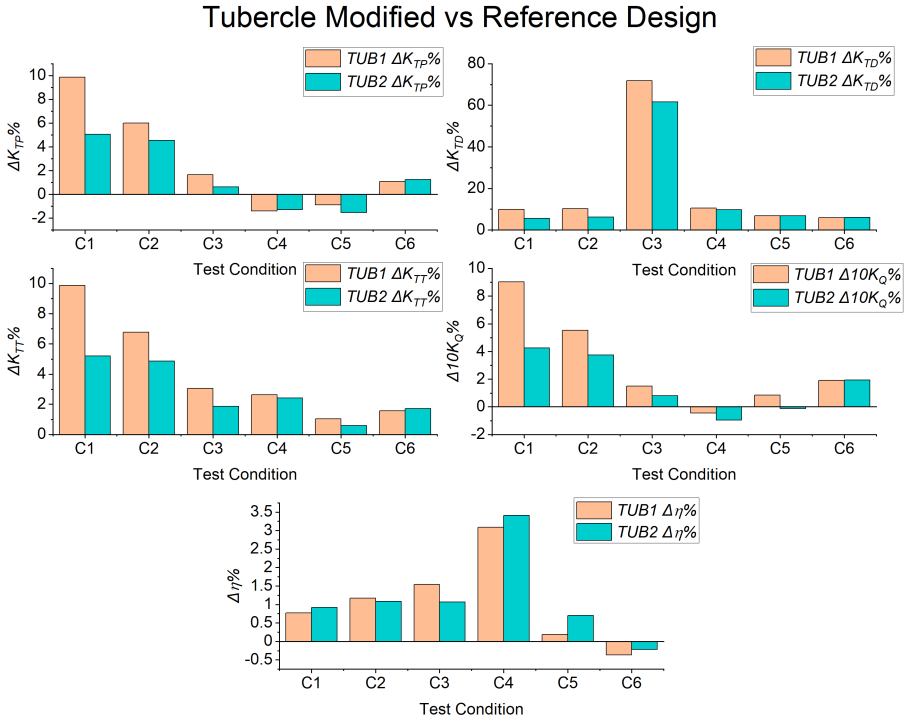

Figure 7.12: Percentage change in key performance variables for each tubercle design as compared to the reference design at all conditions considered

Another 4 test cases were analysed in the heavy-cavitating conditions to collect more raw data (σ_N=1.3, J = 0.12, 0.14, 0.2 and 0.4) and a cubic spline curve was fitted to each propulsor data set. The propulsive efficiency for each propulsor design was then calculated under the same C_t using interpolation over each spline curve fitted. The raw data can be shown in Figure 7.13a and Figure 7.13b with the interpolation points shown by the dashed lines. The percentage improvement in propulsive efficiency at the same thrust loading conditions can be shown in Figure 7.13c, the maximum efficiency improvement achieved was 6.5% by TUB1 and 3.9% TUB2 in near bollard pull condition with a minor shift in the J number

(as shown in Figure 7.13d). .

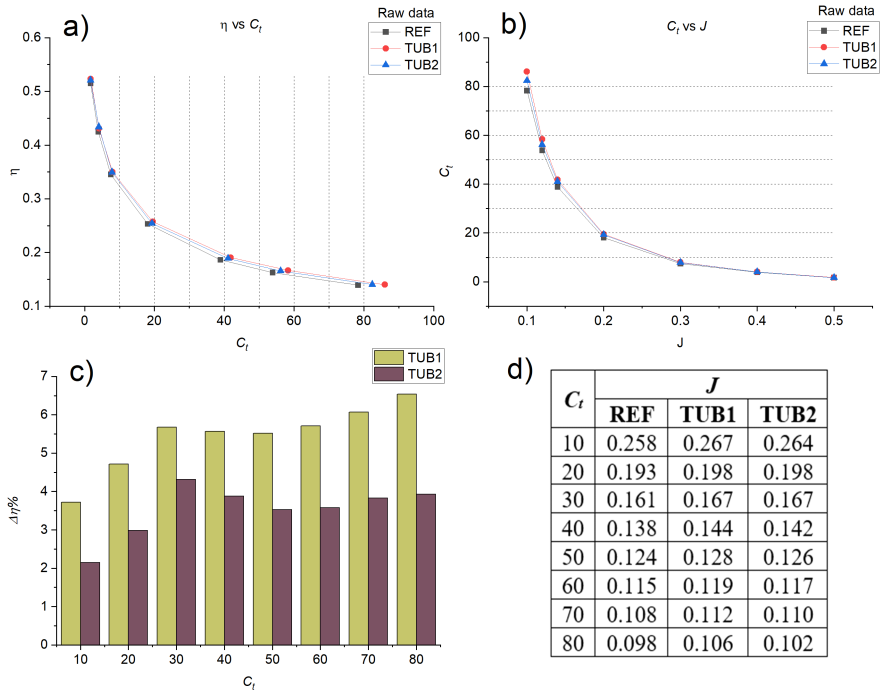

C_t	J		
	REF	TUB1	TUB2
10	0.258	0.267	0.264
20	0.193	0.198	0.198
30	0.161	0.167	0.167
40	0.138	0.144	0.142
50	0.124	0.128	0.126
60	0.115	0.119	0.117
70	0.108	0.112	0.110
80	0.098	0.106	0.102

Figure 7.13: a) raw data of η vs. C_t and interpolation points b) raw data C_t vs. J and interpolation points c) Percentage improvement in propulsive efficiency when comparing at the same C_t for tubercle propellers compared to REF, d) J number at each C_t considered within the interpolation in heavy-cavitating conditions

7.2.2.2 Transient Hydrodynamic Performance

The presence of cavitation can incur strong fluctuations in the hydrodynamic variables thrust and torque of the propulsor, therefore, the transient hydrodynamic characteristics were extracted over one propeller revolution in conditions C1-C6 presented in Figure 7.14 and Figure 7.15, respectively. The transient data for the propeller was acquired from a single propeller blade to accurately capture the fluctuations experienced as opposed to the summation of the fluctuations from all four blades. The time-averaged values of the hydrodynamic characteristics from

the REF design were used to normalise the data.

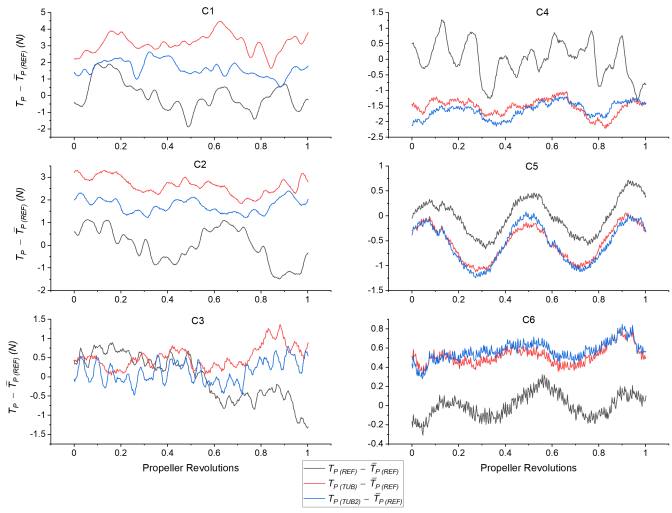

Figure 7.14: Transient propeller thrust, T_P (single blade), over one propeller revolution at C1-C6 for all propeller designs, normalised by time-averaged total thrust from REF design

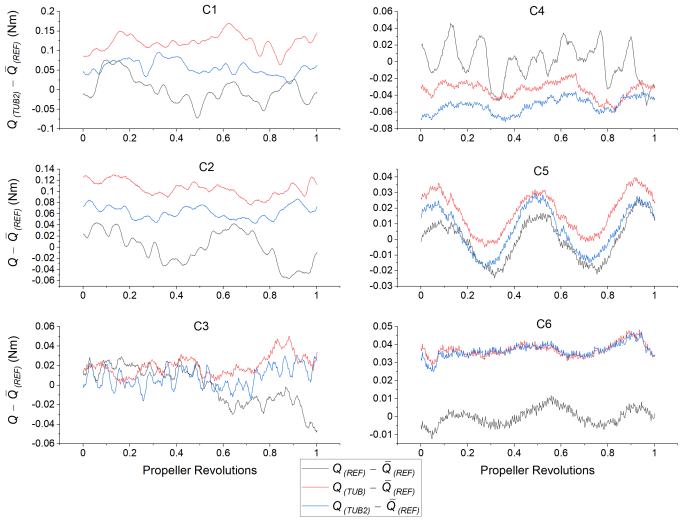

Figure 7.15: Transient torque, Q (single blade), over one propeller revolution at C1-C6 for all propeller designs, normalised by time-averaged total torque from REF design

Firstly, the fluctuations of propeller thrust can be observed in Figure 7.14. The percentage improvement in thrust shown in Figure 7.12 from the tubercle propeller designs can be observed clearly in the transient fluctuations. In the light-cavitating conditions (C3-C6), the fluctuations can be seen to form a regular sinusoidal pattern, particularly in the higher advance ratios (C5 and C6) when compared to the heavy-loading condition (C4). In the heavy-cavitating conditions (C1-C3), more chaotic fluctuations in the propeller thrust can be observed, where the amplitude in fluctuation is particularly large for the lower advance ratios (C1 and C2) when compared to C3, although C3 experiences fluctuations more frequently. Comparing the fluctuations between propeller designs, the fluctuation of total thrust is larger for the REF propeller design when compared to the tubercle models, therefore showing the thrust delivery of the propulsor is more favourable for the tubercle designs where not only can time-averaged total thrust be improved, but the fluctuation in the propeller thrust is mitigated, particularly for the heavy-loaded, heavy-cavitating conditions (C1 and C2). Similar findings can be observed for the transient torque analysis (Figure 7.15), where the fluctuation in the torque can be seen to be less extreme for the TUB and TUB2 propeller designs when compared to the REF design, particularly in the heavy-loading conditions, $J = 0.1$ (C1 and C4).

FFT analysis was conducted on the propeller thrust of a single blade for all propeller designs at conditions C1-C6 and is shown in Figure 7.16. Comparing the cavitating conditions at the higher advance ratio, $J = 0.55$ to the lower advance ratio, $J = 0.1$, the blade-passage frequency (60s^{-1}) is much more distinct in the spectrum for the lower-blade loading condition, $J = 0.55$, which corresponds to the smooth sinusoidal waveform of thrust in the time domain seen at C6 (Figure 7.14). In addition, the blade passage frequency is much more distinct in the light-cavitating conditions than the heavy-cavitating conditions. Where cavitation

is most severe (C1-C3), the signal is much more chaotic than when compared to the light-cavitating condition counterparts (C4-C6). When comparing the cavitating conditions in the low J to the high J, it can be shown the signal is more chaotic for the lower J conditions. The tubercle propeller designs have smaller amplitude peaks over the spectra when compared to the baseline case for the most severe cavitating conditions (C1-C4), however negligible difference is seen at conditions where a small volume of cavitation is present (C5 and C6), although at C6 the peak at the BPF can be seen to be reduced for the tubercle designs when compared to the REF. This reduction in fluctuation could bring further benefits in the form of reductions in fatigue loading, vibrational excitation and radiated noise.

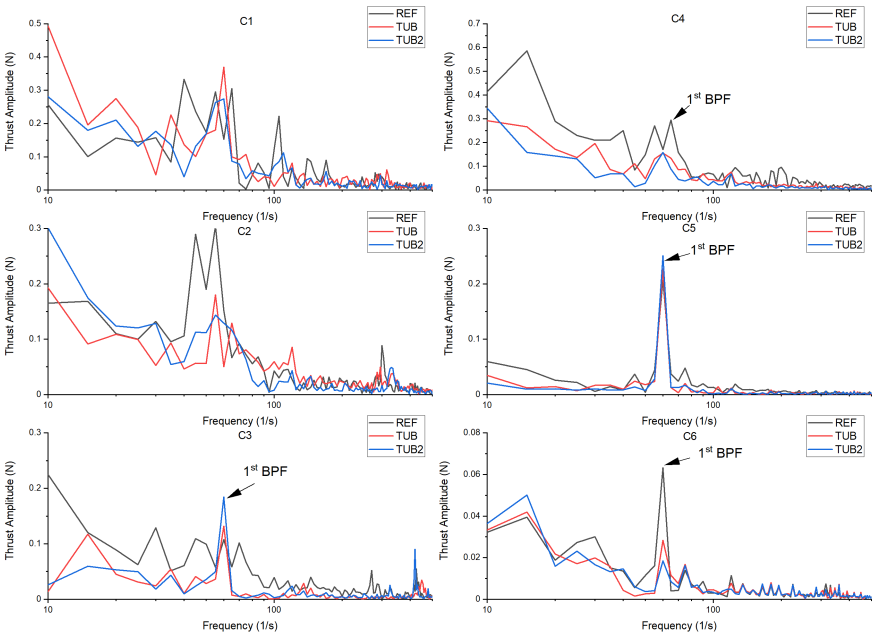

Figure 7.16: Frequency spectra of propeller thrust from a single blade for all propeller designs at C1-C6

7.2.2.3 Sheet Cavitation Observations

Figure 7.17 also summarises the $\Delta\%$ in time-averaged cavitation volume of all tubercle propeller designs when compared to the baseline design, the cavitation volume was predicted by using the volume integral of the vapour fraction present within the computational domain. At all conditions considered for both tubercle propeller designs; the sheet cavitation volume was reduced. A general trend can be observed for both models, where cavitation reduction is small where the highest cavity volume is present (C1 and C2), the reduction then reaches a peak where mid cavity volume is present (C4) and then the reduction becomes smaller where a smaller cavity volume is present (C5 and C6). The maximum reduction of sheet cavitation was roughly 50% and therefore reducing the severity of cavitation by modifying the Kaplan blade with leading-edge tubercles leads to the recovery of duct thrust in cavitating conditions (see Figure 7.12). Generally, TUB2 is more successful in reducing the cavitation than TUB1 at C3-C6 although this is reversed at C1 and C2. The differences are marginal between the different wavelengths of tubercle, however the differences would be expected to be clearer if the wavelength was drastically changed or the amplitude was varied considerably from the current design, although further work would be necessary to confirm this.

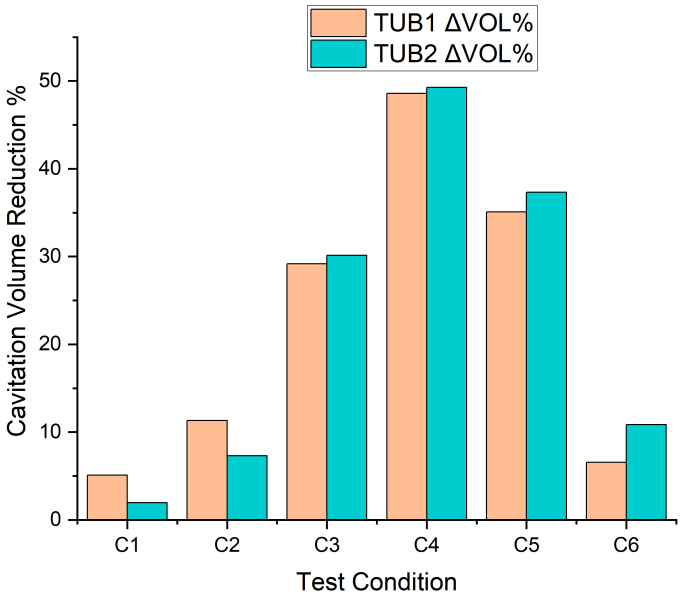

Figure 7.17: Cavitation volume reduction % for each tubercle design as compared to the reference design

Figure 7.18 and Figure 7.19 show the cavitation patterns predicted on all propeller designs, displayed using an iso-surface of the vapour fraction ($\alpha = 0.1$) at all advance ratios considered at $\sigma_N = 1.3$ and $\sigma_N = 1.9$, respectively. In addition to the influence of LE tubercles on the physical quantity of cavitation, the distribution along the blade can be shown to be influenced as well. A cavitation funnel pattern can be shown to be induced by all tubercle propellers with a clear visual funnel effect at C4 by TUB1, at this condition, the funnel effect creates a segmentation between the cavitation occurring over the blade surface and tip gap (see Figure 7.19). The cavitation is constrained in and behind the trough regions, which can be controlled with the geometrical configuration of the LE tubercle. This phenomenon is believed to be accredited to the streamwise counter-rotating vortex pair introduced by the tubercles which alters the local pressure field on the blade suction side. The location of the tubercle trough with respect to the sheet

cavitation is also important. It is found that TUB1 is more successful in reducing cavitation in the heavy-cavitating conditions (Figure 7.17), which is because of the tubercle geometrical wavelength which encourages the cavitation behind the trough region and restricts the cavitation from further progressing to the blade root because of the location of the tubercle peak, where the tubercle peak is located approximately at the blade mid-section.

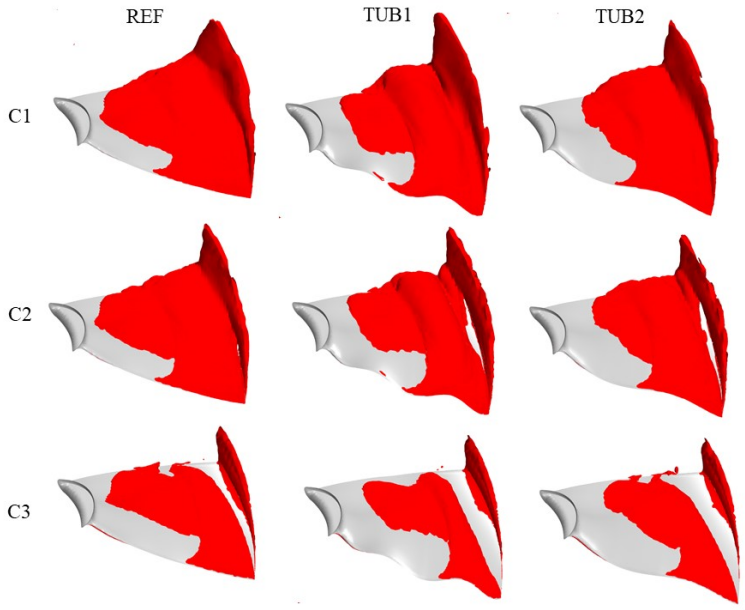

Figure 7.18: Iso-surface of vapour fraction ($\alpha = 0.1$) for all propeller designs at $\sigma_N = 1.3$

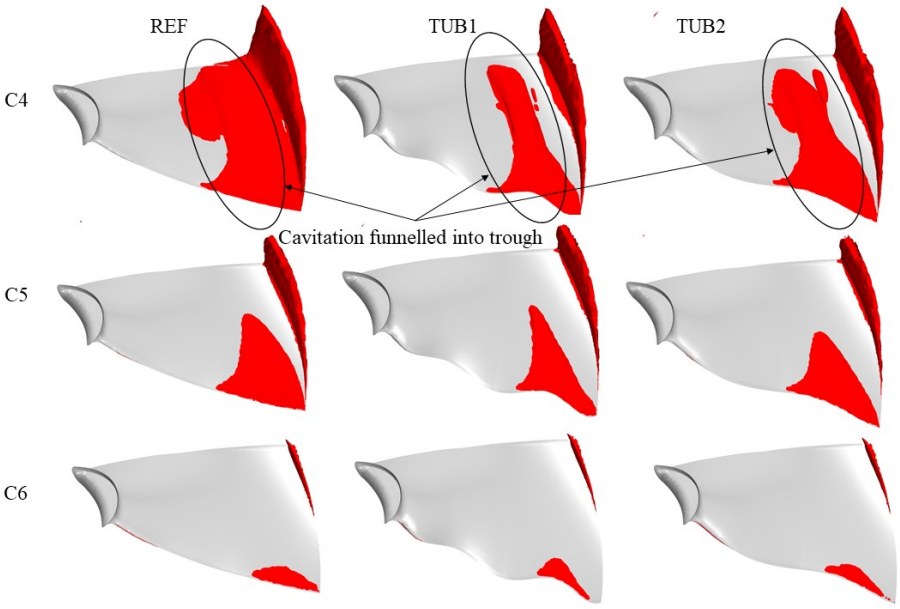

Figure 7.19: Iso-surface of vapour fraction ($\alpha = 0.1$) for all propeller designs at $\sigma_N = 1.9$

Figure 7.20 compares the cavitation pattern of TUB1 to the surface pressure distribution observed in non-cavitating conditions, highlighting that cavitation is occurring behind the low-pressure trough region. At $J = 0.1$ and 0.3, $\sigma_N = 1.9$, the propeller thrust does not improve, due to the significant redistribution of the sheet cavitation which can be seen clearly (see Figure 7.20). The redistributed cavitation, although less in quantity, is concentrated in an area further from the tip than compared to the baseline design. But regardless, the reduction in cavitation volume recovers the duct thrust and as a result the overall thrust coefficient is improved. This is due to the likely improved thrust contribution nearer the blade tip (more tip loaded) from the tubercle combination as it is free from cavitation which will create a larger suction force nearer the duct and thus, increase duct thrust. This is supported by the 2D static pressure coefficient plots of the duct at condition C3 and C4, where all conditions and propeller designs are considered in Figure 7.21. The duct length (x-axis) is normalised by the duct

chord length, L_{DUCT} , where 0 denotes the leading-edge and 1 denotes the trailing edge of the duct. This finding is particularly obvious in heavy cavitating condition from C1 to C3. Furthermore, the duct thrust is extracted and compared further in Figure 7.22 showing enhancement across all the investigated conditions by the tubercle propellers.

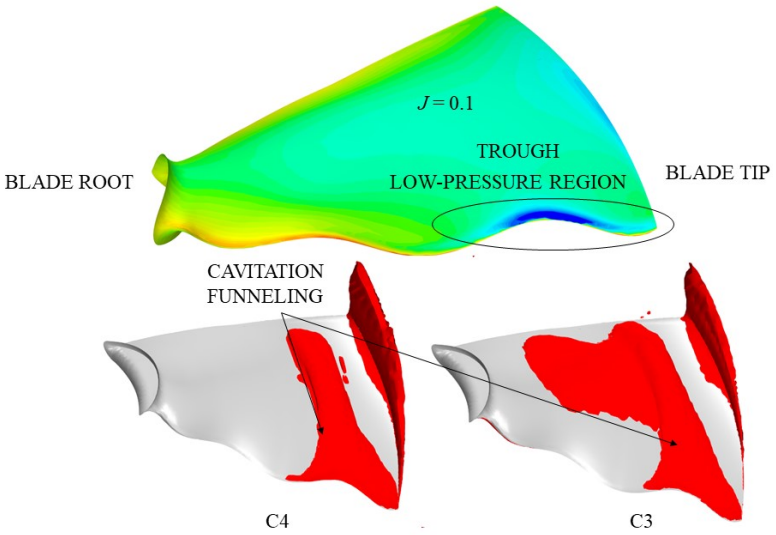

Figure 7.20: Annotated illustration of TUB1 cavitation funnelling effect

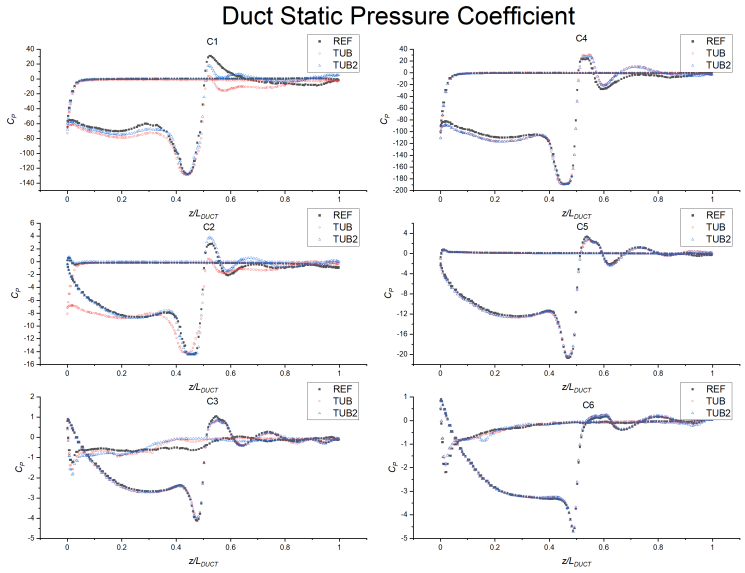

Figure 7.21: 2D static pressure coefficient plots from a section of all ducts surrounding all propeller designs at conditions C1-C6

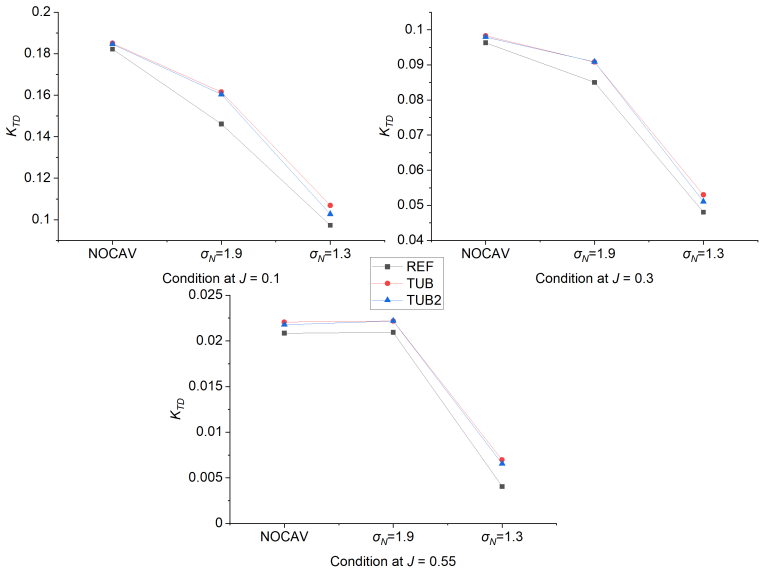

Figure 7.22: Comparison of time-averaged non-cavitating (NOCAV) and cavitating duct thrust data for all ducted propeller designs

Figure 7.23 depicts the variation in cavitation volume over a 1 propeller revolution time-period for test conditions C1-C6. The reduction in time-averaged cavitation is clear. C2-C5 experience a steady oscillating cavitation behaviour whereas the two extreme conditions of both heavy and light cavitation severity, C1 and C6, show a more unsteady cavitation behaviour. The cavitation behaviour over time when comparing the REF, TUB and TUB2 is very similar at C2, C3 and C5. But at C1, C4 and C6 the fluctuations of the cavity volume are more chaotic for the REF propeller when compared to the TUB and TUB2 designs. This is the reason for the reduction in the discrete amplitude peaks from the transient loading analysis previously discussed.

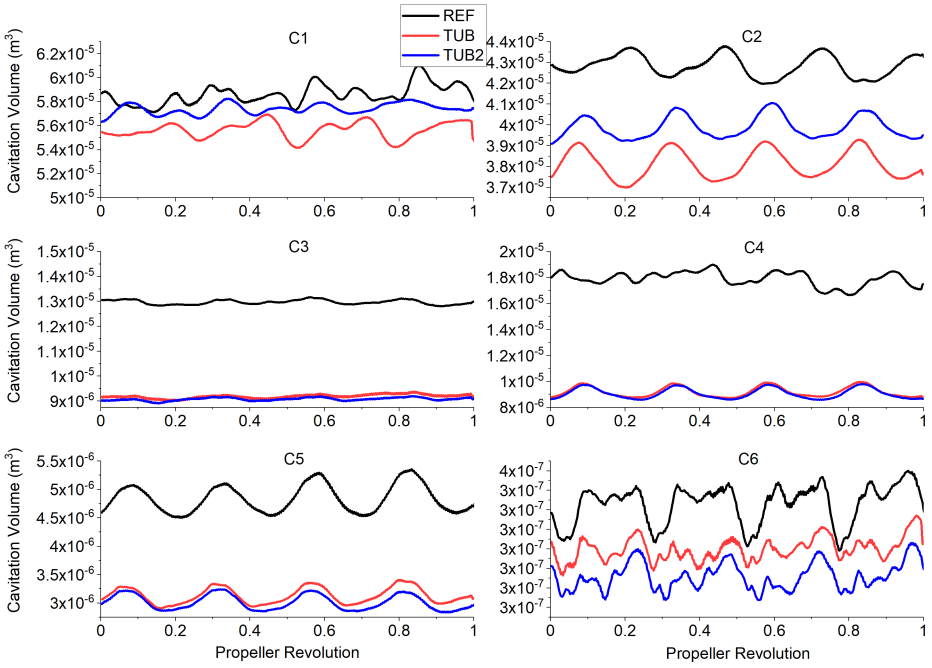

Figure 7.23: Cavitation variation with time for all ducted propeller designs at C1-C6

7.2.2.4 Streamwise Vortex Pairs, Pressure and Cavitation Interaction

Figure 7.24 illustrates the comparison between REF and TUB1 blade designs and the difference in sheet cavitation over the blade surface and how this relates to the streamwise vortex pair induced by the LE tubercle modification at multiple plane sections along the blade span at the condition where the difference in cavitation development between designs is most significant, C4. The cavitation observed within the confines of the current numerical modelling technique can be split into two, the sheet cavitation over the blade surface and the tip-leakage vortex cavitation, rolling up at the leading-edge of the blade tip and trailing behind the blade as annotated. As is shown, initially the cavitation and streamwise vorticity is similar over the leading-edge between designs, but as the sheet cavitation develops over the blade from leading to trailing-edge, the TUB1 design funnels the sheet cavitation behind the trough, segmenting the sheet cavitation from the tip-leakage vortex cavitation. The streamwise vortex pair induced by the LE tubercle modification can be observed inside the cavitation funnel behind the trough region. Therefore, the production of the streamwise counter-rotating vortex pairs behind the trough region by the LE tubercle modification focus the sheet cavitation development into the trough region and encourage cavitation-free zones behind the peaks, depending on the operating condition.

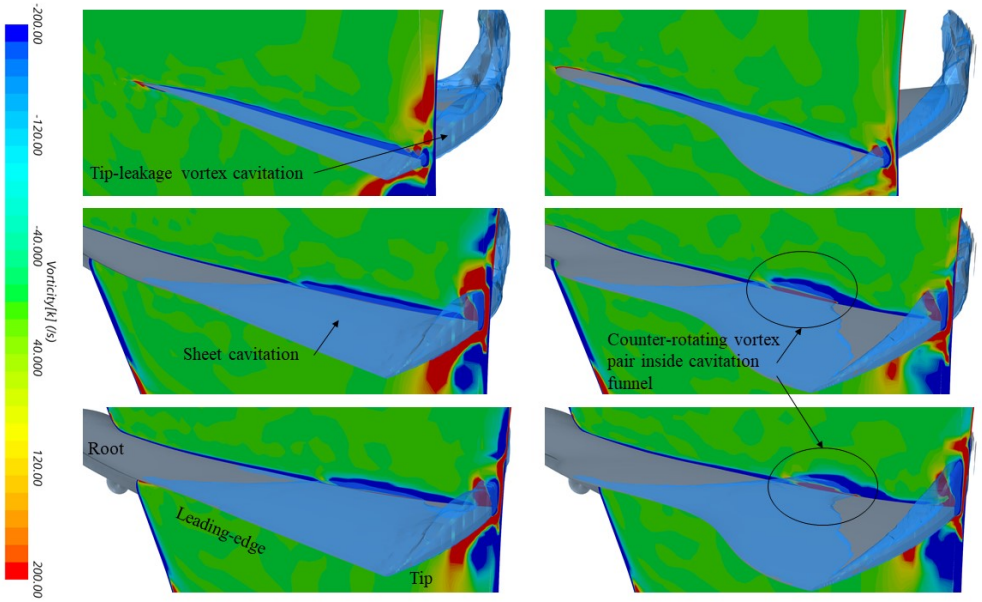

Figure 7.24: Instantaneous cavitation volume and plane-section of streamwise vorticity at three different locations across the blade span for REF and TUB1 designs at C4

Figure 7.25 shows the local pressure field and cavitation of both REF and TUB1 designs at various plane-sections across the blade spans at condition, C4. The relationship between the low pressure regions and the presence of both sheet cavitation and tip-leakage vortex cavitation can be observed. As can be seen, the pressure field is similar at the plane-section nearest the blade leading-edge between designs. As the distance between the plane-section and blade leading-edge is increased, the sheet cavitation is eventually funnelled into the low pressure region induced by the LE tubercles as the streamwise vortex pair develops, while a higher pressure region is induced behind the tubercle peak, reducing the cavitation development at this location and aiding in the segmentation between the sheet cavitation and tip-leakage vortex cavitation when compared to the REF design.

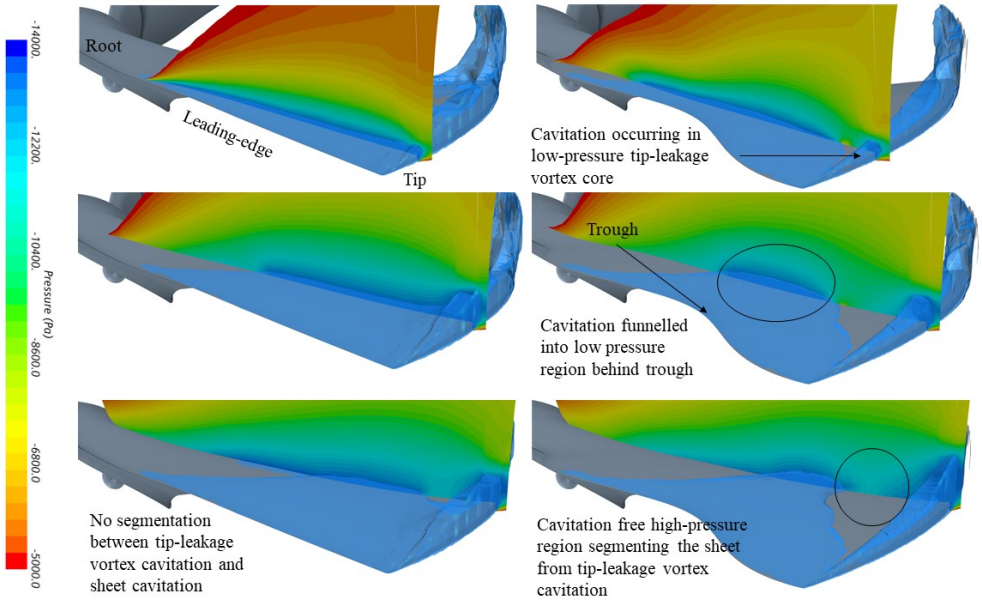

Figure 7.25: Instantaneous cavitation volume and plane-section of pressure at three different locations across the blade span for REF and TUB1 designs at C4

7.2.2.5 Vortex Development

Figure 7.26, 7.27 and 7.28 illustrate the half section Q-criterion iso-surface ($\alpha = 1000/s^2$) coloured by TKE for all ducted propeller designs for cavitating conditions C1-C6. Comparing the heavy-cavitating condition to the light-cavitating condition at the same operating condition, it is shown that in the heavy-cavitating condition the development of the tip-leakage vortex is restricted and cannot fully develop into a helical vortex structure. At C4, the modified ducted propeller produces a stronger helical tip leakage vortex in the propeller slipstream than compared to the reference, which is not distinguishable and is highlighted in Figure 7.29.

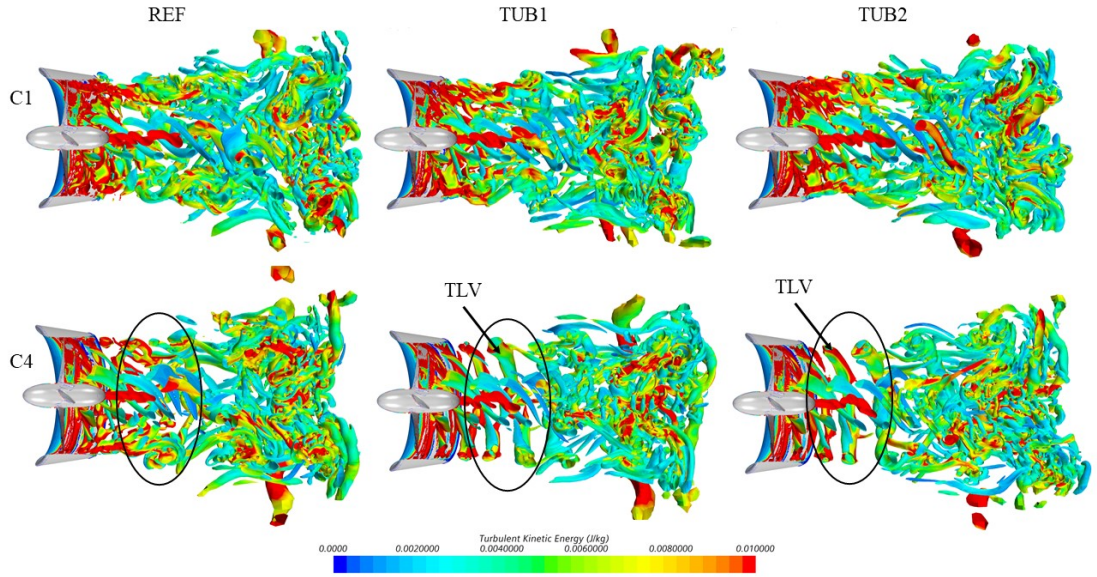

Figure 7.26: Half-section Q-criterion iso-surface ($\alpha = 1000/s^2$) coloured by TKE for all ducted propeller designs at conditions C1 and C4

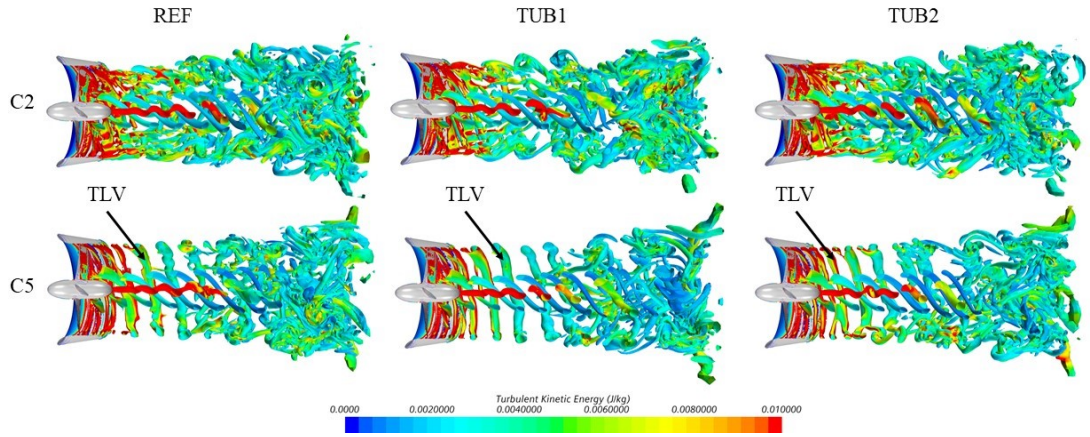

Figure 7.27: Half-section Q-criterion iso-surface ($\alpha = 1000/s^2$) coloured by TKE for all ducted propeller designs at conditions C2 and C5

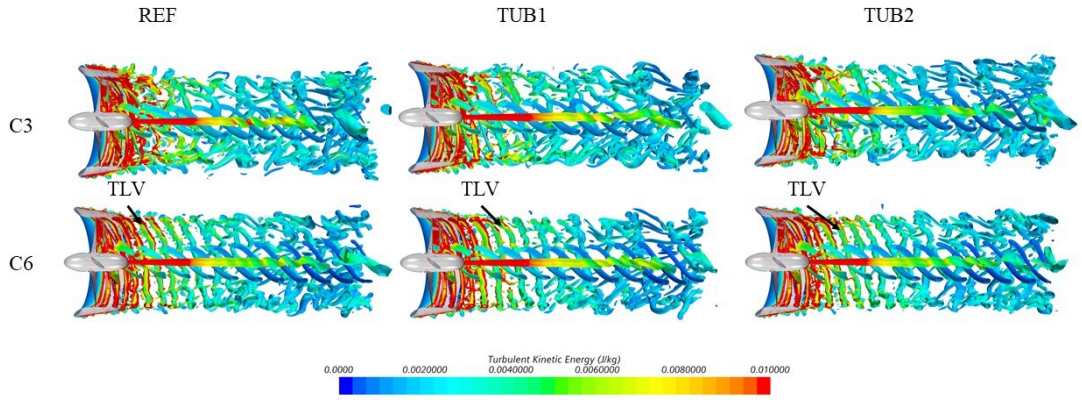

Figure 7.28: Half-section Q-criterion iso-surface ($\alpha = 1000/s^2$) coloured by TKE for all ducted propeller designs at conditions C3 and C6

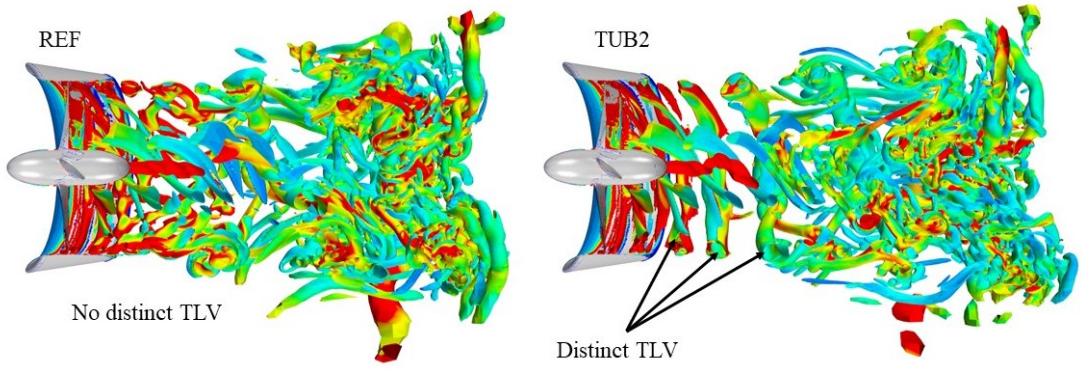

Figure 7.29: Mid-section Q-criterion iso-surface ($\alpha = 1000/s^2$) coloured by TKE at C4 to highlight difference in TLV between blade designs

7.2.2.6 Near-field Pressure

Figure 7.30 depicts the near-field pressure fluctuations 1D from the propeller centre at all cavitating conditions considered, C1-C6. In conditions C2, C4 and C5 the pressure fluctuation reduces when comparing the tubercle ducted propeller blade design to the reference ducted propeller design. At conditions, C1, C3 and C6, there is only slight differences in the pressure signal. Figure 7.31 shows the standard deviation, σ, of the pressure pulse time history for all test conditions for

all ducted propeller designs. It can be shown that for most test conditions, the TUB and TUB2 designs can significantly reduce the fluctuation due to the limited cavitation development. Figure 7.32 shows the FFT analysis of the pressure pulses in the cavitating conditions for all ducted propeller designs. The blade passage frequencies can be observed clearly for most conditions. It can be seen that for most of the conditions the tubercle design can lower the peaks due to the controlled cavitation development, which can be clearly seen in C1, C2, C4 and C5. The difference becomes less distinct in the higher J number due to the reduced blade loading. This is another indication that in some cavitating conditions, the modified ducted propeller blades will provide a noise reduction potential in the near field which will be analysed in the following sections.

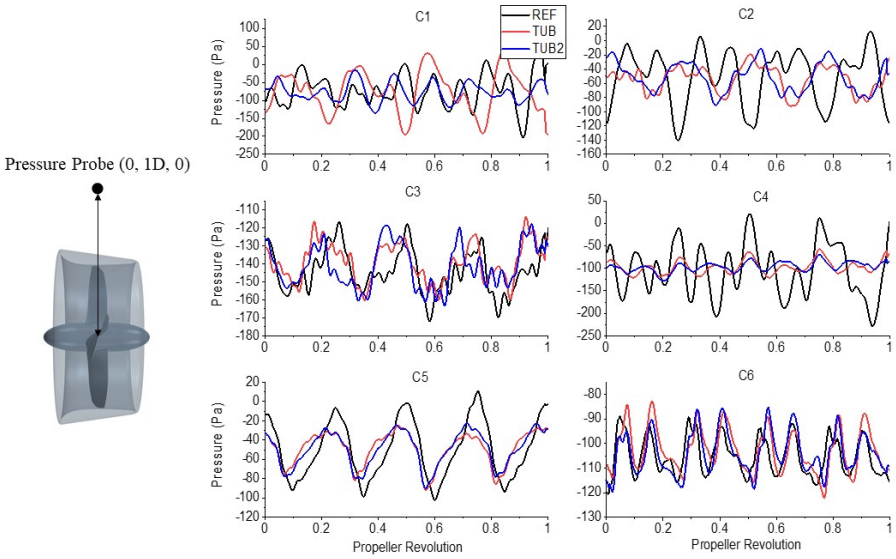

Figure 7.30: Near-field pressure signals for all ducted propeller designs $1D$ radially from propeller centre (M0) at C1-C6

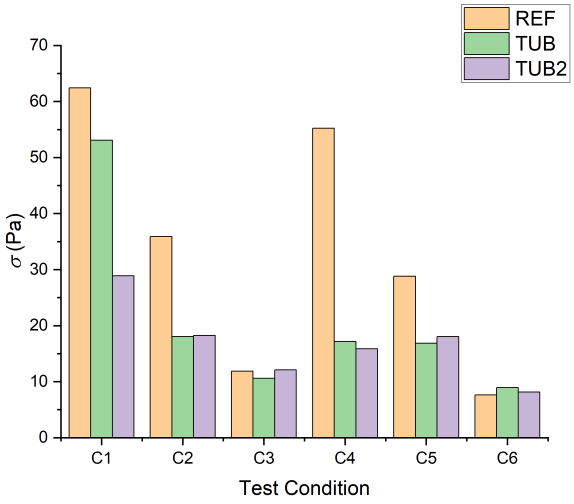

Figure 7.31: Standard deviation, σ, of pressure pulse (Pa) time history in cavitating conditions for all ducted propeller designs

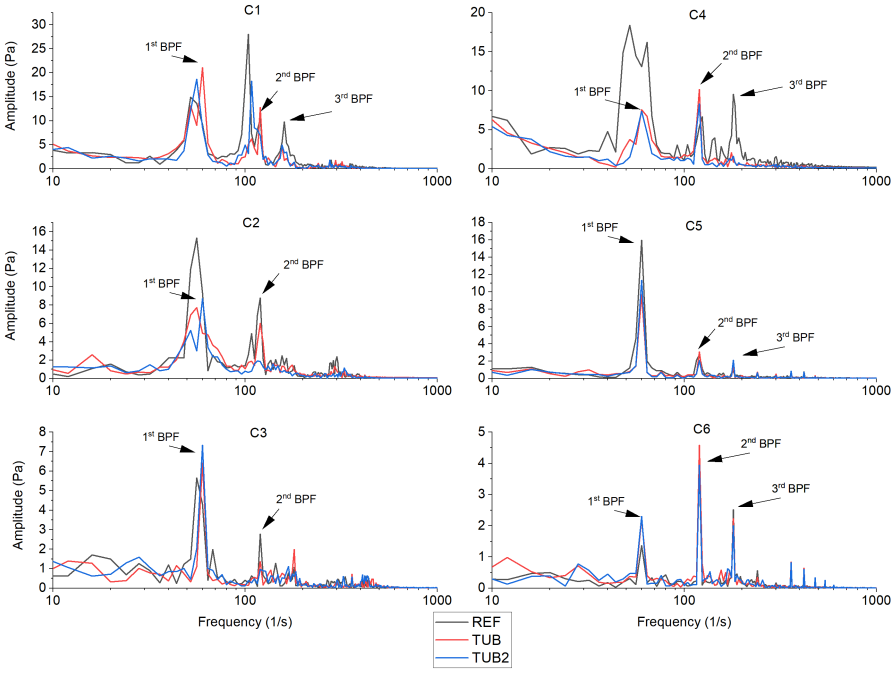

Figure 7.32: Frequency spectra of pressure pulse in cavitating conditions for all ducted propeller designs

7.2.3 Noise Performance

7.2.3.1 Near-Field Noise

From the previous analysis, TUB1 (referred to as TUB herein) was selected for noise performance prediction due to the improved hydrodynamic performance in heavy-cavitating conditions when compared to the TUB2 configuration and can be described as the 'optimal' tubercle blade design candidate.

Figure 7.33-7.36 show the narrowband and 3^{rd} octave band plots for receiver locations M0 and M4 at conditions C1-C6 in the near-field acquired from the direct hydrodynamic pressure. At both receivers, the 1^{st} blade passage frequency (BPF) can be clearly observed at $60s^{-1}$ in all conditions, although less so in conditions C1-C4, $J = 0.1$, where the blade loading and cavitation severity is the highest. The harmonics of the BPF can also be clearly observed at increments of $60s^{-1}$. In the near-field, there is a general noise reduction across most frequency ranges for C1-C5 for all receivers, particularly at C4 and C5 of over 10dB in some frequency ranges. Interestingly, this is the test conditions where the largest reduction in cavitation volume is produced by the modifications on the blade. However, at the condition where cavitation severity is the least, C6, the SPL across the frequency range of both designs are very similar.

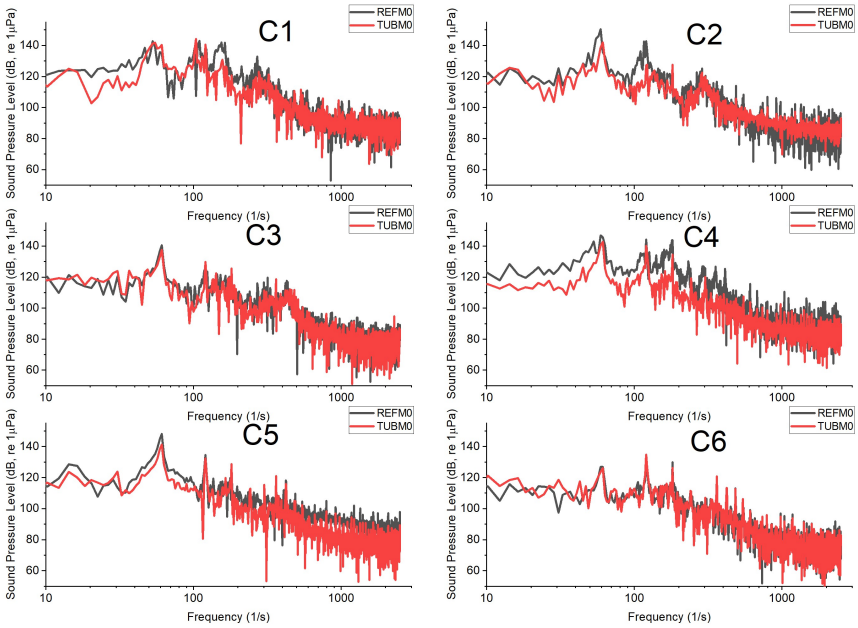

Figure 7.33: Near-field narrowband plots at all test conditions at receiver M0

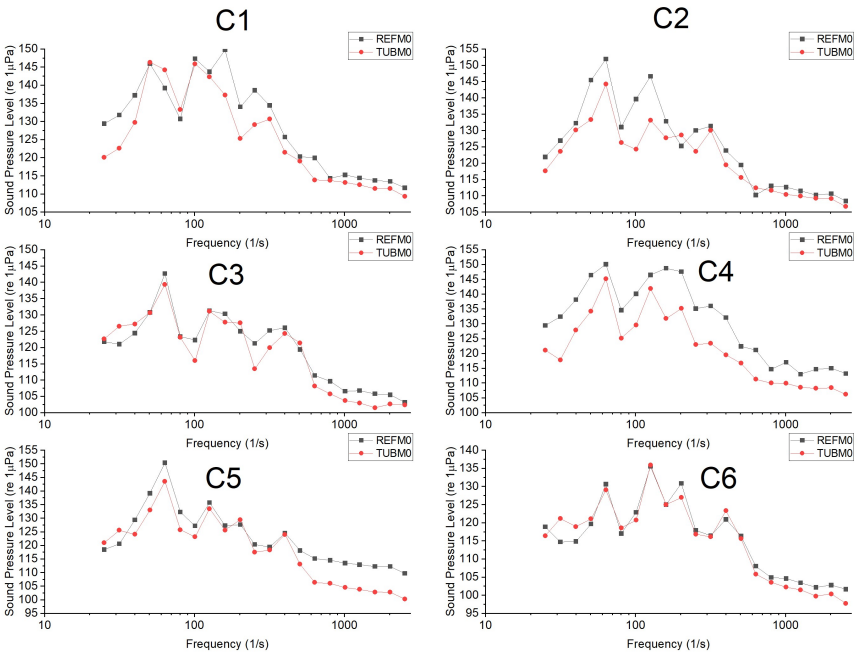

Figure 7.34: 3^{rd}octave band plots at all test conditions at receiver M4

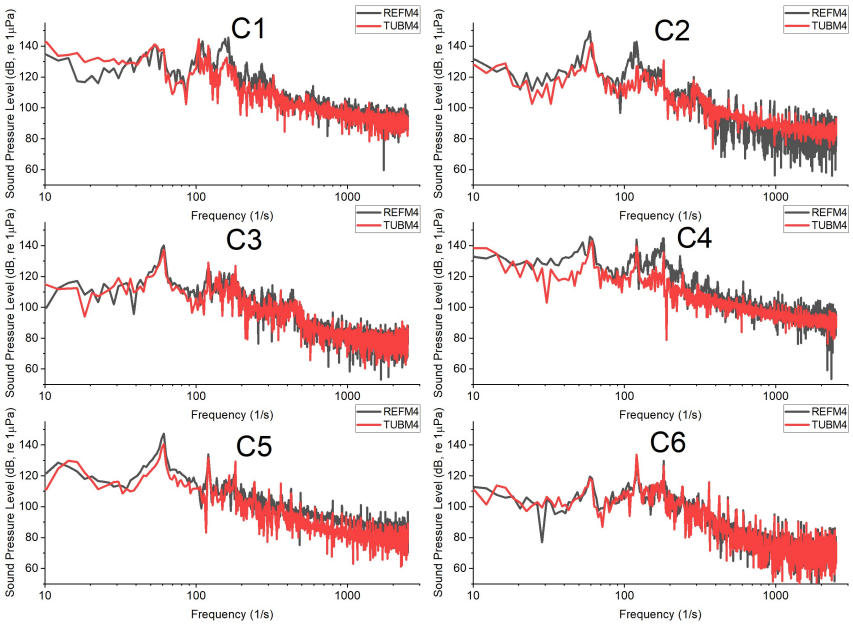

Figure 7.35: Near-field narrowband plots at all test conditions at receiver M4

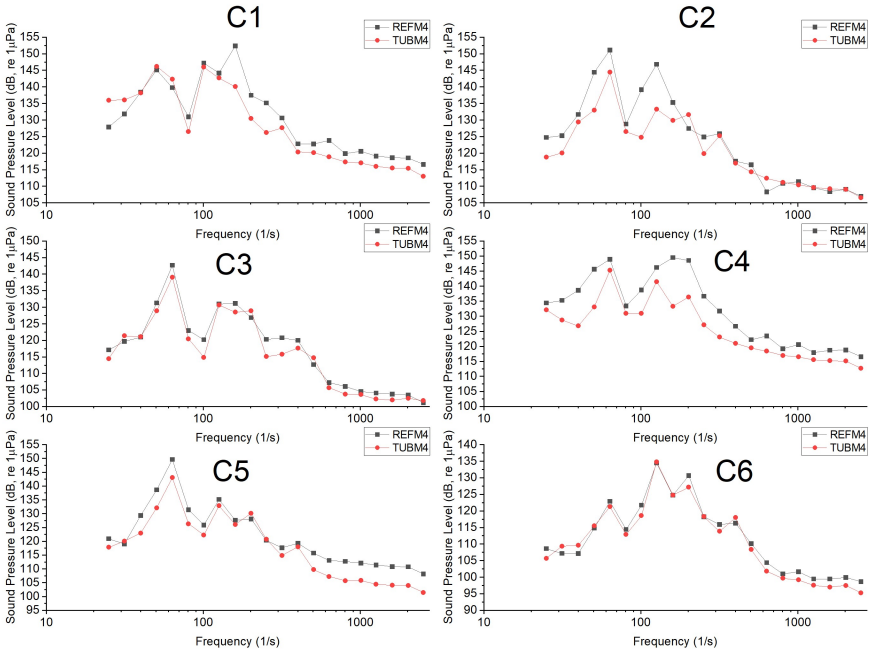

Figure 7.36: 3^{rd}octave band plots at all test conditions at receiver M4

7.2.3.2 Far-Field Noise

Figure 7.37 and 7.38 show the narrowband and 3^{rd} octave band SPL plots of both ducted propeller designs at far-field direction 90 degrees (see Figure 4.13) and are at a distance of 100 propeller diameters ($100D$) away from the propeller centre. At condition C1, there is a reduction in noise in the mid-frequency range of approximately a maximum of 5dB with an increase in noise at the low and high frequency range of approximately 2.5dB. There is a clear noise reduction across most of the frequency range considered at C2 of a maximum 5dB, apart from the low frequency range of 0-30s^{-1} where an approximate increase of 5dB is shown. At condition C3, the TUB design produces less noise than the REF design across the frequency range, although this is marginal at approximately 1-2dB. At C4, the TUB design produces a reduction in noise across most of the frequency range by a maximum of 5dB apart from in the 0-30s^{-1} range, where an increase of roughly 10dB is visible. The peak SPL is observed by the TUB design in the 0-30s^{-1} at C4 for all receivers which dominates the spectrum. At C5, a reduction of approximately 5dB is observed in the low-frequency range by the TUB design, with a slight increase across the rest of the spectrum.

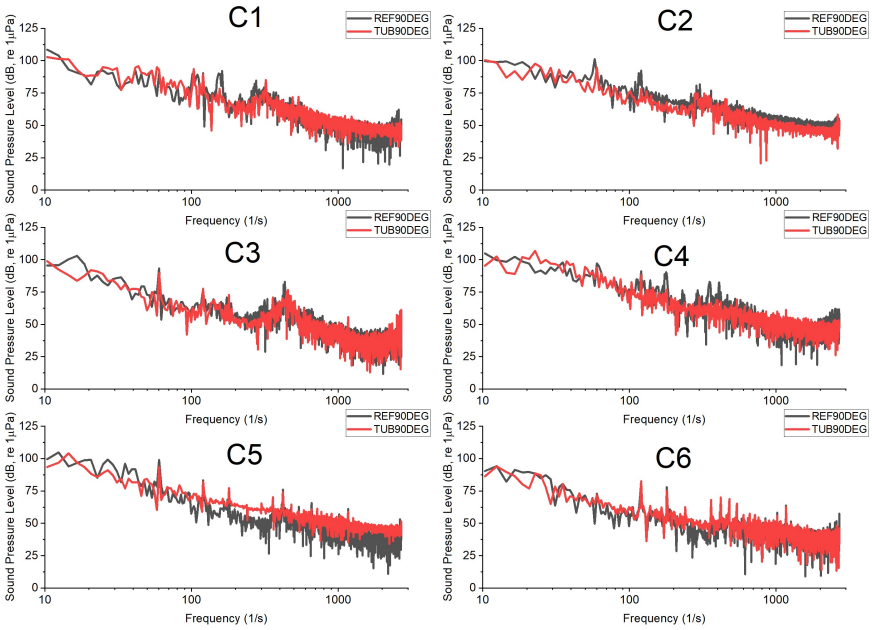

Figure 7.37: Far-field narrowband plots for all test conditions at 90 degree receiver position

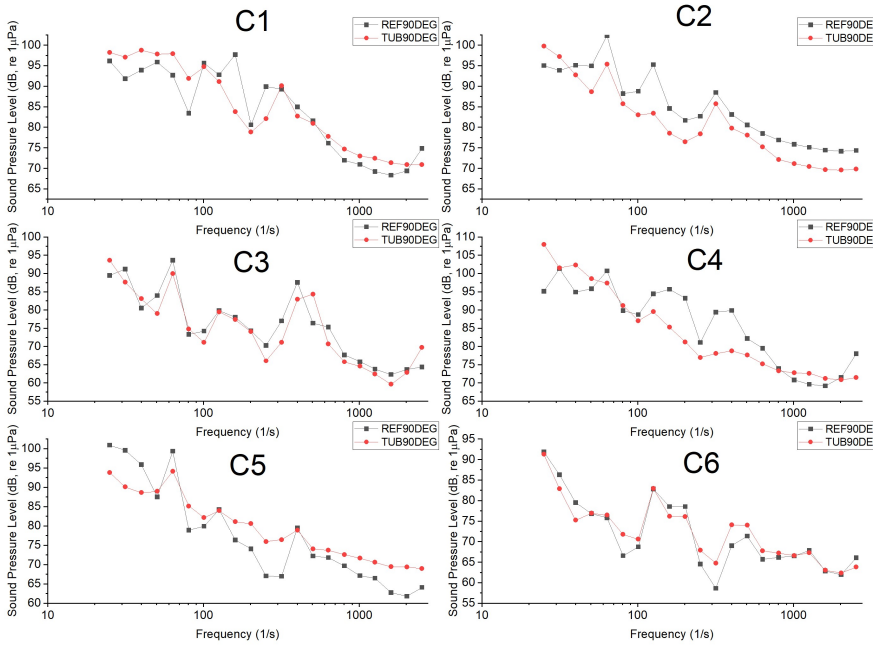

Figure 7.38: Far-field 3^{rd}octave band plots for all test conditions at 90 degree receiver position

Figure 7.39 shows the change in SPL over the frequency spectra between REF and TUB design, where a positive y-value denotes a noise reduce due to the TUB design. Generally, the TUB provides a noise reduction across C1-C6 across most of the frequency range. A maximum reduction of 14dB is observed between 100 and 200s^{-1} at C1.

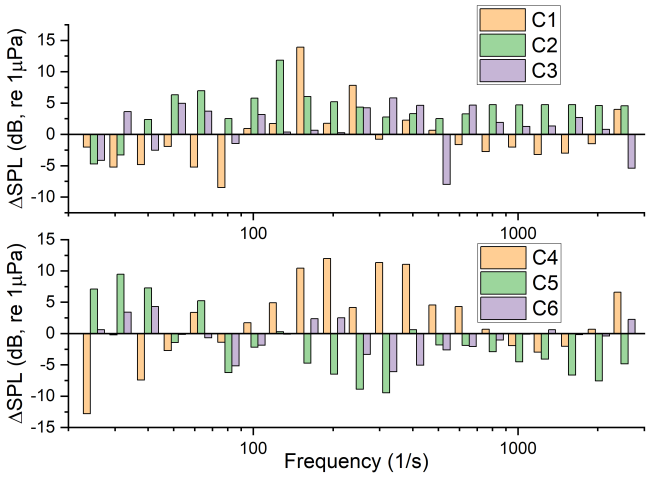

Figure 7.39: Far-field 3^{rd}octave band ΔSPL spectra for conditions C1-C6 (positive y-axis denotes noise reduction by TUB design)

The OASPL directivity plots are shown in Figure 7.40. In conditions C2-C6, there is a reduction in OASPL at all directions considered to a maximum of roughly 6dB at C5. Therefore in the above conditions, noise can be mitigated while simultaneously improving total thrust. This is also the case with propulsive efficiency except for C6. At C1 and C4 where both conditions were at the heaviest-loaded condition considered, $J = 0.1$, the OASPL increased by a maximum of 3.5dB. Nonetheless at both conditions, total thrust and propulsive efficiency are improved. This is due to the increase in the low-frequency noise as shown in the 3^{rd} octave band plots (see Figure 7.38) which is the source of the peak SPL across the spectrum and therefore, has a dominant weighting when calculating OASPL.

Therefore, although cavitation volume is reduced at conditions C1 and C4 in the heavy-loaded condition ($J = 0.1$) and the near-field frequency spectrums show a clear noise reduction, the far-field noise OASPL shows an increase in noise due to the increase in peak SPL in the low-frequency range. If for example, the 0-100s^{-1} range was omitted from the OASPL calculation for C1 and C4 the reduction would be 3 and 7dB OASPL, respectively.

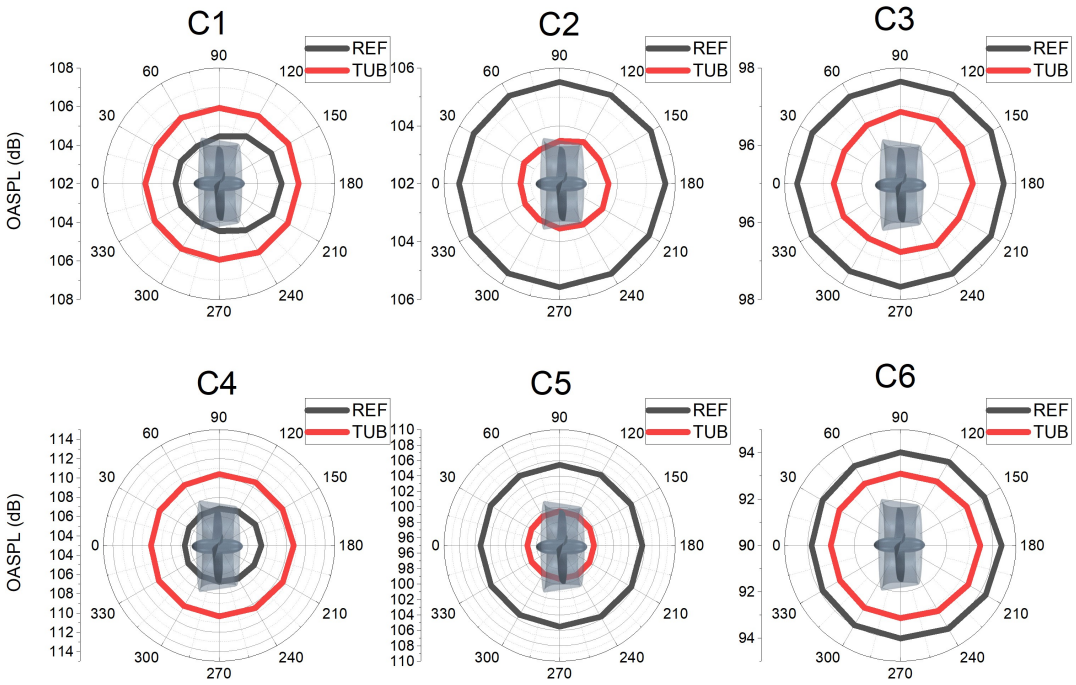

Figure 7.40: Far-field OASPL directivity for conditions C1-C6

7.3 Summary

This chapter has shown the effect on the hydrodynamic and hydroacoustic performance of the implementation of LE tubercles on the propeller of a model scale ducted propeller using a formulation of the DES method to solve the hydrodynamic flow-field and the FW-H acoustic analogy to propagate the noise to the

far-field. A summary of the findings are outlined below:

In summary, the first insights into how leading-edge tubercle blade modifications influence hydrodynamic and hydroacoustic performance of a benchmark model scale ducted propeller in both non-cavitating and cavitating conditions over a range of operating conditions have been investigated. The analysis was carried out using IDDES to solve the hydrodynamic flow-field and the Schnerr-Sauer cavitation model to describe cavitation. The FW-H acoustic analogy was used to propogate the sound to the far-field. The open-water hydrodynamic performance was validated against experimental tests, and the cavitation modelling technique was validated by comparing to experimental cavitation observations. From the analysis of the fundamental fluid dynamics and the propulsive performance, the main conclusions can be drawn:

Based on the above computational investigation, hydroacoustic analysis was conducted on the shorter wavelength tubercle modified blade because it was more optimal than the longer wavelength design in terms of hydrodynamic performance. It was found that the LE tubercle modified ducted propeller blade (TUB1) provided a reduction in OASPL in cavitating-conditions considered at J = 0.3 and 0.55 to a maximum of 6dB in all directions considered in the far-field. In addition to this, it has been evidenced that the application of leading-edge tubercles on a Kaplan-type propeller within a ducted propulsor will provide hydrodynamic merits with enhanced efficiency in most cavitating conditions and in highly loaded non-cavitating conditions.

In the presence of sheet cavitation, the leading-edge modified Kaplan propellers provided an improvement in total thrust coefficient in all operating conditions, to a maximum of 10%. At the same C_t, propulsive efficiency can be improved by a maximum of 6.5% in heavy-cavitating conditions.

The improvement was due to the reduction in cavitation volume at all operat-

ing conditions considered, to a maximum of approximately 50%. The reduction in sheet cavitation is believed to be due to the redistribution of the low-pressure region experiences at the baseline blade leading-edge, which can create a cavitation funnel effect.

Comparing the two tubercle designs where wavelength was varied, the longer wavelength reduced cavitation the most at the majority of conditions considered, although the difference between the two tubercle designs was marginal. On the other hand, in some heavier-cavitating conditions, the shorter wavelength was more successful in reducing cavitation due to the inclusion of the second tubercle closer to the blade root.

In some conditions, the propeller thrust was not improved. This is believed to be because the redistribution of cavitation has been funnelled into areas where contributes more to the thrust around 70% of the blade radius, although more in-depth analysis is required to confirm this statement. Therefore, considerations for future designs on balancing the load contribution and cavitation development are needed, as inspired from this finding. Despite this, due to the reduction in cavitation at all conditions the duct thrust improved, by a maximum of 71%, which resulted in an overall net improvement in total thrust coefficient.

In non-cavitating conditions, the inclusion of leading-edge tubercles can increase the propeller and duct thrust capability but there is also an increase in torque. When comparing the propulsive efficiency at the same thrust loading coefficient it was shown that both tubercle designs provide an improvement in efficiency in heavy-loaded conditions with a small compromise in the lightly-loaded conditions, shifting the operational curve of the propulsor.

Chapter 8

Full-Scale Leading-Edge Tubercle Ducted Propeller Exploration Study

This chapter focuses on the full scale numerical simulations of tubercle ducted propellers. Performance assessment at full scale is crucial as scale effects such as the difference in Reynolds number between model and full scale flows can vary the fundamental fluid dynamics as well as the global hydrodynamic and noise performance of the propulsors. This can result in inaccurate performance enhancement predictions at real scale if conclusions are solely drawn from model scale simulations and experimental test campaigns.

The test case geometry is presented in Section 8.1, while the results are presented and discussed in Section 8.2 and 8.3 and finally, a summary of the chapter in Section 8.4.

8.1 Test Case

Three test case geometries were the same as described in Chapter 6 and 7, the reference ducted propeller geometry (REF) shown in Figure 6.1a, the optimised tubercle duct with reference propeller (SLE), shown in Figure 6.1b and the optimal reference duct with leading-edge tubercle modified propeller blades, shown in Figure 6.1c previously denoted TUB1, is referred within this chapter as TUB. The three geometries considered are shown in Figure 8.1.

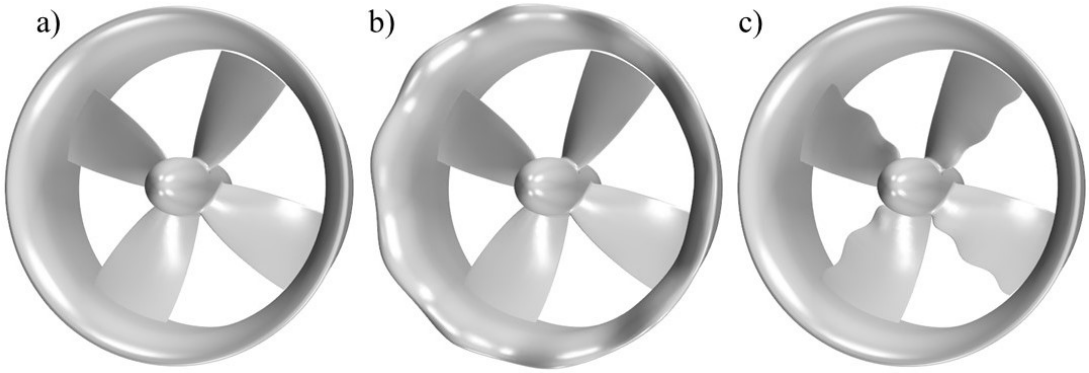

Figure 8.1: Geometry investigated a) REF, b) SLE (LE tubercle duct) and c) TUB, (LE tubercle ducted propeller blades)

8.2 Leading-Edge Tubercle Ducted Propeller Results

8.2.1 Time-Averaged Hydrodynamic Performance

Figure 8.2 shows the percentage difference ($\Delta\%$) of key time-averaged global performance coefficients for the SLE ducted propeller combination when compared to REF at a range of non-cavitating operating conditions. A general trend can be observed, where duct thrust and efficiency improves for all conditions, while propeller torque and thrust are reduced. The maximum improvement in

propulsive efficiency and duct thrust are observed in the heaviest-loaded condition considered, $J = 0.1$, by 2.6% and 3.6%, respectively. In addition, the maximum reduction in propeller thrust and torque is observed at $J = 0.1$ by 5% and 4%, respectively.

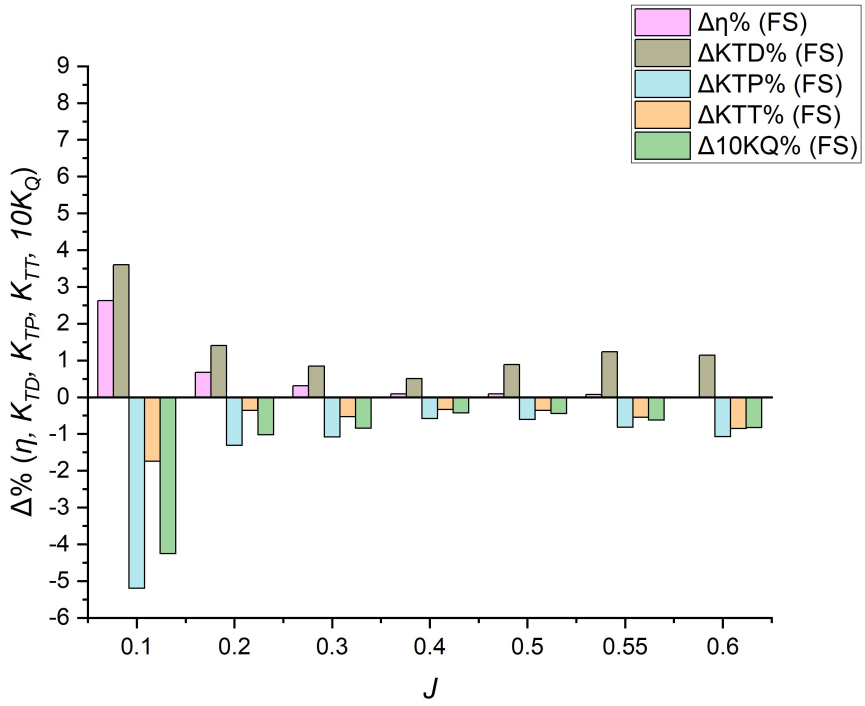

Figure 8.2: Open-water performance variable change when compared SLE to REF ducted propeller

Figure 8.3 shows the percentage difference ($\Delta\%$) of key time-averaged global performance coefficients for the SLE ducted propeller combination when compared to REF at a range of non-cavitating operating conditions in both model (presented in Chapter 6) and the current full scale results. The general trend of variation in coefficients between SLE and REF in both model and full scale is similar in terms of propulsive efficiency improvement across all operating conditions and a reduction in propeller thrust and torque. However, there is variation in results of duct thrust. At the low J the trend is similar whereby an increase in

duct thrust is observed in both model and full scale. In model scale, a reduction in duct thrust is observed by the SLE duct at $J = 0.5$, then an improvement at $J = 0.55$ and another reduction at $J = 0.6$. This was shown in Chapter 6 to be due the SLE's influence on the flow-separation behaviour on the outside of the duct. In the full scale, the flow-separation was delayed until $J > 0.8$, outwith the design envelope of the ducted propulsor. Therefore, duct thrust improvement was observed at $0<J<0.6$ in the full scale, similar to the conditions where no flow-separation on the outside of the duct was observed in the model scale ($0<J<0.4$). Figure 8.4 illustrates the difference in the flow behaviour on the outer duct section at $J = 0.55$ for REF in both model and full scale, showing LE flow separation in model scale but no LE flow separation present in the full scale study. Thus, the increase in scale and subsequent increase in Re resulted in the inception of LE flow separation to occur at a much later advance ratio on the outer duct section. Therefore, Re will affect the flow separation behaviour of the reference ducted propeller and thus, the hydrodynamic performance enhancement capability of LE tubercles as applied to the duct.

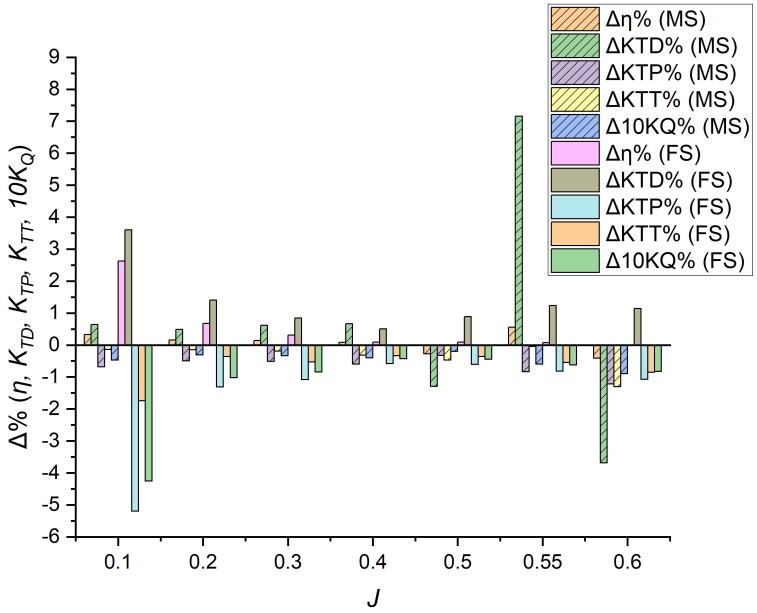

Figure 8.3: Open-water performance variable change when compared SLE to REF ducted propeller in both model and full scale

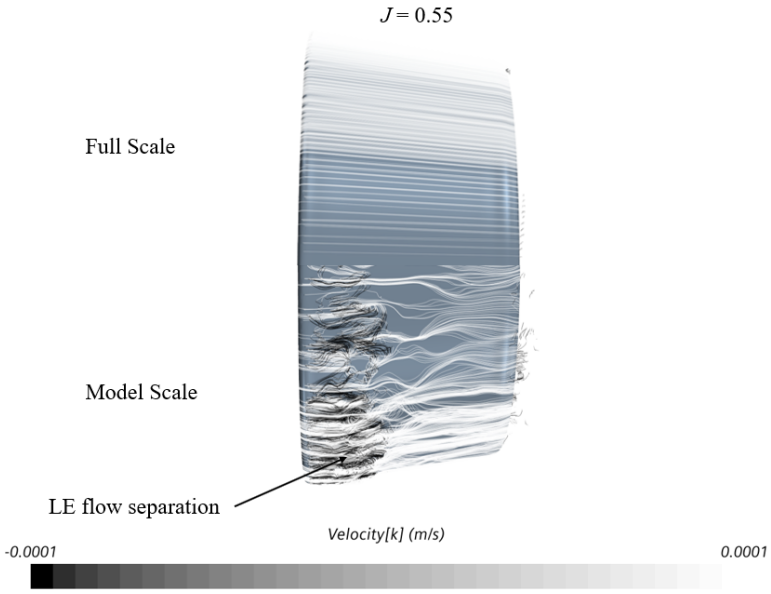

Figure 8.4: Velocity streamline coloured by streamwise velocity comparison on outer duct section of REF at $J = 0.55$ in both model and full scale

Figure 8.5 shows η vs. C_t for both REF and SLE ducted propeller combinations, as can be shown there is minimal difference in the curves between both designs which is a similar finding when conducting the investigation in model scale (presented in Chapter 6), although the SLE does provide a small increase in efficiency when comparing at the same C_t.

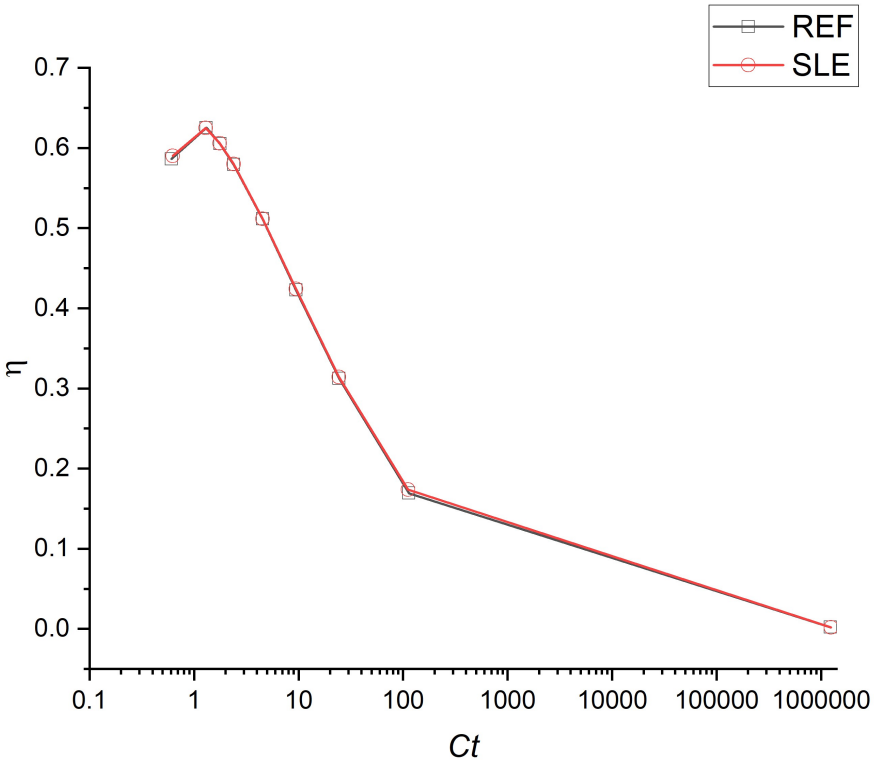

Figure 8.5: C_t vs. η for REF and SLE designs in full scale

8.2.2 Transient Blade Thrust Analysis

Figure 8.6 shows the comparison of single-blade thrust for REF and SLE ducted propeller combinations at $J = 0.1$, 0.3 and 0.55 in time and frequency domains. The peak-to-peak fluctuation in the time domain is more significant for SLE than for REF, particularly in $J = 0.3$, 0.55. In the frequency domain, the amplitude of the BPF reduces with the increase in J (reduction in blade loading). The

1^{st} BPF at $30s^{-1}$ can be observed at all conditions. This is the most significant peak in the frequency spectra at all operating conditions for the REF ducted propeller combination, whereas the tubercle passage frequency (TPF) at $75s^{-1}$ is the dominant peak for the SLE ducted propeller. As shown previously in Chapter 6, this is due to the streamwise vortex pairs induced by the tubercles into the propeller inflow and agrees well with previous model scale findings.

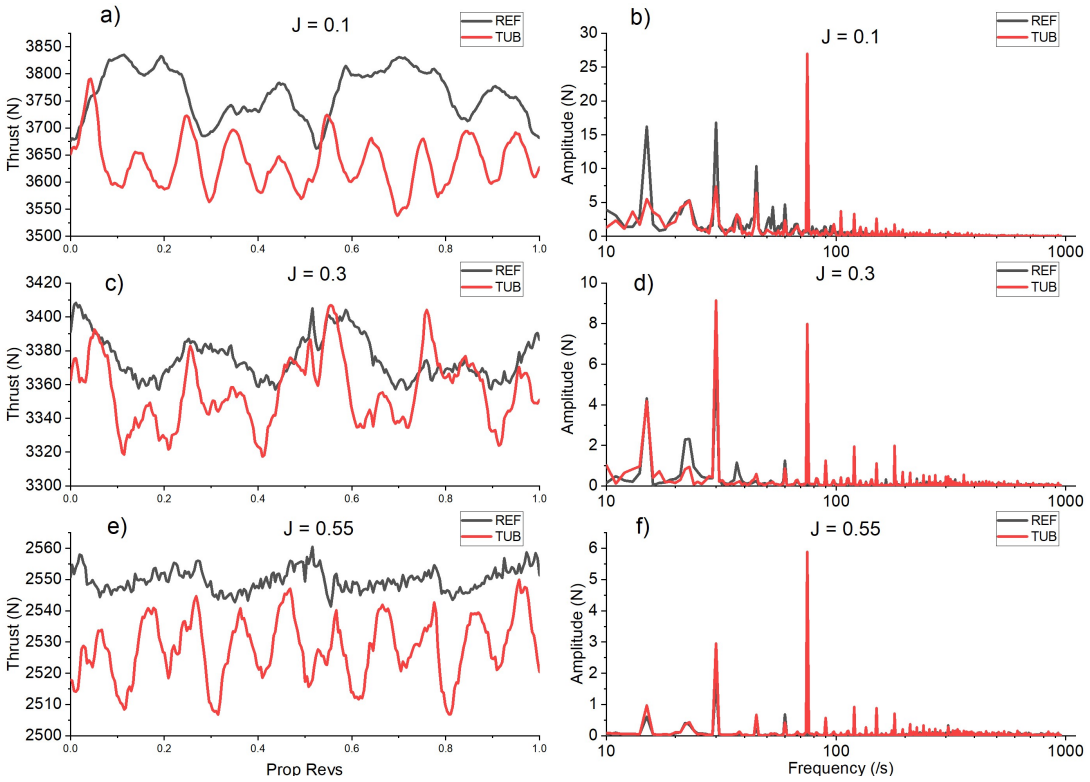

Figure 8.6: Blade thrust analysis in the time (a, c, e) and frequency (b, d, f) domains for REF and SLE ducted propeller combinations at $J = 0.1$, 0.3 and 0.55

8.2.3 Vortex Wake Dynamics

Figure 8.7 shows the Q-criterion plots ($\alpha = 100/s^2$) coloured by TKE of REF and SLE ducts at $J = 0.1$. The grid shows a distance of 1 hub length downstream

behind the boss cap of both ducted propellers, showing that the SLE encourages the vortex breakdown to initiate at a shorter distance from the propeller. When comparing volume integrals of TKE for REF and SLE, a reduction of 6% by SLE was predicted (see Table 8.1), showing that the inclusion of LE tubercles onto the duct can encourage the vortex breakdown and reduce the wake flow TKE from the propulsor, similar findings from the model scale study presented in Chapter 6.

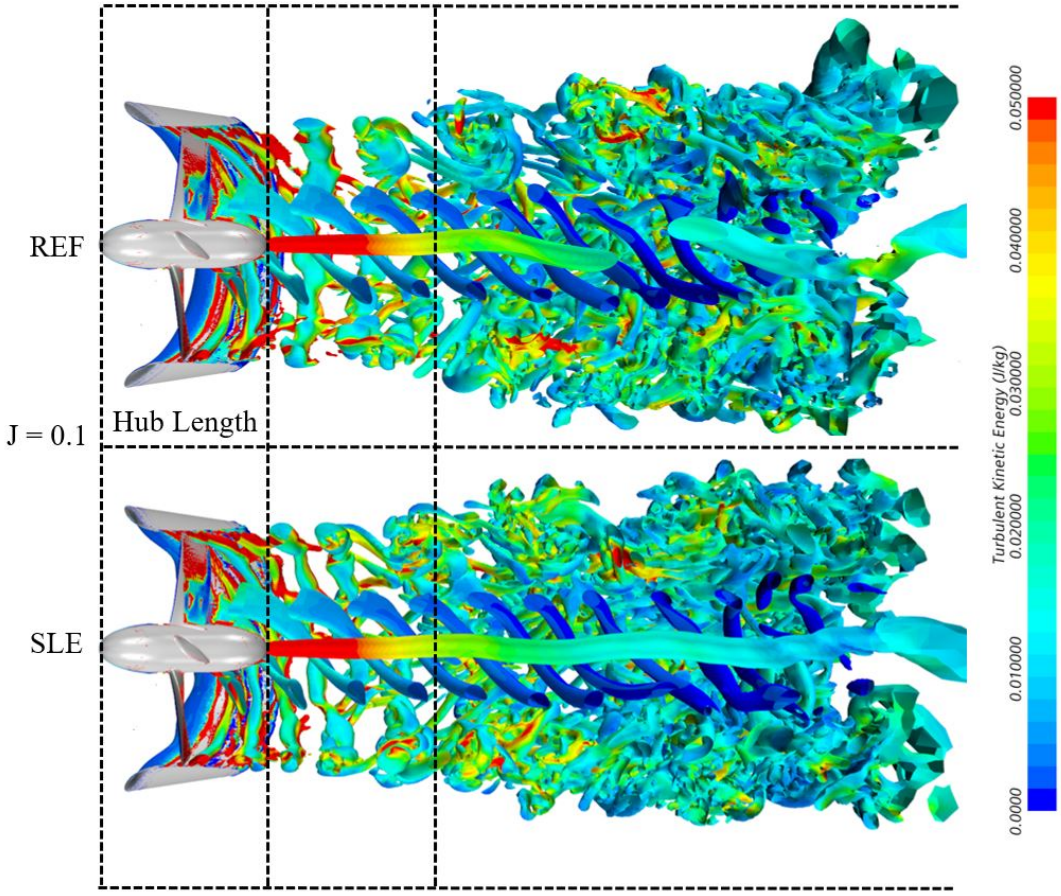

Figure 8.7: Mid-section Q-criterion plots, $\alpha = 100/s^2$ (coloured by TKE) of REF and SLE ducts at $J = 0.1$

Figure 8.8 shows the Q-criterion plots ($\alpha = 100/s^2$) coloured by TKE of REF and SLE ducts at $J = 0.3$ and 0.55 and the grid shows a distance of 1 hub length

downstream from the end of the boss cap. At $J = 0.55$, there is no immediate vortex breakdown as observed at $J = 0.1$. However, the SLE duct appears to introduce additional secondary vortex structures and short-wave instabilities within the main helical tip-leakage vortex which encourages the breakdown further downstream when compared the coherent tip-leakage vortex structure from REF. There is minimal change in TKE from the propulsor at both $J = 0.3$ and 0.55 as shown in Table 8.1.

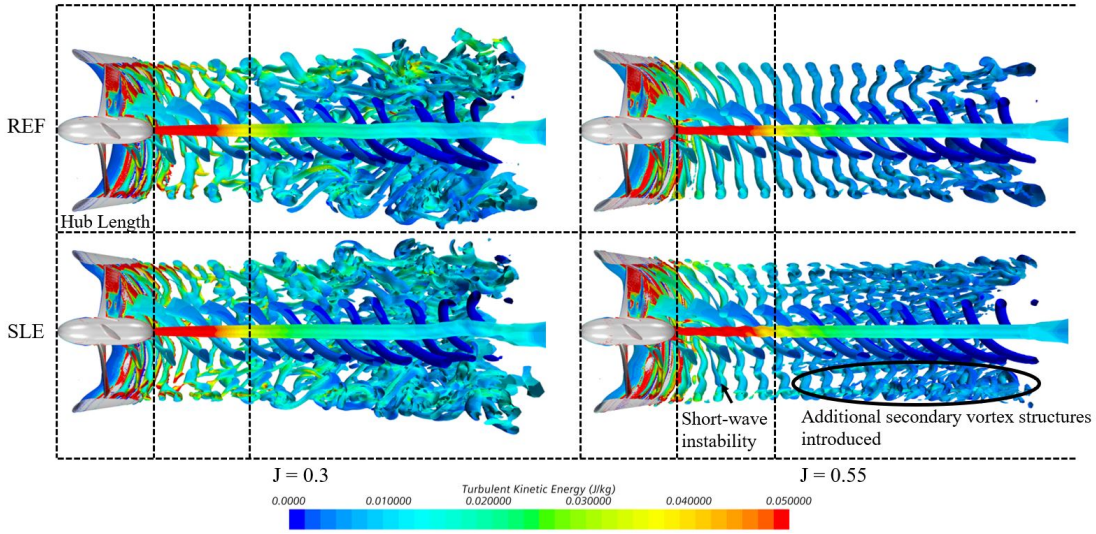

Figure 8.8: Mid-section Q-criterion plots, $\alpha = 100/s^2$ (coloured by TKE) of REF and SLE ducts at $J = 0.3$ and 0.55

Table 8.1 shows the volume integral TKE reduction (denoted as positive) of SLE duct compared to REF in the computational domain for $J = 0.1$, 0.3 and 0.55, respectively. There is negligible difference between REF and SLE at $J = 0.3$ and 0.55, however there is a 6% reduction in TKE by the SLE duct at $J = 0.1$. This is predominantly due to the LE tubercle duct modification's influence on the vortex development in the propeller slipstream at this operating condition.

J	$\Delta TKE\%$
0.1	6.05
0.3	-0.41
0.55	-0.59

Table 8.1: Volume integral TKE reduction (denoted as positive) of SLE duct compared to REF in the computational domain for $J = 0.1$, 0.3 and 0.55, respectively.

8.2.4 Noise Performance

Figure 8.9 shows the SPL vs frequency for near-field receiver M0 for both REF and SLE combinations at $J = 0.1$, 0.3 and 0.55 in the narrowband and 3^{rd} octave band. The 1^{st} BPF at $30s^{-1}$ can be observed clearly as the most distinct tonal peak at all conditions. Comparing the SLE to the REF ducted propeller, there is no significant variation in the SPL spectrum's at M0.

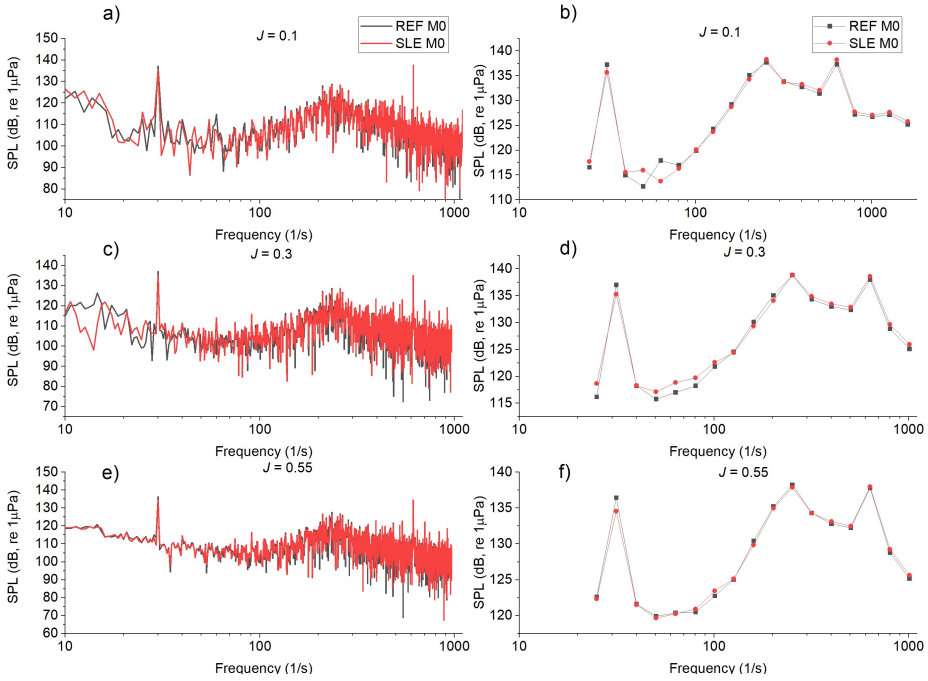

Figure 8.9: SPL plots at M0 in both narrowband and 3^{rd} octave band for REF and SLE

Figure 8.10 shows the SPL vs frequency for near-field receiver M4 for both REF and SLE combinations at $J = 0.1$, 0.3 and 0.55 in the narrowband and 3^{rd} octave band. When comparing to the spectrum plots at M0, it can be observed that the BPF at $30s^{-1}$ is not clearly visible at M4 at $J = 0.1$. This is because of the location of the M4 receiver, which is placed above the turbulent wake of the ducted propulsor when compared to M0 which is placed radially from the propeller plane and the operating condition which creates a high blade loading. Therefore, it shows that the non-linear noise contribution from the turbulence and vorticity of the slipstream wake structure can be significant but is dependant on the receiver location and ducted propeller operating condition which determines the blade loading. Comparing the REF and SLE at M4, it can be shown at $J = 0.1$ that a reduction in low frequency noise below $100s^{-1}$ of approximately 10dB is observed, with minimal difference predicted at $J = 0.3$ and 0.55.

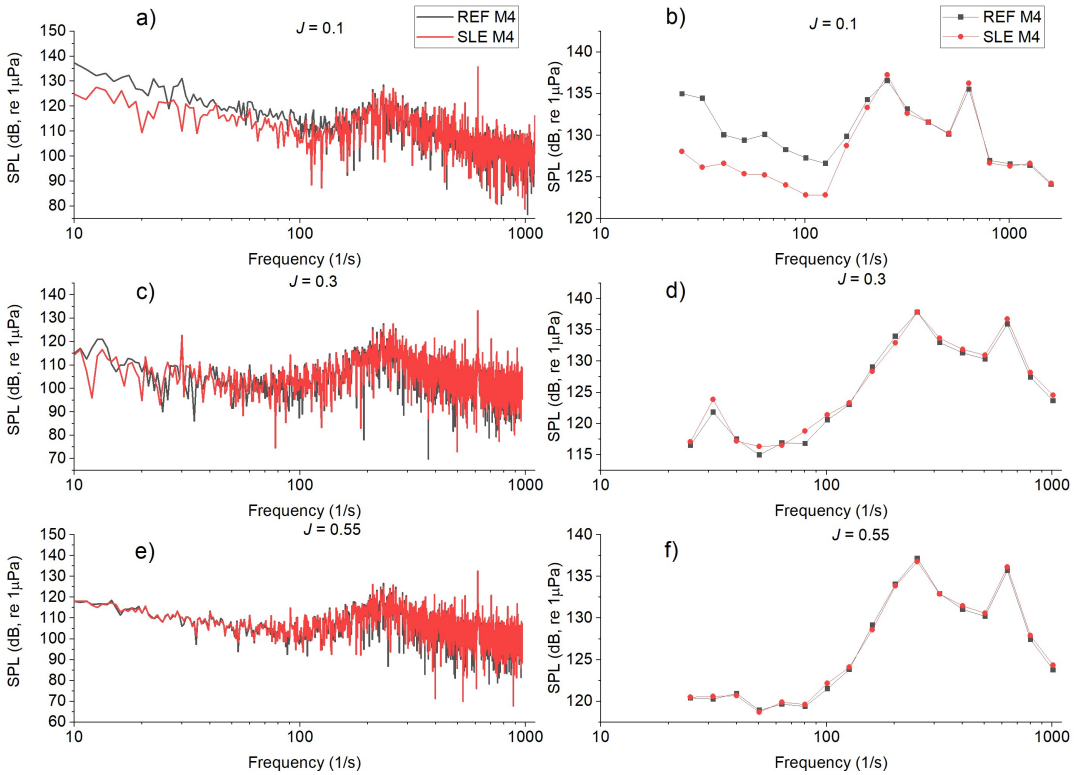

Figure 8.10: SPL plots at M4 in both narrowband and 3^{rd} octave band for REF and SLE

Figure 8.11 illustrates the far-field SPL plots at the 90^0 receiver in both narrowband and 3^{rd} octave band for REF and SLE. It is shown that a clear noise reduction by the SLE is present at $J = 0.1$ across the whole frequency range by approximately 3-4dB. At $J = 0.3$, there is minimal difference in SPL spectra and at $J = 0.55$ there is a small reduction in the low frequency range below $100s^{-1}$ of approximately 3-4dB. The BPF at $30s^{-1}$ is clearly visible at $J = 0.55$ but not observed as a distinct tonal peak at $J = 0.1$ and 0.3. This is due to the significance of the non-linear noise contribution at $J = 0.1$ and 0.3.

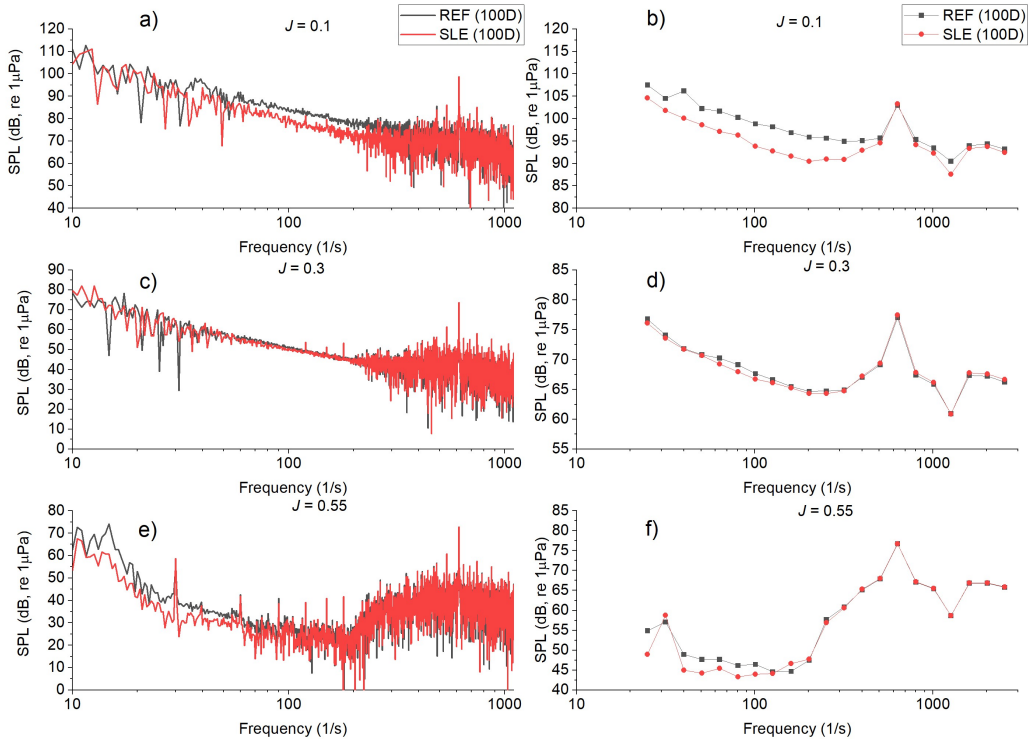

Figure 8.11: Far-field at 90^0 in both narrowband and 3^{rd} octave band for REF and SLE

Figure 8.12 shows the change in SPL between REF and SLE in the far-field 3^{rd} octave band (positive y-axis denotes a noise reduction by SLE). The SLE combination provides a noise reduction to a maximum of roughly 6dB at $J = 0.1$, while there is minimal difference at $J = 0.3$ across the spectrum.

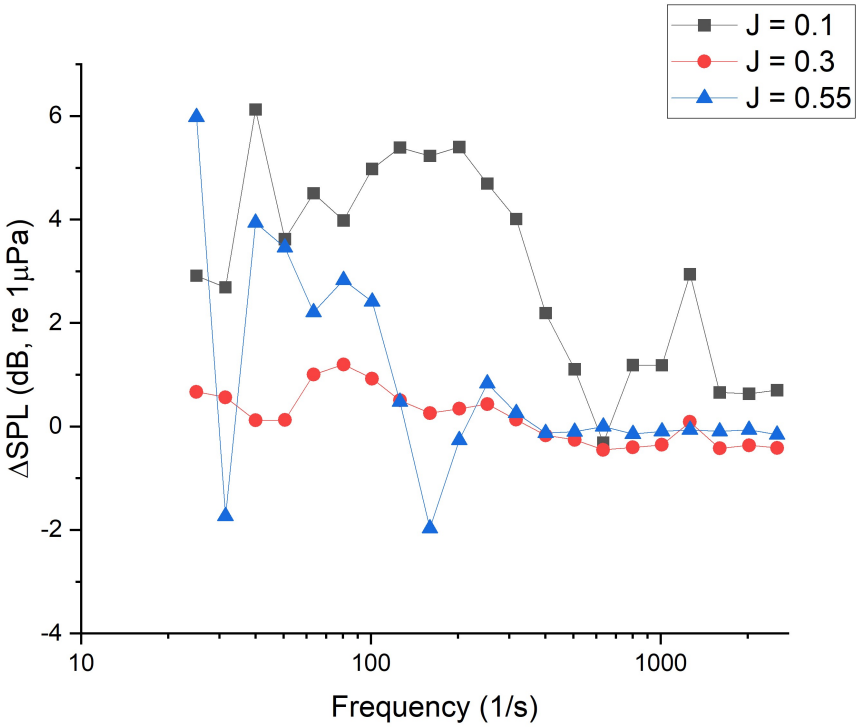

Figure 8.12: Change in SPL between REF and SLE in the far-field 3^{rd} octave band (positive y-axis denotes a noise reduction by SLE)

Figure 8.13 shows the OASPL far-field directivity plots. It shows that the SLE ducted propeller combination can reduce the noise signature in the far-field by 4dB at $J = 0.1$, agreeing well with previous model scale findings in Chapter 6, with minimal difference at $J = 0.3$ and 0.55.

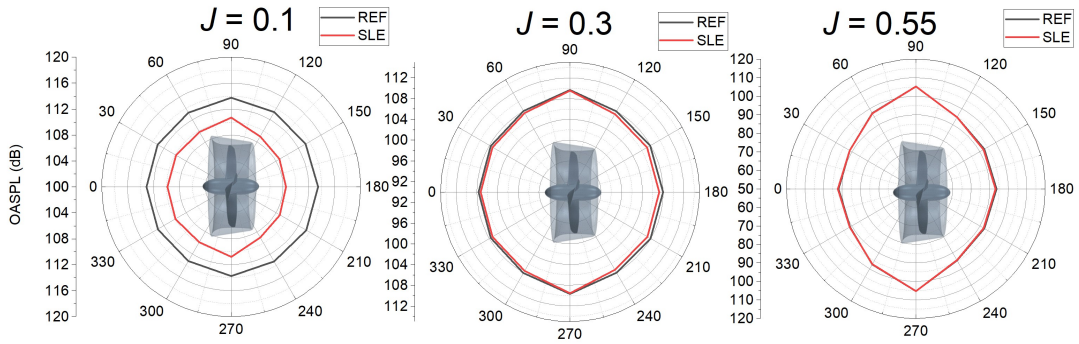

Figure 8.13: OASPL far-field directivity plots

8.3 Leading-Edge Tubercle Ducted Propeller Blades Results

8.3.1 Time-Averaged Hydrodynamic Performance

Figure 8.14 shows the open-water performance variable change in non-cavitating conditions when comparing TUB to the REF ducted propeller combination. At all conditions, the TUB design increases duct thrust, by a maximum of 3.25%, total thrust, by a maximum of 2% and propeller torque, by a maximum of 2.75%. At both $J = 0.3$ and 0.55, propeller thrust is increased by a maximum of 1.75% and propulsive efficiency is reduced marginally by below 0.5%. The general trends agree well with the previous model scale study presented in Chapter 7.

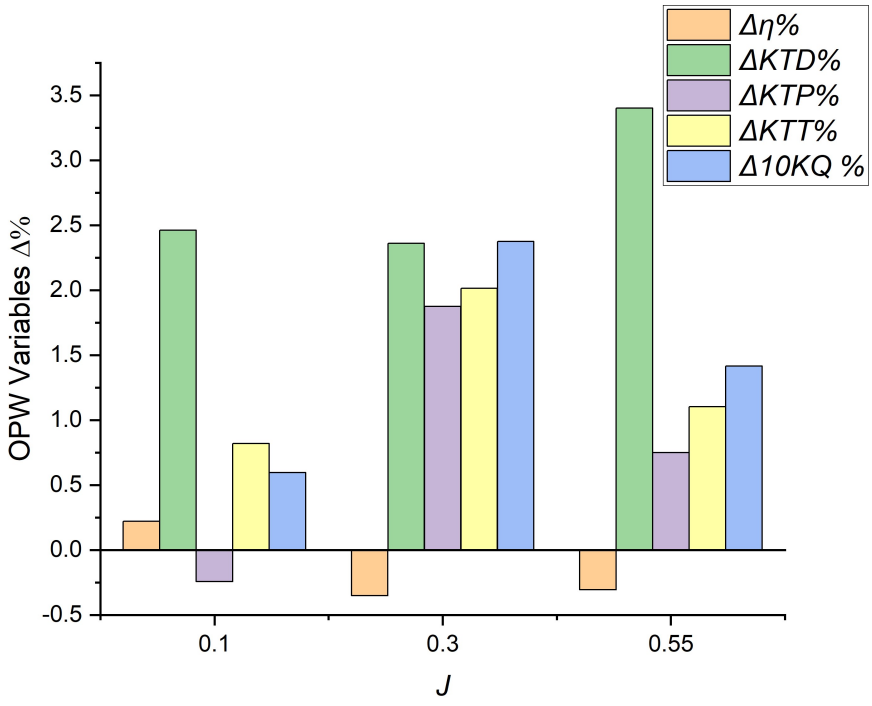

Figure 8.14: Open-water performance variable change comparing TUB to REF ducted propellers in non-cavitating conditions

Figure 8.15 shows the open-water performance variable change in cavitating

conditions when comparing TUB to the REF ducted propeller combination. Generally the overall thrust is improved by a maximum of 7%, while the duct thrust is improved at all conditions up to 32.5%. Propeller thrust increased at C1 by 6% but decreased at C4 by 9%, while at the other conditions there is marginal change, similar to propeller torque where there is an increase of 6% at C1 and a reduction of 4% at C4. Propulsive efficiency increases by a maximum of 6% at C2.

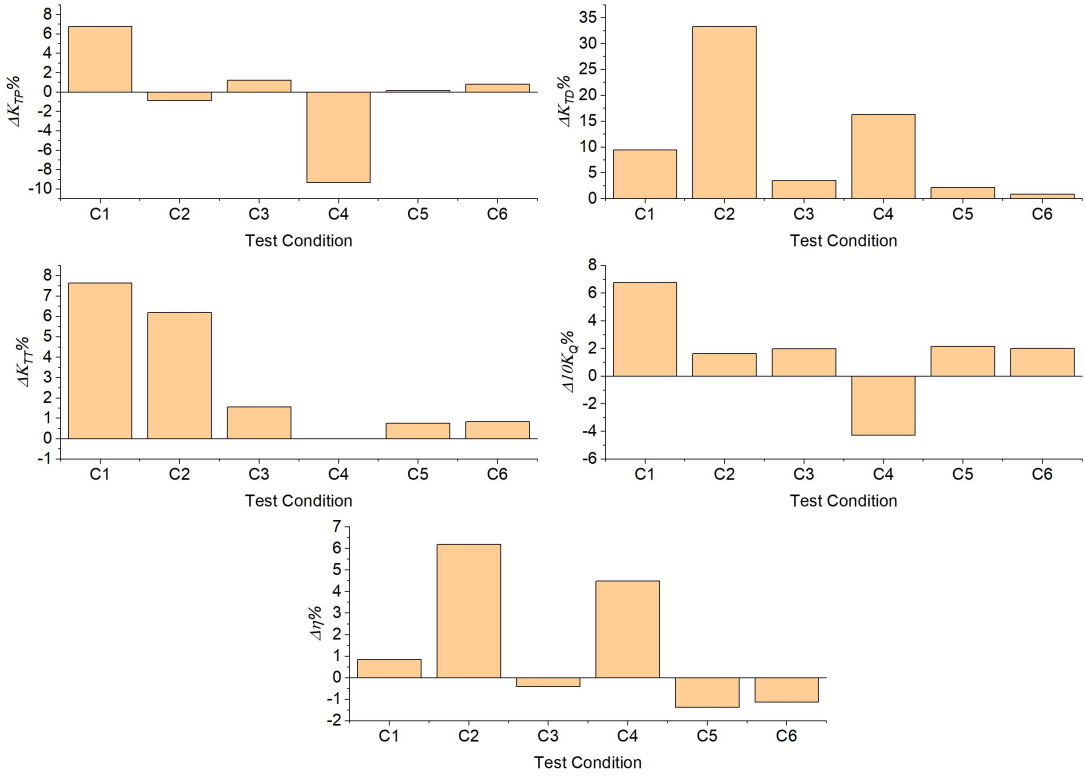

Figure 8.15: Open-water performance variable change when compared TUB to REF ducted propeller in cavitating conditions

Figure 8.16 shows the propulsive efficiency vs thrust loading coefficient for both REF and TUB ducted propeller combinations in heavy-cavitating conditions. An extra 4 test cases were ran at the heavy cavitating condition at $J =$ 0.12, 0.14, 0.2 and 0.4. The propulsive efficiency enhancement by the TUB design

is clearly observed when compared at the same thrust loading condition.

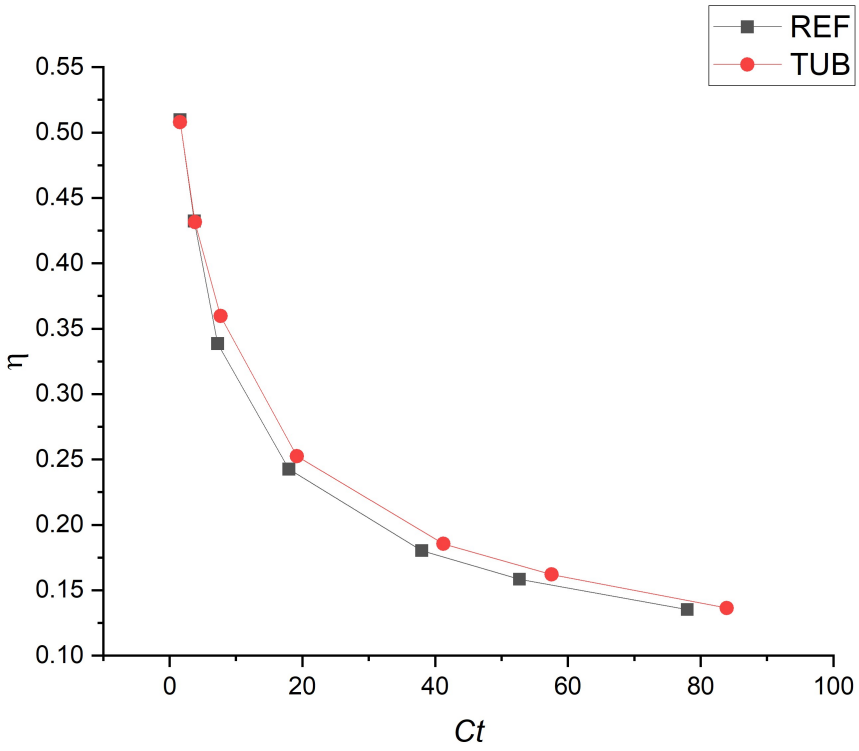

Figure 8.16: η vs. C_t for REF and TUB designs in full scale in heavy-cavitating conditions

Figure 8.17 shows the percentage change in propulsive efficiency when comparing the TUB to REF ducted propeller case at the same thrust loading condition. A maximum efficiency improvement of 7.7% and an average of 6.2% over the 8 loading conditions considered was observed.

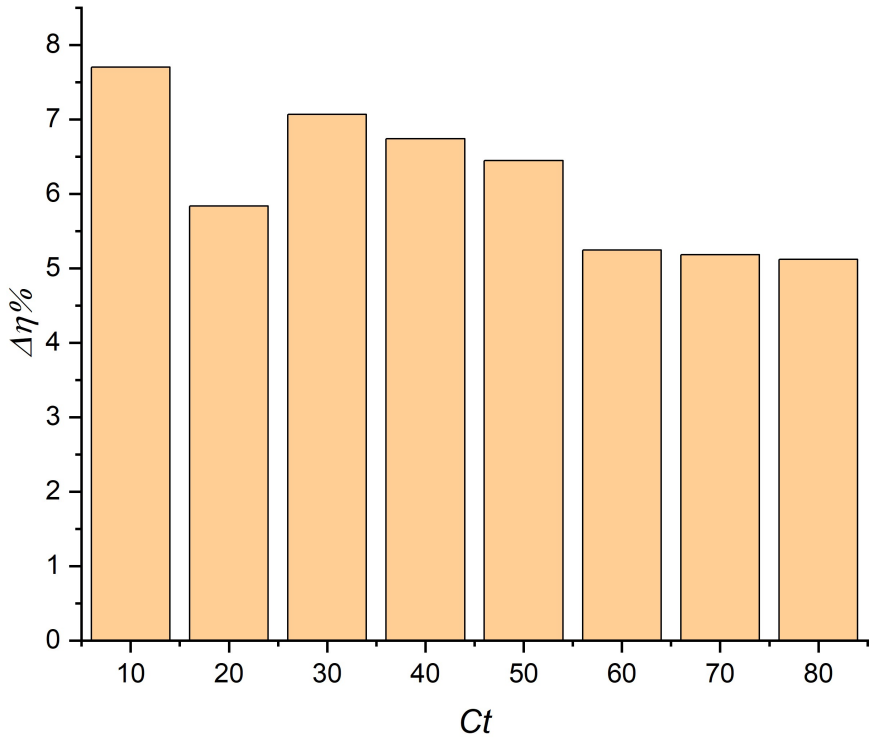

Figure 8.17: Percentage change in η when compared at the same C_t in full scale cavitating conditions

Figure 8.18 shows the percentage change in propulsive efficiency when comparing the TUB to REF ducted propeller case at the same thrust loading condition for both the present full scale study and the previous model scale study (conducted in Chapter 7). The results show the propulsive efficiency enhancement by the TUB design is similar in full scale conditions with an average enhancement of 6.2% in full scale and 5.4% in model scale.

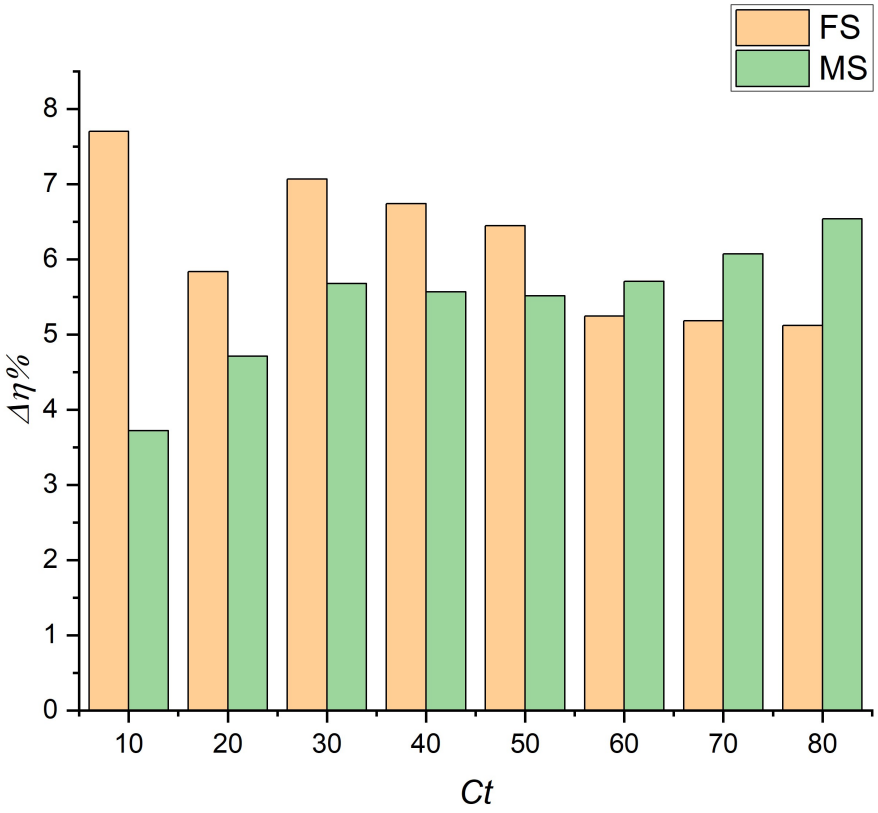

Figure 8.18: Percentage change in η when compared at the same C_t in full scale and model scale cavitating conditions

8.3.2 Transient Load Analysis

Figure 8.19 shows the single-blade thrust fluctuation in the time domain for both REF and TUB ducted propeller combinations in cavitating conditions. The fluctuating nature of the thrust at C3, C5 and C6 is similar between REF and TUB blade designs. A reduction in single-blade thrust fluctuation is clearly observed at C1 and C2 by the TUB design with peak-to-peak values reduced considerably.

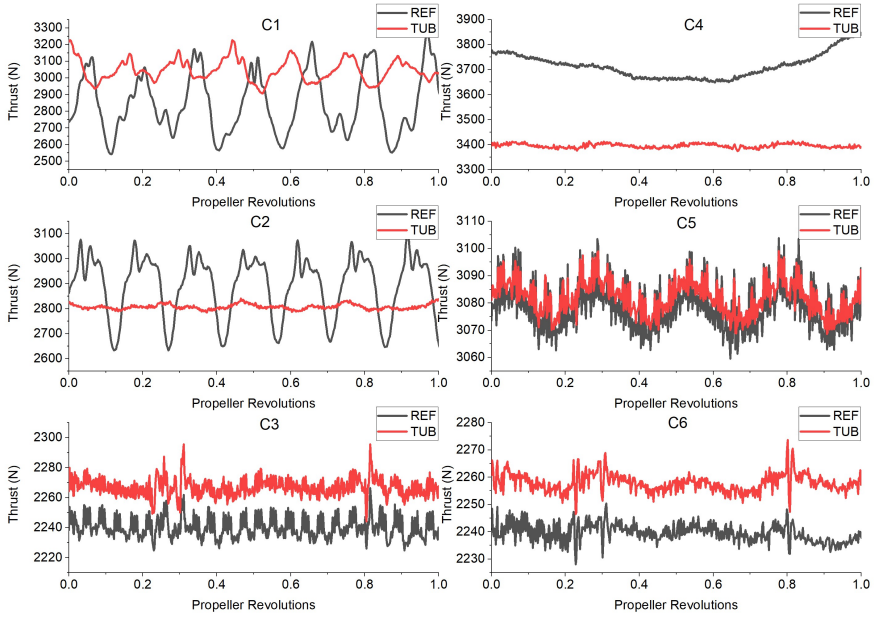

Figure 8.19: Single-blade thrust fluctuation in the time domain for REF and TUB at all cavitating test conditions considered

Figure 8.20 shows the standard deviation of the time domain single-blade thrust data set for REF and TUB ducted propeller combinations. At all conditions the standard deviation of thrust time data for the TUB design is less than the REF design with the exception of C3 of which there is minimal difference.

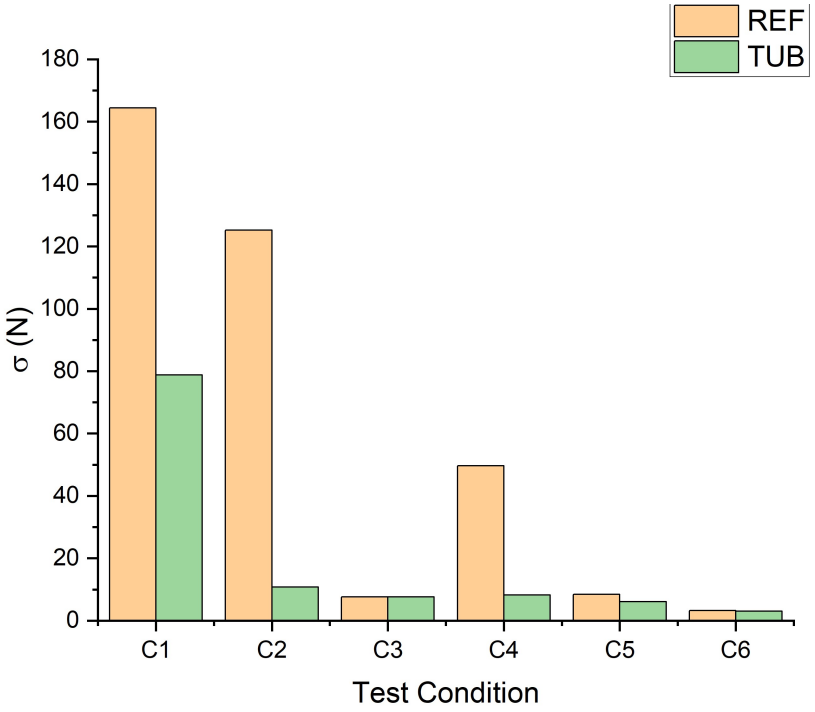

Figure 8.20: Standard deviation of the time domain single-blade thrust data set for REF and TUB

Figure 8.21 shows the single-blade thrust amplitude in the frequency domain for REF and TUB at all cavitating test conditions considered. At C3, C5 and C6, there is minimal different in the spectra between REF and TUB designs. Comparing the REF design across the test conditions, C1 and C2 are dominated by a discrete peak at $50s^{-1}$, while the other conditions are dominated by a discrete peak at the 1^{st} BPF at $30s^{-1}$ in addition to other high frequency peaks at C3 and C6 at $177s^{-1}$ and $1117s^{-1}$, and general low frequency broadband signal at C4, respectively.

Comparing the TUB design to the REF design at C1, a reduction in amplitude at $50s^{-1}$ is observed. At C2, the amplitude at $50s^{-1}$ is the dominant discrete peak for the REF design but is indistinguishable for the TUB design, which is dominated by the 1^{st} BPF although insignificant in amplitude when compared

to the dominant peak for REF design at this condition. At C3, the TUB design reduces the amplitude peak at 177s^{-1} when compared to REF signal, while the amplitude at the 1^{st} BPF is similar for both designs. At C4, the 1^{st} BPF peak is larger in magnitude than the REF, but the REF signal has more of a broadband signal in the low frequency range than the TUB design. At C5 and C6, the REF and TUB signal is dominated by the 1^{st} BPF and are similar in magnitude. However at C6, there is a high amplitude discrete peak at 1117s^{-1} for the REF design that is reduced by the TUB design. Generally, the TUB design can mitigate the dominant discrete peaks in the spectra when compared to the REF design.

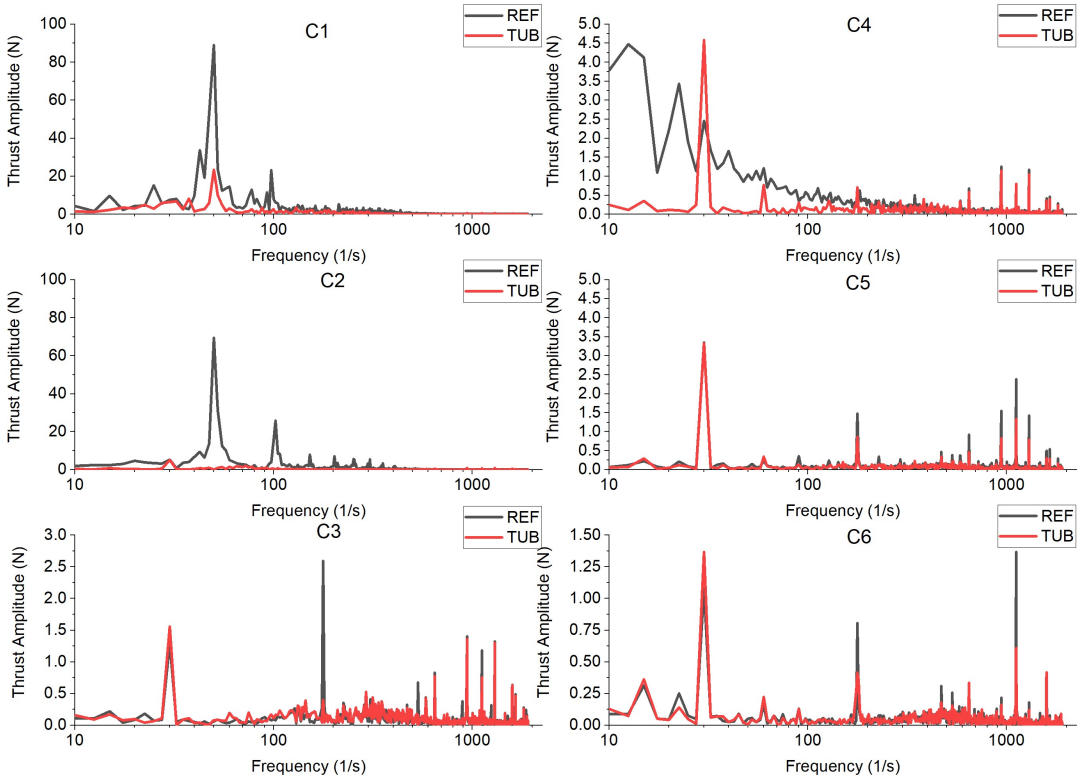

Figure 8.21: Single-blade thrust amplitude in the frequency domain for REF and TUB at all cavitating test conditions considered

8.3.3 Cavitation Development

Figure 8.22 shows the cavitation volume and percentage reduction due to TUB blade when compared to REF. The cavitation volume is reduced with reduced loading condition, increased J. The TUB design can reduce the cavitation extent in all conditions considered by over 60% at C4 and an average of 34%. This agrees well with previous model scale results presented in Chapter 7 where the maximum cavitation volume reduction was also observed at C4.

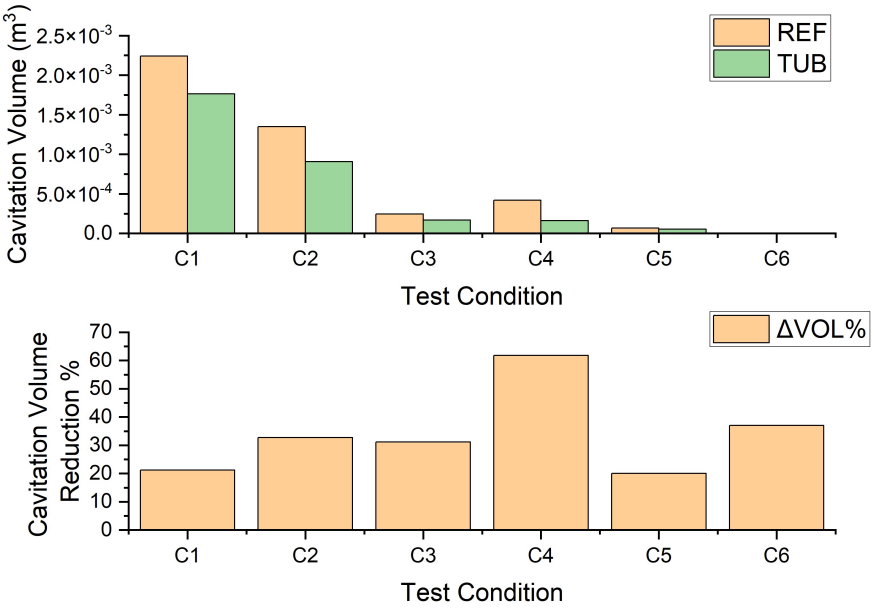

Figure 8.22: Cavitation volume (top) and percentage reduction (bottom) due to TUB blade when compared to REF

Figure 8.23 and 8.24 show the cavitation volume visualisation ($\alpha = 0.1$) for REF and TUB ducted propellers in heavy and light cavitating conditions, respectively. The cavitation volume can be seen to more extensive with increased loading, reduction in J for both cavitation numbers tested. The cavitation funnel effect, whereby the cavitation is encouraged behind the trough of the tubercle is clearly observed at C4, there is also compartmentalisation encouraged between the sheet cavitation and the tip-leakage vortex cavitation in C2. These findings

agree well with previous model scale observations presented in Chapter 7 with the cavitation funnel effect most clear at C4 also. Therefore LE tubercles can reduce the cavitation severity across the blade with varying control depending on the loading condition and location of the cavitation.

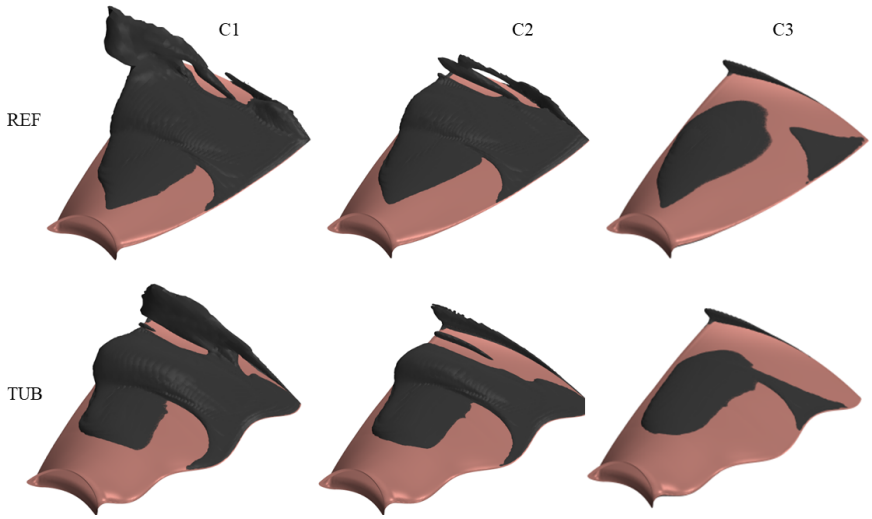

Figure 8.23: Cavitation volume visualisation ($\alpha = 0.1$) for REF and TUB ducted propellers in heavy cavitating conditions

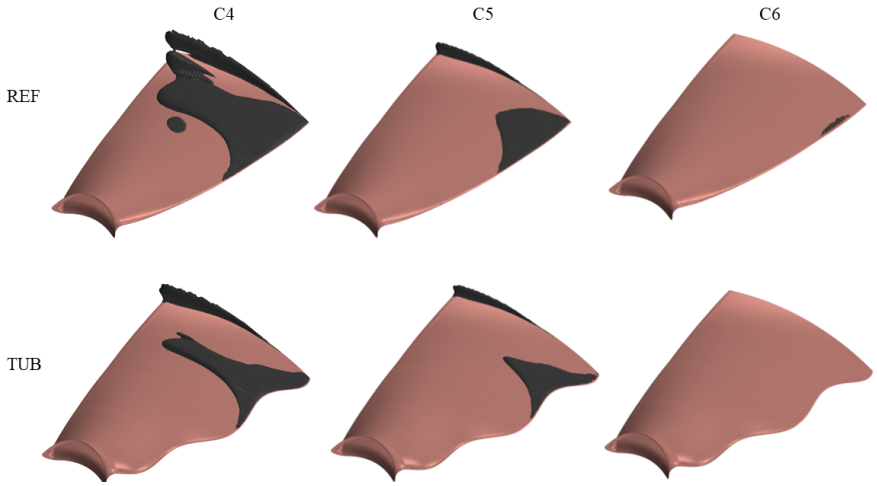

Figure 8.24: Cavitation volume visualisation ($\alpha = 0.1$) for REF and TUB ducted propellers in light cavitating conditions

8.3.4 Noise Performance

Figure 8.25 and 8.26 display the near-field narrowband and 3^{rd} octave band plots for REF and TUB designs at M0 in all cavitating test conditions, respectively. In heavy-cavitating conditions, the BPF is not significant (C1 and C2) when compared to conditions with light cavitation present (C5 and C6), where the BPF is the significant tonal within the spectrum. There is minimal difference observed between REF and TUB design at C3, C4 and C5. However at C1, C2 and C6, a reduction in SPL across the spectra is observed clearly by the TUB design. At C6, the 1^{st} BPF is increased by the TUB design by roughly 10dB, likely due to the increased blade loading for the TUB design at this condition and minimal cavity volume present. At C1, the peak at $50s^{-1}$, observed in the thrust fluctuation spectra at the same condition, is the dominant peak at this condition although it is considerably reduced by the TUB design by 14dB. In addition, the broadband noise is reduced by roughly 5dB below $500s^{-1}$. At C2, the peaks at $50s^{-1}$ and $100s^{-1}$ are dominant in the REF spectrum, but insignificant in the TUB spectrum, reduced by over 30dB. The broadband noise is reduced by the TUB design by roughly 10dB. Generally at M0, in the heavy-cavitating conditions, the noise can be reduced by the TUB design in both tonal noise seen at C1 and C2 and also in the broadband signal.

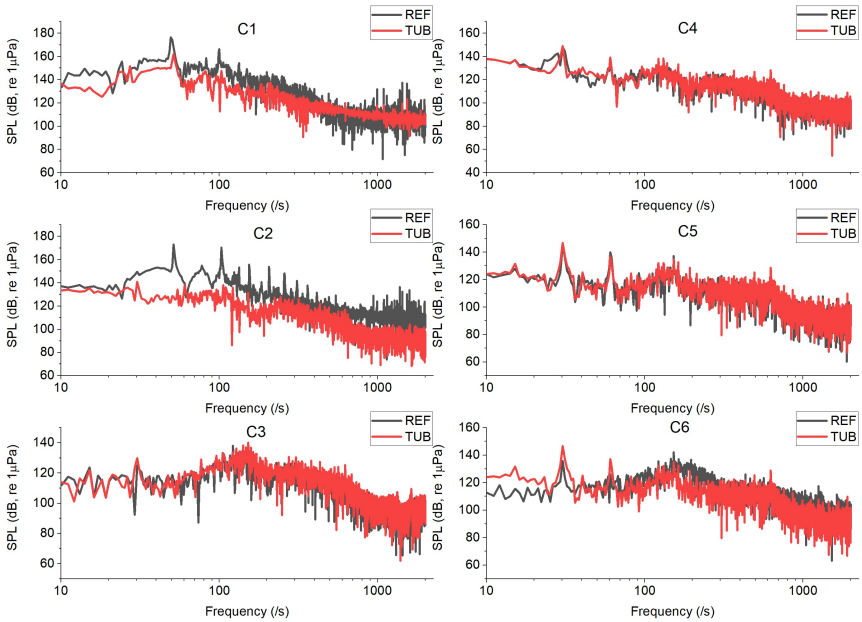

Figure 8.25: Near-field narrowband plots for REF and TUB designs at M0 in all cavitating test conditions

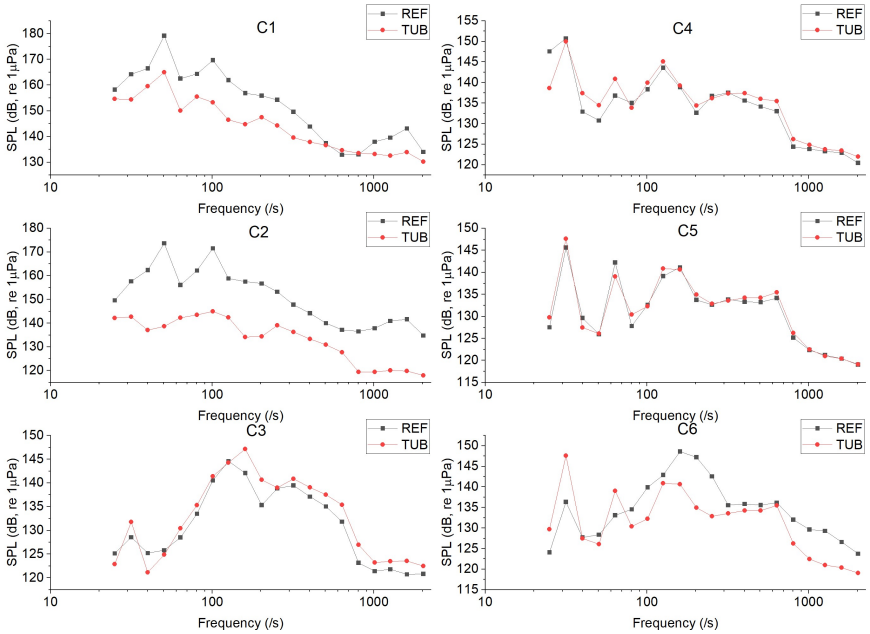

Figure 8.26: Near-field 3^{rd} octave band plots for REF and TUB designs at M0 in all cavitating test conditions

Figure 8.27 and 8.28 display the far-field narrowband and 3^{rd} octave band plots for REF and TUB designs in all cavitating test conditions, respectively. There is no clear difference in the spectra's of REF and TUB at C3, C4 and C6. Comparing the TUB to REF design at C1 and C2, the peak present in the REF spectrum at $50s^{-1}$ and $100s^{-1}$ has been reduced considerably by the TUB design (over 40dB at $50s^{-1}$ at condition C2), similar to the observations in the near-field receiver analysis. The broadband noise at C1 and C2 is also reduced by the TUB design by roughly 5dB. At C5, there is a reduction in low frequency broadband below $60s^{-1}$ by roughly 3dB although there is an increase in broadband noise in the higher frequency range. Therefore, where cavitation extent is severe, in conditions such as C1 and C2, the reduction in cavitation results in a reduction in broadband and peak SPL across the frequency range considered while simultaneously improving the overall thrust coefficient and propulsive efficiency.

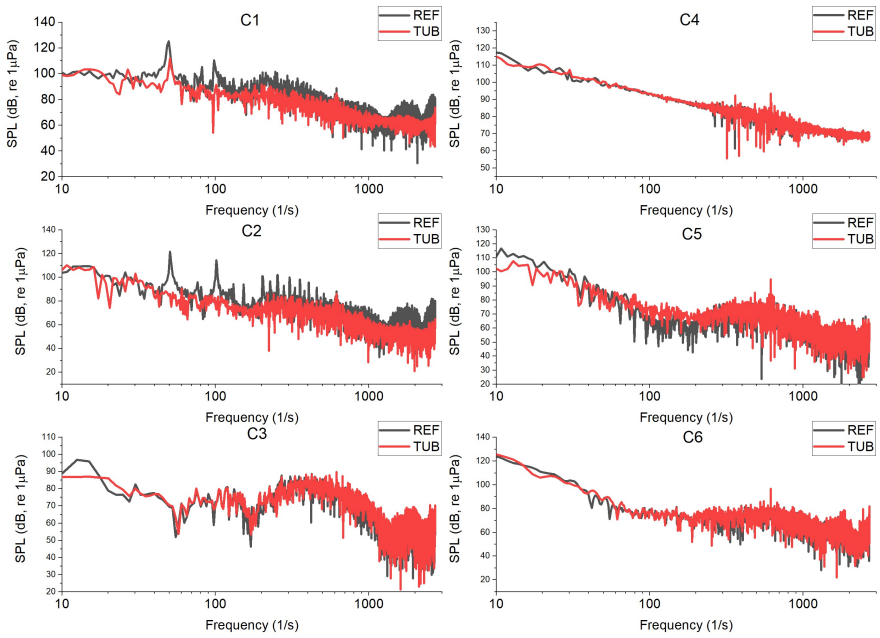

Figure 8.27: Far-field narrowband plots for REF and TUB designs in all cavitating test conditions

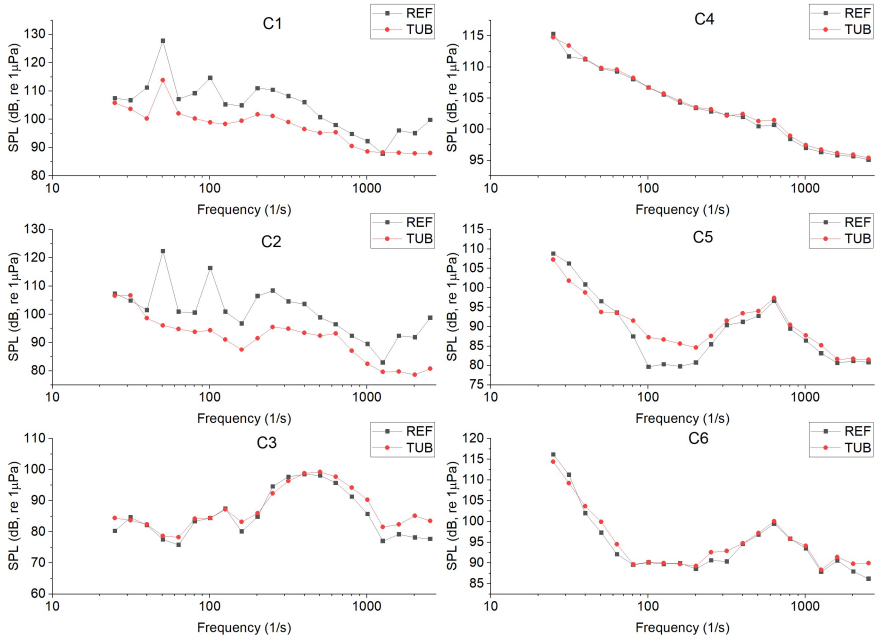

Figure 8.28: Far-field 3^{rd} octave band plots for REF and TUB designs in all cavitating test conditions

Figure 8.29 displays the far-field OASPL directivity plots for REF and TUB designs in all cavitating test conditions. Generally, there is minimal difference in OASPL at C3, C4 and C6 between REF and TUB designs. At C1, C2 and C5, there is a reduction in OASPL of 10, 13 and 2dB by the TUB design, respectively. Therefore the TUB design in full scale conditions can reduce the OASPL in the far-field by a maximum of 13dB, while also improving hydrodynamic performance, particularly in the heavy-cavitating and high blade loading conditions such as C1 and C2.

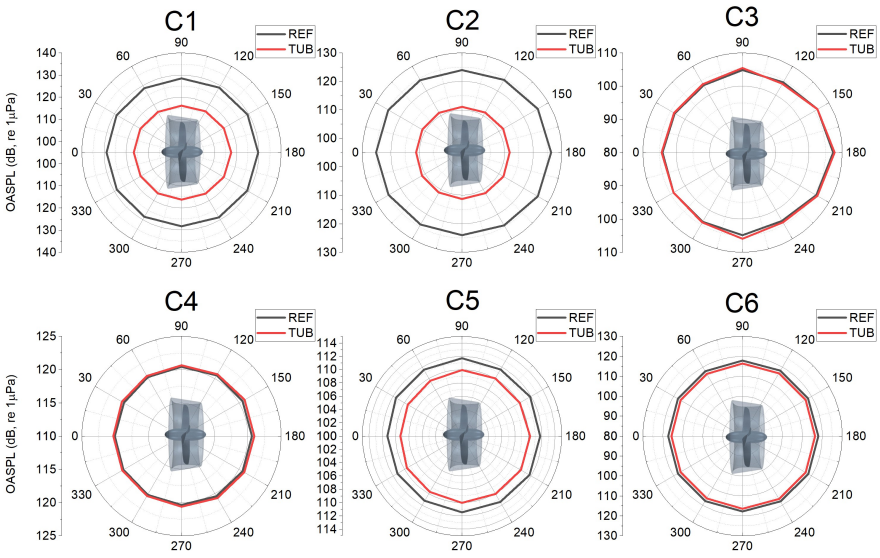

Figure 8.29: Far-field OASPL directivity plots for REF and TUB designs in all cavitating test conditions

8.4 Summary

This chapter has shown the effect on the hydrodynamic and hydroacoustic performance of the implementation of LE tubercles on the duct and propeller of a full scale ducted propeller using a formulation of the DES method to solve the hydrodynamic flow-field and the FW-H acoustic analogy to propagate the noise to the far-field. The following sections summarise the findings for each concept.

8.4.1 Leading-Edge Tubercle Duct Application

Leading-edge tubercles as applied to the duct in full scale conditions enhanced the duct thrust and propulsive efficiency at all non-cavitating test conditions considered. the increase in scale and subsequent increase in Re resulted in the inception of LE flow separation to occur at a much later advance ratio on the outer duct section. Therefore, Re will affect the flow separation behaviour of the

reference ducted propeller and thus, the hydrodynamic performance enhancement capability of LE tubercles as applied to the duct. The counter-rotating streamwise vortices resulted in a discrete peak in the single-blade thrust spectra related to the vortex pair number and the propeller rotation rate which was not observed from the reference design. In the far-field, the leading-edge tubercle modified duct reduced the OASPL by 4dB at $J = 0.1$. The general trends observed within the current study agree well with the conclusions drawn in the model scale study presented in Chapter 6

8.4.2 Leading-Edge Tubercle Ducted Propeller Blade Application

Leading-edge tubercle modified ducted propeller blades in full scale conditions reduced the OASPL in the far-field by a maximum of 13dB, while also improving hydrodynamic performance, particularly in the heavy-cavitating and high blade loading conditions such as C1 and C2. At the same thrust loading condition, the propulsive efficiency was enhanced by a maximum of 7.5%. The sheet cavitation was mitigated by the leading-edge tubercles by up to 60%. In addition, the load fluctuation of the single-blade thrust was mitigated in the heavy-cavitating conditions, which could improve the life of the component. The general trends observed within the current study agree well with the conclusions drawn in the model scale study presented in Chapter 7.

Chapter 9

Conclusions and Recommendations for Future Work

Chapter 9 presents an overall review of the research study with an emphasis on the original contributions made to the state-of-the-art while achieving the aim and objectives of the research study which involved an investigation into the feasibility of hydrodynamic and hydroacoustic performance enhancement of ducted propulsors through leading-edge tubercle duct and blade modifications. The chapter also summarises the main conclusions of the research as well as providing recommendations for future research.

The overall review of the thesis and contributions to the state-of-the-art are presented in Section 9.1. The main conclusions are outlined in Section 9.2. Finally, the recommendations for future research are given in Section 9.3.

9.1 Overall Review of the Thesis and Contributions to the State-of-the-art

Leading-edge tubercles have shown promising hydrodynamic and noise benefits on a variety of applications like aerofoils and tidal turbines. However, before the

initiation of this research study, they had not yet been applied to marine ducted propulsors to investigate potential hydrodynamic and hydroacoustic performance improvements.

With the aim of exploring the feasibility of enhancing the hydrodynamic and noise performance of marine ducted propulsors, this PhD research study has made original and useful contributions to the state-of-the-art research in applying the LE tubercle concept to both the duct and blade design and demonstrated its positive effects on the marine ducted propulsor performance. In order to meet the research aim of the study, the thesis presents for the first time a systematic set of numerical investigations using this biomimetic concept for performance improvement on marine ducted propulsors. Within the research's limitations, the supporting findings not only provide confidence in applying this biomimetic concept to marine ducted propulsors in a full scale demonstration but also provide invaluable insights into the influence of leading-edge tubercles on the fundamental fluid dynamics of marine ducted propulsors that can be further exploited on a wide variety of applications.

The research study had six main objectives stated in Chapter 1 and these were successfully addressed within the subsequent chapters. The state-of-the-art literature was reviewed in regards to marine propulsor noise sources, the leading-edge tubercle concept and the numerical and experimental methodologies within Chapter 2, addressing *Objective 1.* Chapter 2 indicated that extremely limited research was available on the application of leading-edge tubercles on marine ducted thrusters and their effect on the hydrodynamic and noise performance of the propulsor, which was identified as the main research gap that needed to be addressed and bridged. This would require further investigation to understand if leading-edge tubercles could improve the hydrodynamic and noise performance of marine ducted propulsors in addition to enhancing the knowledge of the fun-

damental fluid dynamics of the tubercle concept behind any performance change. Chapter 2 also identified additional research gaps and appropriate methodologies used to conduct the main investigative studies presented in the main chapters of the thesis.

Chapter 3 satisfied *Objective 2* by selecting the reference ducted propulsor and Chapter 4 outlined the numerical methodology used in the subsequent chapters. Chapter 5 satisfied *Objective 3* by conducting an initial design and optimisation study by investigating tubercle-modified ducts with varying geometrical parameters amplitude and wavelength using CFD. This allowed for an optimal leading-edge tubercle design to be proposed for further analysis. This provided a unique contribution to the state-of-the-art, as this was the first systematic design and optimisation study of leading-edge tubercles on ducted propellers to the author's knowledge.

Chapter 6 further analysed the optimised tubercle geometry on the duct as well as investigating two tubercle-modified blade combinations based on current and previous optimisation studies as an initial attempt using high-fidelity DES. This study was used to investigation the influence of leading-edge tubercles on the hydrodynamic and noise performance of the ducted propulsor in the model scale. This provided an insight into the fundamental fluid dynamics of leading-edge tubercles in a marine ducted thruster context, therefore satisfying *Objective 4*. This was another contribution to the state-of-the-art whereby the hydrodynamic and noise performance of a marine ducted propeller with a LE tubercle modified duct was investigated, as well as in-depth fluid dynamics behaviour for the first time to the author's knowledge.

Chapter 7 further analysed the optimised tubercle geometry on the propeller blade based on current and previous optimisation studies as an initial attempt using high-fidelity DES. This study was used to investigation the influence of

leading-edge tubercles on the hydrodynamic and noise performance of the ducted propulsor in the model scale. This provided an insight into the fundamental fluid dynamics of leading-edge tubercles in a marine ducted thruster context, therefore satisfying *Objective 5*. This was another contribution to the state-of-the-art whereby the hydrodynamic and noise performance of a marine ducted propeller with LE tubercle modified blades was investigated, as well as in-depth fluid dynamics behaviour for the first time to the author's knowledge.

Chapter 8 built on the fundamental findings in the model scale analysis in Chapter 6 and 7 and expanded on this by investigating the same optimised tubercle geometry on both the duct and propeller blade in the full scale, satisfying *Objective 6*. This contributed further to the state-of-the-art by being able to compared the leading-edge tubercle modified ducted propulsors influence on hydrodynamic and noise performance in the model scale to the full scale. This was conducted for the first time to the author's knowledge.

In addition to reporting the research in this thesis, during the PhD the author has also published parts of the research in numerous respected journals and international conferences, they are listed as follows:

1. C. Stark, W. Shi and M. Troll. Cavitation funnel effect: Bio-inspired leading-edge tubercle application on ducted marine propeller blades. *Applied Ocean Research*, *116*, p.102864, 2021.

2. C. Stark, W. Shi and M. Atlar. A numerical investigation into the influence of bio-inspired leading-edge tubercles on the hydrodynamic performance of a benchmark ducted propeller. *Ocean Engineering*, *237*, p.109593, 2021.

3. C. Stark, and W. Shi. Hydroacoustic and hydrodynamic investigation of bio-inspired leading-edge tubercles on marine-ducted thrusters. *Royal Society Open Science*, *8*(9), p.210402, 2021.

4. C. Stark, Y. Xu, M. Troll, and W. Shi. Marine ducted thruster underwater radiated noise control through leading-edge tubercle blade modifications - a numerical hybrid approach. In *the 41st International Conference on Ocean, Offshore and Arctic Engineering: OMAE 2022, Hamburg, Germany.* June, 2022

5. C. Stark, and W. Shi. The influence of leading-edge tubercles on the hydrodynamic performance and propeller wake flow development of a ducted propeller. In *the 31st(2021) International Ocean and Polar Engineering Conference*: ISOPE-2021. June, 2021

6. C. Stark and W. Shi. The influence of leading-edge tubercles on the sheet cavitation development of a benchmark marine propeller. In *the 40th International Conference on Ocean, Offshore and Arctic Engineering: OMAE 2021.* June, 2021.

The author has also been involved in secondary projects which did not directly relate to the research within the thesis. The publications from the secondary projects are listed below as follows:

1. C. Stark, Y. Xu, M. Zhang, Z. Yuan, L. Tao, and W. Shi. Study on applicability of energy-saving devices to hydrogen fuel cell-powered ships. *Journal of Marine Science and Engineering*, *10*(3), p.388, 2022.

2. M. Falchi, F. Otrolani, W. Shi, C. Stark, G. Aloiso, S. Grizzi and G. Dubbioso. Experimental investigation on the effect of leading-edge tubercles on the performance of marine propellers in fully wet condition. *Ocean Engineering*, *225*, 2022.

3. M. Troll, W. Shi, and C. Stark. Leading-Edge Tubercles Applied Onto a Flapped Rudder. In *the 41st International Conference on Ocean, Offshore*

and Arctic Engineering: OMAE 2022, Hamburg, Germany. June, 2022.

4. Y. Xu, W. Shi, and C. Stark. Hydrodynamic Investigation of a Remora-Inspired Autonomous Underwater Vehicle Docking Onto a Benchmark Submarine. In *the 41st International Conference on Ocean, Offshore and Arctic Engineering: OMAE 2022, Hamburg, Germany.* June, 2022.

5. M. Troll, W. Shi, and C. Stark. The influence of leading-edge tubercles on wake flow dynamics of a marine rudder. In *the 9th International Conference on Computational Methods in Marine Engineering.* June, 2021.

6. M. Atlar, P. Fitzsimmons, P. Zoet, M. Troll, C. Stark, S. Sezen, W. Shi, B. Aktas, N. Sasaki, S. Turkmen. and D. Taylor. Underwater noise measurements with a ship retrofitted with PressurePores^{TM} noise mitigation technology and using HyDrone^{TM} system. In *the 11th International Symposium on Cavitation.* May, 2021.

In addition the the publication of journal articles and conference papers, the preliminary results prompted industrial sponsor BAE Systems Plc. to file numerous patent applications related to the innovative concepts developed throughout the course of the research study, of which the author of the thesis is a co-inventor. The published patents are listed as follows:

1. W. Shi, C. Stark, M. Troll, M. Thompson, and M. Atlar. BAE Systems Plc. *Arrangements, Duct arrangements and Methods*, WO2022018414A1, 2022.

2. W. Shi, C. Stark, M. Troll, M. Thompson, M. Atlar and L.M. Sweet. BAE Systems Plc. *An Arrangement for Influencing Liquid Flow and a Method*, WO2022018415A1, 2022.

3. W. Shi, C. Stark, M. Troll, M. Thompson, M. Atlar and L.M. Sweet. BAE Systems Plc, 2022. *An Arrangement for Influencing Liquid Flow and a Method*, WO2022018416A1, 2022.

9.2 Main Conclusions

Complimenting the conclusion and summary of each chapter stated earlier, the following are the main conclusions that can be drawn from the study within the thesis:

1. The investigations conducted within the thesis which explored the feasibility of mitigating the URN of ducted propulsors have made an original and useful contribution to the state-of-the-art research in applying the leading-edge tubercle concept for hydrodynamic and hydroacoustic performance enhancement of ducted propuslors.

2. Leading-edge tubercles applied to the duct were found to improve the noise performance of the ducted propulsor, this is largely due to the introduction of the counter-rotating streamwise vortex pairs into the propeller inflow, which disrupts the coherency of the vortex development in the propeller slipstream and encourages the dissipation in turbulent kinetic energy with minimal impact on the hydrodynamic performance of the propulsor.

3. Leading-edge tubercles applied to the propeller blades were found to improve the noise performance of the ducted propulsor, this is due to the introduction of the counter-rotating streamwise vortex pairs which funnel the sheet cavitation into the trough region and encourage cavitation-free zones behind the tubercle peaks. In addition, the propulsive efficiency of the ducted propulsor could be enhanced when comparing at the same thrust loading and load fluctuation could be reduced in cavitating conditions.

4. The wavelength and amplitude of the leading-edge tubercle design on the duct influenced the hydrodynamic performance of the duct thrust. The change in amplitude had a larger impact on the duct thrust performance than the change in wavelength. Therefore, an investigation into tubercle parameters is important to reach a balanced design.

5. The inclusion of leading-edge tubercles on the duct improved the maximum duct thrust capability at most operating conditions, the maximum at the optimum efficiency point. At this condition, the improvement was largely due to the compartmentalisation of flow separation observed on the outer side of the duct.

6. Comparing the two leading-edge tubercle blade designs where wavelength was varied, the longer wavelength reduced sheet cavitation the most at the majority of conditions considered, although the difference between the two tubercle designs was marginal. On the other hand, in some heavier-cavitating conditions, the shorter wavelength was more successful in reducing sheet cavitation due to the inclusion of the second tubercle closer to the blade root.

7. The magnitude of the hydrodynamic and hydroacoustic performance enhancement of leading-edge tubercles was influenced by the change in scale, however key general conclusions drawn from model scale investigations were confirmed in the full scale study.

9.3 Recommendations for Future Research

The research conducted and outlined in the thesis has opened avenues to further understand and optimise LE tubercles on marine propulsors. Although the author is confident that they did their best to satisfy the aim and objectives

of their thesis within the limitation of the time and resources of this project, the recommendations by the author to further the current state-of-the-art are as follows:

An investigation into leading-edge tubercle modified ducted propulsors in the behind hull condition, as the non-uniform wake can have an impact on the hydrodynamic and hydroacousitc propulsive characteristics

A direct study comparing the hydroacoustic performance and vortex breakdown of LE tubercle-modified ducts with varying tubercle geometries could further optimise the current design in terms of acoustic performance.

Although an in-depth optimisation study was conducted for tubercles as applied to the duct, an in-depth blade optimisation has yet to be conducted. This could result in further optimisation of the cavitation and noise performance of the leading-edge tubercle modified ducted propeller blade.

Optimisation study conducted in full scale non-uniform flow conditions for hydroacoustic performance as non-uniform flow conditions can change the hydrodynamic and hydro-acoustic characteristics of the ducted propulsor and potentially influence the performance enhancement capability of leading-edge tubercles.

The leading-edge tubercle ducted propeller blades would benefit from a model scale test campaign in a cavitation tunnel to validate the influence on sheet cavitation behaviour and noise signature in the numerical findings within the thesis. Further understanding of other tubercles influence on other types of cavitation mechanisms such as the collapsing of cloud cavitation and its associated noise would also be achieved due to limitations with the numerical modelling used within the present study.

An experimental model test campaign and a full scale sea trial to investigate both hydrodynamic and noise performance for both concepts would provide invaluable validation to the current work in addition to insights into LE tubercle

modified ducted propellers in conditions that would occur in real sea operations. The current numerical modelling technique neglects cloud cavitation and the associated radiated noise from the bubble collapsing due to the incompressibility assumption.

Applying the leading-edge tubercles onto other ducts such as the decelerating duct or diverging nozzles commonly found on pumpjet propulsors and other propeller designs could widen the impact of LE tubercles on the range of propulsor designs used within the maritime transport sector. In addition, applying the leading-edge tubercles onto energy saving devices such as the Gate Rudder or the Mewis Duct may provide additional benefits in off-design conditions.

Finally, it is worth bearing in mind that the fundamental mechanisms behind the performance benefit of LE tubercles have crossovers to the aerospace domain, and that it would be encouraged to further research the LE tubercle concept on aerospace blade and duct applications.

References

[1] IMO, "Guidelines for the reduction of underwater noise from commercial shipping to address adverse impacts on marine life," *Marine Environment Protection Committee (MEPC)*, 2014. 1, 13

[2] European Commission, "Commission decision (EU) 2017/848 of 17 May 2017 laying down criteria and methodological standards on good environmental status of marine waters and specifications and standardised methods for monitoring and assessment, and repealing decision 2010/477/EU," *Official Journal of the European Union L*, vol. 125, pp. 43–74, 2017. 2

[3] H. Johari, C. Henoch, D. Custodio, and A. Levshin, "Effects of leading-edge protuberances on airfoil performance," *AIAA journal*, vol. 45, no. 11, pp. 2634–2642, 2007. 4, 36, 39, 40, 45, 132

[4] D. Miklosovic, M. Murray, L. Howle, and F. Fish, "Leading-edge tubercles delay stall on humpback whale (megaptera novaeangliae) flippers," *Physics of fluids*, vol. 16, no. 5, pp. L39–L42, 2004. xvi, 4, 36, 37, 38, 39

[5] K. Hansen, R. Kelso, and C. Doolan, "Reduction of flow induced airfoil tonal noise using leading edge sinusoidal modifications," *Acoustics Australia*, vol. 40, no. 3, pp. 172–177, 2012. xvi, 4, 36, 40, 41

[6] Z. Wei, T. New, and Y. Cui, "An experimental study on flow separation

control of hydrofoils with leading-edge tubercles at low reynolds number," *Ocean Engineering*, vol. 108, pp. 336–349, 2015. xvi, 4, 39

[7] W. Shi, M. Atlar, R. Rosli, B. Aktas, and R. Norman, "Cavitation observations and noise measurements of horizontal axis tidal turbines with biomimetic blade leading-edge designs," *Ocean Engineering*, vol. 121, pp. 143–155, 2016. xvii, 4, 36, 49, 50

[8] W. Shi, R. Rosli, M. Atlar, R. Norman, D. Wang, and W. Yang, "Hydrodynamic performance evaluation of a tidal turbine with leading-edge tubercles," *Ocean Engineering*, vol. 117, pp. 246–253, 2016. 4, 36, 49

[9] C. Peng, X. Zhao, and G. Liu, "Noise in the sea and its impacts on marine organisms," *International journal of environmental research and public health*, vol. 12, no. 10, pp. 12304–12323, 2015. 10

[10] C. Erbe, S. A. Marley, R. P. Schoeman, J. N. Smith, L. E. Trigg, and C. B. Embling, "The effects of ship noise on marine mammals—a review," *Frontiers in Marine Science*, vol. 6, p. 606, 2019. 10

[11] H. Bertschneider, J. Bosschers, G. H. Choi, E. Ciappi, T. Farabee, C. Kawakita, and D. Tang, "Specialist committee on hydrodynamic noise," *Final report and recommendations to the 27th ITTC. Copenhagen, Sweden*, vol. 45, 2014. 10, 11, 73

[12] J. Carlton, *Marine propellers and propulsion*. Butterworth-Heinemann, 2018. xv, 10, 25, 77, 150, 172

[13] H. Seol, B. Jung, J.-C. Suh, and S. Lee, "Prediction of non-cavitating underwater propeller noise," *Journal of Sound and Vibration*, vol. 257, no. 1, pp. 131–156, 2002. 10, 55, 65

[14] T. Lloyd, *Large eddy simulations of inflow turbulence noise: application to tidal turbines*. PhD thesis, University of Southampton, 2013. xv, 11, 12

[15] D. Wittekind and M. Schuster, "Propeller cavitation noise and background noise in the sea," *Ocean Engineering*, vol. 120, pp. 116–121, 2016. 11

[16] Q. Zhang and R. K. Jaiman, "Numerical analysis on the wake dynamics of a ducted propeller," *Ocean Engineering*, vol. 171, pp. 202–224, 2019. xvi, 12, 30, 31, 32, 160

[17] S. Sharma, K. Mani, and V. Arakeri, "Cavitation noise studies on marine propellers," *Journal of sound and vibration*, vol. 138, no. 2, pp. 255–283, 1990. 13, 18, 19, 28

[18] S. A. Kinnas, "An international consortium on high-speed propulsion," *Marine Technology and SNAME News*, vol. 33, no. 3, p. 203, 1996. xv, 14

[19] M. A. F. Chekab, P. Ghadimi, S. R. Djeddi, and M. Soroushan, "Investigation of different methods of noise reduction for submerged marine propellers and their classification," *American journal of mechanical engineering*, vol. 1, no. 2, pp. 34–42, 2013. 14

[20] A. Ebrahimi, A. Razaghian, M. Seif, F. Zahedi, and A. Nouri-Borujerdi, "A comprehensive study on noise reduction methods of marine propellers and design procedures," *Applied Acoustics*, vol. 150, pp. 55–69, 2019. xv, 14, 18

[21] P. Andersen, J. J. Kappel, and E. Spangenberg, "Aspects of propeller developments for a submarine," in *First international symposium on marine propulsors, Trondheim, Norway*, 2009. xv, 15

[22] Renilson Marine Consulting Pty Ltd, "Reducing underwater noise pollution from large commercial vessels," 2009. xv, 15, 21, 22, 28

[23] H. W. Lerbs, "Moderately loaded propellers with a finite number of blades and a arbitrary distribution of circulations," *Trans. SNAME*, vol. 60, pp. 73–123, 1952. 15

[24] S. V. Andersen and P. Andersen, "Hydrodynamic design of propellers with unconventional geometry," *Royal Institution of Naval Architects Transactions*, vol. 129, 1987. 15

[25] P. Andersen and H. Schwanecke, "Design and model tests of tip fin propellers," 1992. 16

[26] P. Andersen, J. Friesch, J. J. Kappel, L. Lundegaard, and G. Patience, "Development of a marine propeller with nonplanar lifting surfaces," *Marine technology and SNAME news*, vol. 42, no. 03, pp. 144–158, 2005. 16

[27] P. Andersen, J. Friesch, and J. Kappel, "Development and full-scale evaluation of a new marine propeller type," in *Schiffbautechnische Gesellschaft*, pp. 465–476, Springer Verlag, 2004. 16

[28] G. Pérez and J. Gonzalez-Adalid, "Tip loaded propellers (clt) justification of their advantages over conventional propellers using the momentum theory," 1995. 16

[29] G. Gennaro and J. Gonzalez-Adalid, "Improving the propulsion efficiency by means of contracted and loaded tip propellers," *The Society of Naval Architects & Marine Engineers, Athens, Greece*, 2012. 16, 28

[30] L. Klaren and J. Sparenberg, "On optimum screw propellers with end

plates, inhomogeneous inflow," *Journal of Ship Research*, vol. 25, no. 04, pp. 252–263, 1981. 16

[31] J. A. Sparenberg and J. de Vries, "An optimum screw propeller with end-plates," *International shipbuilding progress*, vol. 34, no. 395, pp. 124–133, 1987. 17

[32] K. d. Jong, J. Sparenberg, *et al.*, "Model testing of an optimally designed propeller with two-sided shifted end plates on the blades," 1994. 17

[33] S. Gaggero, M. Viviani, D. Villa, D. Bertetta, C. Vaccaro, and S. Brizzolara, "Numerical and experimental analysis of a clt propeller cavitation behavior," in *Trabajo presentado en el CAV 2012 8th International Symposium on Cavitation*, 2012. 17

[34] D. Bertetta, S. Brizzolara, E. Canepa, S. Gaggero, and M. Viviani, "Efd and cfd characterization of a clt propeller," *International Journal of Rotating Machinery*, vol. 2012, 2012. 17

[35] J. G. Adalid and G. Gennaro, "Latest experiences with contracted and loaded tip (clt) propellers," *Sustainable M*, 2012. 17

[36] M. Atlar, P. Fitzsimmons, P. Zoet, M. Troll, C. Stark, S. Sezen, W. Shi, B. Aktas, N. Sasaki, S. Turkmen, *et al.*, "Underwater noise measurements with a ship retrofitted with pressureporestm noise mitigation technology and using hydronetm system," in *11th International Symposium on Cavitation*, 2021. xv, 18, 19, 20, 28

[37] B. Aktas, N. Yilmaz, M. Atlar, N. Sasaki, P. Fitzsimmons, and D. Taylor, "Suppression of tip vortex cavitation noise of propellers using pressurepores technology," *Journal of Marine Science and Engineering*, vol. 8, no. 3, p. 158, 2020. 18, 19, 28

[38] A. Asnaghi, U. Svennberg, R. Gustafsson, and R. E. Bensow, "Propeller tip vortex cavitation mitigation using roughness," in *MARINE VIII: proceedings of the VIII International Conference on Computational Methods in Marine Engineering*, pp. 383–392, CIMNE, 2019. 19

[39] A. Asnaghi, U. Svennberg, R. Gustafsson, and R. E. Bensow, "Investigations of tip vortex mitigation by using roughness," *Physics of Fluids*, vol. 32, no. 6, p. 065111, 2020. 19

[40] A. Asnaghi, U. Svennberg, R. Gustafsson, and R. E. Bensow, "Propeller tip vortex mitigation by roughness application," *Applied Ocean Research*, vol. 106, p. 102449, 2021. xv, 19, 20, 28

[41] S. Sezen, D. Uzun, R. Ozyurt, O. Turan, and M. Atlar, "Effect of biofouling roughness on a marine propeller's performance including cavitation and underwater radiated noise (urn)," *Applied Ocean Research*, vol. 107, p. 102491, 2021. 19, 28

[42] F. Mewis and U. Hollenbach, "Special measures for improving propulsive efficiency," *HSVA NewsWave*, vol. 1, 2006. 20, 28

[43] K. Ouchi, M. Tamashima, and K. Arai, "Reduction of propeller cavitation noise by pbcf (propeller boss cap fins)," 1991. 21

[44] M. TM, "Underwater noise comparison of pre-and post-retrofitted maersk g-class container vessels," 2017. 21

[45] Y. Sun, T. Wu, Y. Su, and H. Peng, "Numerical prediction on vibration and noise reduction effects of propeller boss cap fins on a propulsion system," *Brodogradnja: Teorija i praksa brodogradnje i pomorske tehnike*, vol. 71, no. 4, pp. 1–18, 2020. 21, 28

[46] T. Van Beek, R. Verbeek, and C. Schneiders, "Saving fuel cost: Improving propulsive efficiency with special devices and designs," 1986. 23

[47] H. Schneekluth and V. Bertram, *Ship design for efficiency and economy*, vol. 218. Butterworth-Heinemann Oxford, 1987. 23

[48] F. Çelik, "A numerical study for effectiveness of a wake equalizing duct," *Ocean Engineering*, vol. 34, no. 16, pp. 2138–2145, 2007. xv, 23

[49] F. Mewis, "A novel power-saving device for full-form vessels," in *First International Symposium on Marine Propulsors SMP*, vol. 9, pp. 443–448, 2009. xv, 23, 24, 28

[50] X. Chang, S. Sun, Y. Zhi, and Y. Yuan, "Investigation of the effects of a fan-shaped mewis duct before a propeller on propulsion performance," *Journal of Marine Science and Technology*, vol. 24, no. 1, pp. 46–59, 2019. 24

[51] R. Bontempo, M. Cardone, and M. Manna, "Performance analysis of ducted marine propellers. part i–decelerating duct," *Applied Ocean Research*, vol. 58, pp. 322–330, 2016. 25

[52] S. Gaggero, C. M. Rizzo, G. Tani, and M. Viviani, "Efd and cfd design and analysis of a propeller in decelerating duct," *International Journal of Rotating Machinery*, vol. 2012, 2012. 25

[53] M. Oosterveld, "Model tests with decelerating nozzles," *International Shipbuilding Progress*, vol. 15, no. 166, pp. 206–220, 1968. 25, 28

[54] D. Qin, G. Pan, S. Lee, Q. Huang, and Y. Shi, "Underwater radiated noise reduction technology using sawtooth duct for pumpjet propulsor," *Ocean Engineering*, vol. 188, p. 106228, 2019. xv, 26, 27, 28, 55, 65

[55] Y. Sun, W. Liu, and T.-y. Li, "Numerical investigation on noise reduction mechanism of serrated trailing edge installed on a pump-jet duct," *Ocean Engineering*, vol. 191, p. 106489, 2019. 26, 28, 55, 65

[56] S. Ianniello, R. Muscari, and A. Di Mascio, "Ship underwater noise assessment by the acoustic analogy. part i: nonlinear analysis of a marine propeller in a uniform flow," *Journal of marine science and technology*, vol. 18, no. 4, pp. 547–570, 2013. 29, 55, 65, 68, 70, 104, 105, 112, 121

[57] S. Sezen, T. Cosgun, A. Yurtseven, and M. Atlar, "Numerical investigation of marine propeller underwater radiated noise using acoustic analogy part 1: The influence of grid resolution," *Ocean Engineering*, vol. 220, p. 108448, 2021. xvii, 29, 67, 68, 70, 105

[58] S. E. Widnall, "The stability of a helical vortex filament," *Journal of Fluid Mechanics*, vol. 54, no. 4, pp. 641–663, 1972. xvi, 29, 30

[59] P. Watts, F. E. Fish, *et al.*, "The influence of passive, leading edge tubercles on wing performance," in *Proc 12th Internat Symp Unmanned Untethered Submersible Tech. Durham, NH: Autonomous Undersea Systems Institute*, 2001. 36, 37

[60] I. Ibrahim and T. New, "Tubercle modifications in marine propeller blades," in *10th Pacific Symposium on Flow Visualization and Image Processing*, pp. 1–11, Naples, Italy, 2015. 36, 50, 173

[61] N. Charalambous and I. Eames, "A computational analysis of a marine propeller with tubercle and its contribution in reducing sheet cavitation," in *Sixth International Symposium on Marine Propulsors*, Rome, Italy, 2019. 36, 50, 51

[62] M. J. Stanway, "Hydrodynamic effects of leading-edge tubercles on control surfaces and in flapping foil propulsion," Master's thesis, Massachusetts Institute of Technology, 2008. 36, 38

[63] P. W. Weber, L. E. Howle, M. M. Murray, *et al.*, "Lift, drag, and cavitation onset on rudders with leading-edge tubercles," *Marine technology*, vol. 47, no. 1, pp. 27–36, 2010. xvi, 36, 41, 43, 44, 45, 49, 52

[64] K. L. Hansen, R. M. Kelso, and B. B. Dally, "Performance variations of leading-edge tubercles for distinct airfoil profiles," *AIAA journal*, vol. 49, no. 1, pp. 185–194, 2011. 36, 40, 45

[65] F. R. Butt and T. Talha, "Numerical investigation of the effect of leading-edge tubercles on propeller performance," *Journal of Aircraft*, vol. 56, no. 3, pp. 1014–1028, 2019. 36

[66] L. Bellequant and L. E. Howle, "Whalepower wenvor blade," 2009. 36

[67] M. Ibrahim, A. Alsultan, S. Shen, and R. S. Amano, "Advances in horizontal axis wind turbine blade designs: introduction of slots and tubercle," *Journal of Energy Resources Technology*, vol. 137, no. 5, 2015. 36

[68] W. Shi, M. Atlar, R. Norman, B. Aktas, and S. Turkmen, "Numerical optimization and experimental validation for a tidal turbine blade with leading-edge tubercles," *Renewable Energy*, vol. 96, pp. 42–55, 2016. 36

[69] W. Shi, M. Atlar, and R. Norman, "Detailed flow measurement of the field around tidal turbines with and without biomimetic leading-edge tubercles," *Renewable Energy*, vol. 111, pp. 688–707, 2017. xvii, 36, 49, 50

[70] H. Carreira Pedro and M. Kobayashi, "Numerical study of stall delay on

humpback whale flippers," in *46th AIAA aerospace sciences meeting and exhibit*, p. 584, 2008. 38

[71] N. Rostamzadeh, K. Hansen, R. Kelso, and B. Dally, "The formation mechanism and impact of streamwise vortices on naca 0021 airfoil's performance with undulating leading edge modification," *Physics of Fluids*, vol. 26, no. 10, p. 107101, 2014. 38

[72] K. L. Hansen, N. Rostamzadeh, R. M. Kelso, and B. B. Dally, "Evolution of the streamwise vortices generated between leading edge tubercles," *Journal of Fluid Mechanics*, vol. 788, pp. 730–766, 2016. 38

[73] D. S. Miklosovic, M. M. Murray, and L. E. Howle, "Experimental evaluation of sinusoidal leading edges," *Journal of aircraft*, vol. 44, no. 4, pp. 1404–1408, 2007. 40, 50

[74] H. Arai, Y. Doi, T. Nakashima, and H. Mutsuda, "A study on stall delay by various wavy leading edges," *Journal of aero aqua bio-mechanisms*, vol. 1, no. 1, pp. 18–23, 2010. 40

[75] H. Yoon, P. Hung, J. Jung, and M. Kim, "Effect of the wavy leading edge on hydrodynamic characteristics for flow around low aspect ratio wing," *Computers & Fluids*, vol. 49, no. 1, pp. 276–289, 2011. 40

[76] A. S. Lau, S. Haeri, and J. W. Kim, "The effect of wavy leading edges on aerofoil–gust interaction noise," *Journal of Sound and Vibration*, vol. 332, no. 24, pp. 6234–6253, 2013. 41

[77] J. Wang, C. Zhang, Z. Wu, J. Wharton, and L. Ren, "Numerical study on reduction of aerodynamic noise around an airfoil with biomimetic structures," *Journal of Sound and Vibration*, vol. 394, pp. 46–58, 2017. 41

[78] D. Custodio, C. Henoch, and H. Johari, "Cavitation on hydrofoils with leading edge protuberances," *Ocean Engineering*, vol. 162, pp. 196–208, 2018. xvii, 43, 44, 45, 46, 49

[79] D. Li, Q. Yang, W. Yang, H. Chang, and H. Wang, "Bionic leading-edge protuberances and hydrofoil cavitation," *Physics of Fluids*, vol. 33, no. 9, p. 093317, 2021. 45

[80] A. S. Brown, "from whales to fans," *Mechanical Engineering*, vol. 133, no. 05, pp. 24–29, 2011. 48

[81] L. E. Howle, "Whalepower wenvor blade: A report on the efficiency of a whalepower corp. 5 meter prototype wind turbine blade," 2009. 48

[82] F. E. Fish, P. W. Weber, M. M. Murray, and L. E. Howle, "The tubercles on humpback whales' flippers: application of bio-inspired technology," 2011. xvii, 49, 52

[83] W. Shi, *Biomimetic improvement of hydrodynamic performance of horizontal axis tidal turbines*. PhD thesis, Newcastle University, 2017. 50, 126, 172

[84] D. Ross and W. Kuperman, "Mechanics of underwater noise," 1989. 55

[85] S. Sezen, M. Atlar, P. Fitzsimmons, N. Sasaki, G. Tani, N. Yilmaz, and B. Aktas, "Numerical cavitation noise prediction of a benchmark research vessel propeller," *Ocean Engineering*, vol. 211, p. 107549, 2020. 55, 60, 63, 65, 70, 71, 102, 112

[86] J. Sørensen, "2.08 - aerodynamic analysis of wind turbines," in *Comprehensive Renewable Energy* (A. Sayigh, ed.), pp. 225–241, Oxford: Elsevier, 2012. 56

[87] M. A. G. Terán, E. Olguín-Díaz, A. Flores-Abad, and M. Nandayapa, "Experimental validation of an aerodynamic sectional modeling approach in fixed-wing unmanned aerial vehicles," *IEEE Access*, vol. 6, pp. 74190–74203, 2018. xvii, 57

[88] D. Zhao, N. Han, E. Goh, J. Cater, and A. Reinecke, "Chapter 1 - general introduction to wind turbines," in *Wind Turbines and Aerodynamics Energy Harvesters* (D. Zhao, N. Han, E. Goh, J. Cater, and A. Reinecke, eds.), pp. 1–20, Academic Press, 2019. 57

[89] F. Stern, H. Kim, V. Patel, and H. Chen, "A viscous-flow approach to the computation of propeller-hull interaction," *Journal of Ship Research*, vol. 32, no. 04, pp. 246–262, 1988. 58

[90] S. Goldstein, "On the vortex theory of screw propellers," *Proceedings of the Royal Society of London. Series A, Containing Papers of a Mathematical and Physical Character*, vol. 123, no. 792, pp. 440–465, 1929. 58, 98

[91] G. Hough and D. Ordway, "The generalized actuator disk," tech. rep., THERM ADVANCED RESEARCH INC ITHACA NY, 1964. 58

[92] S. Sezen, A. Dogrul, C. Delen, and S. Bal, "Investigation of self-propulsion of darpa suboff by rans method," *Ocean Engineering*, vol. 150, pp. 258–271, 2018. 58, 63

[93] R. Bontempo, M. Cardone, M. Manna, and G. Vorraro, "Ducted propeller flow analysis by means of a generalized actuator disk model," *Energy Procedia*, vol. 45, pp. 1107–1115, 2014. 58

[94] StarCCM+, "User guide," *SIEMENS*, 2020. xvii, 59, 61, 63, 70, 84, 85, 88, 93, 94, 95

[95] A. Bhattacharyya, V. Krasilnikov, and S. Steen, "A cfd-based scaling approach for ducted propellers," *Ocean Engineering*, vol. 123, pp. 116–130, 2016. 60, 63, 119, 120

[96] A. Bhattacharyya, J. C. Neitzel, S. Steen, M. Abdel-Maksoud, and V. Krasilnikov, "Influence of flow transition on open and ducted propeller characteristics," in *Fourth International Symposium on Marine Propulsors, Austin, Texas, USA*, 2015. 60, 63

[97] S. Sezen and O. K. Kinaci, "Incompressible flow assumption in hydroacoustic predictions of marine propellers," *Ocean Engineering*, vol. 186, p. 106138, 2019. 63, 64, 70, 91, 121

[98] F. Menter, "Zonal two equation kw turbulence models for aerodynamic flows," in *23rd fluid dynamics, plasmadynamics, and lasers conference*, p. 2906, 1993. 63, 91

[99] R. Muscari and A. Di Mascio, "Detached eddy simulation of the flow behind an isolated propeller," in *Third International Symposium on Marine Propulsors*, pp. 218–226, University of Tasmania, Lanceston Tasmania, Australia, 2013. 63

[100] E. Guilmineau, G. B. Deng, A. Leroyer, P. Queutey, M. Visonneau, and J. Wackers, "Wake simulation of a marine propeller," in *11th World Congress on computational mechanics*, 2014. 63, 147

[101] M. Breuer, N. Jovičić, and K. Mazaev, "Comparison of des, rans and les for the separated flow around a flat plate at high incidence," *International journal for numerical methods in fluids*, vol. 41, no. 4, pp. 357–388, 2003. 63, 152

[102] Z. L. Nitzkorski, *A novel porous Ffowcs-Williams and Hawkings acoustic methodology for complex geometries*. PhD thesis, University of Minnesota, 2015. 65

[103] J. F. Williams and D. L. Hawkings, "Sound generation by turbulence and surfaces in arbitrary motion," *Philosophical Transactions for the Royal Society of London. Series A, Mathematical and Physical Sciences*, pp. 321–342, 1969. 65, 103

[104] M. J. Lighthill, "On sound generated aerodynamically i. general theory," *Proceedings of the Royal Society of London. Series A. Mathematical and Physical Sciences*, vol. 211, no. 1107, pp. 564–587, 1952. 65

[105] A. Hirschberg and S. W. Rienstra, "An introduction to aeroacoustics," *Eindhoven university of technology*, vol. 5600, 2004. 66

[106] A. K. Lidtke, *Predicting radiated noise of marine propellers using acoustic analogies and hybrid Eulerian-Lagrangian cavitation models*. PhD thesis, University of Southampton, 2017. xvii, 66, 74, 105

[107] P. Di Francescantonio, "A new boundary integral formulation for the prediction of sound radiation," *Journal of Sound and Vibration*, vol. 202, no. 4, pp. 491–509, 1997. 66, 104

[108] F. Farassat, "Derivation of formulations 1 and 1a of farassat," tech. rep., 2007. 66, 104

[109] V. Krasilnikov, "Cfd modeling of hydroacoustic performance of marine propellers: Predicting propeller cavitation," in *Proceedings of the 22nd Numerical Towing Tank Symposium, Tomar, Portugal*, vol. 29, 2019. 67, 70, 105

[110] S. Ianniello, R. Muscari, and A. Mascio, "Hydroacoustic characterization of a marine propeller through the acoustic analogy," *Sustainable Maritime Transportation and Exploitation of Sea Resources*, pp. 991–1000, 2012. 67, 70, 104, 121

[111] A. K. Lidtke, T. Lloyd, and G. Vaz, "Acoustic modelling of a propeller subject to non-uniform inflow," in *Proc. 6th Int. Symp. Mar. Propulsors, SMP'19, Rome, Italy*, 2019. 68, 70, 71, 112

[112] S. Sezen, T. Cosgun, A. Yurtseven, and M. Atlar, "Numerical investigation of marine propeller underwater radiated noise using acoustic analogy part 2: The influence of eddy viscosity turbulence models," *Ocean Engineering*, vol. 220, p. 108353, 2021. 68, 70, 105

[113] S. Sezen, *Marine propeller hydrodynamic and hydroacoustic performance with roughness effects*. PhD thesis, University of Strathclyde, 2022. 68, 70

[114] D.-Q. Li, J. Hallander, and T. Johansson, "Predicting underwater radiated noise of a full scale ship with model testing and numerical methods," *Ocean Engineering*, vol. 161, pp. 121–135, 2018. 71

[115] N. Sakamoto and H. Kamiirisa, "Prediction of near field propeller cavitation noise by viscous cfd with semi-empirical approach and its validation in model and full scale," *Ocean Engineering*, vol. 168, pp. 41–59, 2018. 71

[116] G. Tani, M. Viviani, M. Felli, F. H. Lafeber, T. Lloyd, B. Aktas, M. Atlar, S. Turkmen, H. Seol, J. Hallander, *et al.*, "Noise measurements of a cavitating propeller in different facilities: Results of the round robin test programme," *Ocean Engineering*, vol. 213, p. 107599, 2020. 71

[117] F. H. Lafeber, J. Bosschers, and E. van Wijngaarden, "Computational and

experimental prediction of propeller cavitation noise," in *OCEANS 2015-Genova*, pp. 1–9, IEEE, 2015. 71

[118] F. H. Lafeber and J. Bosschers, "Validation of computational and experimental prediction methods for the underwater radiated noise of a small research vessel," in *Proceedings of PRADS*, 2016. 71

[119] J. Bosschers, *Propeller tip-vortex cavitation and its broadband noise*. PhD thesis, University of Twente, 2018. 71

[120] B. Aktas, *A systematic experimental approach to cavitation noise prediction of marine propellers*. PhD thesis, Newcastle University, 2017. 73

[121] ITTC, "Recommended procedures and guidelines procedure," in *International Towing Tank Conference*, 2014. 73, 113

[122] P. W. Weber, L. E. Howle, M. M. Murray, and D. S. Miklosovic, "Computational evaluation of the performance of lifting surfaces with leading-edge protuberances," *Journal of Aircraft*, vol. 48, no. 2, pp. 591–600, 2011. 146, 152

[123] J. Jeong and F. Hussain, "On the identification of a vortex," *Journal of fluid mechanics*, vol. 285, pp. 69–94, 1995. 158

[124] P. J. Roache, *Verification and validation in computational science and engineering*, vol. 895. Hermosa Albuquerque, NM, 1998. 114

[125] L. F. Richardson, "Ix. the approximate arithmetical solution by finite differences of physical problems involving differential equations, with an application to the stresses in a masonry dam," *Philosophical Transactions of the Royal Society of London. Series A, Containing Papers of a Mathematical or Physical Character*, vol. 210, no. 459-470, pp. 307–357, 1911. 114

[126] I. B. Celik, U. Ghia, P. J. Roache, and C. J. Freitas, "Procedure for estimation and reporting of uncertainty due to discretization in cfd applications," *Journal of fluids Engineering-Transactions of the ASME*, vol. 130, no. 7, 2008. 114, 115

[127] ITTC, "Recommended procedures and guidelines procedure," in *International Towing Tank Conference*, 1999. 114

[128] J. Moulijn, J. Bosschers, S. Tornros, C. Schreiber, D. Grassi, I. Goedbloed, and M. Bijlard, "Validation studies of a boundary element method for ducted propellers," in *Sixth International Symposium on Marine Propulsors, SMP*, vol. 19. xviii, 120, 121

[129] M. Abdel-Maksoud and H. Heinke, "Scale effects on ducted propellers," in *Proceedings of the 24th symposium on naval hydrodynamics*, pp. 744–759, 2002. 120

[130] F. Mewis and T. Guiard, "Mewis duct–new developments, solutions and conclusions," in *Second International Symposium on Marine Propulsors, Hamburg, Germany*, 2011. 97

[131] W. M. Batten, M. Harrison, and A. Bahaj, "Accuracy of the actuator disc-rans approach for predicting the performance and wake of tidal turbines," *Philosophical Transactions of the Royal Society A: Mathematical, Physical and Engineering Sciences*, vol. 371, no. 1985, p. 20120293, 2013. 98

[132] A. Travin, M. Shur, M. Strelets, and P. Spalart, "Physical and numerical upgrades in the detached-eddy simulation of complex turbulent flows," in *Advances in LES of complex flows*, pp. 239–254, Springer, 2002. 85

[133] P. L. Seidel, *Ueber ein verfahren, die gleichungen, auf welche die methode*

der kleinsten quadrate führt, sowie lineäre gleichungen überhaupt, durch successive annäherung aufzulösen, vol. 11. Verlag d. Akad., 1873. 87

[134] C. F. Curtiss and J. O. Hirschfelder, "Integration of stiff equations," *Proceedings of the National Academy of Sciences*, vol. 38, no. 3, pp. 235–243, 1952. 86

[135] P. R. Spalart and C. L. Rumsey, "Effective inflow conditions for turbulence models in aerodynamic calculations," *AIAA journal*, vol. 45, no. 10, pp. 2544–2553, 2007. 92

[136] P. R. Spalart, "Comments on the feasibility of les for wings, and on a hybrid rans/les approach," in *Proceedings of first AFOSR international conference on DNS/LES*, Greyden Press, 1997. 92

[137] S. Sezen, M. Atlar, and P. Fitzsimmons, "Prediction of cavitating propeller underwater radiated noise using rans & des-based hybrid method," *Ships and Offshore Structures*, vol. 16, no. sup1, pp. 93–105, 2021. 95

[138] M. L. Shur, P. R. Spalart, M. K. Strelets, and A. K. Travin, "A hybrid rans-les approach with delayed-des and wall-modelled les capabilities," *International journal of heat and fluid flow*, vol. 29, no. 6, pp. 1638–1649, 2008. 92, 93